Studies of quarkonium production and polarisation with early data at ATLAS

Darren David Price

MA(Cantab) MSc

Particle Physics Group

Department of Physics

September 2008

A thesis submitted to Lancaster University for the degree of
Doctor of Philosophy in the Faculty of Science and Technology

CERN-THESIS-2008-098
13/11/2008

Contents

List of Figures

List of Tables

Studies of quarkonium production and polarisation with early data at ATLAS.

Darren David Price MA(Cantab) MSc

A thesis submitted for the degree of Doctor of Philosophy, September 2008

Abstract

This thesis presents a range of studies of the production cross-section and polarisation of quarkonium at the ATLAS experiment at the LHC. As data-taking has not yet begun, these studies are conducted on fully simulated and reconstructed Monte Carlo samples.

The main studies of this thesis are an analysis of the production cross-sections of J/ψ and Υ mesons at ATLAS with 10 pb^{-1} of data, along with an analysis of the polarisation of the J/ψ and Υ that can provide information towards understanding the underlying QCD production mechanism. In addition, we are able to predict the observability of the three χ_c states through its radiative decays to J/ψ.

I present details of a new method of data-driven muon reconstruction efficiency determination using Inner Detector tracking information in quarkonium decays, and studies into the uses of quarkonia for detector performance, commissioning and data quality monitoring.

Using a new method of measuring the polarisation distribution that reduces systematic errors, 10 pb^{-1} of data (corresponding to around one week of well-calibrated data-taking) will allow the J/ψ polarisation to be measured to an accuracy of $0.02 - 0.06$ (dependent on the level of polarisation itself). This is competitive with the best measurements published from the Tevatron, but with just $1/100^{\text{th}}$ the integrated luminosity and at higher transverse momenta than probed at any previous experiment. Similar sensitivities are expected for Υ polarisation with 100 pb^{-1} of data. The differential production cross-sections at such integrated luminosities are expected to be measured to an accuracy of 1%.

Declaration

No portion of the work referred to in this thesis has been submitted in support of an application for another degree or qualification at this or any other institute of learning.

1. Copyright in text of this thesis rests with the Author. Copies (by any process) either in full, or of extracts, may be made **only** in accordance with instructions given by the Author and lodged in the Lancaster University Library. Details may be obtained from the Librarian. This page must form part of any such copies made. Further copies (by any process) made in accordance with such instructions may not be made without the permission (in writing) of the Author.

2. The ownership of any intellectual property rights which may be described in this thesis is vested in Lancaster University, subject to any prior agreement to the contrary, and may not be made available for use by third parties without the written permission of the University, which will prescribe the terms and conditions of any such agreement.

The Author

The author was educated at St. Joseph's RC Comprehensive School, Port Talbot, before reading Mathematics at Sidney Sussex College, University of Cambridge. The author then obtained an MSc with distinction in Experimental Particle Physics at the University of Manchester, before joining the High Energy Physics group at Lancaster University in 2005.

The work presented in this thesis was conducted at Lancaster University and CERN, Geneva between October 2005 and September 2008.

The author goes on to take up a postdoctoral fellowship with Indiana University, working jointly on the DØ experiment at Fermilab, Chicago and the ATLAS experiment at CERN, Geneva.

Acknowledgments

First and foremost I would like to thank my supervisor Vato Kartvelishvili for his support, guidance and advice throughout my PhD. His extraordinary patience with my many questions, and our common indulgence of many an hour spent investigating some strange effect in some reconstructed distribution or efficiency plot whilst other deadlines loomed near, helped unquantifiably to improve my overall understanding and inspire new analysis strategies and techniques.

Thanks also must go to Mária Smižanská, to whom I owe much for her advice and the opportunities she provided me through my activities with the ATLAS B-Physics group during my attachment to CERN.

I would also like to thank James Catmore, both for his assistance in teaching me to use the ATLAS software and the grid during my first year, which was invaluable, and for his continued willingness to indulge my questions ever since. Thanks also to Eva Bouhova-Thacker and Rob Henderson at Lancaster University for their help and advice with software, for interesting discussions and enjoyable lunches!

I am grateful for the friendship of all those people with whom I have spent the last three years, both in the UK and in Geneva, in particular (and in strictly alphabetical order!): Alastair, Chris T, Dave, David, Freya, Georgie, James K, Laurence, Lee, Ruth, Sean, Sue and Tim W.

I am also indebted to the Science and Technology Facilities Council (formerly the Particle Physics and Astronomy Research Council) for funding my research and my two-year attachment to CERN.

This research would not have been possible without the work of the entire ATLAS Collaboration, for building, commissioning and study of the detector, development of the software framework and the tremendous wealth of continuing activity in detector and physics studies that will allow exciting and meaningful results to be obtained from such a complex endeavour.

Finally, I thank my parents for their continuing and unfailing support and encouragement in everything I do, without which none of this would be possible, and to whom this thesis is dedicated.

Darren D. Price, September 2008

Dedicated to my parents.

1

Introduction

In late 2008 the Large Hadron Collider (LHC) at CERN, Geneva will start colliding intense beams of protons at far higher energies than its natural predecessor, the Tevatron, near Chicago, Illinois, ushering in a new era of high energy particle physics. At various collision points around the accelerator ring are positioned complex detectors, which will be used to analyse the outcome of these collisions. Their purpose is to attempt to extend our knowledge of our universe through study of the known fundamental particles and forces of nature. The LHC will allow for further high precision tests of quantum chromodynamics (QCD), electroweak interactions, and flavour physics. The unprecedented energies and rates will allow for in-depth study of top quark physics, a variety of searches for the Higgs boson or the underlying mechanism for electroweak symmetry breaking, searches for new gauge bosons, supersymmetric particles and the possibility of extra dimensions.

This thesis is concerned with early data studies using one of the detectors at the LHC, the ATLAS detector, focusing on investigations of the production properties of quark-antiquark bound states known as quarkonium and applications of these particles to the vast commissioning and calibration effort underway for the various detector, trigger, and software components of ATLAS as a whole.

In the following chapter I give an overview of the Standard Model of particle physics and detail the motivations for studying quarkonia, first from a historical standpoint and then in the context of recent theoretical predictions and experimental results. Chapter 3 presents an overview of the ATLAS detector and introduces its main sub-detector systems. Chapter 4 documents some of the Monte Carlo tuning and simulations I performed for quarkonium production in ATLAS along with studies of the main lowp_T background processes relevant to the analysis, ending with predicted Monte Carlo-level cross-section predictions for these processes at ATLAS. Following this, Chapter 5 discusses the reconstruction of these events once they have passed through the ATLAS detector simulation, including details of trigger and efficiency studies, along with methods of background separation and suppression.

After reconstruction and event selection are performed, J/ψ and Υ may be used for a wide variety of data quality and commissioning tasks with early data in ATLAS. Chapter 6 includes an overview of some of these early data performance and data quality studies I have been involved in: using quarkonia for study of Inner Detector vertexing performance, a new method of muon identification and reconstruction efficiency measurement from data, identification of misalignments and material distortions in ATLAS, and monitoring of the high level trigger algorithms.

Chapter 7 combines the studies from prior chapters to present a new method of measuring both the prompt J/ψ and Υ production cross-sections and the polarisation of these quarkonium states, to greater precision than currently available, in kinematic regimes never before investigated. I also present an initial study of the observability of χ_c and χ_b states at ATLAS in radiative decays to J/ψ and Υ respectively.

Chapter 8 summarises the expected yields of quarkonia we expect to see in early data, performance studies that will be undertaken and expected sensitivity and range of production cross-section and polarisation measurements of J/ψ and Υ at ATLAS. I provide a brief outlook of the expected results at integrated luminosities of 10 pb^{-1} and 100 pb^{-1}, and measurements at higher luminosities.

Finally, Appendix A contains details of related software studies I performed on electron tracking algorithms for Inner Detector tracking performance focusing on the handling of bremsstrahlung in ATLAS, that do not naturally fit into the main narrative of the thesis.

Contributions to publications

The studies performed for this thesis led to significant contributions to a number of publications. My contributions to publications [1] and [2] are based on the studies described in Chapter 4. Contributions from Chapters 5 and 6 are included in publications [3] and [4]. The analysis performed in Chapters 5 and 7 led to the publications [5] and [6].

"Nothing happens at random, but everything from reason and by necessity."

Leucippus, c. 500 B.C.

2

Theoretical motivations

This chapter begins with an overview of the Standard Model of particle physics before focusing on the main theoretical ideas underpinning the study of quarkonium production, detailing first the determined properties of quarkonia and then the various models proposed for the production of quarkonium bound states in light of experimental evidence, ending with the current state of theory and experiment as motivation for study at the LHC.

2.1 The Standard Model of particle physics

The Standard Model is a non-abelian broken gauge theory based on the gauge symmetry group $SU(3)_C \otimes SU(2)_L \otimes U(1)_Y$ representing the current model of strong and electroweak interactions, where C is the colour charge, L refers to the left handed coupling of the weak isospin doublets, and Y is the weak hypercharge. We require the Lagrangian describing the theory to have both a global symmetry such that the Lagrangian remains invariant under the same gauge transformations at every space-time point, and a local symmetry allowing different transformation parameters at different space-time points.

The theory comprises three 'generations' of particles (of increasing mass) each containing a pair of leptons and a pair of quarks (as well as their antiparticles), and the gauge bosons. The left-handed chirality parts of the particles transform as doublets:

$$
\begin{array}{lccccc}
 & & \text{GENERATION} & & & \text{CHARGE} \\
 & \text{I} & \text{II} & \text{III} & & \\
\text{QUARKS} & \begin{pmatrix} u \\ d \end{pmatrix}_L & \begin{pmatrix} c \\ s \end{pmatrix}_L & \begin{pmatrix} t \\ b \end{pmatrix}_L & & \begin{array}{c} +\frac{2}{3} \\ -\frac{1}{3} \end{array} \\
\text{LEPTONS} & \begin{pmatrix} \nu_e \\ e^- \end{pmatrix}_L & \begin{pmatrix} \nu_\mu \\ \mu^- \end{pmatrix}_L & \begin{pmatrix} \nu_\tau \\ \tau^- \end{pmatrix}_L & & \begin{array}{c} 0 \\ -1 \end{array}
\end{array}
$$

whilst the right-handed parts transform as singlets under $SU(2)_L$ symmetry. The e^-, μ^- and τ^- all have electric charge -1 (in units of e, the charge of an electron) whilst the neutrino (ν) has no charge. The up, charm and top quarks we call 'up-type quarks' and have charge $+\frac{2}{3}$, the down, strange and bottom quarks we call 'down-type quarks' and have charge $-\frac{1}{3}$. Note that by convention neutrinos do not have right-handed components in the Standard Model as the weak force couples only to the left-handed chirality fields and neutrinos are assumed to be massless[1)].

The interactions between the quarks and leptons are mediated by the exchange of virtual gauge vector bosons associated with the four fundamental forces of nature: the electromagnetic

[1)]Experiments have shown that the neutrinos do indeed have mass, although very small. Studies into the nature of neutrino mass, how this mass is generated and the implications this has to the wider field of particle physics are extremely active areas of research, but are beyond the scope of this thesis.

force (mediated by the photon), the weak force (mediated by the $W^{\pm}$ and Z bosons), the strong force (mediated by eight gluons g_i) and gravitation, which is not yet incorporated within the Standard Model but plays no significant role at the scales and energies involved in high energy particle physics.

Noether's Theorem implies that each conserved quantity we observe in our theories represents a global symmetry. From classical field theory we have a conserved quantity called charge which gives the global symmetry. The gauge bosons in the Standard Model arise from our application of the gauge principle from which we require this global symmetry to be elevated to a local symmetry.

The 'spontaneous' breaking of the symmetry in the Standard Model is a result of allowing gauge bosons (and leptons and quarks through Yukawa couplings) to acquire mass without violating gauge invariance and whilst retaining the renormalisability of the theory. The effect of this spontaneous symmetry breaking is to reduce the gauge structure of the Standard Model to one described by the group $SU(3)_C \otimes U(1)_Q \otimes SU(2)_L$, where Q is the electric charge.

2.1.1 Quantum Electrodynamics

Quantum Electrodynamics (QED) is an abelian gauge invariant theory based on the $U(1)_Q$ symmetry group, which describes the interaction between electrically charged fermions and the photon. QED is motivated by symmetry principles linked to the conservation of electric charge. Consider first the Dirac Lagrangian with no interactions,

$$\mathscr{L}_D = \overline{\psi}(x)(i\gamma_\mu \partial^\mu - m)\psi(x) \tag{2.1}$$

(where ψ is a Dirac spinor representing the fermion fields, m is the mass parameter associated with these fields and the γ_i are the Dirac gamma matrices).

Now suppose we insist on a *local* phase invariance under $U(1)$ transformations such that

$\psi \xrightarrow{U(1)} e^{i\theta(x)}\psi$, then we find that as constructed the Lagrangian is not symmetric:

$$m\overline{\psi}\psi \quad \xrightarrow{U(1)} \quad m\overline{\psi}\psi \tag{2.2}$$

$$\overline{\psi}\gamma_\mu\partial^\mu\psi \quad \xrightarrow{U(1)} \quad \overline{\psi}\gamma_\mu((i\partial^\mu\theta)\psi + \partial^\mu\psi). \tag{2.3}$$

To correct this, we replace ∂_μ with D_μ (called the covariant derivative) and we define D_μ with the property that $D_\mu\psi \xrightarrow{U(1)} e^{i\theta}D_\mu\psi$ and introduce a vector field A_μ such that the choice

$$D_\mu = \partial_\mu + ieA_\mu \tag{2.4}$$

will make the Lagrangian invariant so long as a suitable transformation for A_μ is chosen:

$$A_\mu \xrightarrow{U(1)} A'_\mu = A_\mu + \frac{1}{e}\partial_\mu\theta \tag{2.5}$$

Our simple requirement of $U(1)$ gauge symmetry now gives us an interaction term

$$\mathscr{L}_D \xrightarrow{U(1)} \mathscr{L}'_D = \mathscr{L}_D - eA_\mu\overline{\psi}\gamma^\mu\psi \tag{2.6}$$

between the new field A_μ and the fermion field in the Lagrangian of our previously non-interacting theory. By demanding invariance of the theory under spacetime-dependent phase transitions we have added dynamics to the previously non-interacting theory.

This new field is made physical by adding a kinetic term to the Lagrangian of $-\frac{1}{4}F_{\mu\nu}F^{\mu\nu}$ where $F_{\mu\nu} = \partial_\mu A_\nu - \partial_\nu A_\mu$ is the field strength tensor. A mass term $\frac{1}{2}m_A^2 A_\mu A^\mu$ is disallowed by gauge symmetry[2)], so the gauge boson represented by this field must be massless. We can now identify this massless gauge boson as being the photon which mediates the electromagnetic interaction, and the Lagrangian as being that which describes Quantum Electrodynamics.

[2)] As this field was introduced to keep the symmetry, we should not break it now.

2.1.2 The weak interaction

The weak interaction is a flavour-changing, parity-violating fundamental force of nature, associated with three spin-1 massive bosons which mediate the force. Of these three vector bosons, the $W^{\pm}$ (carrying a charge of ± 1) mediate charged-current interactions, while the neutral vector boson Z mediates the neutral-current interactions. The $W^{\pm}$ and Z couple to both leptons and quarks as well as to each other. The weak interaction is (maximally) parity violating as its mediating bosons only couple to left handed fermions.

The term "weak interaction" came from the observed lifetimes of some reactions such as the pion decay $\pi^- \to \mu^- \overline{\nu}_\mu$, which were seen to be much longer than that from any other type of known interaction, providing evidence that an additional force with a weak coupling strength must exist. The weak interaction (and in particular nuclear β-decay) was originally described by a Fermi four-point coupling, which originally did not incorporate parity violation and was ultimately insufficient to explain the lifetimes of the interactions.

Replacement of the four-point interaction with a mediating boson exchange, of considerable mass, led to a more comprehensive theory of weak interactions and eventually the unification of the electromagnetic and weak forces via these mediating bosons in a framework described by Glashow, Weinberg and Salam in the 1960's.

2.1.3 Electroweak unification

Glashow, Weinberg and Salam proposed [7] the unification of the electromagnetic and weak forces into a single gauge field theory, known as electroweak theory. The simplest group structure that allows for a parity-violating weak force and a parity-conserving electromagnetic force was $SU(2)_L \otimes U(1)_Y$. At the time, only charged-current ($W^{\pm}$) interactions had been observed, but the theory also predicted the existence of neutral-current interactions that were subsequently seen in neutrino scattering experiments [8].

With the discovery [9] of the $W^{\pm}$ and Z bosons by UA1 and UA2 at CERN in 1983, electroweak theory became established. An important issue that remained was by what mechanism the Z and $W^{\pm}$ get their substantial mass (latest global fit results [10] give $M_Z = 91.1876 \pm 0.0021$ GeV and $M_{W^{\pm}} = 80.398 \pm 0.025$ GeV).

2.1.4 Electroweak symmetry breaking

The Lagrangian for electroweak theory originally contains terms for massless fermions as well as massless gauge bosons. Bare mass terms in the Lagrangian are not permitted as these would break gauge invariance, as in QED. A way was needed to introduce masses to the $W^{\pm}$ and Z (but not the photon), whilst retaining gauge invariance and renormalisability of the theory. The solution was electroweak symmetry breaking. This mechanism allows us to spontaneously break the $SU(2)_L \otimes U(1)_Y$ symmetry to a $U(1)_Q$ symmetry in a way that allows us to exactly preserve the original electromagnetic symmetry whilst associating masses to the vector bosons associated with the weak interaction.

In a similar manner to QED, we may introduce a general (covariant) Lagrangian for the symmetry group

$$\mathscr{L}_\phi = (D_\mu \phi)^\dagger (D^\mu \phi) + \mu^2 \phi^\dagger \phi - \frac{\lambda}{4}(\phi^\dagger \phi)^2 - \frac{1}{4}\mathbf{F}_{\mu\nu} \cdot \mathbf{F}^{\mu\nu} - \frac{1}{4} G_{\mu\nu} G^{\mu\nu} \tag{2.7}$$

where ϕ is a complex scalar $SU(2)$ doublet containing fields associated with the creation and annihilation of both charged and neutral particles in the theory. The covariant derivative is given by $D_\mu \phi = (\partial_\mu + ig\tau \cdot \mathbf{W}_\mu/2 + ig' B_\mu/2)\phi$ where the τ are the Pauli matrices and the g and g' are gauge coupling constants for the $\mathbf{W}_\mu$ and B_μ fields respectively. The $\mathbf{W}$ represent the $SU(2)_L$ gauge fields and the B represents the $U(1)_Y$ gauge field. The corresponding field strength tensors are given by $\mathbf{F}^{\mu\nu} = \partial^\mu \mathbf{W}^\nu - \partial^\nu \mathbf{W}^\mu - g\mathbf{W}^\mu \times \mathbf{W}^\nu$ and $G^{\mu\nu} = \partial^\mu B^\nu - \partial^\nu B^\mu$. A particular choice of fields for ϕ, utilising local gauge freedom is then introduced

$$\phi = \sqrt{\frac{1}{2}} \begin{pmatrix} 0 \\ v + H(x) \end{pmatrix} \tag{2.8}$$

to spontaneously break the symmetry via a non-vanishing vacuum expectation value $v = \sqrt{2/\lambda}\mu$. The neutral Higgs field $H(x)$ arises from perturbations about this minimum. Substituting into the Lagrangian for ϕ and keeping kinetic and mass terms we find:

$$\begin{aligned}
\mathscr{L}_{EW} &= \frac{1}{2}(\partial_\mu H)^\dagger(\partial^\mu H) + \mu^2 H^2 \\
&\quad -\frac{1}{4}F_{1\mu\nu}F_1^{\mu\nu} + \frac{1}{8}g^2v^2W_{1\mu}W_1^\mu \\
&\quad -\frac{1}{4}F_{2\mu\nu}F_2^{\mu\nu} + \frac{1}{8}g^2v^2W_{2\mu}W_2^\mu \\
&\quad -\frac{1}{4}F_{3\mu\nu}F_3^{\mu\nu} - \frac{1}{4}G_{\mu\nu}G^{\mu\nu} + \frac{1}{8}v^2(gW_{3\mu} - g'B_\mu)(gW^{3\mu} - g'B^\mu)
\end{aligned} \tag{2.9}$$

From the first line in this Lagrangian we can see we have introduced a new scalar field with an undetermined mass $\sqrt{2}\mu$, that we identify as the Higgs boson[3)]. The components W_1 and W_2, from the weak sector in the unbroken theory, acquire a mass $M_{W_1} = M_{W_2} = gv/2 \equiv M_W$ and we see that the B_μ and the W_3 quantum-mechanically mix to produce the combination $gW_3 - g'B$ with a particular mass. We can separate this mixed state into two decoupled fields in the Lagrangian by defining:

$$Z^\mu = \cos\theta_W W_3^\mu + \sin\theta_W B^\mu \tag{2.10}$$

$$A^\mu = -\sin\theta_W W_3^\mu + \cos\theta_W B^\mu \tag{2.11}$$

where

$$\cos\theta_W \equiv g/(g^2+g'^2)^{1/2}, \qquad \sin\theta_W \equiv -g'/(g^2+g'^2)^{1/2} \tag{2.12}$$

and in this way we can redefine the last line of Equation 2.9 as:

$$-\frac{1}{4}F_{Z\mu\nu}F_Z^{\mu\nu} + \frac{1}{8}v^2(g^2+g'^2)Z_\mu Z^\mu - \frac{1}{4}F_{\mu\nu}F^{\mu\nu} \tag{2.13}$$

where we define $F_{Z\mu\nu} = \partial_\mu Z_\nu - \partial_\nu Z_\mu$ and $F_{\mu\nu} = \partial_\mu A_\nu - \partial_\nu A_\mu$.

[3)] Introducing a scalar Higgs also has the effect of cancelling the divergence in WW scattering processes that would otherwise violate unitarity at a centre-of-mass energy of around 1 TeV.

Then we can read off the masses $M_Z = \frac{1}{2}v(g^2+g'^2)^{1/2} = M_W/\cos\theta_W$ and $M_A = 0$, which we identify as the massive Z boson and massless photon A_μ respectively. The degree of mixing between the neutral gauge fields is determined by the weak mixing angle θ_W and the charged-current interactions are mediated by the combinations $W^\pm = (W_1 \pm iW_2)/\sqrt{2}$ corresponding to the physical $W^\pm$ bosons.

The Higgs mechanism generates masses not only for the gauge bosons, but also for the fermions. Direct mass terms for fermions are, as previously mentioned, not allowed due to gauge-invariance. However, the Lagrangian before symmetry breaking does allow Yukawa couplings of the Higgs doublet ϕ to either quark doublets and up- or down-type quark singlets, or to a lepton doublet and a charged lepton singlet. After spontaneous symmetry breaking the Yukawa couplings become mass terms of the form $(m_X)_{ij}\overline{X}_{Li}X_{Rj}$, where the X_k are either all up-type quarks, all down-type quarks, or a particular lepton. In this way the electron, muon and tau acquire mass[4)]. Note however, that charged-current interactions change the flavour of the mass eigenstates of the quarks. The quark weak eigenstates q that couple to the W can be re-expressed in terms of the mass eigenstates q' by the Cabibbo-Kobayashi-Maskawa (CKM) matrix [11], a unitary matrix V satisfying the condition $V^\dagger V = \mathbb{1}$. It describes this mixing in the quark sector and is given by

$$\begin{pmatrix} d' \\ s' \\ b' \end{pmatrix} = \begin{pmatrix} V_{ud} & V_{us} & V_{ub} \\ V_{cd} & V_{cs} & V_{cb} \\ V_{td} & V_{ts} & V_{tb} \end{pmatrix} \begin{pmatrix} \mathrm{d} \\ \mathrm{s} \\ \mathrm{b} \end{pmatrix} \tag{2.14}$$

where the V_{ij} are complex constants that are related to the amplitudes of the transition from a quark of flavour i to a quark of flavour j. Complex terms in the CKM matrix suggest the presence of CP-violation in the quark sector, something that has been demonstrated successfully at a number of experiments [12].

[4)] Note that we are left with massless neutrinos, as in the Standard Model there are no $SU(2)$ singlet right-handed neutrinos, which are a requirement for a mass term such as for the electron.

2.1.5 Quantum Chromodynamics

Quantum Chromodynamics (QCD) is the gauge field theory based on the $SU(3)$ gauge group, which describes the strong interactions of coloured quarks and gluons, and is one of the components of the Standard Model. Its structure is similar to that of QED except that the gauge group is non-Abelian and hence gluons can have self-interactions. As such, the theory has the properties of asymptotic freedom [13] at short distances and confinement of quarks, which ensure that only colour singlet states propagate over macroscopic distances.

The Lagrangian density describing the interactions of quarks and gluons in QCD is:

$$\mathscr{L}_{QCD} = -\frac{1}{4}F^{(a)}_{\mu\nu}F^{(a)\mu\nu} + i\sum_q \overline{\psi^i_q}\gamma^\mu(D_\mu)_{ij}\psi^j_q - \sum_q m_q\overline{\psi^i_q}\psi_{qi} + \mathscr{L}_{gauge} + \mathscr{L}_{ghost} \tag{2.15}$$

where

$$F^{(a)}_{\mu\nu} = \partial_\mu A^a_\nu - \partial_\nu A^a_\mu - g_s f_{abc} A^b_\mu A^c_\nu \tag{2.16}$$

$$(D_\mu)_{ij} = \delta_{ij}\partial_\mu + ig_s\sum_a \frac{(\lambda^a)_{ij}}{2}A^a_\mu \tag{2.17}$$

and where $\mathscr{L}_{gauge}$ and $\mathscr{L}_{ghost}$ represent the gauge-fixing and resultant Faddeev-Popov ghost terms respectively. The interaction terms of the theory result from imposing local gauge invariance on the classical Lagrangian density for non-interacting quarks and gluons.

The ψ^i_q are the 4-component Dirac spinors associated with the quark fields (of colour i and flavour q) and the A^a_μ represent the eight gluon fields. The form of the kinetic term $-\frac{1}{4}F^{(a)}_{\mu\nu}F^{(a)\mu\nu}$, required for invariance of the Lagrangian, ensures that gluons are self-interacting via three- and four-point vertices, giving rise to the property of asymptotic freedom: a significant departure from the $U(1)_Y$ case of QED where no self-interaction is possible due to the commutation of the field operators.

The f_{abc} are the structure constants that, along with the Gell-Mann matrices λ satisfying the property $[\lambda_a, \lambda_b] \equiv 2i f_{abc}\lambda_c$, define the Lie algebra of $SU(3)$. From this Lagrangian density, Feynman rules for QCD can be derived. Apart from gluon self interaction vertices, the only difference from the QED rules is the additional colour structure.

Running of the coupling constant α_s

The QCD coupling constant in Equations 2.16 and 2.17 is denoted by g_s and by convention is usually substituted (in analogy with the fine structure constant from QED) with $\alpha_s \equiv g_s^2/(4\pi)$. The strong coupling constant α_s becomes larger as the energy scale of the interaction decreases due to the anti-screening effect of the gluon self-interaction. As such, the 'running' of α_s with a given scale μ goes like [14]:

$$\alpha_s(\mu) \simeq \frac{2\pi}{(11 - \frac{2}{3}n_f)\ln(\mu/\Lambda)} \tag{2.18}$$

where n_f is the number of active quark flavours below μ, and Λ is the intrinsic QCD scale usually denoted Λ_{QCD} with a value of around $200-400$ MeV. The strong coupling constant diverges when μ approaches Λ_{QCD} and as such perturbative QCD calculations cannot be carried out in these low energy regimes. In this region the expansion parameter α_s is no longer small, so the perturbation approximation is no longer valid.

Quark masses

An important set of parameters in the QCD Lagrangian are the quark masses. The quarks are generally divided into the light ($m_Q \ll \Lambda_{QCD}$: up, down and strange) and heavy ($m_Q \gg \Lambda_{QCD}$: charm, bottom, top). The light quark masses are difficult to calculate precisely as it is both hard to define what is meant by a free quark mass and, as they lie in the non-perturbative Λ_{QCD} region, energy from non-perturbative gluons play the dominant role in contributing to any hadron mass that may contain light quarks. The quark masses are couplings of the QCD Lagrangian[5)] and to be used in physical calculations should be defined in a physical way. For their analogue in QED, the electron, this poses no serious ambiguity as we can take the classical limit as the mass. Due to confinement, no such procedure makes sense for quarks.

[5)] There is no gauge-invariant way of including gluon masses however, as there is for the photon in QED.

It might seem appropriate to use the pole mass as a definition of the quark mass, where m_q is defined as the pole of the quark propagator $i(\not{p}+m_q)/(p^2-m_q^2)$. This definition is gauge-invariant and infrared safe [15, 16] but is problematic as the definition is related to the concept of the mass of a free quark, not seen in nature. It has the additional problem that for energy scales near this pole mass this is meaningful, but generates a running of the mass at higher scales. Another possibility is to simply use the constituent quark mass. This definition takes from measured hadron masses a best fit for each of the quark masses, given the quark content of each of the hadrons considered. The constituent mass is effectively a physical definition at very low Q^2 (as close to the pole as is possible to achieve). This method assumes that the mass of a hadron is completely determined by the quark content however, and ignores contributions from the dynamical effects of confinement.

A common and successful definition of the quark mass is based on the $\overline{MS}$ scheme [17], which regulates QCD with the use of dimensional regularisation at a renormalisation scale μ. Using chiral perturbation theory one can calculate ratios of quark masses to determine the so-called current-quark masses. Current estimates of the (current-quark) light masses using the $\overline{MS}$ mass independent subtraction scheme at a scale $\mu = 2$ GeV give ranges of:

$$m_u = 1.5 - 3.0 \text{ MeV} \qquad m_d = 3 - 7 \text{ MeV} \qquad m_s = 95 \pm 25 \text{ MeV} \tag{2.19}$$

The heavy quark masses are better known and in this scheme have values of:

$$m_c = 1.25 \pm 0.09 \text{ GeV} \qquad m_b = 4.70 \pm 0.07 \text{ GeV} \qquad m_t = 172.5 \pm 2.7 \text{ GeV} \tag{2.20}$$

Other methods of defining the quark masses include the ‘threshold mass’ [18, 19] approach, which resolves the $\overline{MS}$ shortcomings in describing non-relativistic quarks.

At both current and future B-physics experiments, determination of the values of the bottom and charm quark masses and their uncertainties will become increasingly important for precise measurement of the CKM parameters and the search for new physics.

2.2 From quarks to quarkonium

Prior to the successes of the Standard Model and of QCD however, there was much uncertainty about how to explain the panoply of hadrons that had been discovered in the fifties. First the particles were grouped depending on their properties, in a method, proposed independently by Murray Gell-Mann and Yuval Ne'eman, known as "the eight-fold way" that organised the baryons and mesons into octets. From this composition came the suggestion that the structure of the groups could be explained by the existence of the fundamental particles we now know as quarks, and from which the hadrons are constructed.

Direct searches for free quarks failed due to what we now understand to be the phenomenon of confinement. As such, it was unclear whether the quark formalism represented a useful mathematical tool or whether the quarks had a true existence. With evidence for partons from deep inelastic scattering experiments at SLAC in 1969 and the discovery of asymptotic freedom in strong interactions in 1973, the case for the physicality of quarks was growing.

A time of greater understanding began with the introduction of the GIM mechanism (named after its proposers Glashow, Iliopoulos and Maiani [20]) that proposed the existence of a fourth quark, the charm quark, to eliminate the unobserved but otherwise predicted tree-level flavour changing neutral currents in theories of the time. Although largely ignored when first announced in 1974, it was the GIM mechanism which was to prove to be a turning point in the eventual acceptance of the quark model.

It was the discovery [21] in late 1974 of a resonance at 3.1 GeV in the energy distribution of electron-positron pairs at Brookhaven National Laboratory (with subsequent verification from Stanford Linear Accelerator Center (SLAC) [22]) (see Figure 2.1), confirming the presence of a new particle now known as the J/ψ, which eventually secured the quark's place as a fundamental particle in the emerging theories.

After the J/ψ discovery, its properties presented intriguing questions: the J/ψ could decay hadronically, so why was the total width so much smaller than would be expected in usual hadronic decays? Indeed, the total width included the contribution from leptonic decays too

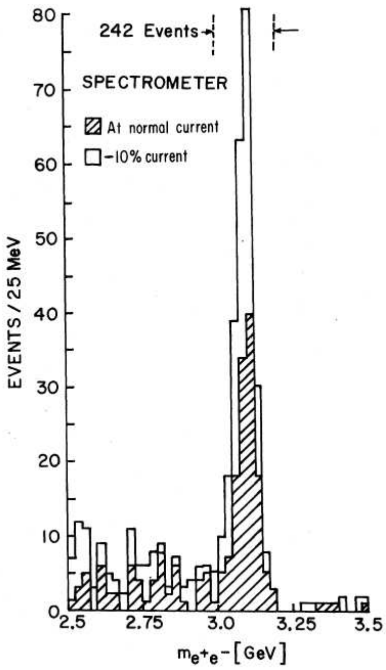

(a) BNL J/ψ signal

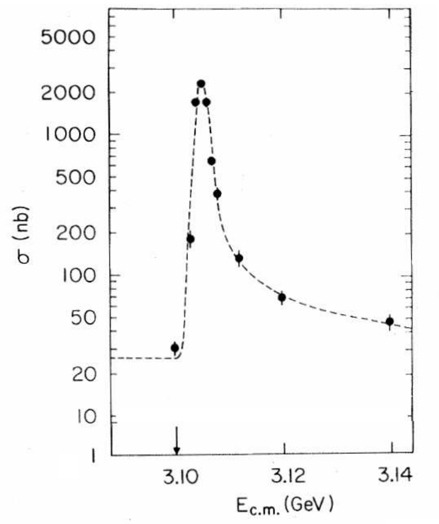

(b) SLAC J/ψ signal

Figure 2.1: *Illustration of the first observation in 1974 of the J/ψ in (a) the di-electron mass spectrum from Brookhaven National Laboratory ($p+Be$ collisions) [21] and (b) cross-section versus centre-of-mass energy at SLAC (e^+e^- collisions) with J/ψ going to a hadronic final state [22].*

which were quite significant (of order 6% for both *ee* and $\mu\mu$ modes) – why were the leptonic modes competitive with the hadronic modes?

To understand this, consider that the heavy quark pair will annihilate into the smallest number of gluons permissible. A decay via a single gluon is disallowed due to colour conservation; two gluons are not allowed as this decay would violate C-parity. This means that the lowest order strong decay that can occur is via three gluon decay (which subsequently decay into light quark pairs). However, gluon emission from heavy quarks is known to be suppressed: Okubo, Zweig, and Iizuka (OZI) [23] independently suggested a rule in the 1960's, that strong interaction processes where the final states can only be reached through quark-antiquark annihilation are suppressed. Rephrased, this means that strongly occurring processes in which a Feynman diagram can be split into two by cutting only internal gluon lines will be suppressed.

In contrast, leptonic decays do not suffer such restrictions: quarkonium decay may proceed via a single photon, and while this decay would normally be suppressed by additional $\alpha_{\rm em}$ terms the suppression of strong decays from the OZI rule makes the contribution from leptonic modes comparable. Due to the conditions on the hadronic decay, quarkonia have a lifetime far longer than would otherwise be expected if OZI-suppression were not to be an issue and as lifetime is inversely proportional to decay width this explains why the width of the J/ψ is narrower than would otherwise be expected. Happily, the large leptonic branching fraction of the J/ψ and Υ is what makes them easily extractable from the large hadronic background at modern colliders and thus the subject of this thesis.

The discovery of the J/ψ was soon followed by the discovery of the $\psi(2S)$ in the same di-electron decay mode. The χ_c states were found later, from the decay of $\psi(2S)$, seen via the detection of the radiated photon. The picture was becoming clearer but at this point charm was still hidden in charm-anticharm bound states. It became understood that the lightest open charm meson (a bound state of a charm and light quark, here labelled D) would be found above 1843 MeV due to the narrow width of the $\psi(2S)$ (so could not be decaying into D pairs), which ensured $2m_D > m(\psi(2S))$. The upper bound came from the R ratio plateau (see below) where four quark flavours became active. The D_0 meson was eventually found in $K^{\pm}\pi^{\mp}$ decays by Goldhaber [24] in 1976 and has a mass of 1864 ± 0.4 MeV. Measurement of other D mesons followed, and measurement of their properties further validated the existence of charm.

R is the ratio of the total cross-section of producing hadrons in e^+e^- collisions normalised to the cross-section of the reaction $e^+e^- \to \mu^+\mu^-$ at a given centre-of-mass energy $\sqrt{s}$, shown in Equation 2.21.

$$R(s) = \frac{\sigma(e^+e^- \to \text{hadrons})(s)}{\sigma(e^+e^- \to \mu^+\mu^-)(s)} \tag{2.21}$$

Measurements of R are sensitive to the hadronic decays of resonant states as well as providing information on specific quark flavours. The J/ψ resonance at SLAC had a much larger R-ratio on resonance than off, implying that J/ψ had direct hadronic decays. The R parameter was a source of additional tests of the quark model – at low energies R can be approximated by

$$R \approx n_c \sum_{n_f} Q_f^2 \tag{2.22}$$

where n_c is the number of colours, n_f is the number of active flavours and Q_f is the charge of the quark. This model thus predicts a ratio of two for $n_f = 3$ (u, d, s) if quarks had the property of colour, and crucially a new plateau at a value of $10/3$ once the charm quark was active, and additional plateaus with each heavier quark activation.

These quark plateaus can be seen in Figure 2.2, which shows the R ratio experimentally measured[6)] in three regions: the u, d, s quark region; the region where the effects of the charm quark plays its role and where the resonances from various charmonium states can be seen; and the region where beauty quarks and bottomonium play a role.

The analogue to charmonia in the beauty sector was first seen with the discovery [26] of the $\Upsilon(1S)$ at Fermilab in 1977, with excited states again following soon after. As for J/ψ, the Υ was narrower than expected due to the same OZI mechanism, whereas the $\Upsilon(4S)$ state, above the flavour threshold for open beauty (allowing decays to two B mesons) has a natural width three orders of magnitude higher than other Υ states (see Figure 2.2).

The Standard Model picture of heavy quarks is not complete without mention of the top quark. The final quark predicted in the third generation, its discovery had to wait until CDF published evidence [27] of its production in 1994, constraining the top mass to be approximately 174 GeV. After charm- and bottomonium discoveries, a natural extension was to search for 'toponium' [28]. With the CDF results it was clear that a $t\bar{t}$ bound state could not exist. At masses greater than around 130 GeV the lifetime of the single top is shorter than the annihilation time of a $t\bar{t}$ state and as such cannot form a bound state before decaying, largely via $t \rightarrow b + W$.

[6)] Most experimental results did not use Equation 2.21 as written, but instead used an approximation where the denominator was replaced with the leading-order QED result $\frac{4\pi\alpha^2}{3s}$ to reduce statistical errors. This approximate relation is often written R_{had} to distinguish it from the full QCD-derived term.

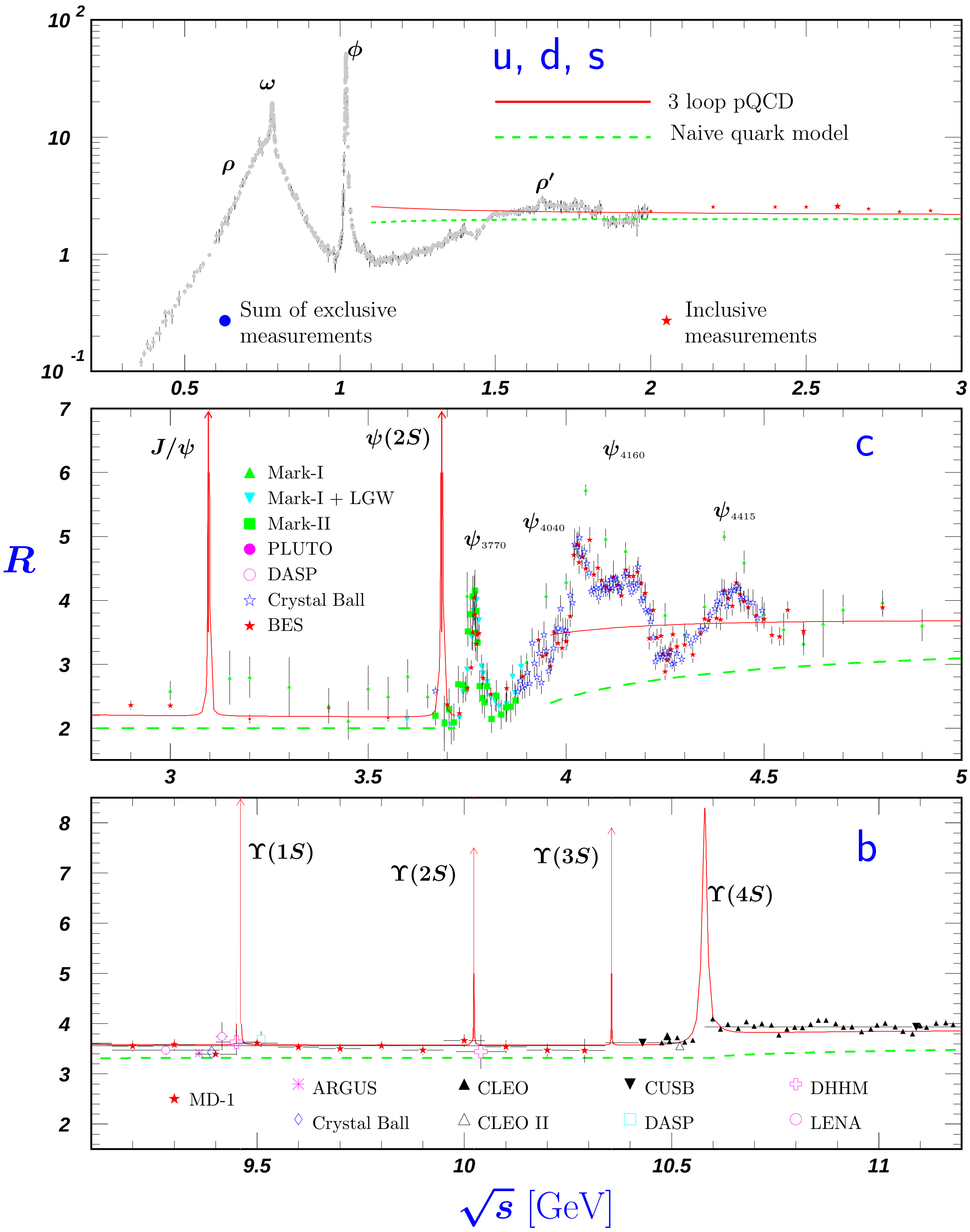

Figure 2.2: *R in the light-flavour, charm, and beauty threshold regions [25].*

2.3 The quarkonium spectrum

In the framework of QCD for a non-relativistic system, a quarkonium state can be characterised by S the total spin of the quark-antiquark pair, L the total orbital angular momentum and J the total angular momentum (where $\mathbf{J} = \mathbf{L} + \mathbf{S}$). Charge conjugation $C = (-1)^{L+S}$ and parity $P = (-1)^{L+1}$ are exactly conserved quantities in this framework. Heavy quarkonia are believed to be a largely non-relativistic system and thus are normally labelled using such numbers using the notation J^{PC} and sometimes with the additional information of isospin, I, and G-parity[7)], G, in the form I^G. At leading order, the quarkonium bound state is assumed to be formed of a quark-antiquark pair. As such, the pair must be in an angular momentum state consistent with the quantum numbers with the meson; this provides an additional spectroscopic notation $n^{2S+1}L_J$ (n here is the principal quantum number).

Meson name	$n^{2S+1}L_J$	$I^G(J^{PC})$	Mass (MeV)	Full width
η_c	1^1S_0	$0^+(0^{-+})$	2980.4 ± 1.2	25.5 ± 3.4 MeV
J/ψ	1^3S_1	$0^-(1^{--})$	3096.916 ± 0.011	93.4 ± 2.1 keV
$\chi_{c0}(1P)$	1^3P_0	$0^+(0^{++})$	3414.76 ± 0.35	10.4 ± 0.7 MeV
$\chi_{c1}(1P)$	1^3P_1	$0^+(1^{++})$	3510.66 ± 0.07	0.89 ± 0.05 MeV
$\chi_{c2}(1P)$	1^3P_2	$0^+(2^{++})$	3556.20 ± 0.09	2.06 ± 0.12 MeV
$\psi(2S)$	2^3S_1	$0^-(1^{--})$	3686.093 ± 0.034	337 ± 13 keV
η_b	1^1S_0	$0^+(0^{-+})$	$9388.9^{+3.1}_{-2.3} \pm 2.7$ [29]	Undetermined
$\Upsilon(1S)$	1^3S_1	$0^-(1^{--})$	9460.30 ± 0.26	54.02 ± 1.25 keV
$\chi_{b0}(1P)$	1^3P_0	$0^+(0^{++})$	$9859.44 \pm 0.42 \pm 0.31$	Undetermined
$\chi_{b1}(1P)$	1^3P_1	$0^+(1^{++})$	$9892.78 \pm 0.26 \pm 0.31$	Undetermined
$\chi_{b2}(1P)$	1^3P_2	$0^+(2^{++})$	$9912.21 \pm 0.26 \pm 0.31$	Undetermined
$\Upsilon(2S)$	2^3S_1	$0^-(1^{--})$	10023.26 ± 0.31	31.98 ± 2.63 keV
$\chi_{b0}(2P)$	2^3P_0	$0^+(0^{++})$	$10232.5 \pm 0.4 \pm 0.5$	Undetermined
$\chi_{b1}(2P)$	2^3P_1	$0^+(1^{++})$	$10255.46 \pm 0.22 \pm 0.50$	Undetermined
$\chi_{b2}(2P)$	2^3P_2	$0^+(2^{++})$	$10268.65 \pm 0.22 \pm 0.50$	Undetermined
$\Upsilon(3S)$	3^3S_1	$0^-(1^{--})$	10355.2 ± 0.5	20.32 ± 1.85 keV

Table 2.1: *Properties and standard notation of quarkonia significant to these studies.*

Table 2.1 summarises the properties [25] of the quarkonia of interest in this study along with their quantum number labels. Note that as the $J^{PC} = 1^{--}$ states have the same quantum

7) G-parity is defined by $G = Ce^{i\pi I_2}$, where I_2 is the operator associated with the second component of the isospin vector. It can be visualised as a rotation by π in isospin space, coupled with a charge conjugation.

numbers as the electromagnetic current, they can be produced as resonances in e^+e^- systems, which is indeed how they were first found.

Evidence for the η_b state included in Table 2.1 has recently been released by the BABAR Collaboration [29], from observation of the radiative decay of $\Upsilon(3S) \to \gamma\eta_b$. As of the present time, very little information has been collected on this state.

In contrast, the properties and decays of the $^3S_1$ states are extremely well-known. The most precise single mass determinations of J/ψ and $\psi(2S)$ dominate the global average and come from a specifically-designed experiment KEDR [30], which uses a resonance depolarisation technique to drastically reduce systematic error on the measurement. The results of the experiment give $m(J/\psi) = 3096.917 \pm 0.010 \pm 0.007$ MeV and $m(\psi') = 3686.111 \pm 0.025 \pm 0.009$ MeV. Similar studies have been conducted at CUSB, OLYA and DORIS using the same technique to achieve high precision $\Upsilon(1S)$ [31, 32], $\Upsilon(2S)$ [32, 33] and $\Upsilon(3S)$ [32] mass measurements.

The charm-anticharm bound states first received their name when a paper [34] describing the new mesons was published in 1974 that called them "charmonium" for the first time, making an analogy to positronium which exhibits a similar bound state structure as in Figure 2.3. Figures 2.3 and 2.4 together give a summary of the spectrum of quarkonium states and their decays as we understand them today.

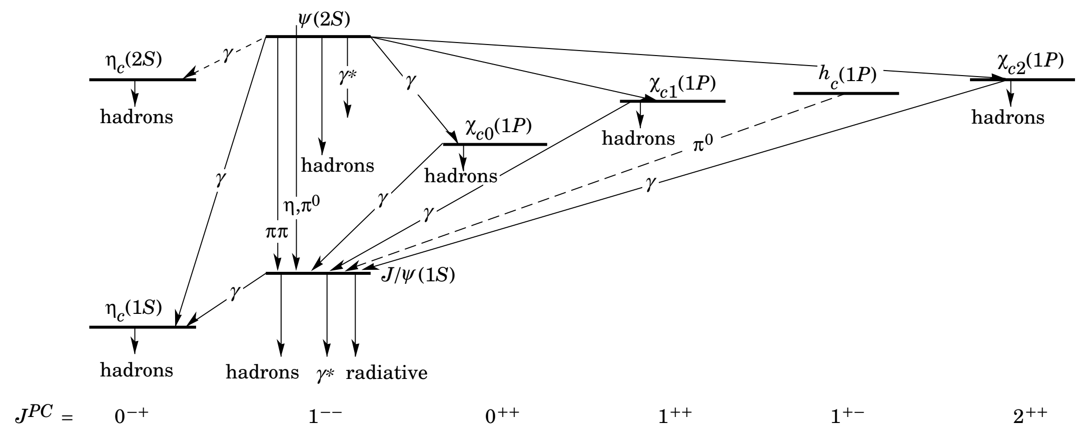

Figure 2.3: *Diagram of the charmonium system, illustrating the decay modes of the various $c\bar{c}$ states below the open charm threshold [25].*

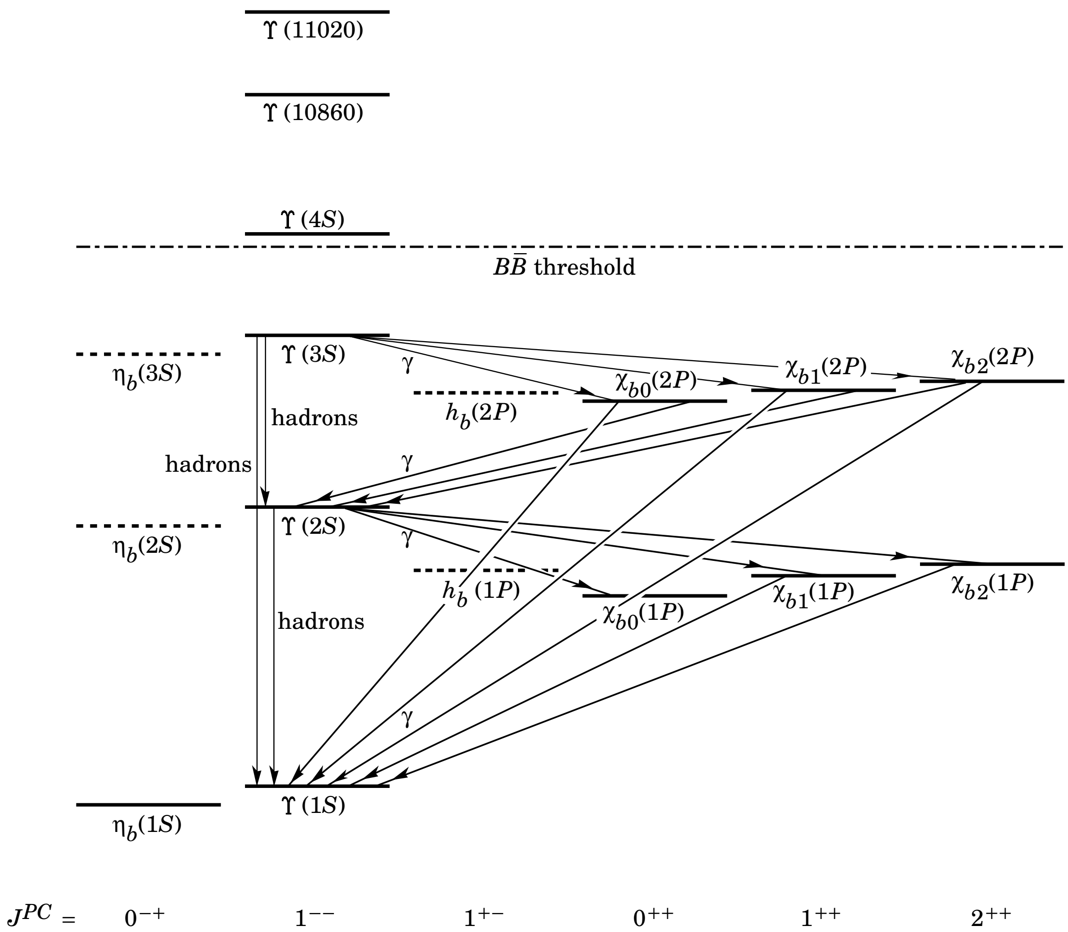

Figure 2.4: *Diagram of the bottomonium system, illustrating the decay modes of the various $b\bar{b}$ states. The threshold for open beauty production is shown along with Υ bound states above this threshold [25].*

2.4 Quarkonium production

The production of any given quarkonium state is believed to be factorisable into two parts: the first, where a heavy quark and antiquark pair are produced, is driven by perturbative QCD; the second, concerning the formation of a physical bound state, is under the auspices of non-perturbative QCD and models have been proposed, with varying degrees of success, to explain the properties of quarkonium production. With precise measurements of quarkonia and a large quantity of data available, the mechanism underlying the production of quarkonia still remains elusive, being more complicated than initially expected.

Much theoretical interest over the years since the discovery of J/ψ has brought a number of approaches to the study of quarkonium production. In this section I outline some of the main techniques and models, their predictive power and relevant experimental results. For brevity, I limit myself to discussion of results and predictions for hadronic collisions, although these techniques have application to quarkonium production at fixed-target experiments, e^+e^- annihilation and deep inelastic scattering and in various other processes. Review articles [35, 36, 37] are available that cover these topics in detail.

2.4.1 Potential models

An observation was made by Appelquist and Politzer [38] that quarks should form positronium-like bound states. Like positronium, the quarkonia have various spin states with different energy levels. As such, it was felt that quarkonium could help with the understanding of hadronic dynamics in the same way that the hydrogen atom played a central role in the understanding of atomic physics. In the least complicated model one assumes that the quark dynamics can be determined by treating quarkonia as a non-relativistic system, applying the Schrödinger equation with particular choices of potential.

Leading non-relativistic approximation

In the leading non-relativistic approximation, quarkonium is modelled as a quark and antiquark positioned a distance r away from each other. For the non-relativistic picture to hold, r should be smaller than the size of a typical hadron, $\Lambda_{\mathrm{QCD}}^{-1} \sim 1$ fm. For heavy quarks, the size of a bound state is small ($r = 0.2 - 1.0$ fm): the large mass ensures the bound state is small enough to be considered an asymptotically free system (an assumption that does not hold for light quarks). At leading order, the interquark force is dominated by the exchange of a gluon. The exchange of gluons between the two slow quarks is analogous to the electromagnetic interaction in QED, described by the Coulomb potential:

$$V_{em}(r) = -\frac{\alpha_{em}}{r} \tag{2.23}$$

Because of confinement however, it is clear that the interaction between quarks can not be completely described by a simple analogy to the Coulomb law for electrical charges. To model confinement, it is necessary that the gluonic Coulomb-type interaction be amended with a term $f(r)$ increasing with charge separation, resulting in the form of the potential shown in Equation 2.24. This model was originally proposed for charmonium and is detailed in references [38, 39].

$$V_s(r) = -\frac{4}{3}\frac{\alpha_s(r)}{r} + f(r) \tag{2.24}$$

The factor of $4/3$ arises from the SU(3) colour factors. The Coulombic term must take into account the running of $\alpha_s(r)$. The form of this coupling in this Coulomb-like framework has been calculated [40] at the one and two-loop level.

Particular formulations of this basic model have been investigated by various groups. One of the most widely known forms of the potential in Equation 2.24 is the Cornell potential (from references [41, 42]), which has

$$V_s(r) = -\frac{a}{r} + \frac{r}{b^2} \tag{2.25}$$

with numerical coefficients $a = 0.52$, $b = 2.34$ GeV^{-1}. This model, with refinements can describe the fine and hyperfine structures of charmonium levels, but can only define these features down to a certain level of precision within the leading non-relativistic treatment.

Power potentials such as $V_s(r) = A + Br^{0.1}$ (as in reference [43]) have also had some success in describing the quarkonium spectra, as have logarithmic potentials which try to account for various additional QCD effects [44, 45].

One can use the Schrödinger equation with one of these potential models to retrieve the binding energy solutions (and hence the mass spectra) as well as the quarkonium wavefunction $\Psi(r) = \Psi_{nL}(r).Y_{Lm}(\theta,\phi)$, where r is the three-dimensional separation between quark and antiquark in the bound state, and $\Psi_{nL}(r)$ and $Y_{Lm}(\theta,\phi)$ are the radial and orbital parts of the wavefunction respectively.

Figure 2.5 shows the wavefunctions calculated from various potential models for the J/ψ and $\psi(2S)$. These wavefunctions play a key role in predictions of cross-sections in the models

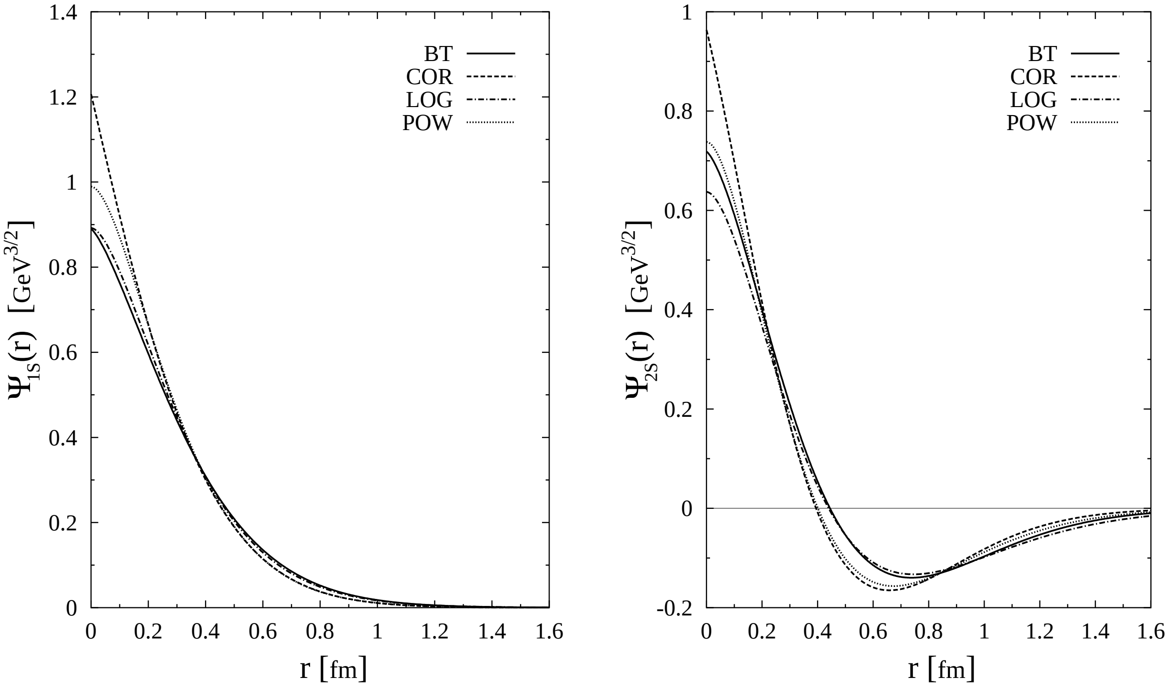

(a) $J/\psi(1S)$ (b) $\psi(2S)$

Figure 2.5: *Radial wave function $\Psi_{nL}(r)$ for the (a) $J/\psi(1S)$ and (b) $\psi(2S)$ states (taken from reference [46]) for: two logarithmic potentials, BT [47] and LOG [44]; the Cornell [41] potential and a power law [43] potential.*

of quarkonium production. Note the uncertainties in the wavefunctions at the origin, the values of which can differ by around 25–35% by using different forms of the potential, despite being in good agreement at larger distances. Such potential models are inherently limited however, as they neglect contributions from relativistic and quantum effects, in particular spin dependence and mixing between S and D states.

Spin-dependent interactions

Potential model descriptions can be extended by the inclusion of spin-dependent interactions. The three different types of interaction present in the additional spin-dependent potential term in Equation 2.26 are V_{LS} and V_L, the spin-orbit and tensor terms describing the fine structure and mixing of the states, and V_{SS}, the spin-spin term giving the spin-singlet/triplet splittings.

$$V_{\text{spin}}(r) = V_{LS}(r)(\mathbf{L}\cdot\mathbf{S}) + V_T(r)\left[S(S+1) - \frac{3(\mathbf{S}\cdot\mathbf{r})(\mathbf{S}\cdot\mathbf{r})}{r^2}\right] + V_{SS}(r)\left[S(S+1) - \frac{3}{2}\right] \quad (2.26)$$

Reference [48] motivates the form of these potential terms. It should be noted that results calculated using this method are still only limited approximations.

2.4.2 Early production predictions: the Colour Singlet Model

Whilst potential models form an important starting point and provide good understanding of quarkonium spectroscopy, additional theories were needed to explain the production properties of quarkonia (to which the wavefunction calculations from potential models can form an important input). The major difficulty with determining the theoretical principles underpinning the formation of a bound state is the necessity to be able to take into account, at least to some level, the non-perturbative dynamics implicit in such a process.

The Colour Singlet Model (CSM) was originally proposed in the Seventies as a model to predict the properties of quarkonium production, and seemed the most promising and natural model given understanding at the time. The CSM assumes that any particular quarkonium states can only be produced from a heavy quark pair that has the same quantum numbers. In particular, the quark pair must have the same spin and colour state as the final quarkonium state.

As quarkonia are physical objects they must be in a colour singlet state, this implies that the quark pair in the CSM must also be produced in a singlet state, and also precludes any transitions after formation of the quark pair that could affect the spin state. This means that the type of quarkonium that is produced (e.g. J/ψ, η_b, χ_c) is completely determined by the state of the original quarks. The requirement that the quark pair is produced in a colour singlet state is what gives the model its name. At leading order in α_s (that is α_s^3) the classes of diagrams relevant to production of ${}^3S_1$ and ${}^3P_J$ states are as shown in Figure 2.6.

Equation 2.27 gives the general form of the cross-section $\mathrm{d}\sigma$ for production of a quarkonium state H in a proton-proton collision. The term $\mathrm{d}\hat{\sigma}(ij \to H+X)$ governs how the process evolves

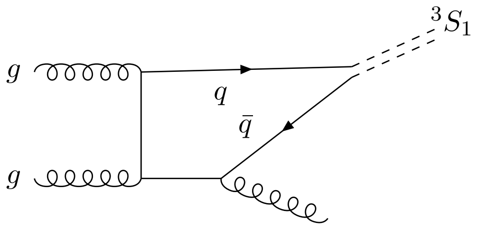

(a) Leading-order singlet $^3S_1$

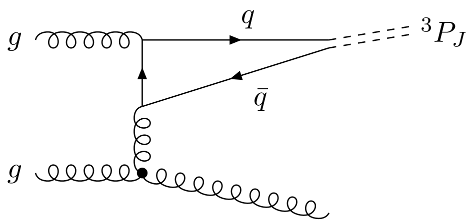

(b) Leading-order singlet ^3P_J

Figure 2.6: *Examples of leading order diagrams for Colour Singlet $^3S_1$ and ^3P_J quarkonium production.*

from initial partons (i and j) to the final quarkonium state.

$$\mathrm{d}\sigma(pp \to H+X) = \sum_{i,j} \int \mathrm{d}x_1 \mathrm{d}x_2\, f_{i/A}(x_1,\mu_F)\, f_{j/B}(x_2,\mu_F) \mathrm{d}\hat{\sigma}(ij \to H+X) \qquad (2.27)$$

The $f_{i/A}(x_1,\mu_F)$ and $f_{j/B}(x_2,\mu_F)$ are the parton distribution functions that determine the quark and gluon content of the proton at different scales μ_F.

Note on Parton Distribution Functions

The parton distribution functions (PDFs) evaluated at a momentum fraction x_k are represented by $f_{i/A}(x_1,\mu_F)$ and $f_{j/B}(x_2,\mu_F)$ in Equation 2.27. The parton content of the proton differs dependent on the scale at which it is probed.

The PDFs are calculated at an appropriate factorisation scale μ_F that determines a separation scale at which parton processes are included in the parton density functions rather than being included in the hard interaction $\mathrm{d}\hat{\sigma}_{i,j\to H}$. Whilst it is not possible to perturbatively calculate the PDF, once measured at a scale μ the PDF can be evolved to other scales using the Dokshitzer-Gribov-Lipatov-Altarelli-Parisi (DGLAP) equations [49], albeit with some uncertainty.

An example of the change in parton content at different scales is illustrated in Figure 2.7. Figure 2.7(a) shows the contributions of all the partons to the overall proton content using the CTEQ6L1 Leading Order (LO) PDF set [50]. At Q^2 and x_k relevant to quarkonium production at ATLAS, the gluon contribution to the proton clearly dominates. Figure 2.7(b) shows the evolution of the CTEQ6L1 gluon PDF on a larger scale, along with the next-to-leading order

(NLO) CTEQ6M and MRST2001LO [51] PDF sets for comparison.

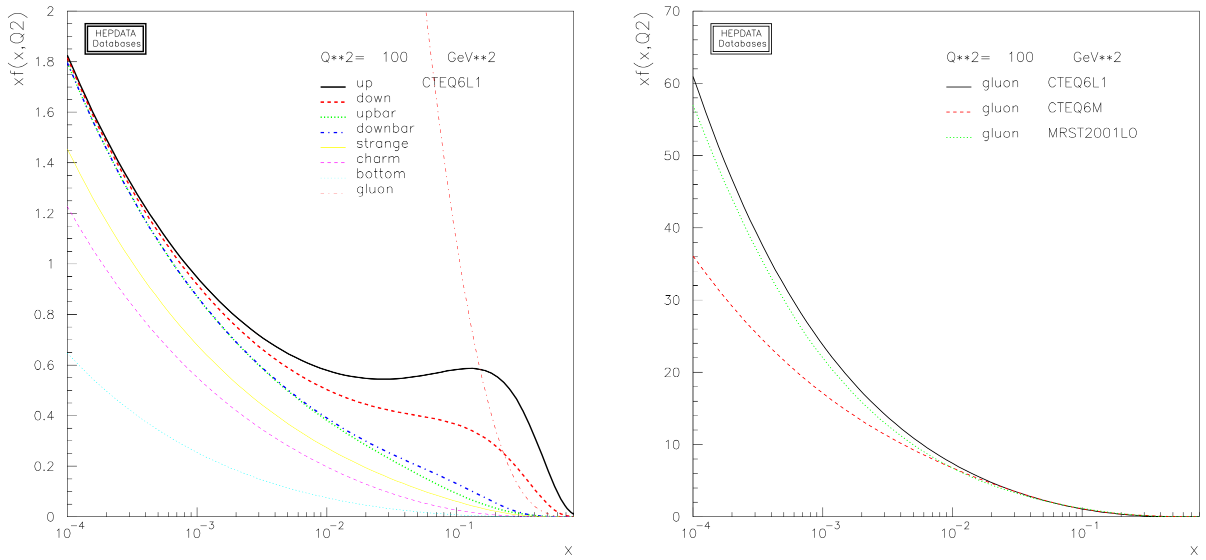

(a) PDFs for CTEQ6L1 (b) Comparison of gluon PDFs

Figure 2.7: *Examples of parton distribution functions for (a) all partons with the CTEQ6L1 set and (b) variations in gluon distribution functions with modern LO and NLO PDF sets (produced using* HEPDATA *[52]).*

Formalism of the Colour Singlet Model

The Colour Singlet Model assumes that the production of quarkonia can be factorised into two processes: first, the heavy quark pair is produced at a short relative distance where α_s is small and the calculation is perturbative; second, the subsequent formation of a bound state is non-perturbative and can be parameterised into a single constant. Long distance gluons are assumed to have no effect on colour or angular momentum quantum numbers of the quark pair. The form of the factorisation in the CSM relies on the factorisation theorem [53] and is generally believed to be valid for production at hadron colliders. Equation 2.28 shows the form that $\mathrm{d}\hat{\sigma}(ij \to H+X)$ takes in the Colour Singlet Model:

$$\mathrm{d}\hat{\sigma}(ij \to H+X) = \mathrm{d}\sigma'(ij \to q\bar{q}[n^{2S+1}L_J]+X)|\Psi^{(k)}_{nL}(0)|^2 \tag{2.28}$$

The heavy quark production term $d\sigma'(ij \to q\bar{q}[n^{2S+1}L_J]+X)$ can be calculated from perturbation theory. The non-perturbative dynamics can be calculated in the CSM as the model assumes the quarks in the meson have zero relative velocity (known as the static approximation), and as such the non-perturbative physics is completely parameterised in one term. For S-wave states this is simply $\Psi_{nL}(0)$, the radial wavefunction at the origin; for P-wave states, $\Psi_{nL}(0)$ is zero so we must consider the next term in the expansion of the cross-section amplitude for the approximation, which is $\Psi'_{nL}(0)$ (the first derivative of the wavefunction).

The CSM was a popular model as it had clear predictive power and universality. The model could predict production cross-sections for all quarkonium states and could be applied not only to hadronic collisions but also to e^+e^- annihilation and deep inelastic scattering experiments, providing many opportunities for cross-checks and comparisons. The only inputs to the model were the probability density functions and the wavefunction of quarkonium, calculable either from potential models (see Section 2.4.1) or alternatively determined experimentally from the decay width of quarkonium states as follows (J/ψ shown as an example):

$$\Gamma(J/\psi \to e^+e^-) \approx \frac{4\alpha_{\mathrm{em}}^2}{9m_c^2}|\Psi_{J/\psi}(0)|^2 \tag{2.29}$$

As such, the CSM could provide absolutely normalised predictions for experiments. The CSM was first applied [54] to hadronic collisions and later to electron-proton collisions and was initially very successful in its predictions.

The first problems started to appear in J/ψ analyses at UA1 [55] where the p_T dependence of the J/ψ cross-section was found to be steeper in data than in theoretical models. Greater understanding came when predictions were extended to the Tevatron [56] and problems were seen in CDF data, where cross-section predictions for ψ' production [57] were a more than an order of magnitude below[8)] what was seen in CDF once various prompt and non-prompt charmonium contributions could be separated and the p_T dependence was again different from that which was predicted (see Figure 2.8). Discrepancies between the CSM and data were again

[8)] Discrepancies become greater at higher values of p_T.

seen in later analyses of radiative decays of χ_c [58] and in Υ production [59].

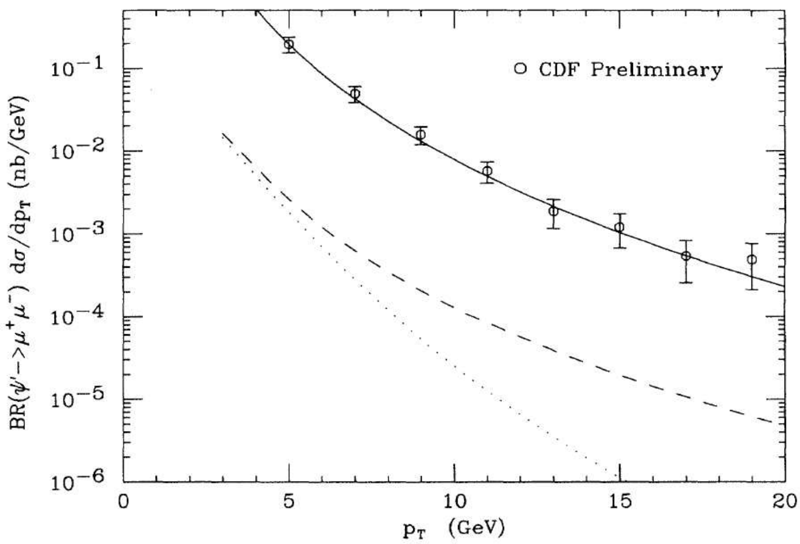

Figure 2.8: *Differential cross-section of ψ' production [60]: data points from CDF, colour singlet predictions are represented by the dotted line. The dashed line includes the contribution from singlet fragmentation processes (see Section 2.4.3) and the solid line is with additional colour octet fragmentation contributions (described in Section 2.4.6).*

2.4.3 Fragmentation contributions

It became clear from experimental results that the Colour Singlet Model needed modification if it were to accurately describe quarkonium production. Additional contributions were required to bring the differential production cross-section rate up to that seen at the Tevatron. The leading order contributions to $d\sigma/dp_T^2$ in α_s and v scale as $1/p_T^8$ for S-waves and $1/p_T^6$ for P-waves, but for high centre-of-mass energies and p_T (compared to hadron masses) one would expect the short-distance cross-section to scale like $1/p_T^4$ from dimensional grounds[9)]. From this it was clear that some additional class of process had not been considered.

In 1993 it was suggested [61] that fragmentation processes could account for the discrepancies seen in p_T dependence in CDF data. In fragmentation processes a high p_T parton (typically a gluon in high-energy hadronic collisions) fragments into a $Q\overline{Q}$ pair, which then hadronises into

[9)] As for a single-particle inclusive cross-section.

a heavy quarkonium state. An example of a contributing diagram (at order α_s^5) to $^3S_1$ production through gluon fragmentation is shown in Figure 2.9.

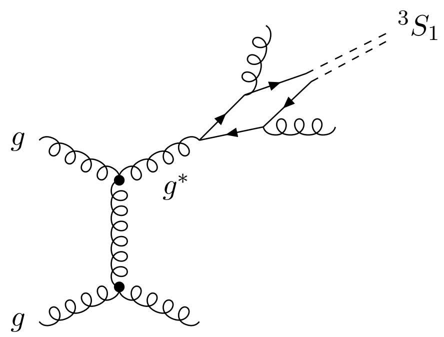

Figure 2.9: *Production of $^3S_1$ singlet state through gluon fragmentation.*

In leading order (non-fragmentation) singlet processes, the produced quarks tend to fly apart and require an additional large momentum transfer to ensure they fly together to allow formation of a bound state: this additional requirement manifests itself as adding additional powers of $1/p_T^2$ in those processes. Fragmentation processes are of higher order in α_s but still dominate over leading order singlet production as we go higher in p_T (see Figure 2.8). Thus, in the case of a fragmenting gluon the two quarks already are produced with low relative momentum so although gluon fragmentation contributions are of a higher order compared to leading order singlet contributions they are enhanced by a power of $p_T^4/(2m_Q)^2$ at large p_T and thus can dominate the cross-section at $p_T \gg 2m_Q$. It is precisely this region that the Tevatron measurements were able to probe, and will be the main region of study at the ATLAS experiment at the LHC.

In this fragmentation process, by virtue of the different scales at which the hard interaction and fragmentation take place, it is possible to factorise the cross-section $\mathrm{d}\hat{\sigma}(ij \to H+X)$ from Equation 2.27 into a component $\mathrm{d}\sigma_g$, which represents the hard interaction, and $D_{g\to H}(z)$ representing the gluon fragmentation function specifying the probability for a parton to hadronise into a quarkonium state H as a function of its momentum fraction z:

$$\mathrm{d}\hat{\sigma}(ij \to H+X) \simeq \int_0^1 \mathrm{dz}\mathrm{d}\sigma_g \left(\frac{p_T(H)}{z}\right) D_{g\to H}(z) \tag{2.30}$$

For S-wave resonances the fragmentation function is calculable, but for P-wave this introduces an infrared divergence associated with the soft limit of the final state gluon. This spoils the factorisation assumption and is corrected for artificially in the Colour Singlet Model with the introduction of an energy cutoff.

With the inclusion of the fragmentation contributions the p_T dependence of the theoretical predictions were made to match to those of experimental results, but still the overall normalisation was larger in experimental data compared to theory. As such, it became clear that despite the advances in understanding which the Colour Singlet Model had provided, it was not adequate to describe quarkonium production at contemporary colliders as the theoretical model at the time did not include unknown, but significant, additional contributions. The experimental failure of the model is also reflected by the infrared divergences present in the theory.

2.4.4 Colour Evaporation Model

At around the same time as the Colour Singlet Model was presented, another model known as the Colour Evaporation Model (CEM) was proposed [62] (sometimes known as the "local duality approach") and was more recently reintroduced [63] to explain the discrepancies of CSM seen at the Tevatron. The CEM relies on a statistical approach to the production of particular quarkonia. In the CEM, the role of colour in selection of quarkonia states is ignored: the quark pair is not restricted to being produced in a colour singlet state, but may be produced in an octet state. Colour and spin are then assumed to be modified via numerous soft interactions with the colour field (the eponymous "colour evaporation").

The cross-section for the production of quarkonium in the CEM is said to be proportional to the rate of production of heavy quarks in the invariant mass range between twice the heavy quark mass and the threshold for open charm (or beauty) meson production, as shown in Equation 2.31:

$$\hat{\sigma}_{\text{onia}} = \frac{1}{9}\int_{2m_Q}^{2m_{D/B}} \mathrm{d}m \frac{\mathrm{d}\sigma_{Q\overline{Q}}}{\mathrm{d}m} \tag{2.31}$$

Here $2m_{D/B}$ is taken to represent the $D\overline{D}$ or $B\overline{B}$ production threshold for charmonia and bottomonia respectively. The $\frac{1}{9}$ coefficient simply comes from the probability of a $\mathbf{3}\times\overline{\mathbf{3}}$ quark-antiquark pair forming a singlet state. This gives the rate of production of all quarkonia. In the CEM, the rate for production of individual states comes from the statistical distribution of this total cross-section across all possible quarkonium states.

The cross-section $\hat{\sigma}_H$ for a particular state H can be projected out from $\hat{\sigma}_{\text{onia}}$ by multiplication by a density coefficient ρ_H:

$$\hat{\sigma}_H = \rho_H \hat{\sigma}_{\text{onia}} \tag{2.32}$$

This non-perturbative ρ_H parameter is specific to a particular quarkonium type, the colliding particles and collision energy, and must be determined from fits to data. As such, this model cannot provide predictions of absolute cross-sections, but the nature of the CEM approach means that the ρ_H should have no dependence on p_T or x in the ratios of production cross-sections of various quarkonia and in that sense are universal constants.

As such, the CEM provides us with some specific predictions: there should be no net polarisation of quarkonia, as any polarisation should be randomised by the soft interactions, and the production of specific quarkonium states should occur in fixed ratios independent of p_T. The Colour Evaporation Model thus specifically predicts that the $J = 0, 1, 2$ χ states will be produced in the ratio $1:3:5$ (from the $2J+1$ spin combinations).

Whilst the CEM shows good agreement with low energy data [64], more recent results from CLEO [65, 66], giving an upper limit to the ratio $\text{Br}(B \to \chi_{c2}(\text{direct})X)/\text{Br}(B \to \chi_{c1}(\text{direct})X) < 0.44$ at a 95% confidence interval, and similar CDF results [67] are in striking contrast with the $5/3$ prediction of CEM. It is clear that the Colour Evaporation approach, whilst useful for low energy phenomenological descriptions for charmonia [68], is not successful in offering predictions for quarkonium production at high energy colliders.

Indeed, the most serious drawback of the CEM model for application at the Tevatron and the LHC is that as it is simply a phenomenological model there is no way of calculating the higher order QCD corrections that are important at the high p_T probed at these colliders and thus the model lacks any predictive power in this high energy regime.

2.4.5 Soft Colour Interactions

The Soft Colour Interaction (SCI) model takes much inspiration from the Colour Evaporation Model. Originally introduced to address questions in rapidity gap events in deep inelastic scattering (DIS) [69] at HERA, the model was then applied to hadronic colliders [70, 71]. In this model, soft interactions below a particular scale are taken into account in addition to the perturbative interactions. Whilst there is no rigorous way to deal with this soft physics, the SCI approach stresses that only colour should be significantly affected by these interactions.

The mechanism by which this model is implemented is thus to simulate the events in Monte Carlo event generators, with a single parameter R, the probability of colour exchange between two partons. This parameter is tuned from HERA DIS data to be $R = 0.5$. No exchange of colour is allowed between perturbative partons, but otherwise in such a model a quark-antiquark colour octet state may transform into a colour singlet state (or vice-versa) provided the quark-antiquark pair are of appropriate mass. In this way, the procedure for obtaining the quarkonium cross-section is similar to CEM in Equation 2.31 but in this case the $d\sigma_{Q\overline{Q}}$ term is modified by the presence of the soft colour interactions.

In the SCI model, a further modification to the CEM equations gives the cross-section for a given quarkonium state H with total angular momentum J_H to be:

$$\hat{\sigma}_H = \frac{\Gamma_H}{\sum_i \Gamma_i} \hat{\sigma}_{\mathrm{onia}} \tag{2.33}$$

where $\Gamma_i = (2J_H + 1)/n_i$ is a partial width, putting the ρ_H parameter of CEM on firmer ground. One weakness is a strong dependence of the predictions on the heavy-quark masses used (understood to be due to the resultant changes in limits in the integration in a modified Equation 2.31).

This framework provides absolutely normalised predictions for the Tevatron, with good agreement seen in p_T distributions and relative rates of of ψ and Υ production [70], and testable predictions made for the LHC [71]. Some discrepancies have been seen at larger p_T and this is an aspect easily testable at the LHC with a high rate expected in the high p_T region.

2.4.6 NRQCD and the Colour Octet Mechanism

Another approach to quarkonium production, building on the understanding gained from the Colour Singlet Model, was proposed [72, 60] in the early Nineties and, as for the CEM and SCI, makes use of the possibility of coloured quark-antiquark pairs in the formation of quarkonium bound states. This proposal is known as the Colour Octet Mechanism (COM). The Colour Octet Mechanism proposes that the heavy quark pairs produced in the hard process do not necessarily need to be produced with the quantum numbers of physical quarkonium but could evolve into a particular quarkonium state through radiation of soft gluons late on in the production process: a possibility not considered by the CSM, but similar in philosophy to the CEM.

In contrast to the CSM/CEM, which attempt to make plausible approximations at the price of dispensing with QCD, the COM has the advantage of being rigorously motivated through the framework of an effective field theory known as Non-Relativistic Quantum Chromodynamics, or NRQCD. Using a factorisation approach motivated by arguments from perturbative QCD and through the formalism of effective field theory, the perturbative and non-perturbative dynamics can be formally separated.

Theoretical formalism

Effective field theories allow for a systematic approach to the factorisation of different scales in the dynamics of processes described by the theory. Quarkonia are assumed to be non-relativistic systems in this framework, motivated in part by the success of potential models in describing certain aspects of quarkonia using this assumption.

As a non-relativistic system, quarkonium can be characterised by three energy scales: the typical kinetic energy $m_Q v^2$, the typical momentum transfer $m_Q v$ and the mass m_Q of the heavy quark (and v is the relative quark velocity in the bound state). The quark mass determines the scale at which perturbative QCD is usable. The momentum scale defines the length scale for the size of a quarkonium state and thus separates out the long-distance evolution of a $Q\overline{Q}$ pair into physical quarkonium. Finally, the energy scale determines the splittings between various quarkonium states and is identified with the Λ_{QCD} scale. For the non-relativistic condition to hold, these scales must be well-separated:

$$(m_Q v^2)^2 \ll (m_Q v)^2 \ll m_Q^2 \tag{2.34}$$

For charmonia $v_c^2 \simeq 0.25$ and for bottomonia $v_b^2 \simeq 0.09$ (using the relation that $m_Q v^2 \sim \Lambda_{\text{QCD}}$).

Starting from full QCD, the most general effective NRQCD Lagrangian of such a theory can be constructed by replacing the usual 4-component Dirac spinor by two 2-component Pauli spinors[10)], namely the annihilation operator ψ and creation operator χ. By requiring $SU(3)$ gauge symmetry, rotational symmetry, **C** and **P** symmetries and heavy quark phase symmetry of these fields and using the effective field theory framework, one obtains:

$$\begin{aligned}
\mathscr{L}_{\text{NRQCD}} &\equiv \mathscr{L}_{\text{light}} + \mathscr{L}_{\text{heavy}} + \delta\mathscr{L} &(2.35)\\
\mathscr{L}_{\text{light}} &= -\frac{1}{2}\text{tr}\, G_{\mu\nu}G^{\mu\nu} + \sum \overline{q} i \not{D} q &(2.36)\\
\mathscr{L}_{\text{heavy}} &= \psi^\dagger \left(iD_0 + \frac{\mathbf{D}^2}{2m_Q} \right) \psi + \chi^\dagger \left(iD_0 - \frac{\mathbf{D}^2}{2m_Q} \right) \chi &(2.37)
\end{aligned}$$

where the covariant derivative is given by $D^\mu \equiv \partial^\mu + ig_s A^\mu$, the gauge field is $A^\mu = (\phi, \mathbf{A}^\mu)$ and the QCD coupling g_s is given by $\sqrt{4\pi\alpha_s}$. The term $\mathscr{L}_{\text{light}}$ is the standard relativistic QCD Lagrangian for gluons and light quarks.

The term $\delta\mathscr{L}$ incorporates all possible operators consistent with symmetries of QCD; the leading relativistic corrections are bilinear in the heavy quark fields:

$$\begin{aligned}
\delta\mathscr{L}_{bilinear} = \; & \frac{c_1}{8m_Q^3}\psi^\dagger \mathbf{D}^4 \psi + \frac{c_2}{8m_Q^2}\psi^\dagger (i\mathbf{D}\cdot g_s\mathbf{E} - g_s\mathbf{E}\cdot\mathbf{D})\psi \\
& + \frac{c_3}{8m_Q^2}\psi^\dagger (i\mathbf{D}\times g_s\mathbf{E} - g_s\mathbf{E}\times i\mathbf{D})\cdot\sigma\psi \\
& + \frac{c_4}{2m_Q}\psi^\dagger g_s\mathbf{B}\cdot\sigma\psi + \text{charge conjugate terms}
\end{aligned} \tag{2.38}$$

where the chromoelectric and chromomagnetic field operators are given by $E^i = G^{0i}$ and $B^i =$

[10)]Through a block diagonalisation used to decouple the heavy quark and antiquark degrees of freedom

$\frac{1}{2}\varepsilon^{ijk}G^{jk}$ respectively. Of course, in addition to $\delta\mathscr{L}_{bilinear}$ terms, higher dimension operators also play a role in the dynamics, and QCD results can in principle be reproduced to any desired accuracy by adding additional terms to the effective Lagrangian matching scattering amplitudes between the two theories.

Within NRQCD, the total cross-section[11)] for inclusive production of a quarkonium state H can be expressed as follows:

$$\mathrm{d}\hat{\sigma}(ij \to H+X) = \sum_{n_i} \mathrm{d}\sigma_{Q\bar{Q}}(ij \to Q\bar{Q}[n_i]+x)\langle \mathscr{O}^H[n_i]\rangle \tag{2.39}$$

The summation is over the quantum numbers of all possible states of the quark-antiquark pair. The NRQCD factorisation hypothesis for quarkonium production [72, 60] states that the cross-section can be written as sum of short distance coefficients that describe creation of $Q\overline{Q}$ pair in state n_i multiplied by a process-dependent matrix element containing all of the interactions of the non-relativistic $Q\overline{Q}$ pair. In this way the NRQCD approach allows for isolation of the non-perturbative physics from the perturbative hard process and parametrises the former in a long-distance matrix element defined [72] by

$$\langle \mathscr{O}^H[n_i]\rangle = \sum_{\lambda,X} \langle 0|\,\chi^\dagger \kappa_{n_i}\phi\,|H(\lambda)X\rangle\,\langle H(\lambda)X|\,\psi^\dagger \kappa'_{n_i}\chi\,|0\rangle \tag{2.40}$$

summing over all polarisations λ and light hadrons X. The 'kernels' κ_{n_i} and κ'_{n_i} specify the angular momentum, spin and colour of the quark-antiquark pair.

Velocity scaling

In NRQCD it is not possible to predict the exact values of the octet matrix elements [12)] and so-called 'power counting', or velocity scaling, rules can be used to determine the relative

[11)]For hadronic production this cross-section term must of course be convoluted with the parton density functions by insertion into Equation 2.27.

[12)]Whilst this free parameter can be considered a weakness of the model, the universality of these matrix elements means that their values can be calculated independently from a number of different processes including photoproduction [73] and deep inelastic scattering [74].

importance of these terms. The velocity scaling rules [72, 75] suggest that a general matrix element scales like:

$$\langle \mathscr{O}[^{2S+1}L_J^{(1,8)}] \rangle \sim v^{3+2L+2E_1+4M_1} \tag{2.41}$$

where E_1 and M_1 denote the minimum number of chromoelectric ($\Delta L = \pm 1,\ \Delta S = 0$) and chromomagnetic ($\Delta L = 0,\ \Delta S = \pm 1$) transitions required to reach the dominant quarkonium Fock state from the $^{2S+1}L_J^{(1,8)}$ state. The superscript $(1,8)$ denotes whether the quarkonium is in a colour singlet or octet state. Note that all octet terms are suppressed by powers of v^2 relative to the singlet terms, due to the necessity of an E_1 or M_1 transition in any case to get to the correct final state.

A particular quarkonium state $|H\rangle$ in NRQCD can be realised as the infinite sum of contributions of states in the Fock space in which the theory is defined. This takes the form of a double expansion in α_s and v (the relative quark velocity in the bound state). By applying these scaling rules, one can determine which terms in the series need to be taken into account and which terms may be neglected in order to maintain a certain order of precision. In this fashion, the J/ψ can be expressed as:

$$\begin{aligned} |J/\psi\rangle \;=\; & O(1)\left|Q\overline{Q}[^3S_1^{(1)}]\right\rangle + O(v)\left|Q\overline{Q}[^3P_J^{(8)}]g\right\rangle \\ & + O(v^2)\left|Q\overline{Q}[^3S_1^{(1,8)}]gg\right\rangle + O(v^2)\left|Q\overline{Q}[^1S_0^{(8)}]g\right\rangle \\ & + O(v^2)\left|Q\overline{Q}[^3D_J^{(8)}]gg\right\rangle + \dots \end{aligned} \tag{2.42}$$

A solution to the infrared divergence problem

A key strength (and indeed key motivation) of the Colour Octet Mechanism is its ability to resolve [76] the Colour Singlet Model problem of infrared divergences at next-to-leading order in P-wave decays, simply through the additional Fock state contributions that arise from the presence of octet states. The leading terms in the Fock state decomposition of the P-wave state are as follows:

$$|\chi_J\rangle = O(1)\left|Q\overline{Q}[^3P_J^{(1)}]\right\rangle + O(v)\left|Q\overline{Q}[^3S_1^{(8)}]g\right\rangle \dots \tag{2.43}$$

Note how the new contribution to the $|\chi_J\rangle$ state (in addition to the singlet term as in CSM) is a $c\bar{c}$ pair in a $^3S_1$ configuration in a colour octet state, plus a gluon. This gluon modifies the quantum numbers of the quark pair by its emission, allowing it to evolve into a singlet P-wave physical quarkonium state. Figure 2.10 illustrates the conceptual difference between the Colour Singlet Model P-wave production diagram, and the additional one from NRQCD.

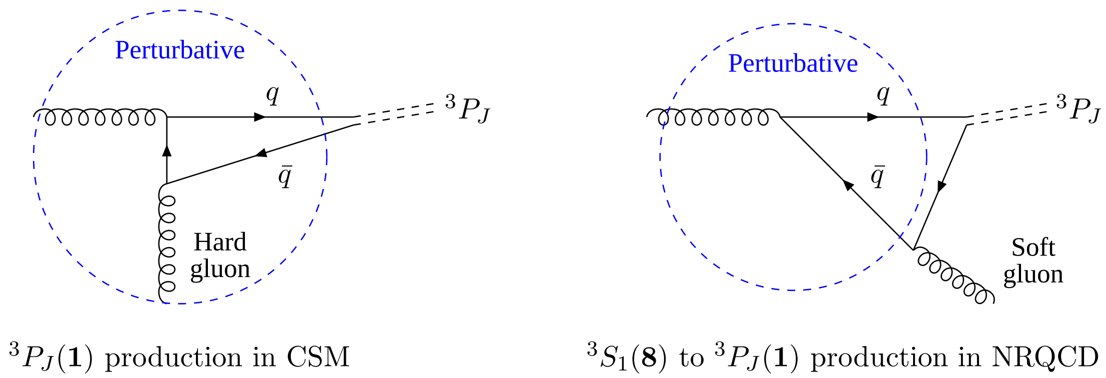

Figure 2.10: *Illustration of how the soft gluon divergence of P-wave states in the CSM is dealt with in NRQCD (see also Equation 2.43).*

This additional octet diagram is also infrared divergent, but crucially this singularity exactly cancels [76] with the matching singularity in the singlet P-wave short distance cross-section in the CSM. In this way the removal of the infrared divergence problem rigorously extends to all orders and does not have to rely on an arbitrary infrared cutoff imposed on the model as for the CSM. The NRQCD matrix element $\langle\mathcal{O}_1^{\chi_{QJ}(nP)}[^3P_J]\rangle$ thus encompasses the infrared-sensitive terms that would otherwise appear in cross-section.

The role of colour octet contributions and NRQCD matrix elements

The corresponding expansion for S-wave states shown in Equation 2.42 also includes similar colour octet terms at higher order. Whilst there was no theoretical necessity for these unlike in the P-wave case their presence suggested that, whilst suppressed by powers of v, these octet contributions could play an important role in the production of quarkonium.

As an example, the term $\left|Q\overline{Q}[^3S_1^{(8)}]gg\right\rangle$ in the expansion of the S-wave state can be produced through gluon fragmentation into an octet state with a suppression of v^4. However, this contribution is compensated by being of order α_s rather than α_s^3, as it would be for the corresponding singlet fragmentation process. As α_s and v^2 are of comparable size for quarkonium, this means that the two channels are competitive. Once a full calculation is carried out additional numerical factors appear [72] that leave the colour octet diagrams to be by far the dominant contribution.

For the octet contribution to correct for the theoretical deficit seen at CDF (Figure 2.8), it is sufficient that $\langle\mathcal{O}[^3S_1^{(8)}]\rangle \sim \frac{2}{\pi^2}v^4\langle\mathcal{O}[^3S_1^{(1)}]\rangle$ (see reference [77] for details), as is implied by Equation 2.42. In this way, it is clear that the Colour Octet Mechanism offers not just a more robust theoretical explanation of quarkonium production, but also the possibility of successfully explaining (and predicting) quarkonia cross-sections. As we have seen, the matrix elements are free parameters of the NRQCD theory but through theoretical arguments their relative magnitudes may at least be estimated.

Without additional constraints on these matrix elements however, there would be no predictive power: there are far too many to constrain from data. There are a number of techniques that can be used to reduce the number of free parameters. As in the CSM the singlet matrix elements can still be expressed in terms of the radial wavefunctions at the origin of the quarkonium state[13)], and as such are in principle fully calculable in NRQCD. Equations 2.44 and 2.45 illustrate the form of these singlet matrix elements for the $^3S_1$ and ^3P_J states along with their velocity scaling order in NRQCD:

$$\begin{aligned}
\langle\mathcal{O}^{\psi(nS)}[^3S_1^{(1)}]\rangle &= 3\frac{N_C}{2\pi}|\Psi_{nS}(0)|^2 = O(m_Q^3v_Q^3) &(2.44)\\
\langle\mathcal{O}^{\chi_{QJ}(nP)}[^3P_J^{(1)}]\rangle &= (2J+1)\frac{3N_C}{2\pi}|\Psi'_{nP}(0)|^2 = O(m_Q^5v_Q^5) &(2.45)
\end{aligned}$$

In addition, heavy-quark spin-symmetry holds to leading order in v^2 and can be used to provide approximate linear relations between both the colour singlet and octet matrix elements of various quarkonium states to reduce the number of independent parameters.

Using both velocity scaling rules and spin-symmetry relations then, the NRQCD factorisa-

[13)]This should not come as a surprise: after all, the CSM is in effect an approximation of NRQCD where we keep just the leading terms in v.

tion formula of Equation 2.39 can be expanded and reduced to just a few terms. As an example, the cross-section for production of an Υ state can be written:

$$\begin{aligned} \mathrm{d}\hat{\sigma}[\Upsilon(nS)] &= \mathrm{d}\sigma[b\bar{b}(^3S_1^{(1)})]\langle\mathscr{O}^{\Upsilon(nS)}[^3S_1^{(1)}]\rangle \\ &+\mathrm{d}\sigma[b\bar{b}(^3S_1^{(8)})]\langle\mathscr{O}^{\Upsilon(nS)}[^3S_1^{(8)}]\rangle+\mathrm{d}\sigma[b\bar{b}(^1S_0^{(8)})]\langle\mathscr{O}^{\Upsilon(nS)}[^1S_0^{(8)}]\rangle \\ &+\left(\sum_J(2J+1)\mathrm{d}\sigma[b\bar{b}(^3P_J^{(8)})]\right)\langle\mathscr{O}^{\Upsilon(nS)}[^3P_0^{(8)}]\rangle \end{aligned} \tag{2.46}$$

where the $(2J+1)$ term comes from using spin-symmetry relations to reduce the $\langle\mathscr{O}^{\Upsilon(nS)}[^3P_J^{(8)}]\rangle$ terms to a single $\langle\mathscr{O}^{\Upsilon(nS)}[^3P_0^{(8)}]\rangle$, and similarly for χ_{bJ} production the expansion becomes:

$$\begin{aligned} \mathrm{d}\hat{\sigma}[\chi_{bJ}(nP)] &= \mathrm{d}\sigma[b\bar{b}(^3P_J^{(1)})]\langle\mathscr{O}^{\chi_{bJ}(nP)}[^3P_J^{(1)}]\rangle \\ &+(2J+1)\mathrm{d}\sigma[b\bar{b}(^3S_1^{(8)})]\langle\mathscr{O}^{\chi_{b0}(nP)}[^3S_1^{(8)}]\rangle \end{aligned} \tag{2.47}$$

where the same spin-symmetry procedure has been used to remove the dependence on higher χ_{bJ} matrix elements from the $^3S_1^{(8)}$ contribution.

In this way the free parameters of the NRQCD theory are reduced to just three octet matrix elements of importance for $^3S_1$ production, and one octet matrix element for ^3P_J production. By fitting the octet matrix elements to data one can determine the values of these various NRQCD contributions. It is worth noting that due to the similar p_T dependence of the $^1S_0^{(8)}$ and $^3P_0^{(8)}$ contributions there is little to determine the exact contributions of either separately, so in general any fit to data fits a linear combination of the corresponding matrix elements as a single parameter M_k^H, rather than as two independent factors:

$$M_k^H = \langle\mathscr{O}^{\Upsilon(nS)}[^1S_0^{(8)}]\rangle+\frac{k}{m_q^2}\langle\mathscr{O}^{\Upsilon(nS)}[^3P_0^{(8)}]\rangle \tag{2.48}$$

Figure 2.11 shows the application of NRQCD to CDF data where the Colour Octet Mechanism shows excellent agreement in p_T-dependence with the data at high p_T where the theory is on stronger theoretical ground. For accurate description of Υ production at low p_T it is understood [35] that higher order corrections and consideration of multiple gluon radiation is required.

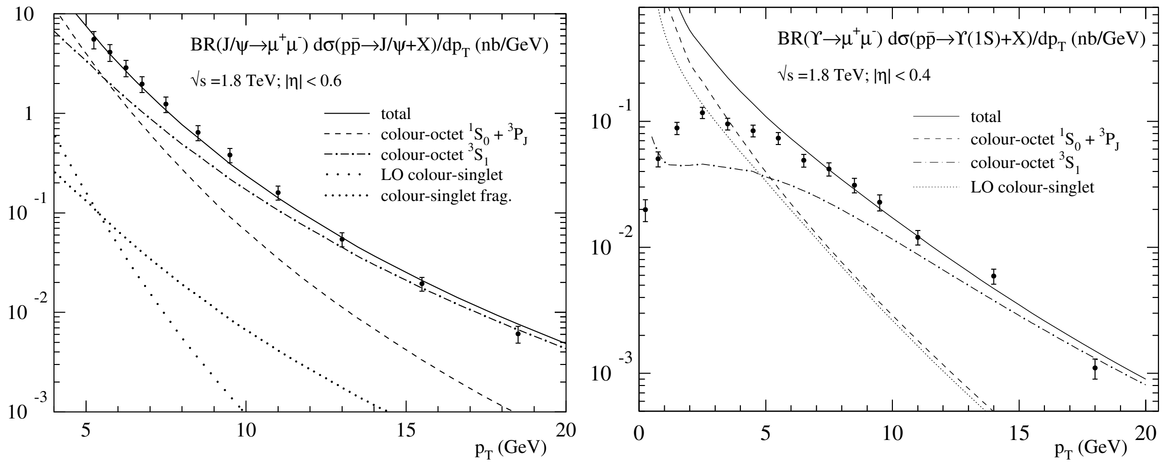

(a) $J/\psi \rightarrow \mu^+\mu^-$ (b) $\Upsilon \rightarrow \mu^+\mu^-$

Figure 2.11: *Differential cross-section of J/ψ and Υ production at CDF with theoretical predictions for colour-singlet and colour-octet model production (from [37]).*

The Colour Octet Mechanism has also had success in describing quarkonium production in other processes, such as deep inelastic scattering and e^+e^- annihilation. Reference [35] contains a comprehensive review of these experimental results. Recent theoretical calculations [78] have given further support for the NRQCD approach by showing that NRQCD factorisation holds in next-to-leading order processes. However, open questions still remain, as in photoproduction data the presence of the colour octet terms is unnecessary[14)] (and indeed unwelcome) [79]. The implementation of NRQCD in Monte Carlo generators for ATLAS and a discussion about matrix elements fits to data may be found in Chapter 4.

The NRQCD approach provides an additional prediction which can be used to test its (and other models) validity. For quarkonium with a p_T much larger than its mass, as has been discussed, the production rate is dominated by gluon fragmentation. At large p_T this gluon is close to its mass shell and as such is transversely polarised, and theoretical arguments suggest that the quark-antiquark bound state should retain this polarisation state that should be evident

[14)] Next-to-leading order calculations for the CSM in photoproduction mean that singlet terms can account for the data quite well without octet contributions. Significant theoretical uncertainties mean however that there is still room for Colour Octet terms so no firm conclusions can be drawn.

in the decay of the physical quarkonium state. As such, this offers a powerful test of the Colour Octet Mechanism.

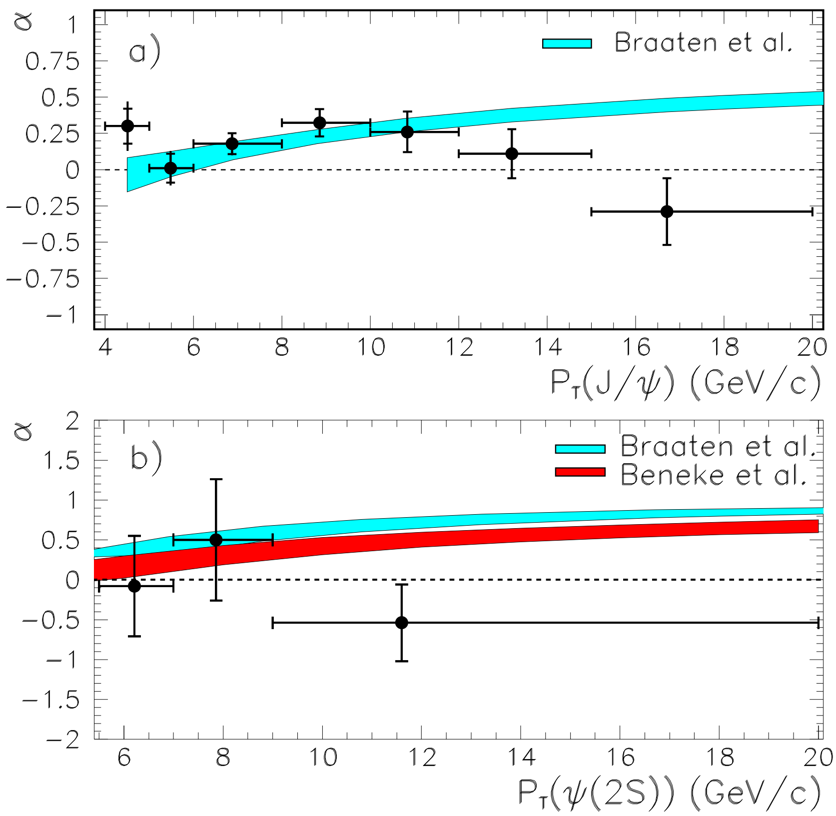

Figure 2.12: *J/ψ and $\psi(2S)$ polarisation as a function of p_T measured at CDF [80]. The shaded band corresponds to NRQCD predictions [81, 82].*

Some current results from the Tevatron (Figure 2.12 for charmonium measurements and Figure 2.13 for bottomonium) shows the polarisation coefficient in $\Upsilon \to \mu\mu$ decay as a function of its transverse momentum, where the NRQCD prediction does not agree well with analysed data. However, as the theoretical predictions are on firmer ground at higher transverse momenta, ATLAS will be in an excellent position to test these models. In Chapter 7 I discuss the prospects for measurement of polarisation of quarkonium at ATLAS, some new and more robust techniques to deal with systematic uncertainties and some predictions for the sensitivity of ATLAS for such an analysis.

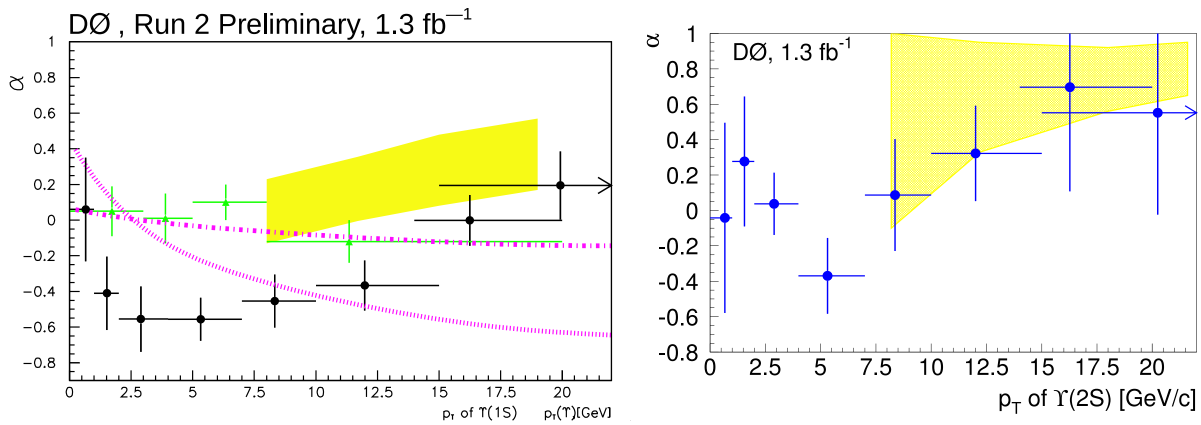

(a) Υ(1*S*) (b) Υ(2*S*)

Figure 2.13: Υ(1*S*) *polarisation (left) measured as a function of* p_T *at DØ (black dots) and CDF (green triangles), compared to limit cases of the* k_T *factorisation model, (dashed and dotted curves) and a band for COM predictions (from [83]).* Υ(2*S*) *polarisation (right) measured [120] at DØ . Here the yellow band indicates the NRQCD prediction.*

2.4.7 Higher-order relativistic corrections

Many other theoretical techniques exist to attempt to explain the properties of quarkonium production. One particular approach using the k_t-factorisation theorem [84] taking into account higher order contributions seemed particularly promising, but has recently been shown [85] to violate factorisation in hadronic collisions, calling the validity of this method into question.

Significant theoretical activity has been ongoing regarding next-to-leading order (NLO) [86, 87] and next-to-NLO (NNLO) [87] corrections to the Colour Singlet Model, motivated by the fact that in Υ production the LO colour singlet predictions did not show as much disagreement from data as in charmonia (which can be explained by recalling that $v_b^2 < v_c^2$ and thus colour octet terms have greater suppression in bottomonia). Additional terms in the CSM, although higher in α_s are countered by scaling like $1/p_T^4$ and $1/p_T^6$ which can give enhanced contributions compared to the leading order terms which scale like $1/p_T^8$.

These higher order calculations offer very promising agreement with Tevatron data and predictions for the LHC (see Figure 2.14). References [87, 88] also offer predictions for quarkonium polarisation (with higher QCD corrections) that differ significantly from those of the CEM and NRQCD frameworks. Most notably, the calculations predict considerable longitudi-

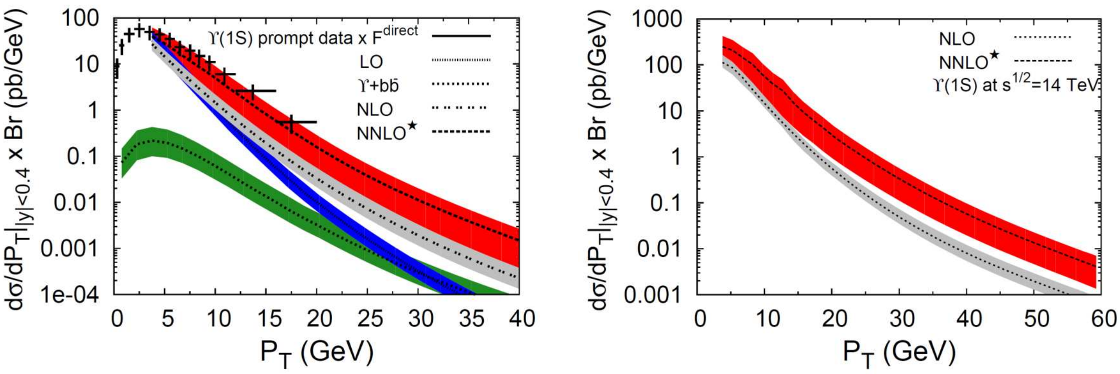

(a) $p\overline{p} \to \Upsilon(1S)X$ at CDF

(b) $pp \to \Upsilon(1S)X$ prediction for LHC

Figure 2.14: *Inclusive prompt $\Upsilon(1S)$ production cross-section as a function of p_T at CDF at $\sqrt{s} = 1.8$* TeV *with overlaid results of theoretical calculations (and error bands) up to NNLO, along with corresponding predictions for the LHC (from [87]).*

nal polarisation at NLO and NNLO in line with Tevatron results [83], which can be investigated further at ATLAS using the methods outlined in this thesis. It is worth noting that currently the theoretical errors on the polarisation still dominate over those from experiment so no clear statement can yet be made regarding the Tevatron results.

Associated hadroproduction

One observable, linked to higher order corrections, is that of associated hadroproduction of quarkonium [89], where a quarkonium state is produced in association with a heavy quark pair. In this method, LO terms in α_s contributing to the $pp(\overline{p}) \to H + q\overline{q}$ process are considered both for predictions at the LHC and correspondence to Tevatron data. The motivation for this study comes from the Belle Collaboration result [90] (in e^+e^- collisions) that production of J/ψ in association with a charm-anticharm pair dominates the inclusive production cross-section:

$$\frac{\sigma(e^+e^- \to J/\psi + c\overline{c})}{\sigma(e^+e^- \to J/\psi X)} = 0.82 \pm 0.15 \pm 0.14 \tag{2.49}$$

If this property holds for hadroproduction as well, the observation of $J/\psi + c\overline{c}$ and $\Upsilon + b\overline{b}$ can serve as an excellent test of colour singlet contributions. The tree-level diagrams for associated hadroproduction have been shown to contribute at NLO to singlet corrections (see Figure 2.14).

2.5 Outlook

The study of quarkonium production has a long history and the J/ψ and Υ continue to surprise and cause us to re-evaluate our current thinking as much now as when they were first discovered. With the intriguing results from Tevatron probing higher energies than ever before we are starting to learn more about how these bound states are produced, but it will fall to the LHC to constrain current theoretical models for hadroproduction. In addition to the behaviour of the production cross-sections, measurement of polarisation and associated hadroproduction offer two methods of determining the production mechanism that are both experimentally accessible and offer distinctive differentiation between the various approaches.

"It is a capital mistake to theorise before one has data. Insensibly one begins to twist the facts to suit theories, instead of theories to suit facts."

Sir Arthur Conan Doyle

3

LHC and the ATLAS detector

The Large Hadron Collider (LHC) is a proton-proton synchrotron collider of 27 km circumference that has recently begun operation at CERN[1)], Geneva. The main LHC ring is fed with a proton beam from a chain of accelerators, beginning with production in a 50 MeV linear accelerator, followed by the 1.4 GeV Proton Synchrotron booster and the 26 GeV Proton Synchrotron, which delivers bunches of 10^{11} protons with 25 ns spacing to the Super Proton Synchrotron where the beams are accelerated to 450 GeV. The proton beams are then finally injected into the LHC for acceleration, focusing and eventually collision, to provide a centre-of-mass energy of 10 TeV and luminosity of 10^{31} cm^{-2}s^{-1} during the initial calibration phase. Ultimately protons will collide with a nominal energy of 14 TeV, the design luminosity of 10^{34} cm^{-2}s^{-1} and with

[1)] European Organisation for Nuclear Research bunch crossings 25 ns apart. At full luminosity this will result in around 23 collisions with every crossing. For further details of the specifications and design performance of the LHC machine itself, I refer the interested reader to reference [91].

Positioned at four collision points around the ring are the main LHC experiments — ALICE, ATLAS, CMS and LHCb (see Figure 3.1). The ATLAS and CMS detectors are general purpose detectors, whilst ALICE and LHCb are detectors specialising in heavy-ion and beauty physics respectively. The LHC provides significant physics potential for precise measurements

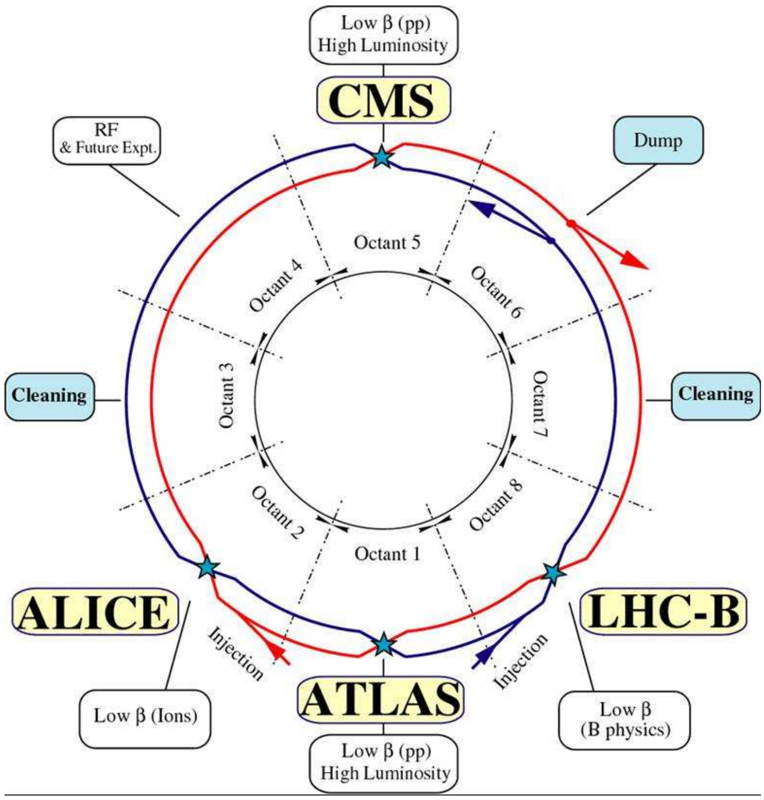

Figure 3.1: *Schematic diagram of the position of the four major LHC experiments on the accelerator ring.*

of parameters both in current theories and in tests of new physics phenomena. A high luminosity and the large cross-sections expected at the LHC mean tests of the Standard Model can be carried out even at relatively small integrated luminosities. The high interaction rates, particle multiplicities and energies involved, as well as the associated high radiation environment, has motivated the design of the particle detectors, which will be discussed in this chapter.

3.1 Overview of the ATLAS detector

The construction of the ATLAS detector (shown in Figure 3.2) has been completed and it awaits data-taking at LHC Point 1, with collisions planned to begin in late 2008. The ATLAS detector is cylindrical in design, of total length 44 m with diameter 25 m and weighing 7000 tonnes, making it the largest particle detector ever constructed. From the inside out the detector consists of an Inner Detector (described in Section 3.2) used for tracking and precision measurement, surrounded by a 2 Tesla solenoid magnet, which itself is enclosed in electromagnetic and hadronic calorimeters used to accurately measure particle energies (described in Section 3.3), ultimately contained within a combination of muon spectrometers (see Section 3.4) and toroidal magnets that define the global detector geometry.

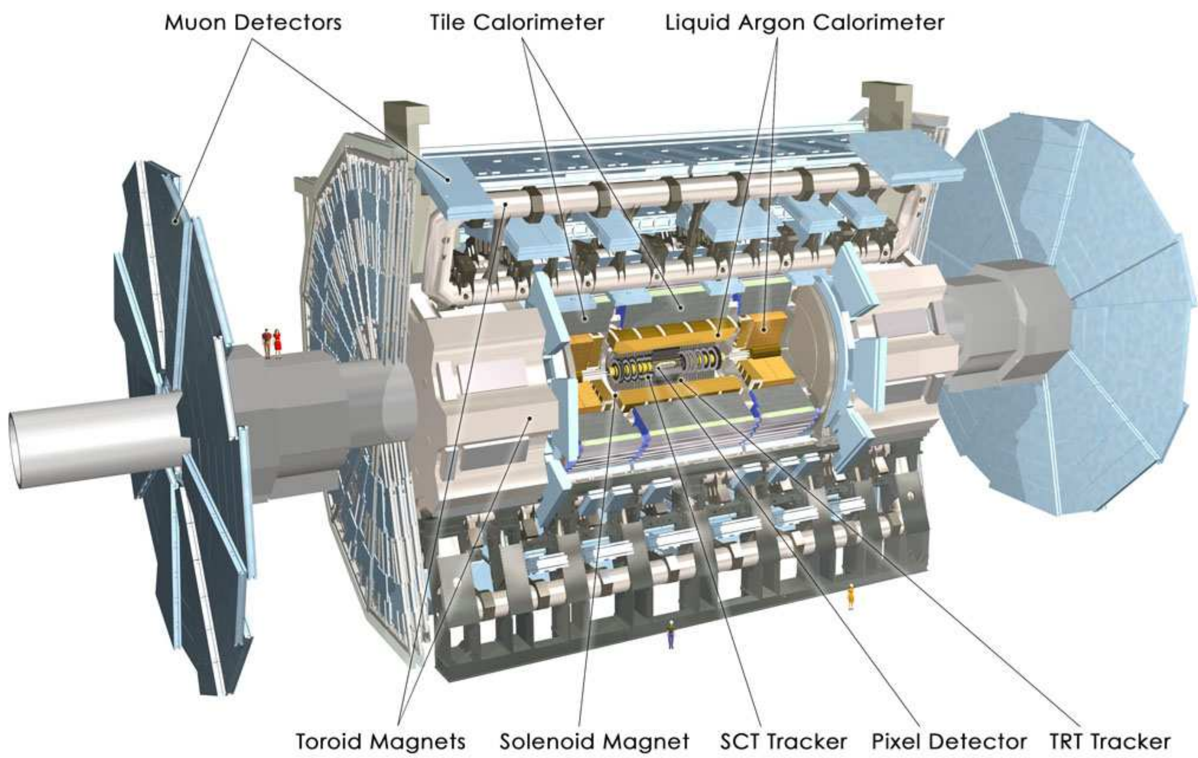

Figure 3.2: *The ATLAS detector, with the main components highlighted.*

ATLAS' strengths are its very good electromagnetic and hadronic calorimetry with coverage over a large pseudorapidity range, the ability to make high precision muon measurements and low p_T threshold triggering capabilities [92]. The coordinate system of ATLAS is defined as follows: the beam direction defines the z-axis, with the $x-y$ plane transverse to the beam direction. The positive z-axis is detector side A, negative being detector side C. The positive x direction is defined by a line pointing from the interaction point to the centre of the ring, and the positive y direction as pointing towards the surface from the detector cavern. The transverse momentum p_T is defined as being in the $x-y$ plane.

The azimuthal angle ϕ measured around the beam axis, combined with the pseudorapidity

$$\eta = -\log\tan\frac{\theta}{2}$$

(where θ, the polar angle, is the angle from the beam pipe) are used to define a position within the detector. The distance ΔR in pseudorapidity azimuthal angle space is given by:

$$\Delta R = \sqrt{\Delta\eta^2 + \Delta\phi^2}$$

The challenging environment in which the LHC detectors operate mean that as well as being able to accurately measure individual particles, the detectors must be fast, radiation-hard and of high granularity to be able to deal with the large particle fluxes and to be able to distinguish hits from many distinct particles in a small amount of space. In addition, requirements for the ATLAS detector were that it should have large acceptance in pseudorapidity with close to full azimuthal angle coverage, good charged particle momentum resolution and high efficiency for Inner Detector track reconstruction. Detectors as close to the beam pipe as possible were required so as to be able to have good secondary vertex resolution. In addition, excellent electromagnetic calorimetry to identify and measure electrons and photons, along with hadronic calorimetry for jet and missing transverse energy measurements, and good muon identification and momentum resolution both at low p_T and high p_T were crucial requirements.

3.2 The Inner Detector

At the centre of ATLAS is the Inner Detector (ID) (see Figure 3.3), bounded by a cylinder of length 6.2 m and diameter 2.1 m. This is surrounded by a superconducting solenoid magnet (kept at 4.5 K) of diameter 2.5 m, providing a magnetic field strength of 2 Tesla at the centre of the Inner Detector, used for charge-identification and momentum measurement. The Inner Detector is a combination of high-resolution semiconductor pixel and silicon microstrip detectors and straw tube tracking detectors required for accurate vertex and momentum measurements close to the interaction point [93].

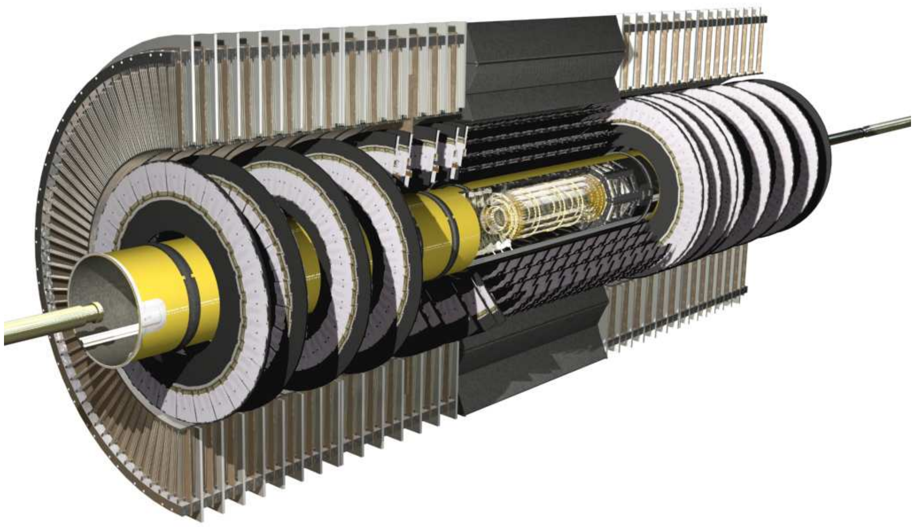

Figure 3.3: *Cutaway view of the Inner Detector, with the TRT visible on the exterior and the SCT barrel and endcaps surrounding the (yellow) support frame of the pixel detector situated at the centre (from [4]).*

The pixel detector

Closest to the centre of ATLAS is the pixel detector, composed of three silicon barrel layers arranged in concentric cylinders around the beam pipe, with inner radii 5.1, 8.9 and 12.3 cm. A charged particle passing through the silicon creates electron-hole pairs that drift towards a readout electrode due to a bias voltage set up across the silicon. A particle hit is recorded if the charge collected is larger than a particular threshold value. The individual pixel sensors are

$50 \times 400\ \mu\text{m}^2$ in size, segmented in $R-\phi$ and z and have an accuracy of 10 μm in $R-\phi$ and 115 μm in z.

Crucial to the accurate identification of promptly produced particles and short-lived particles such as B-hadrons is the ability to accurately reconstruct primary and secondary decay vertices and associated particle decay lengths. To this end, the innermost barrel (called the B-layer) is positioned as close as possible to the beam pipe (which itself has an outer radius of 3.0 cm). Due to the proximity of this layer to the interaction point, it will suffer the heaviest radiation damage, degrading its performance. As such, the detector has been constructed so as to allow replacement of this layer in future. In addition to the barrel layers, the pixel detector has additional silicon in the endcap region ($|\eta| > 1.05$) composed of three disks perpendicular to the beam axis on either side of the barrel region, providing total coverage up to a pseudorapidity of $|\eta| = 1.7$ and complete coverage in azimuthal angle. A typical charged track is expected to pass through three such pixel layers.

The Semi-Conducting Tracker (SCT)

Enclosing the pixel detector is the Semi-Conducting Tracker (SCT) detector consisting of silicon strip detectors which record particle hits in a similar way to that of the pixel detectors. The SCT system is made of four double-sided barrel layers of silicon microstrip detectors of 80 μm strip pitch, with radii 29.9, 37.1, 44.3 and 51.4 cm covering the $|\eta| < 1.4$ region. Each barrel module is composed of a pair of strip detectors wire bonded and glued back-to-back with another pair at a crossing angle of 40 mrad, allowing precision measurement in one direction. Each module has an intrinsic accuracy of 17 μm in $R-\phi$ and 580 μm in z. In addition to the SCT barrel modules there are two SCT endcaps, which consist of nine disks constructed as for the barrel layers, giving extended pseudorapidity coverage and additional space point measurements for charged tracks. Together the pixel and SCT tracking detectors provide pseudorapidity coverage over the region $|\eta| < 2.5$.

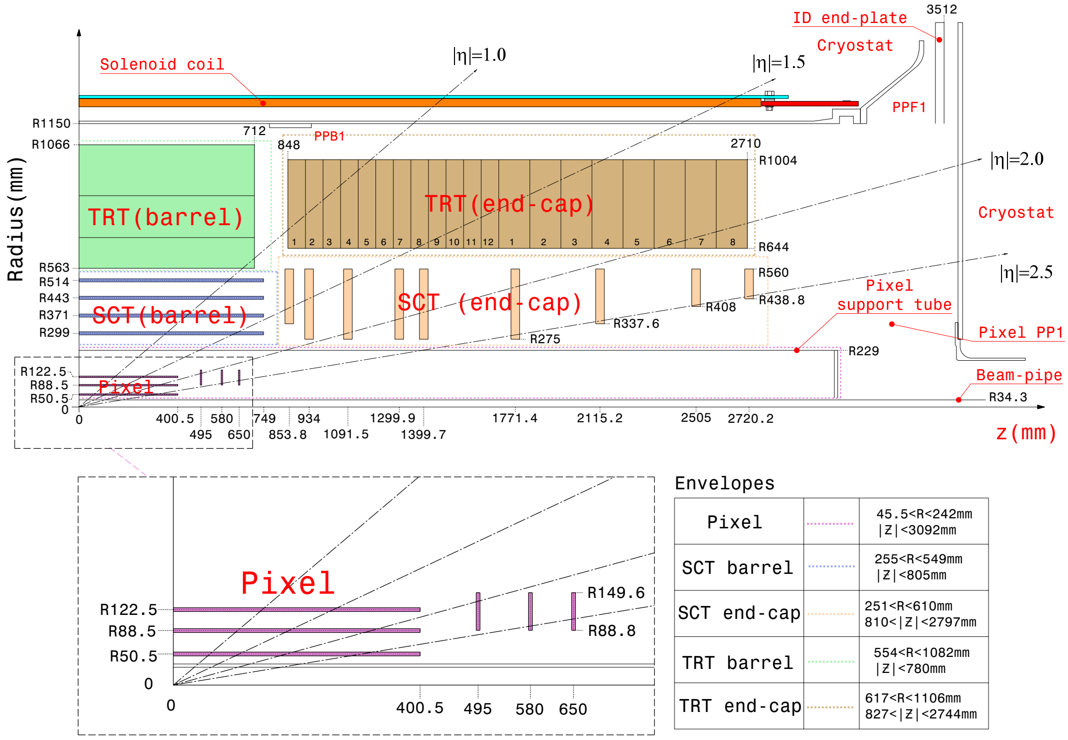

Figure 3.4: *Cross-section of one quadrant of the Inner Detector (from [3]).*

The Transition Radiation Tracker (TRT)

The outermost layer of the Inner Detector is the Transition Radiation Tracker. The position of the TRT relative to the other Inner Detector components is shown in Figure 3.4. The TRT is based on multiwire proportional chamber technology and was chosen so as to cheaply provide extended continuous tracking in the Inner Detector. The barrel section contains 50,000 straw detectors, 144 cm long and of 4 mm diameter, parallel to the beam axis. The wires are divided into two halves at $\eta \approx 0$ to reduce occupancy and thus give a total of 100,000 readout channels within $|\eta| < 0.7$. The TRT endcap contains an additional 320,000 straws aligned radially, of 37 cm in length, covering $0.7 < |\eta| < 2.5$. The straws are filled with a xenon gaseous mixture such that a charged particle traversing the gas causes ionisation, which is detected on the wire readout in a similar way as the silicon detectors, using a threshold of collected charge and timing information to determine track hits and their position. The TRT is capable only of providing $R-\phi$ information, and does so with a resolution of 130 μm in both the barrel and endcap.

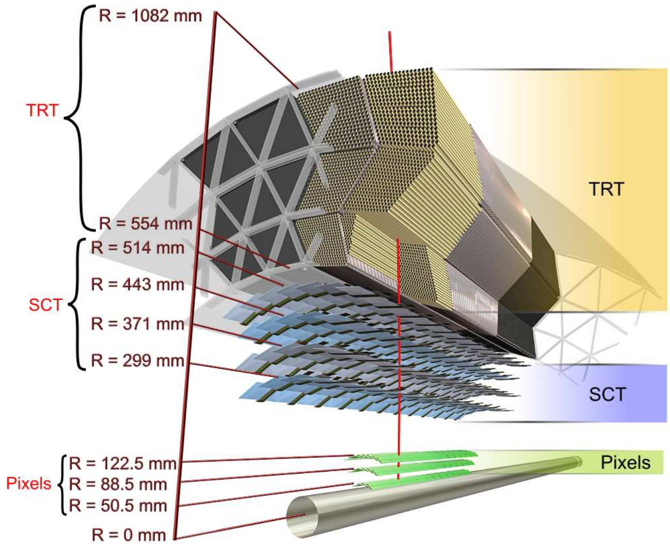

Figure 3.5: *Sensor and structural components traversed by a 10 GeV p_T charged particle passing through the barrel region of the Inner Detector (from [3]).*

Radiator material placed between the straws causes the emission of transition radiation photons at the boundary between the radiator material and the straws. The emitted photons cause greater ionisation in the xenon than would be caused by a standard particle hit alone. A second, higher threshold on the ionisation recorded, used to determine whether the TRT hit has additional transition radiation, provides a measure of the particle velocity and hence allows for some limited electron/pion separation. In addition, straw hits at larger radii contribute significantly to the momentum measurement of a particle. A particle originating at the interaction point can expect to cross at least three pixel layers and four SCT layers and around 36 TRT straws, the combination of which allows for a precise Inner Detector track measurement.

The inverse transverse momentum tracking resolution in the Inner Detector[4] is given by:

$$\sigma(\frac{1}{p_T}) = (0.34 - 0.41 \ \ \mathrm{TeV}^{-1}) \left(1 \oplus \frac{(44 - 80 \ \ \mathrm{GeV})}{p_T}\right)$$

where the range represents the variation of resolution from lower to higher $|\eta|$ values. Figure 3.5 summarises the path of a charged particle passing from the interaction point through the entire Inner Detector, highlighting the constituent sub-detectors and structural components it encounters along its flight.

Inner Detector material budget

Ideally, a detector would be able to measure the tracks of charged particles without interfering with the particle itself. The effect of the Inner Detector on a particle traversing it is largely due to the cumulative effect of material encountered by the particle. The performance requirements of the ATLAS Inner Detector are far greater than any previous tracking detector and the required fine detector granularity allowing for accurate track reconstruction comes with a consequent rise in material density.

Additionally, the high rates expected at the LHC make it impossible to transmit signals from the detector to electronics outside of the tracking volume. As such, the electronics must be integrated into the active volume itself which, along with the requisite cabling and cooling systems, as well as the ID support structure, inevitably lead to increased material in the Inner Detector.

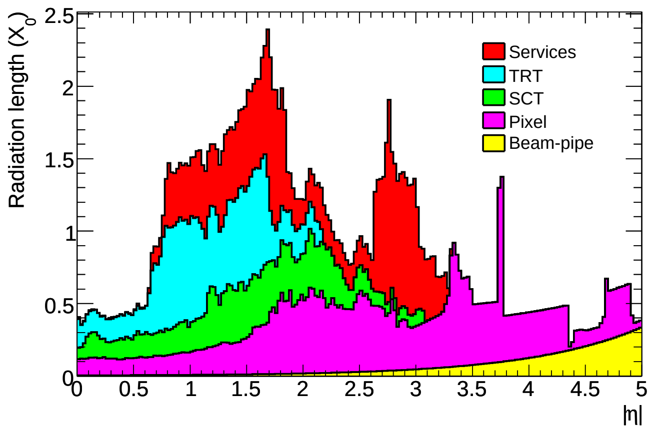

Figure 3.6: *Cumulative material within the Inner Detector in radiation lengths X_0 as a function of absolute pseudorapidity, averaged over azimuthal angle (from [4]).*

Figure 3.6 gives a breakdown of the cumulative material in the various components of the Inner Detector in terms of radiation length[2)], as a function of pseudorapidity. The consequences of the presence of this material is significant: the high material budget in the Inner Detector means that the probability of multiple scattering or bremsstrahlung (discussed in greater de-

[2)]Radiation length is the distance over which high-energy electrons lose on average $1/e$ of their energy.

tail in Appendix A) is high and affects measurement of the track momentum and the energy measurement in the calorimeter.

In the case of photons produced in the Inner Detector, around 40% convert into an electron-positron pair before reaching the calorimeters, which can cause significant tails in their reconstructed invariant mass distributions. An unintended by-product of this however is that we can use reconstructed photon conversions to provide an 'X-ray' image of the Inner Detector (shown in Figure 3.7) that reflects the distribution of material in the various detector components.

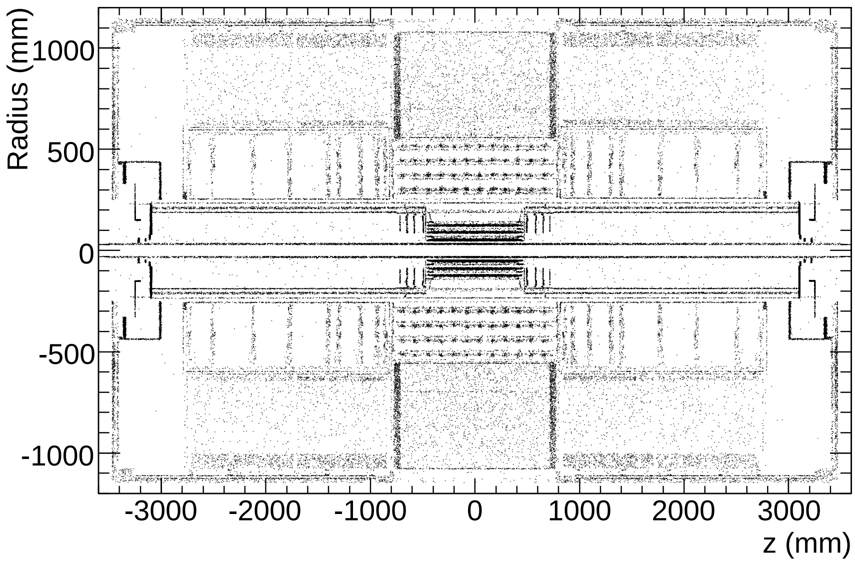

Figure 3.7: *An 'X-ray' image of the Inner Detector produced from detector simulation of photon conversions as a function of z and radius. From this it is possible to see the distribution of material in various structures throughout the detector (from [3]).*

The effect of scattering and bremsstrahlung (of particular importance for electrons), if not properly modelled in simulation and corrected for in track pattern recognition algorithms, can cause large tails in energy and invariant mass distributions, smear distributions of other track parameters and can cause a drop in efficiency if, for example, an electron undergoing late bremsstrahlung in the ID is then not correctly associated with a calorimeter hit.

3.3 Calorimeters

Surrounding the Inner Detector and solenoid is the electromagnetic and hadronic calorimetry, measuring the energy of both charged and neutral particles, providing pseudorapidity coverage up to $|\eta| = 4.9$. An overview of the ATLAS calorimetry system is given in Figure 3.8.

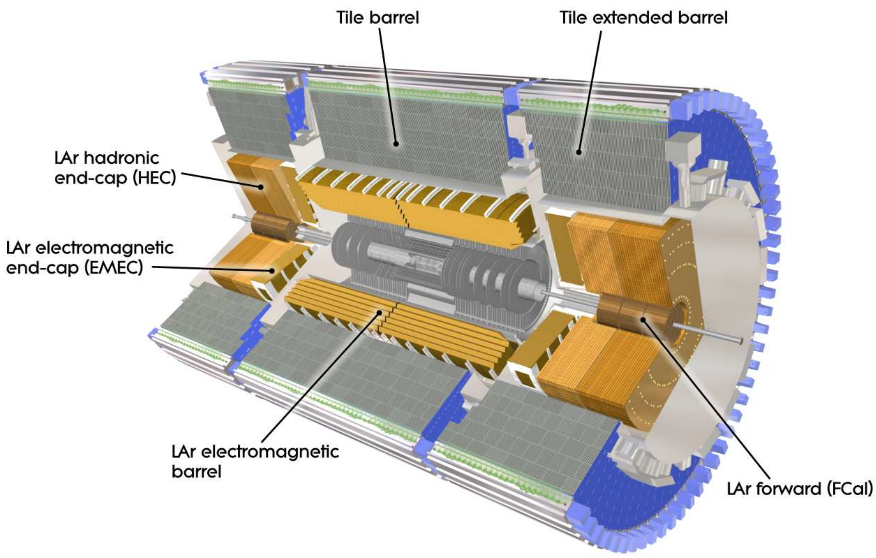

Figure 3.8: *Cutaway view of the ATLAS calorimetry system, surrounding the Inner Detector at the centre (from [3]).*

Electromagnetic calorimeter

The electromagnetic calorimeter (ECAL) is composed of a barrel and two endcaps, used to measure the energy of electrons and photons. The barrel region covers $|\eta| < 1.475$ and has inner radius 2.8 m and outer radius 4.0 m. At $\eta = 0$ is a 6 mm gap where the two barrel sections join. The endcaps are composed of two outer disks covering $1.375 < |\eta| < 2.5$ and two inner disks covering $2.5 < |\eta| < 3.2$. The ECAL shares a cryostat with the central solenoid. The ECAL uses dense 'absorbers' made from lead to cause particle showers, which are interleaved with liquid-argon layers that cause electron ionisation registered on copper electrodes. Liquid argon was chosen as the active detector medium due to its linear behaviour and intrinsic radiation hardness. The accordion geometry of the calorimeters allow for complete ϕ coverage without any azimuthal angle cracks that would otherwise result in a degradation of energy resolution.

In addition to the barrel and endcap sections, in the region $|\eta| < 1.8$ there is a layer of liquid argon which precedes the rest of the calorimeter, called the presampler. This is used to obtain a measurement of the particle energy before the particle crosses material at the entrance to the main calorimeter, and allows correction for the concurrent energy loss.

The ECAL has a granularity varying across η and at each layer, in the range $\Delta\eta = 0.003 - 0.1$ and $\Delta\phi = 0.025 - 0.1$. This calorimeter has a total of 24 radiation lengths in the barrel and 26 in the endcap, to contain all the energy from electromagnetic showers. The overall energy resolution of the electromagnetic calorimeter is given by:

$$\frac{\Delta E}{E} = \frac{11.5\%}{\sqrt{E}} \oplus 0.5\%$$

(with energy, E, of the particle measured in GeV).

Hadronic calorimeter

The hadronic calorimeter (HCAL) is composed of barrel, endcap and forward calorimetry. A hadronic barrel and two extended barrel tile calorimeters cover $|\eta| < 1.0$ and $0.8 < |\eta| < 1.7$ respectively, and consist of iron plates interspersed with plastic scintillator tiles to alternately start and measure hadronic showers. The hadronic calorimeter must be thick enough to stop punch-through of hadrons into the surrounding muon system. The HCAL is 11 interaction lengths[3)] thick at $\eta = 0$, which reduces the presence of particles other than muons (and neutrinos) reaching the muon spectrometer to manageable levels.

The hadronic calorimeters in the endcaps, which extend the calorimeter region over $1.5 < |\eta| < 3.2$, are not made from the same tile technology as the barrel regions due to the high levels of radiation in the forward region, but instead are of the liquid argon type used by the ECAL, here using copper as the passive material. The liquid argon is cooled by the Inner Detector cryostat. The barrel scintillator tiles provide a granularity of up to 0.1×0.1 in $\eta \times \phi$,

[3)] Hadronic interaction length is the mean free path of a high-energy hadron before undergoing an interaction.

the endcaps have a granularity of 0.2×0.2. The energy resolution of the HCAL in the $|\eta| < 3.2$ region is

$$\frac{\Delta E}{E} = \frac{50\%}{\sqrt{E}} \oplus 3\%.$$

In the very forward region $3.1 < |\eta| < 4.9$, the forward calorimeter (FCAL) acts as a combined electromagnetic and hadron calorimeter and has to deal with particularly high levels of radiation, primarily the bulk of the proton remnant. The calorimetry here is of a high-density liquid argon design constructed from copper and tungsten so as to limit the width and depth of showering, reduce the leakage from the FCAL into neighbouring calorimeters and decrease radiation background in the muon spectrometer. In the forward region the energy resolution is

$$\frac{\Delta E}{E} = \frac{100\%}{\sqrt{E}} \oplus 10\%$$

3.4 Muon spectrometer

Muons leave tracks in the Inner Detector and pass through the calorimeters depositing on average 4 GeV of energy (see Figure 3.9(a)) before continuing onwards to be detected in the muon spectrometer that surrounds the calorimetry. When they reach the muon spectrometer, further momentum and charge measurements are possible due to a superconducting toroidal magnet system integrated into the muon system. By the time muons reach the muon spectrometer they have passed through on average 100 radiation lengths of material, compared with 1–2 radiation lengths in front of the presampler, as illustrated in Figure 3.9(b). From parametrisations of the energy loss from simulations and measurements of energy deposits in the various calorimeter subsystems it is possible to correct for this energy loss [94]. Associating tracks from the Inner Detector to energy deposits in the calorimeter can provide useful additional information for identification and reconstruction of muons, as is described later in this section.

Final state high-p_T muons provide a clean signal for many interesting physics studies and are relatively easy to identify and trigger on. The frame of ATLAS is dominated by the muon

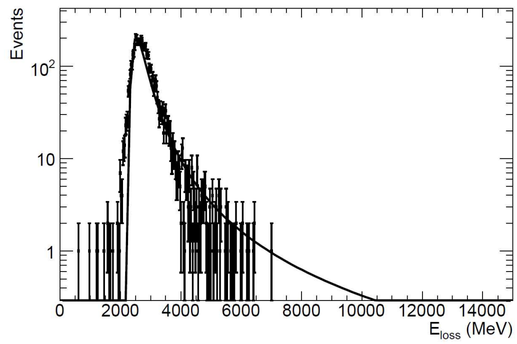

(a) Energy loss of muons through calorimeters

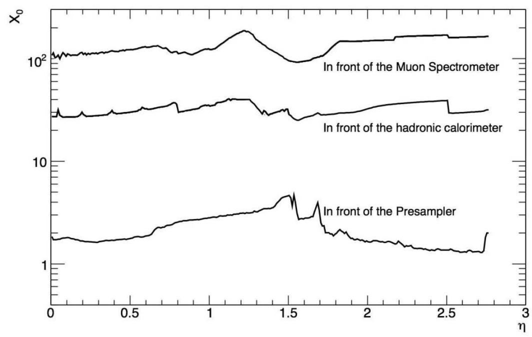

(b) Cumulative X_0 at entry to muon spectrometer

Figure 3.9: *Distribution of energy loss from 10 GeV muons in the calorimeters (for* $|\eta| < 0.15$*) (left), and cumulative material (in radiation lengths,* X_0*) encountered by a particle entering the muon spectrometer as a function of* $|\eta|$ *and averaged over azimuthal angle (right), (from [94]).*

spectrometer, and the shape of this is dictated by the independent air-core toroidal magnet system, which in the barrel extends over a length of 25 m, has an inner and outer radius of 4.7 m and 10 m respectively, and has two endcap toroids of 5 m length inserted into it. The toroids are each composed of eight superconducting coils distributed radially, providing a field strength of 0.5 Tesla. At these outer reaches of the ATLAS detector, three barrel chambers of radii 5, 7.5 and 10 m surround the central calorimetry in the range $|\eta| < 1.0$ whilst endcap chambers in the form of four disks at distances of 7.4, 10.8, 14 and 21.5 m from the interaction point cover the pseudorapidity region $1.0 < |\eta| < 2.7$. An overview of the ATLAS muon system is given in Figure 3.10.

Active volumes in the spectrometer can be classified as either precision measurement chambers or dedicated trigger chambers[4)]. Precision measurement of muon tracks is provided by Monitored Drift Tubes (MDTs) in the barrel and most of the endcap. The MDTs use aluminium tubes of 30 mm diameter with a central tungsten wire and argon gas to provide a track position resolution of 80 μm (35 μm chamber resolution in R). At higher pseudorapidities ($2.0 < |\eta| < 2.7$), Cathode Strip Chambers (CSCs) are used at inner layers of the spectrometer,

[4)] With sub-systems and a magnetic field independent of the rest of the detector, if desired, the muon spectrometer can run in standalone mode, providing measurement of muon tracks independently of the Inner Detector.

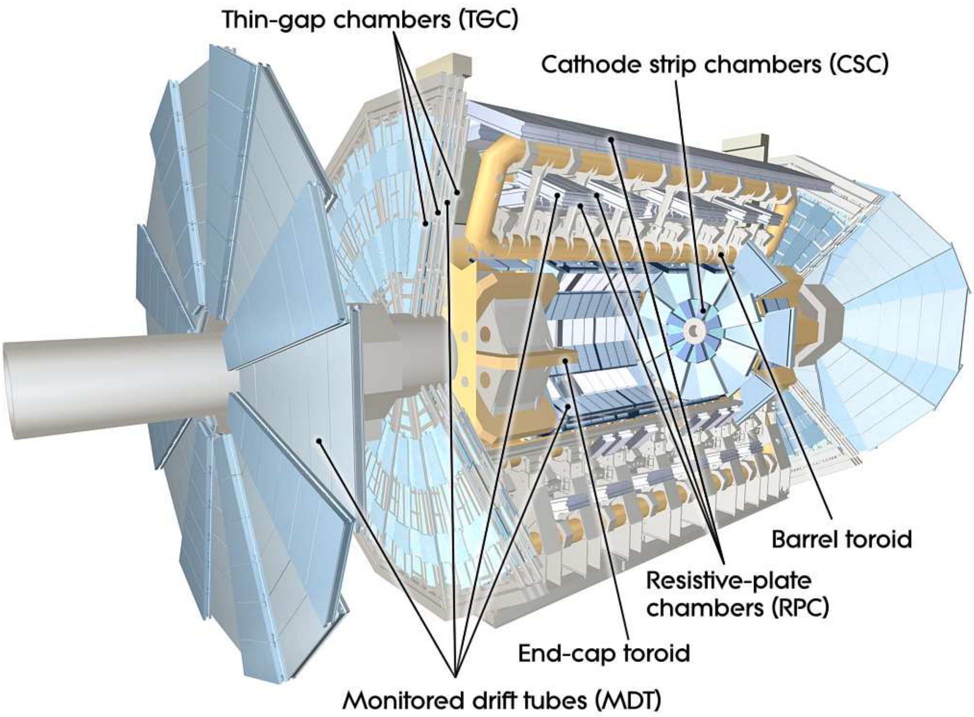

Figure 3.10: *Schematic of the Muon Spectrometer systems (from [3]).*

in addition to MDTs, as their greater granularity and faster readout times make them particularly suited to operating in the forward region. The CSCs are multi-wire proportional chambers providing a spatial resolution of 60 μm. The performance goal for the muon spectrometer is the achievement of a standalone p_T resolution of 10% on a 1 TeV muon (corresponding to a sagitta of 0.5 mm measured to better than 50 μm accuracy).

At the centre of the detector ($\eta = 0$), a gap exists in muon system coverage to allow access for services to the solenoid magnet, calorimetry and Inner Detector. The size of the gap varies through the detector but the angular range from the interaction point, through which a straight track can expect to miss all three muon chamber layers is a maximum of $\pm 4.8^\circ$, corresponding to $|\eta| < 0.08$. Additional drops in efficiency appear at $\phi \approx 1.2$ and $\phi \approx 2.2$ for $|\eta| < 1.2$ due to gaps caused by the 'feet' of the muon spectrometer.

Muons can be identified and measured with high efficiency with transverse momenta from around 3 GeV to 3 TeV. Muons must have at least a p_T of 2.5 GeV to have the possibility of reaching the muon system to allow for identification (due to the energy loss in the calorimetry, as described above). At low p_T the resolution of the muon spectrometer is dominated by the energy loss in the calorimeter, and also by multiple scattering effects. At high p_T it becomes increasingly difficult to measure the tracks with any precision, and chamber alignment and intrinsic resolution become the dominant effects. The contributions of various factors to momentum resolution, as a function of transverse momentum, are shown in Figure 3.11.

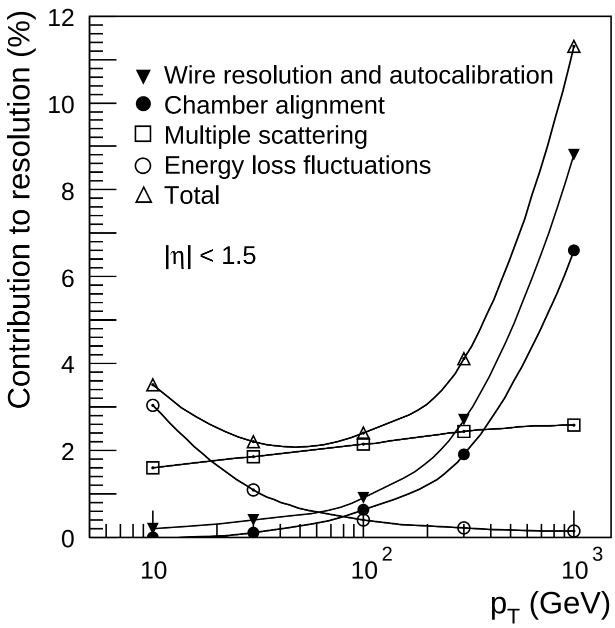

Figure 3.11: *Momentum resolution for muons reconstructed in the Muon Spectrometer as a function of transverse momentum for* $|\eta| < 1.5$*, with an alignment uncertainty of 20* μ*m.*

Due to the remote distance of the muon system from the interaction point, the time taken for a muon from a particular event to register in the muon spectrometer is far greater than the bunch spacing of the LHC, so specialised trigger systems have been introduced to quickly identify events with high-p_T muons. These systems cover pseudorapidities up to $|\eta| = 2.4$ and are composed of Resistive Plate Chambers (RPCs) in the barrel region ($|\eta| < 1.05$) and Thin Gap Chambers (TGCs) in the forward region. In addition, these systems provide the muon position in the direction orthogonal to that determined by the precision tracking chambers (providing measurement capability up to $|\eta| = 2.7$, further than that available for triggering). Details of relevant trigger algorithms for muons and quarkonium can be found in Section 3.5.

Muon identification and reconstruction

Currently in ATLAS there are two main families of muon algorithms that use different methodologies for identification and reconstruction of tracks: the first, and currently default in ATLAS for physics analysis, is the Staco collection that includes muons from the Muonboy, Staco and MuTag algorithms (see reference [95]); the second is the Muid collection that includes the Moore [96], MuIdCombined [97] and MuGirl [98] algorithms. In future both collections may be used and even combined (with removal of overlapping identified muons) to provide even better identification and reconstruction capabilities. The reconstructed muon collections can be categorised by three main types of identified muon (reflecting the presence of three algorithms in each collection): standalone, combined and tagged muons.

Muons identified by the muon spectrometer alone are called 'standalone' muons. Identification of these muons relies on hits in two spectrometer stations for low p_T muons (three hits are needed for muons with $p_T > 10$ GeV) to form track segments. In the Muonboy algorithm the muon segments are extrapolated back to the interaction point correcting for energy loss by a parametrisation based on the material traversed (effectively the average expected energy loss). The Moore algorithm corrects for multiple scattering and energy losses in the calorimeter using calorimeter energy measurements and then performs the extrapolation. Standalone algorithms, not dependent on Inner Detector tracks, have the widest coverage in η, out to $|\eta| < 2.7$ compared with $|\eta| < 2.5$ for ID tracks, but suffer from the aforementioned thin gaps in coverage. Reconstruction of low p_T tracks is particularly affected in this standalone mode as they often do not reach the outermost stations. Standalone muon signals are particularly vulnerable [99] to the prevalence of muons from the decay in flight of $K^{\pm}$ and $\pi^{\pm}$, which due to their lengthy decay time, produce muons in the calorimeter that can fake signals of interest for many physics analyses.

'Combined' muons form the mainstay of muons expected to be reconstructed in ATLAS. Algorithms to identify these muons combine information from Inner Detector tracks with muon spectrometer tracks and as such are limited to identification in $|\eta| < 2.5$, but with improved resolutions for $p_T < 100$ GeV due to ID tracking information. The Staco algorithm combines the tracks using a statistical combination of the two independent track measurements, while the MuIdCombined algorithm performs a global refit of all hits associated with the two tracks.

Finally, 'tagged' (or low p_T) muon algorithms try to identify additional muons that, whilst having been measured in the Inner Detector only, have isolated segment hits in the muon spectrometer. Generally this is due to these muons being of such low p_T that they barely escape the calorimetry and so cannot penetrate the muon stations properly. The tagged muon algorithms search for these muons by propagating all Inner Detector tracks with sufficient p_T to the first muon station, and searching nearby for any muon hits, that act as the 'tag' for the track. MuTag uses a χ^2 method to associate tracks to muon tags, whilst MuGirl uses artificial neural network techniques.

Due to the complicated nature of the muon reconstruction algorithms in ATLAS and the wide variety of different thresholds, algorithm approaches, and different types of identified muons it is not very meaningful to give a single figure for muon efficiency or purity. Reference [99] provides a detailed breakdown of the muon ID performance and fake rates in a wide variety of cases. Further details specific to the case of low p_T muons from J/ψ and Υ decays can be found in Chapters 5 and 6 in this thesis.

3.5 Trigger and data acquisition

Whilst the various sub-detectors of ATLAS can provide excellent measurements of the proton collisions at the LHC, the bunch crossing rate of around 40 MHz provides a data rate far too high to be feasibly processed and stored. Some mechanism is therefore needed to reduce the amount of data that has to be processed from ATLAS, as well as the total number of events eventually stored to tape, in a way that is both predictable and allows us to reject events of little interest whilst retaining those events desired for physics analyses.

The ATLAS trigger and data acquisition system (DAQ) [100, 101] utilises three successive levels of online event selection to quickly identify and store such events, reducing the event rate from an initial bunch crossing rate of 40 MHz to around 100–200 Hz. Due to current technology and resource limitations this is the highest rate than can be written to disk for further offline analysis (corresponding to a data throughput of about 300 MB/s [102]). In addition to reducing the overall rate, the DAQ system reduces the computational demands at each trigger level to the bare minimum necessary to decide whether to allow the event to continue to the next level for more detailed consideration. This three-tier trigger system is illustrated in Figure 3.12.

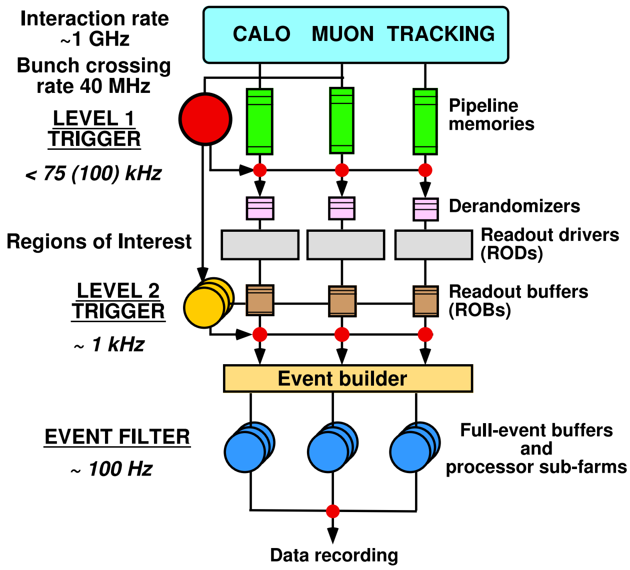

Figure 3.12: *Schematic diagram of the ATLAS trigger system.*

The level-1 (L1) trigger system is hardware-based and has access to the RPC and TGC muon trigger chambers, as well as reduced-granularity ($\Delta\eta \times \Delta\phi = 0.1 \times 0.1$) calorimeter information on which to make a decision on whether to allow the event to proceed to level-2 for further processing. The level-1 algorithm has 2.5 μs in which to make a decision. The hardware uses indications of high-p_T leptons, jets and photons, as well as larger missing and total transverse energies to choose whether the event warrants further investigation. Up to 256 level-1 trigger 'items' can be programmed as features on which to accept the event. These items can be single features such as a high p_T lepton, or can be multi-object items such as the presence of an electron in addition to a tau candidate.

A prescale can be applied to each of these items independently. A prescale N causes the trigger to pass only one in N events to level-2 that otherwise pass level-1, if the rate for such an item would otherwise dominate the throughput. As luminosity drops throughout a run, the prescale can be modified in each one-minute luminosity block to keep the total output rate at maximum. The level-1 trigger reduces the rate to 75–100 kHz, which is then passed to the level-2 software-based trigger system.

The level-2 (L2) trigger uses ‘region-of-interest’ (RoI) information from level-1, in the form of coarse $\eta - \phi$ locations, to further investigate interesting features. The level-2 trigger has full access to event data with full precision from all detector components in these regions-of-interest, and may expand beyond these regions if necessary. Most notably, L2 software has access to Inner Detector tracks for the first time that can be used for additional rejection. The level-2 trigger reduces the event rate to around 1 kHz, with an average event processing time of approximately 40 ms.

This information is then passed to the final trigger stage, known as the Event Filter (EF), for filtering of events based on full detector information. The level-2 trigger together with the event filter are known collectively as the High Level Trigger, or HLT. The Event Filter runs on a farm of 1,800 quad-core CPUs [102] and has around 4 seconds per event in which to make a decision. The L2 trigger decisions are used to seed algorithms used at the EF stage which have access to full vertex reconstruction, track fitting and missing E_T calculations, along with full resolution in the whole detector. With this information the Event Filter performs the most detailed analyses in the trigger chain with which to make the final selection of whether or not to store the event for offline analysis.

At low luminosity trigger selection will be relaxed to allow focus on commissioning of the trigger and detector. As such, many triggers will operate in what is known as ‘pass-through’ mode, in which algorithms are executed but events are stored irrespective of the decision. This will allow for tests of the trigger selections and validation of the various algorithms through trigger data quality monitoring operations.

Di-muon trigger algorithms

Of particular interest to studies of quarkonium detailed in this thesis are the trigger algorithms that will be used for low p_T di-muons. At low luminosity (10^{31} cm^{-2}s^{-1}), at the level-1 trigger, the lowest p_T threshold for muons is 4 GeV (muons can be accepted below this, although with reduced efficiency). At level-1 a single 4 GeV muon trigger item will be in operation with an expected total rate of 1730 Hz, along with a di-muon 4 GeV trigger with a total rate of 70 Hz. Neither of these triggers are expected to need prescales. By contrast, for the electron triggers the lowest threshold is 3 GeV. The 3 GeV di-electron rate is 6500 Hz with no prescale, but the 3 GeV single electron trigger requires a prescale of 60 in order to reduce the rate to 674 Hz (see reference [102] for more details of other trigger items).

Two philosophies exist for the triggering of low p_T di-muons. The first makes use of two separate RoIs at level-1 (a level-1 di-muon trigger) to identify the two muons in the event based on independent hit coincidences in the muon RPCs and TGCs. The level-1 RoIs are of size $\Delta\eta \times \Delta\phi = 0.1 \times 0.1$ if in the barrel or $\Delta\eta \times \Delta\phi = 0.025 \times 0.025$ if in the endcap. At level-2 the two RoIs are processed with full granularity data, confirming the level-1 muon hypothesis, approximating the track and estimating the transverse momentum. Once at the Event Filter the two muons can be combined and an invariant mass cut imposed. This is known as the topological di-muon trigger.

The second approach is to trigger on a single muon at level-1 and then search for an additional muon in an expanded $\eta - \phi$ region at level-2. This is particularly useful for studies of J/ψ and Υ at low p_T as the decay kinematics are well understood (see Chapter 5) so likely regions can be defined relative to the identified muon in which to search for a second muon, were the event to contain a J/ψ or Υ. Inner Detector tracks in the $\eta - \phi$ region are extrapolated to muon spectrometer tracks to try and find a match. If a match is found, a di-muon invariant mass of $M > 2.8$ GeV is imposed and the remaining pairs passed to the EF for analysis as an identified di-muon pair. This is known as the TrigDiMuon algorithm trigger. Further details and trigger performance studies can be found in reference [103].

3.6 Full chain simulation

The production and analysis of data in ATLAS is performed in a number of steps that together are known as the 'full chain'. Data may be sourced from either artificially-produced Monte Carlo computer simulations (as is done currently, and will be used in the data-taking era for comparison of ATLAS results to theories) or from the ATLAS detector itself. A flowchart of the various stages to get from raw data to analysis ntuple is shown in Figure 3.13.

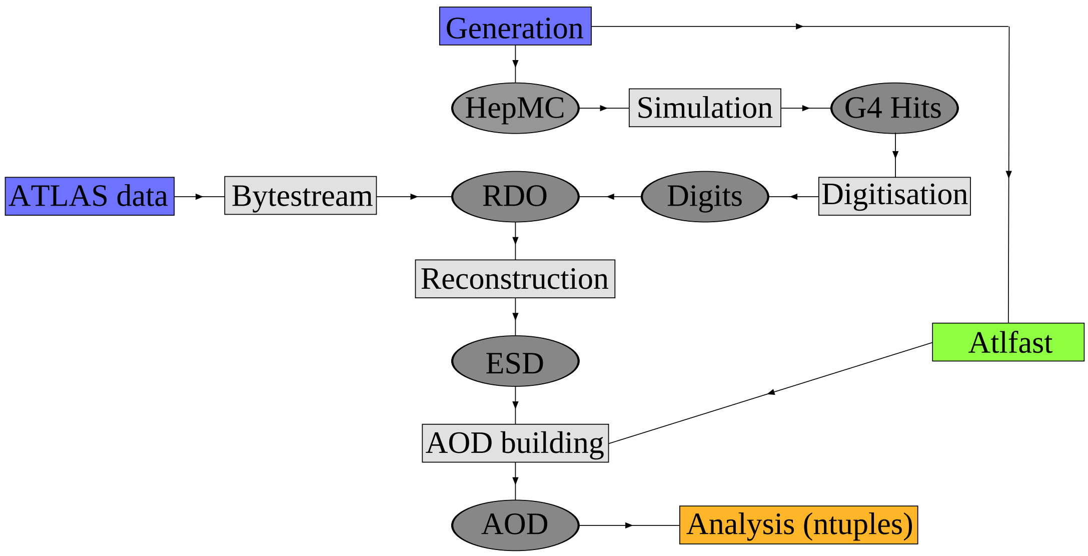

Figure 3.13: *Flowchart of the ATLAS 'full chain' of data analysis starting from either event generation or from raw detector from the ATLAS detector. Main data formats are shown as ovals, computing/conversion steps shown as rectangles.*

From the Monte Carlo source, data are initially produced using 'Monte Carlo event generators' that attempt to implement phenomenological descriptions of currently known high-energy physics collision events in conjunction with new models that one would like to test. A number of different Monte Carlo (MC) generators are used within ATLAS. Some, such as PYTHIA [104] and Herwig++ [105] can be considered "general-purpose" event generators capable of simulating a large number of processes and describing a wide range of physics, while many more specialise in the simulation of particular aspects of specific process types.

The general-purpose generators model the proton-proton collision, subsequent parton interactions, fragmentation and hadronisation and eventual decay of particles into long-lived particles that would be detected in ATLAS. The generators employ a large number of parameters to choose processes to simulate, place kinematic cuts on particles, and tune the physical models used for simulation to data from previous experiments (and eventually from the LHC). These generators are integrated into the central ATLAS software framework, which allow access to the generator parameters by means of 'jobOptions' which control the input to the generator in a centrally-defined way within ATLAS for each process of interest. The studies described in this thesis have been performed using the PYTHIA 6.4 MC event generator as input.

Approximately 1% of proton-proton collisions at the LHC are expected to result in the production of a b (or $\overline{b}$) quark. For study of particular decay channels, only a small fraction of these quarks will hadronise into the particular particle of interest. As the PYTHIA generator freely simulates proton-proton collisions, to produce a high-statistics sample of generated events of interest without intervention would mean having to produce orders of magnitude more events than desired, with limited computing resources (the time needed to simulate such complex events can be of the order of minutes per event). An option would be to force PYTHIA to produce events of interest at the particle level by intervening in the physical models. To do so however is ill-advised and is liable to introduce biases and indeterminable effects to the model.

For this reason a number of B-Physics studies use a specialised interface to PYTHIA called PythiaB [106] for study of decays involving b quarks. PythiaB intervenes in the PYTHIA event generation and checks for the presence of a b quark satisfying certain predetermined kinematic conditions. If none is found, further generation of the event is interrupted, saving CPU time without interfering with PYTHIA's internal statistical algorithms for generation. If a b quark is found, the event is allowed to continue generation. Such an event can then be repeated using a different hadronisation (from a different random seed) to produce another unique event. Internal bookkeeping of such event rejection and event duplication is handled by PythiaB and the final PYTHIA output at the end of a run is corrected for such interventions.

The output from the event generators is stored in a format known as HepMC [107]. This contains information about the particles present in the simulated event, including kinematic information about the particle, production/decay vertex information and data on the ‘parent’ particle (the particle from which a particular particle was produced) and the ‘children’ particles (the particles to which a particular particle decayed). At this stage no consideration of the ATLAS detector is taken into account beyond sharp kinematic cuts placed on final state particles. Chapter 4 details studies that were done at the Monte Carlo level in implementing and tuning simulated samples of quarkonium production in ATLAS, as well as important background samples now used widely within the ATLAS Collaboration.

The HepMC data is then passed to the simulation stage where Geant 4 [108] takes the particles from the event generator and simulates their passage through the ATLAS detector. The Geant 4 software uses an accurate model of the geometry/material description of ATLAS in combination with detailed physical models of the various effects such as energy loss of different particles, ionisation, bremsstrahlung and multiple scattering to accurately model the passage of particles from the eV to TeV range through the detector and the signals that would be seen in the detector as a response. Various detector geometries can be defined at the Geant simulation stage and also need to be taken into consideration at the final analysis stage. These two geometry definitions are not required to be the same and can be used to study effect of a geometry mismatch in real data (between the true geometry and what we believe it to be) and its impact the performance of the detector. These effects are discussed in Chapter 6. The output from the simulation stage is in the form of Geant-4 ‘hits’, that are then converted into ‘digits’ which mimic the different responses of various subdetectors to particle interactions, taking into account aspects such as timings and voltages.

With data coming from the ATLAS detector, rather than event generators, raw data comes from the detector from readout buffers in a ’bytestream’ form similar to that of Geant-4 digits. The ByteStream conversion service converts this raw event data into meaningful C++ representations of these objects known as Raw Data Objects, or RDOs. The same conversion is done in the generator-data case, converting digits to RDOs. Beyond this point the analysis of data is performed irrespective of whether data comes from ATLAS or from Monte Carlo generators.

At this point reconstruction algorithms are used to convert RDOs into high-level physics objects such as tracks, vertices, energy deposits, electrons, muons and jets that are stored in a format called Event Summary Data (ESD). This is the most detailed level of data format that will be available for detector performance and physics analyses, the ESD contains information on individual sub-detector hits in addition to higher level identified objects as well as information regarding which algorithms were used to reconstruct which objects. The resources are unavailable to allow habitual physics analysis at the ESD-level due to a large filesize per event. As such, information is distilled from the ESD to a format called Analysis Object Data (AOD). A program called Atlfast [109] is also available, which takes Monte Carlo data as input and replaces the full simulation and reconstruction phases by smearing Monte Carlo data based on models tuned from studies with full simulation data. In this way Atlfast produces an approximation to the full simulation with output as AOD information that can be used for studies without the resource requirements of full simulation.

The AOD files in both full and Atlfast simulation contain the main physics objects (such as tracks, particles, muons, electrons, jets) but without the detailed information available in the ESD (such as the ability to compare muon reconstruction from different algorithms, individual calorimeter cell responses and detailed Inner Detector surface hit information). More details of the data models for ATLAS can be found in references [110, 111]. From AOD information (and ESD in special cases) dedicated physics analysis algorithms can be run to retrieve data of interest for particular studies, as has been done in this thesis.

3.7 Distributed grid computing

The total data output from the four LHC experiments combined is expected to be approximately 15 Petabytes [112] per year, far exceeding that of any other experiment to date. No single institution or indeed country has the resource capabilities to store and analyse such a data load. As a consequence of this CERN, in collaboration with member states, have been developing a distributed computing infrastructure known as the Worldwide Large Hadron Collider Computing Grid (LCG). The “grid” is a worldwide network of computing sites that are used together as a decentralised but coherent structure of processing and storage facilities that are used for distributed analysis of data from the LHC.

In this model, data from ATLAS would be first recorded on tape at CERN (known as the "Tier-0" centre) before being processed and distributed to large computing sites across the globe deemed "Tier-1" centres that act as dedicated grid storage and support centres. From there, data is again transferred to "Tier-2" centres consisting of many more smaller-scale facilities between which the data from CERN is shared out. At this level further central analysis and processing is performed and from which "Tier-3" sites (which represent university clusters or individual scientist's computers) can access data for physics analysis.

This structure is designed to be largely hidden from a standard user of distributed analysis. For ATLAS (and LHCb), dedicated software known as Ganga [113] is used to define datasets to analyse, code to run and software releases to be used, which then interfaces with grid software to transfer the analysis code to the site where the data is stored, where the code is to be run, with the results (ntuples and logfiles) then returned to the user, all using the same ATLAS software framework as would be used on a local batch computing system. Further details are available in references [112, 113].

"It is unworthy of excellent men to lose hours like slaves in the labour of calculation which could be relegated to anyone else if machines were used."

Gottfried Wilhelm von Leibnitz

4

Monte Carlo studies

This chapter discusses studies performed using the Monte Carlo event generator PYTHIA 6.403 to tune and simulate charmonium and bottomonium production. We work within the framework of the NRQCD production model, although it should be emphasised that the predictions for LHC discussed here have been tuned from Tevatron data and the methods used are not reliant on NRQCD being the underlying model. For the simulated data discussed in this report, initial state radiation is switched on whilst final state shower evolution of the NRQCD colour octet states is switched off. Di-muon p_T and η cuts were added for all studies, unless explicitly stated, both to simulate the effect of the trigger on observed production rates and thus provide a realistic estimate of production rates at the LHC, and to improve the efficiency of generation of these events.

The PYTHIA program can be used to generate high-energy physics events. The objective is to provide as accurate as possible a representation of event properties in a wide range of reactions, within and beyond the Standard Model. This is implemented with emphasis on those events where strong interactions play a role, directly or indirectly, and therefore multihadronic final states are produced. Since our theoretical knowledge here is rather limited the program is based on a combination of analytical results and QCD-based models (see Chapter 2). In the following section we describe the usage of PYTHIA for generation of heavy quarkonium events within Athena, the ATLAS reconstruction and analysis software framework.

4.1 Implementation of colour-octet processes in PYTHIA

Colour-octet simulation has recently become available as standard in PYTHIA and currently implements the leading order diagrams in α_s for quarkonium production in both singlet and octet modes. NRQCD long-distance matrix elements were currently set to unity by default, but Section 4.2 references some values based on fits to experimental data, that have recently become default in PYTHIA for the lowest charmonium and bottomonium states.

PYTHIA now provides a number of intermediate colour-octet quarkonium states (see Table 4.1) that can be produced in colour-octet subprocesses and which subsequently decay into singlet states with the emission of one or more soft gluons.

Particle ID	Octet state
9900441	$c\bar{c}[^1S_0^{(8)}]$
9900443	$c\bar{c}[^3S_1^{(8)}]$
9910443	$c\bar{c}[^3P_0^{(8)}]$
9900551	$b\bar{b}[^1S_0^{(8)}]$
9900553	$b\bar{b}[^3S_1^{(8)}]$
9910553	$b\bar{b}[^3P_0^{(8)}]$

Table 4.1: PYTHIA *codes (KF) for new colour-octet states.*

Currently the branching fractions in PYTHIA have been set such that all charmonium octet states decay exclusively to the J/ψ singlet state (443) plus a gluon, and bottomonium octet states into the Υ singlet state (553) plus a gluon. The masses of the octet states have been chosen to allow this, without too much excess phase space, i.e. the emitted gluon is always very soft. The colour-octet particle codes are 9900000 bigger than that of the corresponding colour-singlet state (and so reside amongst the generator-specific codes).

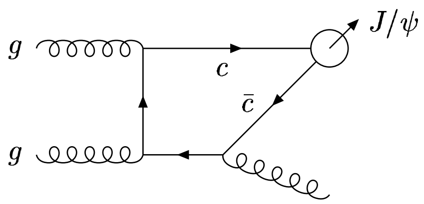

(a) Leading-order colour-singlet ($^3S_1$)

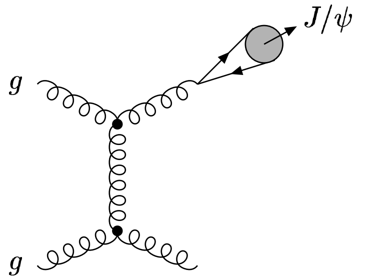

(b) Colour-octet fragmentation ($^3S_1$)

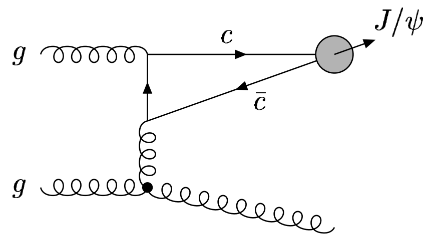

(c) Colour-octet t-channel gluon exchange ($^1S_0$, ^3P_J)

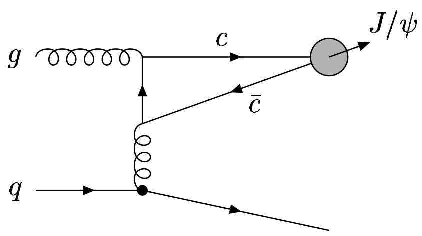

(d) Colour-octet t-channel gluon exchange (gq process)

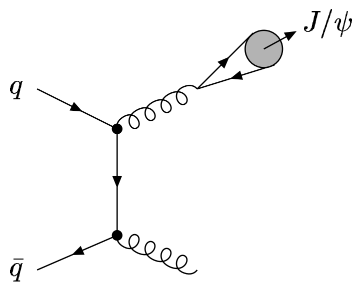

(e) Colour-octet fragmentation ($q\bar{q}$ process)

Figure 4.1: *Example diagrams for singlet and octet J/ψ production mechanisms available in* PYTHIA.

PYTHIA already includes the leading order colour-singlet subprocess for $^3S_1$ production outside of the NRQCD framework:

$$g+g \to Q\,\bar{Q}\,[^3S_1^{(1)}]+g, \quad \text{for} \quad Q=c,b \tag{4.1}$$

(see Figure 4.1(a)), three subprocesses for each of ^3P_J, $J=0,1,2$ as well as the three leading order α_s^3 subprocesses for colour-octet $^3S_1$, $^1S_0$ and ^3P_J production, shown in Table 4.2 (see Figure 4.1), both for charmonium and bottomonium. A summary of all the available colour-singlet and colour-octet production subprocesses available in PYTHIA is given in Table 4.2.

Colour-singlet/octet production in PYTHIA			
Charmonium subprocesses		Bottomonium subprocesses	
421	$g+g \to c\bar{c}[^3S_1^{(1)}]+g$	461	$g+g \to b\bar{b}[^3S_1^{(1)}]+g$
422	$g+g \to c\bar{c}[^3S_1^{(8)}]+g$	462	$g+g \to b\bar{b}[^3S_1^{(8)}]+g$
423	$g+g \to c\bar{c}[^1S_0^{(8)}]+g$	463	$g+g \to b\bar{b}[^1S_0^{(8)}]+g$
424	$g+g \to c\bar{c}[^3P_J^{(8)}]+g$	464	$g+g \to b\bar{b}[^3P_J^{(8)}]+g$
425	$g+q \to q+c\bar{c}[^3S_1^{(8)}]$	465	$g+q \to q+b\bar{b}[^3S_1^{(8)}]$
426	$g+q \to q+c\bar{c}[^1S_0^{(8)}]$	466	$g+q \to q+b\bar{b}[^1S_0^{(8)}]$
427	$g+q \to q+c\bar{c}[^3P_J^{(8)}]$	467	$g+q \to q+b\bar{b}[^3P_J^{(8)}]$
428	$q+\bar{q} \to g+c\bar{c}[^3S_1^{(8)}]$	468	$q+\bar{q} \to g+b\bar{b}[^3S_1^{(8)}]$
429	$q+\bar{q} \to g+c\bar{c}[^1S_0^{(8)}]$	469	$q+\bar{q} \to g+b\bar{b}[^1S_0^{(8)}]$
430	$q+\bar{q} \to g+c\bar{c}[^3P_J^{(8)}]$	470	$q+\bar{q} \to g+b\bar{b}[^3P_J^{(8)}]$
431	$g+g \to c\bar{c}[^3P_0^{(1)}]+g$	471	$g+g \to b\bar{b}[^3P_0^{(1)}]+g$
432	$g+g \to c\bar{c}[^3P_1^{(1)}]+g$	472	$g+g \to b\bar{b}[^3P_1^{(1)}]+g$
433	$g+g \to c\bar{c}[^3P_2^{(1)}]+g$	473	$g+g \to b\bar{b}[^3P_2^{(1)}]+g$
434	$g+q \to q+c\bar{c}[^3P_0^{(1)}]$	474	$g+q \to q+b\bar{b}[^3P_0^{(1)}]$
435	$g+q \to q+c\bar{c}[^3P_1^{(1)}]$	475	$g+q \to q+b\bar{b}[^3P_1^{(1)}]$
436	$g+q \to q+c\bar{c}[^3P_2^{(1)}]$	476	$g+q \to q+b\bar{b}[^3P_2^{(1)}]$
437	$q+\bar{q} \to c\bar{c}[^3P_0^{(1)}]+g$	477	$q+\bar{q} \to b\bar{b}[^3P_0^{(1)}]+g$
438	$q+\bar{q} \to c\bar{c}[^3P_1^{(1)}]+g$	478	$q+\bar{q} \to b\bar{b}[^3P_1^{(1)}]+g$
439	$q+\bar{q} \to c\bar{c}[^3P_2^{(1)}]+g$	479	$q+\bar{q} \to b\bar{b}[^3P_2^{(1)}]+g$

Table 4.2: *Colour-singlet/octet production subprocesses introduced in* PYTHIA *6.324 (also available in later versions), and their corresponding ISUB subprocess numbers.*

Several existing colour-singlet processes are repeated in the new heavy quarkonium framework so as to provide a coherent way of defining wavefunction and matrix element normalisations for both singlet and octet modes. There are some new MSEL values which combine several quarkonium production channels together. These are presented in Table 4.3.

MSEL value	Switches on	ISUB
61	all charmonium processes	421-439
62	all bottomonium processes	461-479
63	both of the above	421-439 and 461-479

Table 4.3: *New MSEL subprocess menus available in* PYTHIA.

Next-to-leading-order calculations for quarkonium production are very recent [86, 87], and as such these higher order subprocesses (such as $g+g \rightarrow Q\,\bar{Q}\,[^3S_1^{(1)}]+g+g$) are not implemented within the PYTHIA framework. Standalone computational techniques for calculating quarkonium amplitudes have however been recently developed [114].

As discussed in Chapter 2, these NLO and NNLO relativistic corrections are non-negligible and so can affect (or even dispense with) the results of NRQCD matrix element fits to Tevatron data. At the current time we continue to use the framework present in PYTHIA and Tevatron fits, with the understanding that these simulations may require updating in light of new data from the LHC.

4.2 NRQCD matrix elements

PYTHIA includes ten long-distance matrix elements: five for charmonium and five for bottomonium production in the NRQCD framework, that were set to unity by default in PYTHIA. In each case there are two singlet matrix elements that are in principle perturbatively calculable (see Section 2.4.6) and three octet matrix elements. From fits to Tevatron data, many studies have provided values for these matrix elements. These matrix elements have been tested at Tevatron energies in the ATLAS framework and those matrix elements used are presented in Table 4.4. These values are used for all studies of J/ψ and Υ production throughout this thesis.

Tests and tunings of matrix elements for higher quarkonium states are described in Section 4.6. It is important to note that all ^3P_J octet states are simulated in PYTHIA using a single NRQCD matrix element $\langle \mathcal{O}(J/\psi)[^3P_0^{(8)}]\rangle$, scaled to other states using the spin-symmetry relation:

$$\langle \mathcal{O}(^3P_J^{(8)})\rangle = (2J+1)\langle \mathcal{O}(^3P_0^{(8)})\rangle. \tag{4.2}$$

Four octet matrix elements have been shown to be sufficient to describe NRQCD production at leading order, but as any differences in the p_T-behaviour of the ^3P_J and $^1S_0$ quarkonium differential cross-sections above 5 GeV is indistinguishable, only a linear combination of the two contributions can be extracted from data. For this reason the matrix elements for these two states may be combined into one effective matrix element [115]. The combined differential cross-section of these two contributions can then be simulated as an appropriately-scaled $^1S_0$ cross-section. Whilst this degeneracy is not the case for bottomonia in the $0 < p_T < 15$ GeV region, the differences between the two contributions are not great enough to reliably fit them separately, so an effective matrix element may also be legitimately used for the ^3P_J and $^1S_0$ contributions in bottomonia production.

PYTHIA parameter	Value	Matrix element
`PARP(141)`	1.16	$\langle \mathcal{O}(J/\psi)[^3S_1^{(1)}]\rangle$
`PARP(142)`	0.0119	$\langle \mathcal{O}(J/\psi)[^3S_1^{(8)}]\rangle$
`PARP(143)`	0.01	$\langle \mathcal{O}(J/\psi)[^1S_0^{(8)}]\rangle$
`PARP(144)`	0.01	$\langle \mathcal{O}(J/\psi)[^3P_0^{(8)}]\rangle/m_c^2$
`PARP(145)`	0.05	$\langle \mathcal{O}(\chi_{c0})[^3P_0^{(1)}]\rangle/m_c^2$
`PARP(146)`	9.28	$\langle \mathcal{O}(\Upsilon)[^3S_1^{(1)}]\rangle$
`PARP(147)`	0.15	$\langle \mathcal{O}(\Upsilon)[^3S_1^{(8)}]\rangle$
`PARP(148)`	0.02	$\langle \mathcal{O}(\Upsilon)[^1S_0^{(8)}]\rangle$
`PARP(149)`	0.02	$\langle \mathcal{O}(\Upsilon)[^3P_0^{(8)}]\rangle/m_b^2$
`PARP(150)`	0.085	$\langle \mathcal{O}(\chi_{b0})[^3P_0^{(1)}]\rangle/m_b^2$

Table 4.4: *Matrix element parameters in* PYTHIA *used in this study for charmonium and bottomonium production in the NRQCD framework (derived from data in [116]).*

For J/ψ production, the effective matrix element can be written in the form:

$$M_{3.5}({}^1S_0^{(8)} + {}^3P_J^{(8)}) = \langle \mathscr{O}[{}^3S_1^{(8)}] \rangle + 3.5 \langle \mathscr{O}[{}^3P_J^{(8)}] \rangle / m_c^2 \tag{4.3}$$

A comparison was conducted between J/ψ events simulated with an effective matrix element of 0.045 for ${}^3P_J$ and ${}^1S_0$ contributions and events simulated with separate matrix element parameters as given in Table 4.4. The two methods produce identical results within statistical errors. For the purposes of this study however, it was decided that the two contributions would be simulated separately (rather than with an effective matrix element) and combined at the analysis stage to ensure that any differences between the two contributions (particularly in the case of bottomonium) are not lost, should they be felt to be important at a later date.

4.3 Generator-level predictions for production at 14 TeV

In the following sections some initial simulation studies of the properties of J/ψ and Υ production at the LHC with a 14 TeV centre-of-mass energy are presented, including the contributions and behaviour of the gg, gq and $q\bar{q}$ subprocesses for both J/ψ and Υ and the individual contributions of ${}^3S_1^{(1)}$, ${}^3S_1^{(8)}$ and ${}^1S_0^{(8)} + {}^3P_J^{(8)}$ states.

Assumed uncertainties on the cross-section are expected [117] to be approximately 10%, largely due to the uncertainty on the parton distribution functions, but this varies with the processes involved and is evaluated as closer to 50% in the case of B-Physics channels discussed in this thesis. Trigger rates and corresponding algorithms use a conservative estimate of the signal and background processes, and it is understood that measurement of the true rate will impact on the initial trigger thesholds and prescales applied.

In these initial studies, the ATLAS di-muon trigger cuts were taken as sharp Monte Carlo level cuts, requiring that one muon should have a $p_t > 6$ GeV and one a $p_t > 4$ GeV, with both being within $|\eta| < 2.5$). A p_t-cut of 4.5 GeV in PYTHIA was made on the hard process for charmonium generation throughout so as to maximise efficiency of generation in the experimentally accessible range.

For bottomonium production, the high mass of the Υ means that it is possible to produce quarkonium with close to zero transverse momentum even after di-muon trigger cuts have been applied, so the default PYTHIA hard process p_t-cut of 1 GeV is used. Colour-octet process simulation in PYTHIA is singular in the limit $p_T \to 0$ and as such cross-section calculation can be problematical at low p_t [104], which is the reason for this 1 GeV cutoff.

For plots of the production cross-sections for various processes at Monte Carlo level a fit is performed following studies in reference [118] using the four-parameter function:

$$F(\alpha_i, p_t) = \alpha_1 \frac{p_t^{\alpha_2}}{(\alpha_3 + p_t^2)^{\alpha_4}}.$$

4.4 Study of contributions to the J/ψ cross-section

Following simulation of the J/ψ singlet and octet production processes, the data was combined according to the quarkonium state produced, to illustrate the behaviour of the various contributions in the NRQCD framework to the differential production cross-section, as shown in Figure 4.2 with no di-muon p_T or η cuts applied. At low p_T both the colour octet and colour singlet states provide large contributions although the $^3S_1^{(8)}$ state eventually dominates at high-p_T, highlighting why the Colour Singlet Model in its original form was sufficient for study of quarkonium at low energies.

Figure 4.3 shows the corresponding pseudorapidity distributions of the J/ψ and the two muons it decays into, for the three main produced states, directly from PYTHIA with no cuts on muons at this stage. We see no significant variation in these distributions depending on production method or resultant quarkonium state.

4.4.1 Effects of muon acceptance cuts on J/ψ production

The effect that di-muon p_T and η cuts ($p_T > 6$ GeV and $p_T > 4$ GeV on each of the two muons respectively, with $|\eta| < 2.5$) have on their observation at ATLAS was simulated to compare

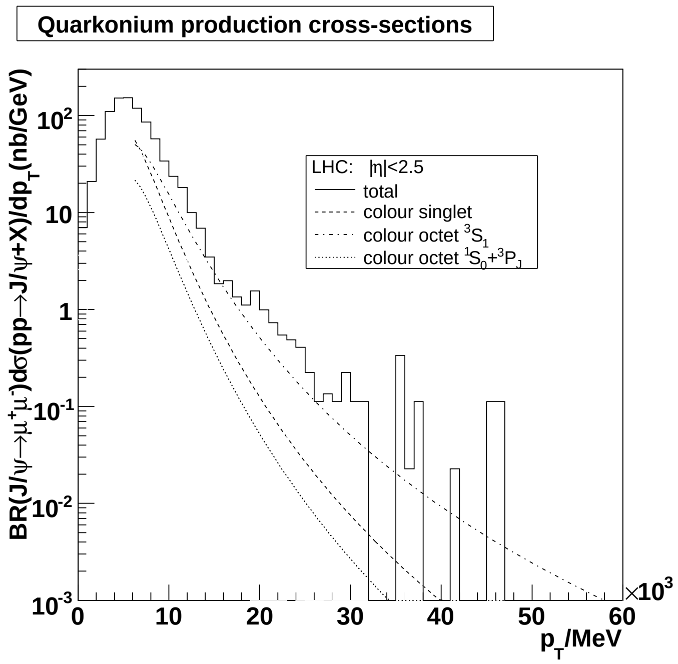

Figure 4.2: *Differential cross-section for J/ψ production at the LHC, highlighting the separate singlet and octet contributions in MC data with no muon p_T or η cuts.*

with MC truth simulation without muon cuts. After muon cuts were applied to this data, no J/ψ are produced below a p_T of 6 GeV (see Figure 4.4), with those that do arising from a situation where another muon in the event (other than from the J/ψ) caused the event to be accepted.

The suppression at low J/ψ p_T is due to the relatively low mass of the J/ψ, which requires that the charmonium state must have sufficient p_T itself to impart to the muons to allow them to pass the threshold cuts. The situation is very different in the case of the Υ, where its larger mass means that it can have very low transverse momentum and still produce back-to-back muons which pass the cuts. High p_T events for the J/ψ are suppressed by a factor of 3–5 due to the reduced phase space and thus restricted angular separation of muons that can be accepted above a particular transverse momentum. A plot of the cross-sections after muon threshold cuts is shown in Figure 4.4 along with the fits to the various process contributions.

The production of J/ψ singlet and octet states in PYTHIA proceeds through a number of processes as discussed in Chapter 2 and above. The leading order gluon-gluon scattering sub-processes provide the dominant source of production, while a negligible ($< 0.05\%$) contribution

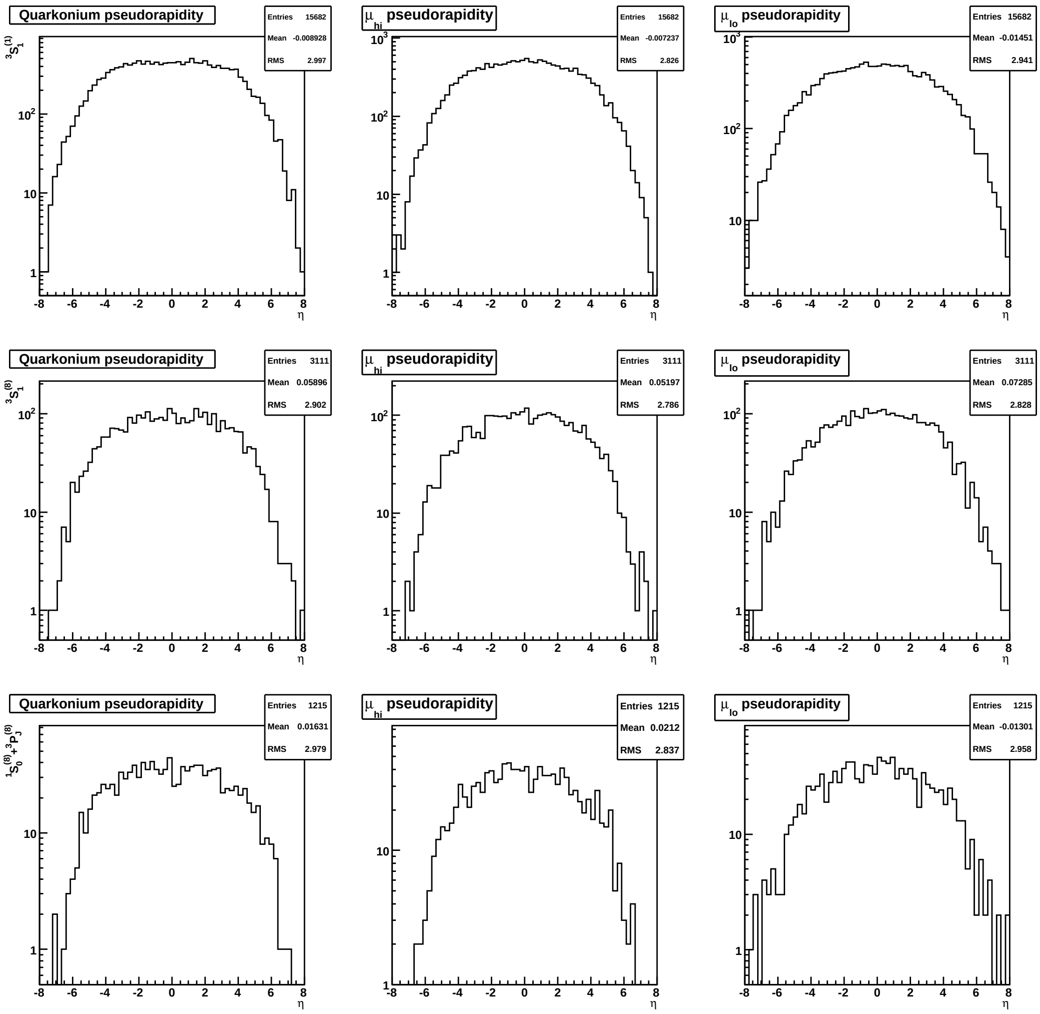

Figure 4.3: *Pseudorapidity distributions for the J/ψ (left), high p_T muon (middle) and low p_T muon (right), for the ${}^3S_1^{(1)}$ (top), ${}^3S_1^{(8)}$ (middle) and ${}^1S_0^{(8)} + {}^3P_J^{(8)}$ (bottom) states, without muon p_T or η cuts.*

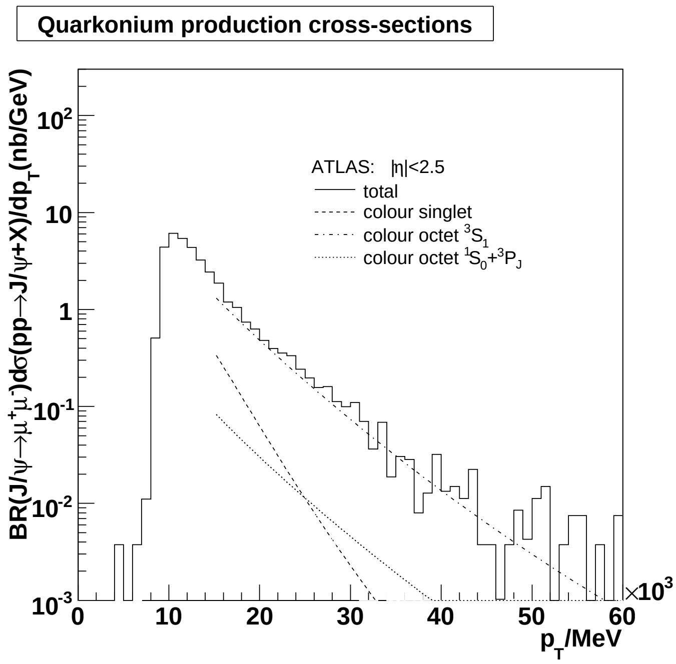

Figure 4.4: *Differential cross-section for J/ψ production at ATLAS, highlighting the separate singlet and octet contributions in MC data after requiring p_T and η cuts on both muons from the J/ψ.*

comes from quark-antiquark scattering (see Table 4.5).

Subprocess	Fraction
$g+g$	81.3%
$g+q$	18.7%
$q+\bar{q}$	negligible

Table 4.5: *Fraction of prompt charmonium states produced via a particular subprocess type, after muon p_T and η cuts.*

Aside from the contributions of individual subprocesses, the normalised contributions [1)] to J/ψ production from ${}^3S_1^{(1)}$, ${}^3S_1^{(8)}$, ${}^3P_J^{(1)}$ and ${}^1S_0^{(8)} + {}^3P_J^{(8)}$ states are shown in Table 4.6.

For charmonium in the particular kinematic region accessible at ATLAS, singlet production accounts for 29.4% of all prompt charmonium events produced, primarily from the contribution of χ cascade decays into J/ψ. From Figures 4.2 and 4.4 one can see the singlet production is largely constrained to dominating in the very low p_T (≤ 6 GeV) region, above which octet

[1)]Correcting for the forcing of the decays $J/\psi \to \mu^+\mu^-$ and $\chi_J \to J/\psi\gamma$ in PYTHIA.

$c\bar{c}$ state	Fraction
$^3S_1^{(1)}$	0.4%
$^3S_1^{(8)}$	62.3%
$^3P_J^{(1)}$	29.0%
$^1S_0^{(8)} + {}^3P_J^{(8)}$	8.3%

Table 4.6: *Fraction of prompt charmonia produced in a particular quarkonium state, after muon p_T and η cuts.*

contributions are orders of magnitude larger than singlet at a given meson p_T. Note that this echoes the findings of CDF which discovered that colour-octet production was an order of magnitude effect [58].

Figure 4.5 illustrates the effect of the di-muon threshold cuts on acceptance of J/ψ events. The Monte Carlo sample used does not have any muon cuts imposed, but various muon p_T trigger cuts (with $|\eta| < 2.5$) under consideration in the rest of this document have been overlaid to illustrate the regions of the J/ψ cross-section accessible in each scenario.

Notice that with p_T cuts under study at ATLAS, the vast majority of the J/ψ production cross-section is out of reach, at far lower p_T thresholds than can be triggered on in ATLAS. The distribution also reveals that although lowering one muon threshold does provide an increase in acceptance, the bulk of the cross-section cannot be accessed without lowering the second muon threshold too.

4.5 Study of contributions to the Υ cross-section

As in the case of J/ψ, the data from all of the singlet and octet production processes for Υ were combined and the differential cross-section for Υ production is given below in Figures 4.6 and 4.8. These figures show that $^3S_1^{(1)}$ singlet production is far more important for Υ production than J/ψ production (cf. Figure 4.2) even once muon cuts have been applied, where singlet production dominates at low p_T.

In J/ψ decays, octet contributions at ATLAS will dominate the entire accessible cross-

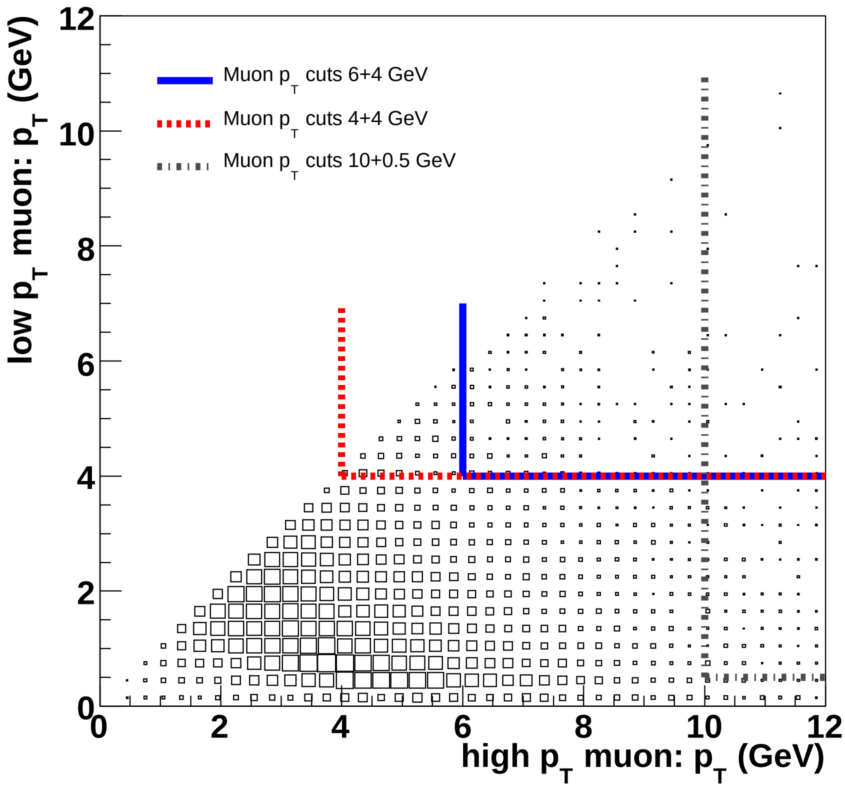

Figure 4.5: *Harder muon p_T versus softer muon p_T from J/ψ decay (MC truth before di-muon p_T and η cuts) at 14 TeV. Events accessible after trigger cuts are bounded from below by the solid lines (corresponding to di-muon trigger cuts considered in this thesis).*

section. This means it is even more important to probe high transverse momentum events to find evidence of colour-octet production for Υ than for the J/ψ, but also means that low p_T Υ at ATLAS can still provide a good test of Colour Singlet Model contributions.

Figure 4.6 shows a summary of the differential cross-section before muon threshold cuts are applied. Note that the differential cross-section for Υ is an order of magnitude smaller than the cross-section for J/ψ despite being able to accept Υ close to rest in the lab frame. Figure 4.7 shows the pseudorapidity distributions for the bottomonium and muons before muon cuts have been applied. A dip in production at $\eta = 0$, more evident for Υ (although it is also present for the J/ψ), an artefact due to the mass of the Υ, is not seen in the true rapidity distribution.

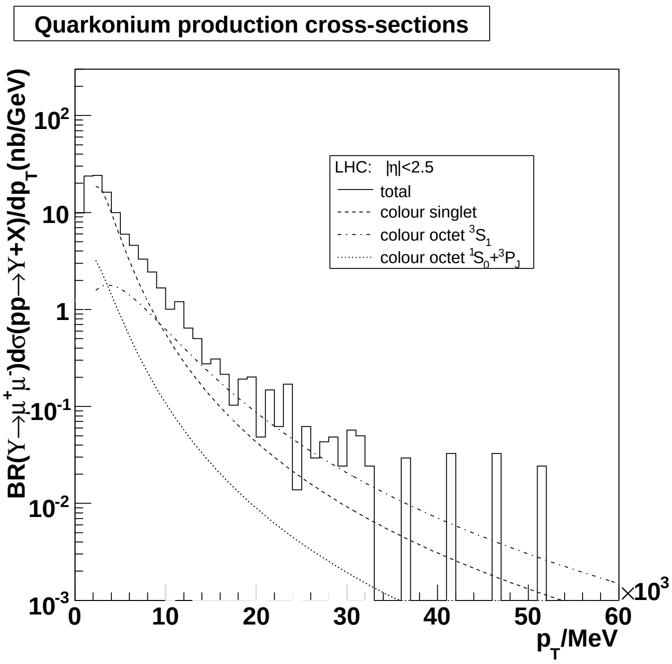

Figure 4.6: *Differential cross-section for Υ production at the LHC, highlighting the separate singlet and octet contributions in MC data with no muon p_T or η cuts.*

4.5.1 Effects of muon acceptance cuts on Υ production

Muon p_T and η cuts have a significant effect on Υ production. Figure 4.8 shows the production cross-section distribution after application of di-muon cuts. Note that unlike in the case of J/ψ production, there still exists a significant contribution to the cross-section down to transverse momenta of $\sim$ 2–4 GeV (although with a steep cutoff in this region).

Due to the higher mass of the Υ it is possible to produce muons back-to-back with enough transverse momentum to pass the threshold cuts while the Υ has very little transverse momentum of its own. Figure 4.8 shows fits to the different contributions along with a fit for the total cross-section distribution. The suppression of the ${}^1S_0^{(8)} + {}^3P_J^{(8)}$ contribution means that for fast simulations, especially where low p_T dependence is not a concern, generation of these processes may be neglected.

The relative contributions of the various production subprocesses are similar in the case of Υ production to those for J/ψ (see Table 4.7). Gluon-gluon subprocesses still dominate, with approximately 82.8% of all events, and quark-antiquark subprocesses again contribute a small

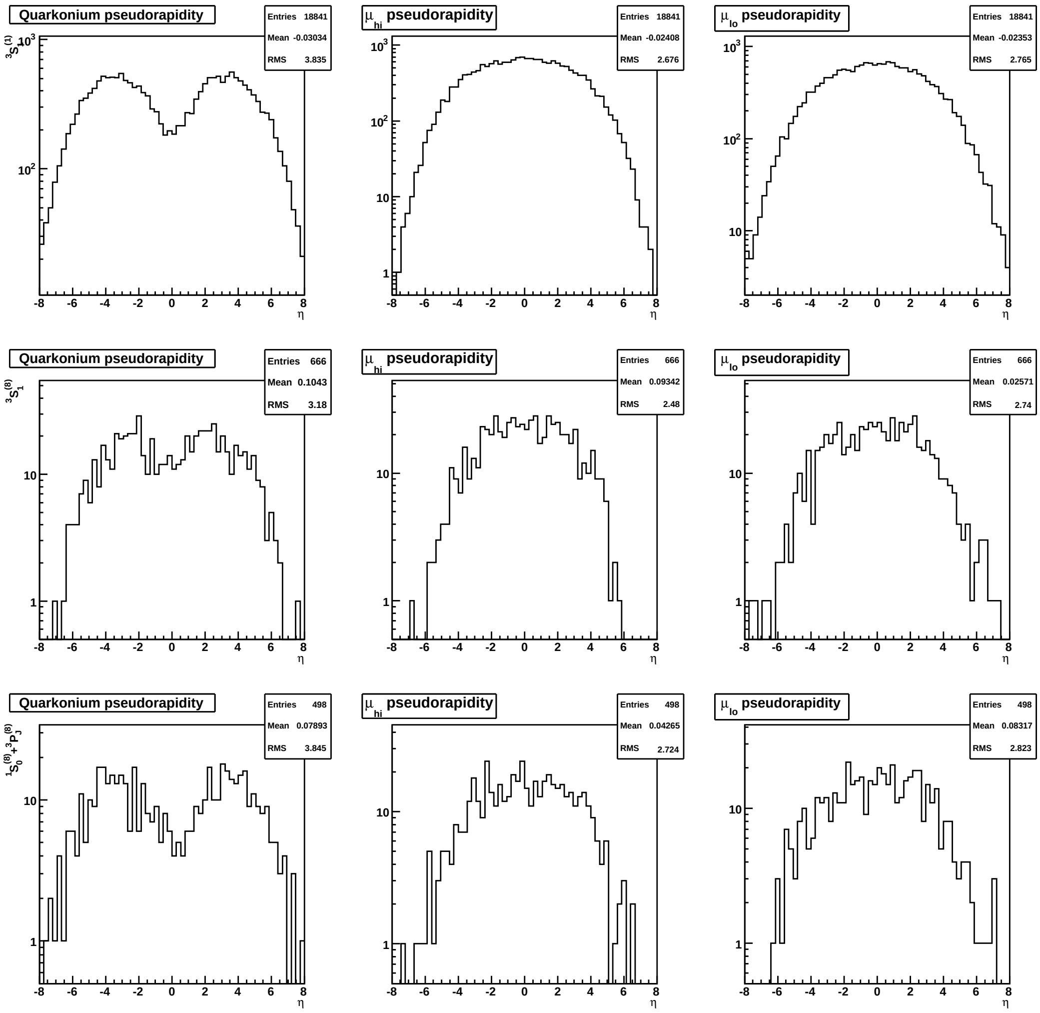

Figure 4.7: *Pseudorapidity distributions for the Υ (left), high p_T muon (middle) and low p_T muon (right), for the ${}^3S_1^{(1)}$ (top), ${}^3S_1^{(8)}$ (middle) and ${}^1S_0^{(8)} + {}^3P_J^{(8)}$ (bottom) states, without muon p_T or η cuts.*

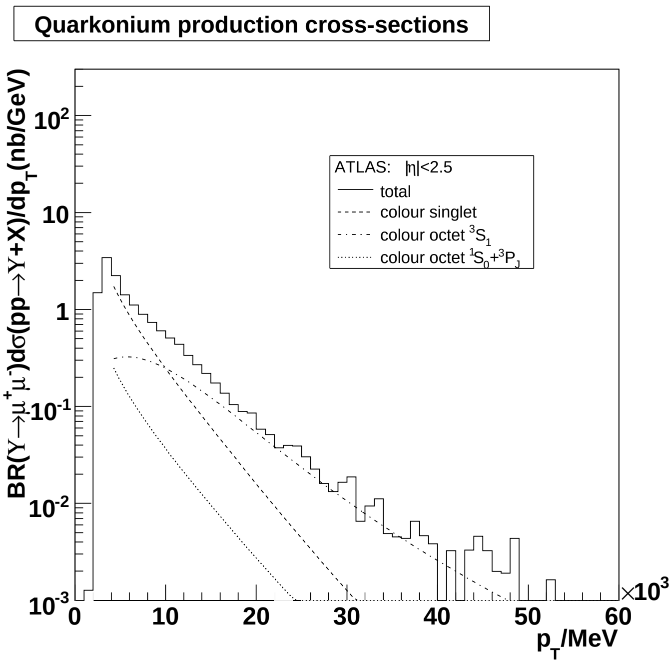

Figure 4.8: *Differential cross-section for Υ production at the LHC, highlighting the separate singlet and octet contributions in MC data after requiring p_T and η cuts on both muons from the Υ.*

amount, this time $\sim 0.1\%$ of all production. Contributions from the various bottomonia production processes (see Table 4.8) are somewhat different than those for charmonia production. The fraction produced through the $^3S_1^{(1)}$ singlet channel is here the significantly dominant contribution. Production through a $^3S_1^{(8)}$ and $^1S_0^{(8)}+{}^3P_J^{(8)}$ octet states provides similar contributions.

Subprocess	Fraction
$g+g$	82.8%
$g+q$	17.1%
$q+\bar{q}$	0.1%

Table 4.7: *Fraction of prompt bottomonium states produced via a particular subprocess type, after muon p_T and η cuts.*

The dominance of singlet state production (which has a lower average p_T than the octet production) has important implications for Υ once muon cuts have been applied, because unlike in the case of J/ψ production, there is still a large cross-section of low p_T quarkonia. Figure 4.9 illustrates this effect in the p_T distribution of the hard and soft muon from Υ decays before di-

$b\bar{b}$ state	Fraction
${}^3S_1^{(1)}$	7.5%
${}^3S_1^{(8)}$	46.9%
${}^3P_J^{(1)}$	6.8%
${}^1S_0^{(8)} + {}^3P_J^{(8)}$	38.8%

Table 4.8: *Fraction of prompt bottomonia produced in a particular quarkonium state, after muon p_T and η cuts.*

muon p_T and η cuts have been applied and the events available after di-muon cuts.

The most noticeable aspect of this plot is that the mass of the Υ has effectively shifted the bulk of the production cross-section in muon-p_T space to larger thresholds of around 5+4 GeV. This means that unlike for J/ψ (Figure 4.5), lowering the di-muon trigger cuts from 6+4 GeV (which sits just above the highest density area of Υ production) to 4+4 GeV, a much higher fraction of the produced Υ can be recorded, leading to a predicted order-of-magnitude increase in the accessible cross-section. This has particular importance for early data-taking, where lower luminosities mean that lower cuts are possible. Predicted rates (at Monte Carlo level) for J/ψ and Υ production at ATLAS are given along with predictions for ψ', $\Upsilon(2S)$ and $\Upsilon(3S)$ in Table 4.13 in Section 4.7.

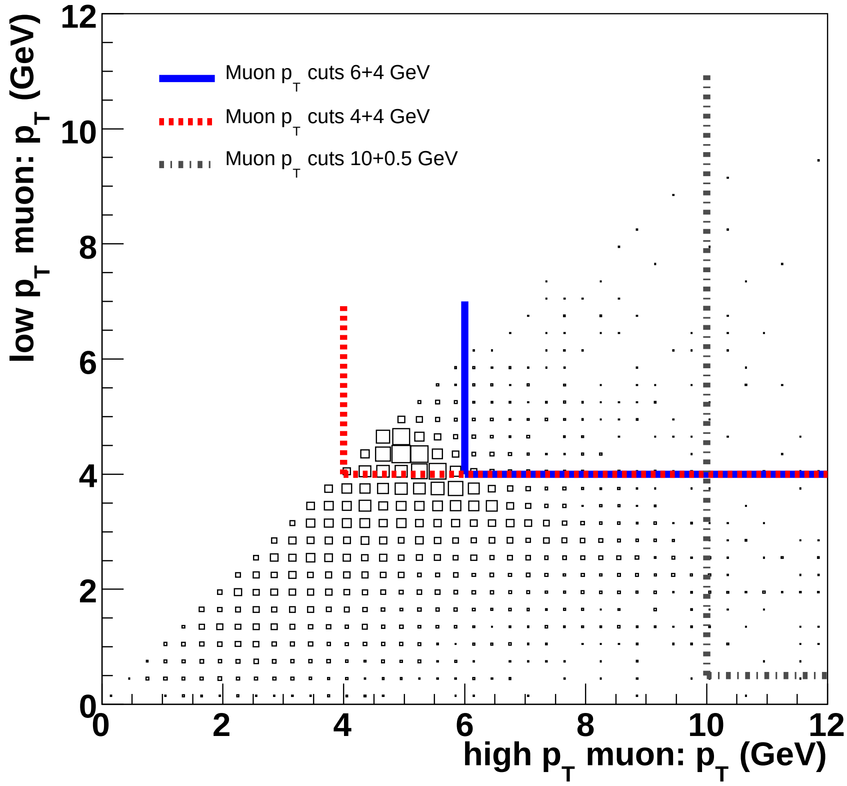

Figure 4.9: *Harder muon p_T versus softer muon p_T from Υ decay (MC truth before di-muon p_T and η cuts) at 14 TeV. Events accessible after trigger cuts are bounded from below by the solid lines (corresponding to di-muon trigger cuts considered in this thesis).*

4.6 Higher state contributions to quarkonium

In addition to the ground state J/ψ and Υ production, higher state $\psi(2S)$, $\Upsilon(2\mathrm{S})$ and $\Upsilon(3\mathrm{S})$ production will also be of interest to study at ATLAS and their contributions through feeddown decays to J/ψ and Υ can make significant contributions to the overall production cross-section. Official simulation and reconstruction of these higher states are not yet available in ATLAS and so are not discussed in the rest of this thesis. In this section I document some of the generator-level tunings and studies that were performed for these states that led to their implementation in ATLAS simulations and expected rates and mass resolutions.

Simulation of the $\psi(2S)$ in PYTHIA required the input of new NRQCD matrix elements for ψ' production, given in Table 4.9. The NRQCD matrix elements for $\psi(2S)$ production are taken from a combination of potential model solutions [119] and fits to Tevatron data [116]. An estimate of the expected cross-section for the $\psi(2S) \to \mu^+\mu^-$ is then calculated in PYTHIA, along with the contribution of feeddown to J/ψ. The cross-section is given for a variety of muon cuts in Table 4.13, where the $\psi(2S)$ feeddown to J/ψ is summed and given as a total J/ψ cross-section. Table 4.28 gives the cross-section for J/ψ without the $\psi(2S)$ contribution.

PYTHIA parameter	NRQCD matrix element	$\psi(2S)$
`PARP(141)`	$\langle\mathscr{O}(\psi(XS))[^3S_1^{(1)}]\rangle$	0.76
`PARP(142)`	$\langle\mathscr{O}(\psi(XS))[^3S_1^{(8)}]\rangle$	0.005
`PARP(143)`	$\langle\mathscr{O}(\psi(XS))[^1S_0^{(8)}]\rangle$	0.0088
`PARP(144)`	$\langle\mathscr{O}(\psi(XS))[^3P_0^{(8)}]\rangle/m_c^2$	0.0039
`PARP(145)`	$\langle\mathscr{O}(\chi_{c0}(XP))[^3P_1^{(1)}]\rangle/m_c^2$	0.0

Table 4.9: *NRQCD matrix element parameters for* PYTHIA *used for generation of ψ' processes, derived from data in [35] and [119].*

For simulation of the $\Upsilon(2\mathrm{S})$and $\Upsilon(3\mathrm{S})$in PYTHIA it was first necessary to change the PMAS values in PYTHIA, effectively defining the $\Upsilon(nS)$ and $\chi_J(nS)$ higher states by changing the mass parameters set for the Υ and $\chi_J(1S)$, forcing the decay processes as necessary and correcting for them later to retrieve the cross-section. Table 4.10 includes the changes to the PYTHIA parameters that were necessary to simulate the $\Upsilon(2\mathrm{S})$and $\Upsilon(3\mathrm{S})$. Note that we also redefine the 'intermediate' octet bound states for $b\bar{b}$ in PYTHIA, scaling them up with the $\Upsilon(nS)$ masses to leave appropriate phase space for the non-perturbative gluon in PYTHIA's implementation of these processes. Table 4.11 were the NRQCD input parameters used for the Υ higher states.

PMAS parameter For Υ(2S)	Value
553	10.023
10551	10.233
20553	10.256
555	10.269
9900551	10.5
9900553	10.5
9910551	10.5

PMAS parameter For Υ(3S)	Value
553	10.355
10551	10.433
20553	10.456
555	10.469
9900551	10.6
9900553	10.6
9910551	10.6

Table 4.10: PYTHIA *PMAS parameters used to create* Υ(2S) *and* Υ(3S) *for use with existing* Υ *subprocesses for higher state generation.*

Table 4.12 shows the feeddown decays that were considered for contributions to the Υ(2S)and Υ(3S)cross-sections, as well as to Υ production. We neglect the contributions from any possible (but as of yet unknown) $\chi_{bJ}(3P)$ feeddown.

PYTHIA parameter	NRQCD matrix element	Υ(1S)	Υ(2S)	Υ(3S)
`PARP(146)`	$\langle\mathcal{O}(\Upsilon(XS))[^3S_1^{(1)}]\rangle$	9.28	4.63	3.54
`PARP(147)`	$\langle\mathcal{O}(\Upsilon(XS))[^3S_1^{(8)}]\rangle$	0.150	0.055	0.039
`PARP(148)`	$\langle\mathcal{O}(\Upsilon(XS))[^1S_0^{(8)}]\rangle$	0.020	0.008	0.005
`PARP(149)`	$\langle\mathcal{O}(\Upsilon(XS))[^3P_0^{(8)}]\rangle/m_b^2$	0.020	0.008	0.005
`PARP(150)`	$\langle\mathcal{O}(\chi_{b0}(XP))[^3P_0^{(1)}]\rangle/m_b^2$	0.085	0.103	0.110

Table 4.11: *NRQCD matrix element parameters for* PYTHIA *used for generation of* Υ(1S), Υ(2S) *and* Υ(3S) *processes, derived from data in [116] and [119].*

Expected cross-sections for Υ(2S)and Υ(3S)are given for various muon p_T thresholds in Table 4.13. The small separation between the masses of three $\Upsilon(nS)$ states combined with the expected mass resolution of ATLAS means that these higher state resonances are unlikely to be separable. Figures 4.10 and 4.11 show examples of the di-muon invariant mass spectrum in the region of the three Υ resonances at DØ and CDF respectively. Figure 4.12 shows the expected picture at ATLAS, with muon $p_T > 4$ GeV and $|\eta| < 2.5$ required for both muons.

Process forced	Branching ratio
$\Upsilon(2S) \to \mu^+\mu^-$	1.93%
$\Upsilon(2S) \to \Upsilon(1S)$	28.11%
$\Upsilon(2S) \to \chi_{0b}(1P) \to \Upsilon(1S)$	0.23%
$\Upsilon(2S) \to \chi_{1b}(1P) \to \Upsilon(1S)$	2.38%
$\Upsilon(2S) \to \chi_{2b}(1P) \to \Upsilon(1S)$	1.54%
$\Upsilon(3S) \to \mu^+\mu^-$	1.81%
$\Upsilon(3S) \to \Upsilon(1S)$	6.50%
$\Upsilon(3S) \to \Upsilon(2S)$	10.80%
$\Upsilon(3S) \to \chi_{0b}(2P) \to \Upsilon(1S)$	0.05%
$\Upsilon(3S) \to \chi_{1b}(2P) \to \Upsilon(1S)$	0.25%
$\Upsilon(3S) \to \chi_{2b}(2P) \to \Upsilon(1S)$	0.96%
$\Upsilon(3S) \to \chi_{0b}(2P) \to \Upsilon(2S)$	2.37%
$\Upsilon(3S) \to \chi_{1b}(2P) \to \Upsilon(2S)$	0.81%
$\Upsilon(3S) \to \chi_{2b}(2P) \to \Upsilon(2S)$	1.85%

Table 4.12: PYTHIA *forcings and branching fractions used for generation of the* $\Upsilon(2S) \to \mu^+\mu^-$ *and* $\Upsilon(3S) \to \mu^+\mu^-$ *processes and cross-section predictions.*

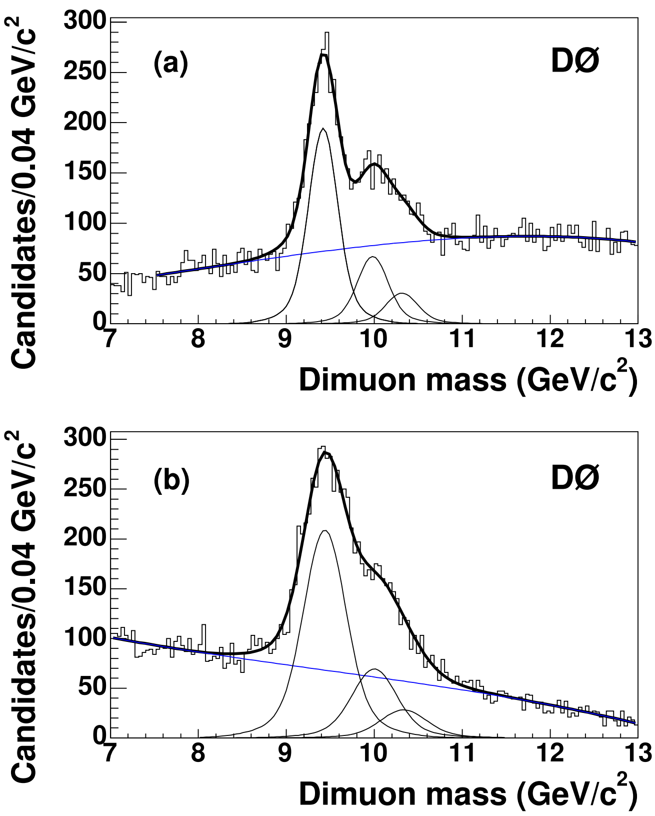

Figure 4.10: *DØ results [120] for* Υ *and higher state di-muon mass spectra in the* Υ p_T *range* $4 < p_T^{\Upsilon}$ (GeV) < 6 *for (a)* Υ *in rapidity* $|y_\Upsilon| < 0.6$ *and (b)* Υ *in* $1.2 < |y_\Upsilon| < 1.8$.

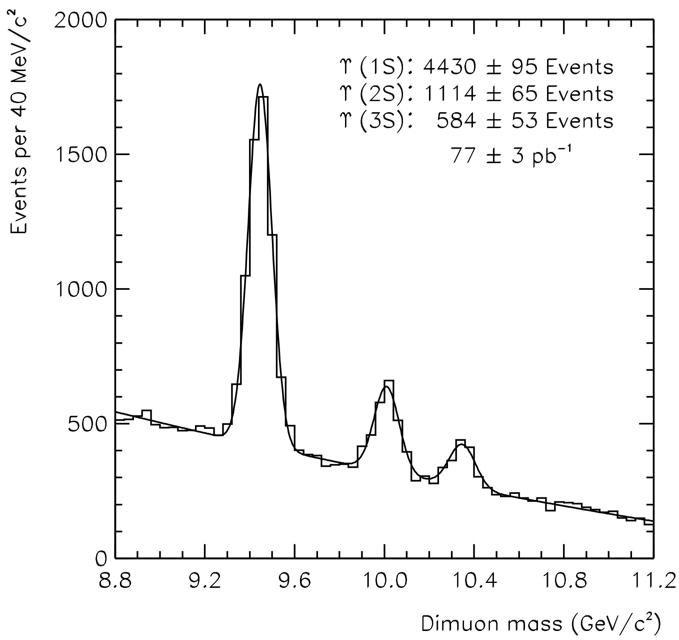

Figure 4.11: *CDF results [121] for* Υ *and higher state di-muon mass spectra within* $|y_\Upsilon| < 0.4$ *and with* $0 < p_T^\Upsilon$ (GeV) < 20.

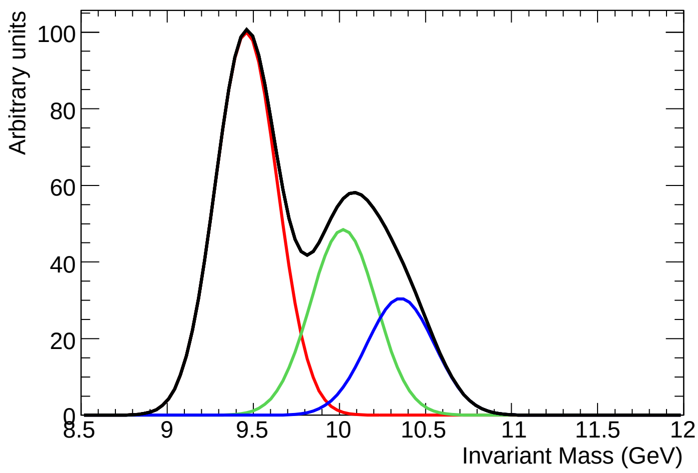

Figure 4.12: *Monte Carlo simulation of the expected di-muon invariant mass distribution of the* $\Upsilon(1S)$, $\Upsilon(2S)$ *and* $\Upsilon(3S)$ *resonances reconstructed from the ATLAS detector with muon* p_T *greater than* 4 GeV *and* $|\eta| < 2.5$. *The width of the peaks are derived from ATLAS full simulation information. Relative normalisations are based on width and MC cross-section predictions only; identical trigger and reconstruction efficiencies are assumed for all* Υ *states.*

The plot has been normalised so as to have the Υ peak at 100 in arbitrary units, but the relative normalisations are as predicted from these PYTHIA implementations (Monte Carlo level predictions only, without trigger or reconstruction efficiencies taken into account). The predicted cross-sections can be seen in Section 4.7. The mass resolution of the $\Upsilon(1S)$ comes from ATLAS full simulation studies (see Section 5.2.1) and the resolutions of higher states scale in proportion to the mass to be able to give an illustration of the expected situation at ATLAS. Note that the cross-section predictions from these models as implemented in PYTHIA have been tuned to describe the Tevatron results and scaled up to the LHC energy. Although care have been taken to ensure stability of this extrapolation, inevitably there is an uncertainty in the overall scale of the predicted cross sections (linked to the uncertainties in the parton distribution functions at small x), which is estimated to be at the level of $\pm 50\%$.

4.7 Monte Carlo predictions for quarkonium production rates

Studies were conducted into producing PYTHIA parameters that could generate samples of prompt quarkonium events for studies of quarkonium production at ATLAS. From these studies I present in Table 4.13 below Monte Carlo level predictions for two di-muon p_T threshold scenarios and one single muon[2)] trigger (all of which are used later in this document). The cross-section overlap between the $\mu 6 \mu 4$ and $\mu 10$ trigger scenarios seen in Figures 4.5 and 4.9 are also shown as they are of interest for polarisation studies described in Chapter 7.

It is likely that the true cross-section accessible by ATLAS in early data will be higher than the values quoted below, as during early running the low p_T muon trigger will run with an open coincidence window in η at the level 1 trigger and no requirement of an additional level 2 di-muon trigger. This trigger item has a turn-on threshold at around 4 GeV (giving the 4+4 GeV trigger scenario quoted) but in practice there is a non-zero trigger efficiency below 4 GeV, which, combined with the large rate of low p_T onia (particularly in the case of J/ψ as shown in

[2)]The single muon $\mu 10$ trigger requires that the second muon have at least 0.5 GeV p_T for reconstruction purposes in the analysis, but we do not trigger on this second muon.

Figure 4.5), may add a significant extra contribution to the overall observed cross-section unless sharp cuts are imposed.

Quarkonium	Cross-section, nb			
	$\mu4\mu4$	$\mu6\mu4$	$\mu10$	$\mu6\mu4 \cap \mu10$
J/ψ	28	23	23	5
ψ'	1.0	0.8	0.8	0.2
Υ(1S)	48	5.2	2.8	0.8
Υ(2S)	16	1.7	0.9	0.3
Υ(3S)	9.0	1.0	0.6	0.2

Table 4.13: *Predicted cross-sections for various prompt vector quarkonium state production and decay into muons, with di-muon trigger thresholds $\mu4\mu4$ and $\mu6\mu4$ and the single muon trigger threshold $\mu10$ (before trigger and reconstruction efficiencies). The last column shows the overlap between the di-muon $\mu6\mu4$ and single muon samples. The 'single' muon sample also requires that the second muon have a $p_T > 0.5$ GeV.*

4.8 Low p_T single and di-muon rates in ATLAS

In addition to studying the rate of quarkonium production that will be observable in ATLAS, the tuning and generation of other di-muon processes (as well as single muon processes) relevant as backgrounds to quarkonium production was performed. In addition to studies of the backgrounds under the J/ψ and Υ resonances, these inclusive muon rates will provide a key signature for commissioning of the detector and the trigger and DAQ systems during ATLAS start-up.

In the following sections I present details of the important generator-level physics parameters used in production of events for each process studied, followed by plots of the non-charge correlated[3)] differential and integrated p_T spectra for the hardest and second-hardest muon in the event. Tabulated values of the p_T bin contents accompany each plot, the differential column showing the cross-section in the corresponding p_T bin, the integral column showing the total integrated cross-section above that p_T threshold for the process in question. Reference [2]

[3)] The rates are plotted without charge-correlation, as these studies were used to provide predictions for low p_T muon trigger rates, for which charge-correlation is not relevant.

contains further details of muon spectra in the non-charge correlated case as well as a study of biases introduced by generator-level cuts.

Section 4.9 contains summary plots of the muon p_T spectra for each of the processes overlaid onto single histograms for ease of comparison. Monte Carlo data produced through PYTHIA 6.403 was used to produce these estimates. Fiducial cuts were applied on all processes to simulate the ATLAS geometrical acceptance and a generator-level filter was used to simulate muon and di-muon trigger conditions, but no trigger or reconstruction efficiency is taken into account.

4.8.1 Muons from decays of beauty and charm

In the following sections I present estimates for muon rates from the decays $bb \to \mu 6X$, $bb \to \mu 6\mu 4X$ and $bb \to J/\psi(\mu 6\mu 4)X$, as well as those from $cc \to \mu 6X$. Muon rates from the quarkonium decays $pp \to J/\psi(\mu 6\mu 4)$ (direct J/ψ) and $pp \to \Upsilon(\mu 6\mu 4)$ (direct Υ) are considered in Sections 4.8.6 and 4.8.7. Note that the beauty decay cross-sections also include contributions from charm cascade decays $b \to c \to \mu$ and indirect quarkonium production.

Each di-muon process is presented along with a page of plots showing the differential and integrated p_T spectra for both the hardest p_T muon μ_1 and the second hardest p_T muon μ_2 in the event. In each case there were no additional p_T cuts applied on the other muon (μ_2 and μ_1 respectively) other than the constraints applied at the generator-level stage.

Each plot in this section additionally has the total p_T spectrum decomposed into two contributions: *'Barrel'* and *'Endcap'* for the single muon channels, and three contributions: *'Both Barrel'*, *'Barrel and Endcap'* and *'Both Endcap'* for the di-muon channels. These spectra correspond to the pseudorapidity region in which the muon(s) in those events are found. The barrel region is defined to be $|\eta| < 1.05$ and the endcap region $1.05 < |\eta| < 2.5$. Di-muon events may have one muon in the barrel and one in the endcap in addition to both being found in the same region, hence the need for three contributions in these cases.

4.8.2 $bb \to \mu 6X$

The process $bb \to \mu 6X$ is generated in PYTHIA without requiring any constraints on the b quarks into muons. PYTHIA is permitted to freely generate events and waits until enough events have been produced satisfying the process requirements that the b quarks in the event are constrained to be within $|\eta| \leqslant 4.5$ and with a $p_T \geqslant 7$ GeV and the final state is required to contain a muon with a $p_T \geqslant 6$ GeV within $|\eta| \leqslant 2.5$. This means that all muon sources are possible provided that at least one b quark is present in the event with an accepted muon.

The cross-section extracted from PYTHIA was $(6.14 \pm 0.02)\mu$b. In Table 4.15 threshold muon trigger rates for the hardest muon in the $bb \to \mu 6X$ event are presented separated into muon barrel and endcap trigger regions. For this process and all other processes considered in this document the rates represent Monte Carlo predictions only, with no consideration of muon trigger efficiencies.

$bb \to \mu 6X$	
Pythia process menu	`msel 1` – QCD jets
Hard scattering cut `ckin(3)`	$\widehat{p}_\perp \geqslant 6$ GeV
Cut on $b\bar{b}$ quarks	$p_T \geqslant 7$ GeV within $\|\eta\| \leqslant 4.5$
Generator level cuts	Require one muon within: $\|\eta\| \leqslant 2.5$ and $p_T \geqslant 6$ GeV
Cross-section	(6.14 ± 0.02) μb

Table 4.14: *Generation parameters and calculated cross-section for $bb \to \mu 6X$*

Hardest p_T muon	Muon trigger rates (Hz), L=10^{33} cm^{-2}s^{-1}	
	Barrel	Endcap
Threshold: 6 GeV	2919.5	3051.4
Threshold: 8 GeV	1185.6	1221.1
Threshold: 10 GeV	558.6	569.5

Table 4.15: *Threshold muon trigger rates (Hz) for the hardest p_T muon in the $bb \to \mu 6X$ event separated into barrel and endcap muon trigger regions.*

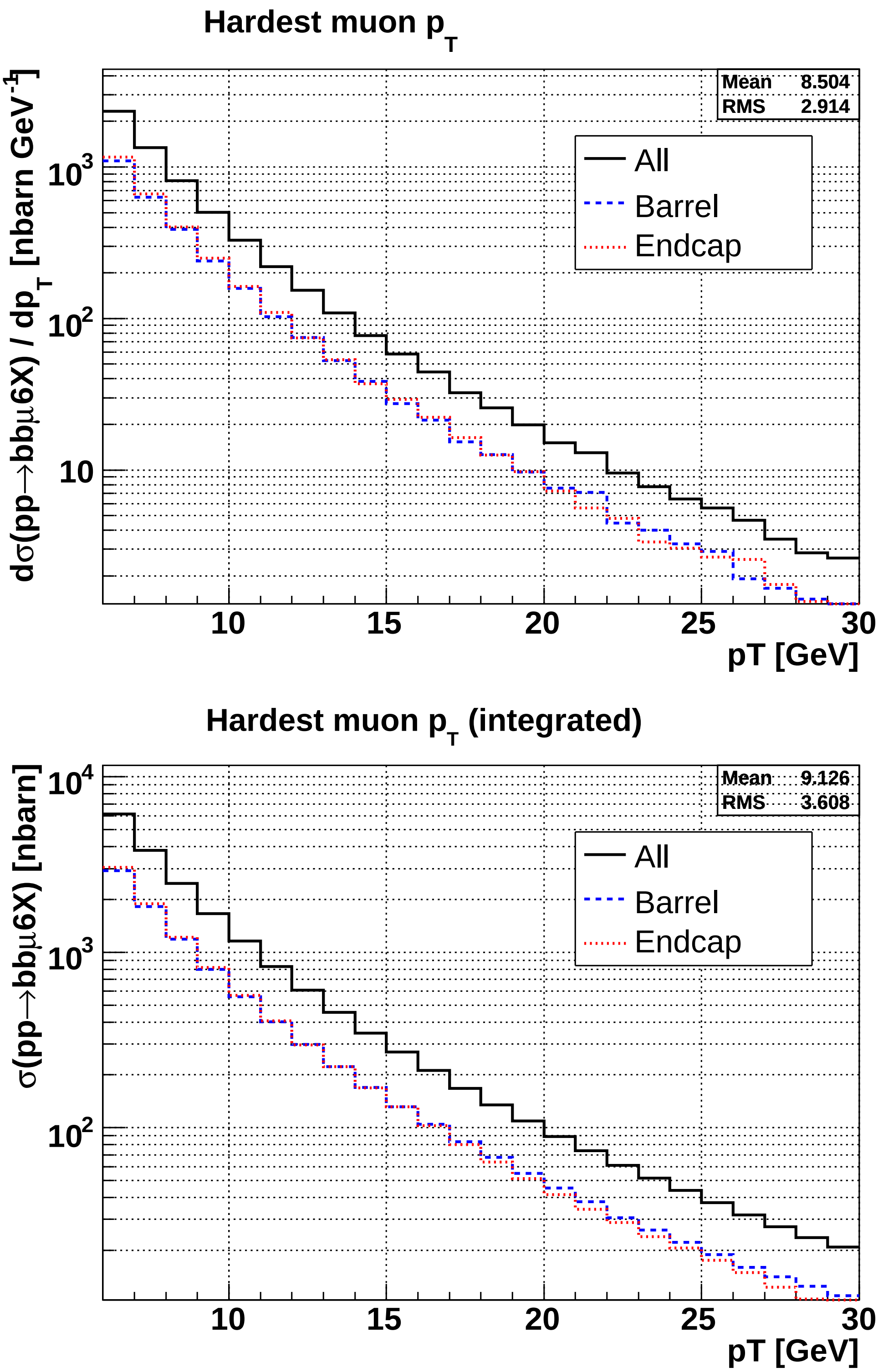

Figure 4.13: *Differential and integrated muon p_T spectra for the hardest muon in the event for the bb $\rightarrow \mu 6X$ process (no charge correlation). See Table 4.16 for corresponding numerical values. Note that 'integrated' here (and following figures) refers to the total integrated cross-section above the muon p_T value in question.*

p_T (GeV)	1^{st} muon cross-section	
	Differential (nb GeV^{-1})	Integrated (nb)
6	2333.083	6144.000
7	1338.353	3810.917
8	811.504	2472.563
9	502.851	1661.059
10	329.733	1158.208
11	219.316	828.475
12	153.556	609.159
13	108.549	455.603
14	77.222	347.054
15	58.173	269.832
16	44.353	211.659
17	32.401	167.306
18	25.748	134.904
19	19.912	109.156
20	15.080	89.244
21	13.0026	74.1636
22	9.5710	61.1610
23	7.7268	51.5900
24	6.4196	43.8632
25	5.6025	37.4436
26	4.6454	31.8411
27	3.5016	27.1957
28	2.8480	23.6941
29	2.6145	20.8461

Table 4.16: *Values of p_T bins in accompanying Figure 4.13 for the hardest (1^{st}) muon in the $bb \rightarrow \mu 6X$ process.*

4.8.3 $bb \to \mu 6 \mu 4 X$

As in the case of the $bb \to \mu 6 X$ process, the process $bb \to \mu 6 \mu 4 X$ is generated in PYTHIA without any muon constraints on the b quarks. PYTHIA is permitted to freely generate events and waits until sufficient events have been produced satisfying the process requirements. The b quarks in the event are constrained to be within $|\eta| \leqslant 4.5$ and with a $p_T \geqslant 7$ GeV and the final state is required to contain a muon with a $p_T \geqslant 6$ GeV within $|\eta| \leqslant 2.5$ (simulating a level 1 trigger cut) and a second muon with a $p_T \geqslant 4$ GeV also within the $|\eta| \leqslant 2.5$ fiducial volume.

Due to the higher overall transverse momentum requirement of the final state, the `ckin(3)` cut on the maximum p_T of the hard process was increased to 10 GeV to improve efficiency of generation without adversely affecting the simulation. The cross-section of the process extracted from PYTHIA was found to be (110.5 ± 0.2) nb. See reference [2] for further details of a comparison study between the generated $bb \to \mu 6 X$ and $bb \to \mu 6 \mu 4 X$ secondary muon distributions.

Figure 4.14 shows the muon differential and integrated p_T spectra in total and separated into muon barrel and endcap trigger regions. Trigger rates for a range of p_T thresholds taken from the figure are given in Table 4.18 for the hardest p_T muon and Table 4.19 for the second hardest p_T muon in the event.

$bb \to \mu 6 \mu 4 X$	
Pythia process menu	`msel 1` – QCD jets
Hard scattering cut `ckin(3)`	$\widehat{p}_\perp \geqslant 10$ GeV
Cut on $b\bar{b}$ quarks	$p_T \geqslant 7$ GeV within $|\eta| \leqslant 4.5$
Generator level cuts	Require one muon within: $|\eta| \leqslant 2.5$ and $p_T \geqslant 6$ GeV and one muon within: $|\eta| \leqslant 2.5$ and $p_T \geqslant 4$ GeV
Cross-section	(110.5 ± 0.2) nb

Table 4.17: *Generation parameters and calculated cross-section for $bb \to \mu 6 \mu 4 X$.*

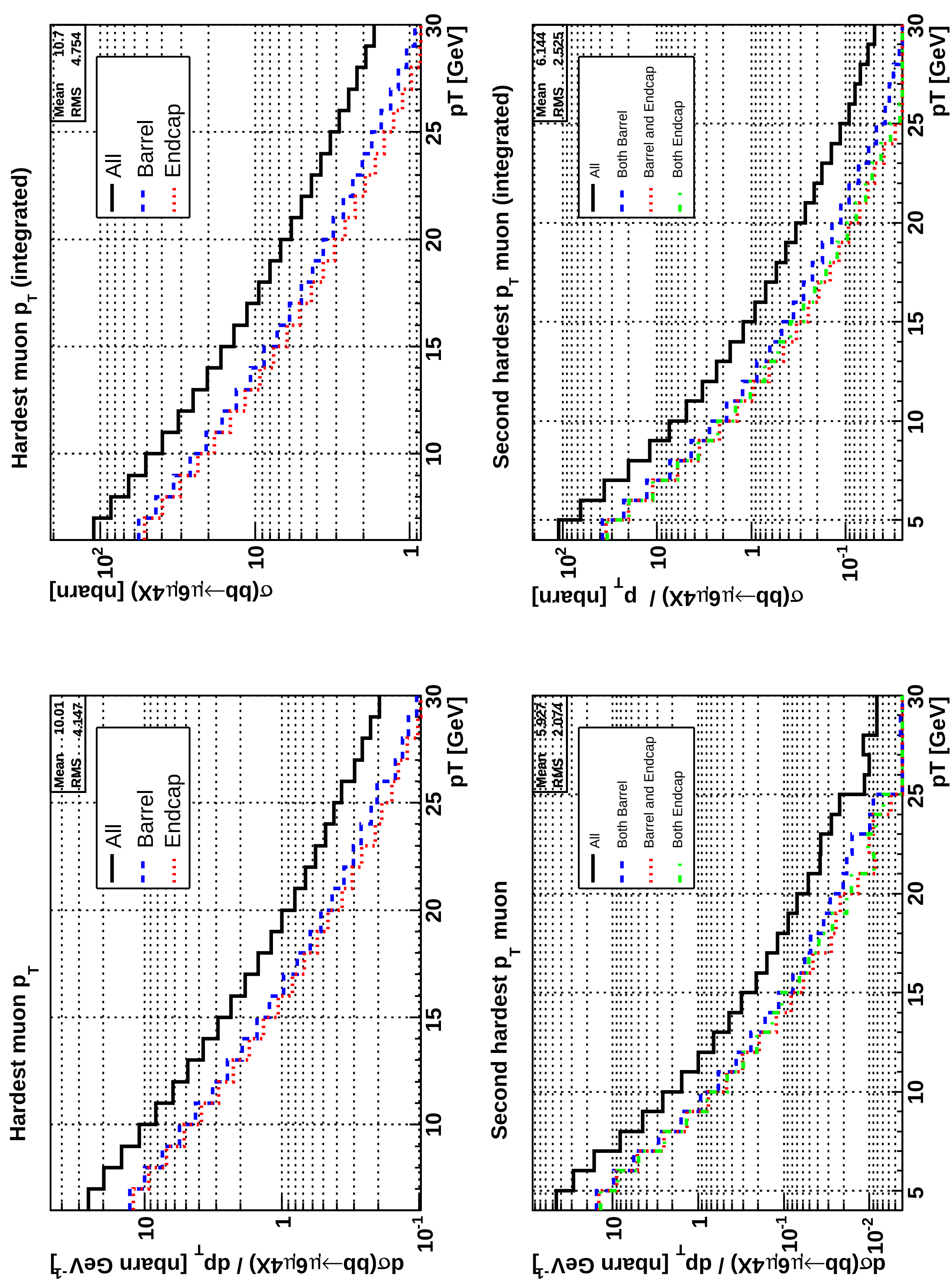

Figure 4.14: *Differential and integrated muon p_T spectra for the hardest and second hardest muon in the event for the bb $\rightarrow \mu 6 \mu 4X$ process (no charge correlation). See Table 4.20 for corresponding numerical values.*

Hardest p_T muon	Muon trigger rates (Hz), L=10^{33} cm^{-2}s^{-1}	
	Barrel	Endcap
Threshold: 6 GeV	56.48	51.80
Threshold: 8 GeV	33.68	30.36
Threshold: 10 GeV	20.64	18.30

Table 4.18: *Threshold muon trigger rates (Hz) for the hardest p_T muon in the $bb \to \mu 6 \mu 4X$ event separated into barrel and endcap muon trigger regions.*

Second hardest p_T muon	Muon trigger rates (Hz), L=10^{33} cm^{-2}s^{-1}		
	Barrel-Barrel	Barrel-Endcap	Endcap-Endcap
Threshold: 4 GeV	38.01	34.58	33.55
Threshold: 6 GeV	12.89	11.15	11.05
Threshold: 8 GeV	4.35	3.53	3.63
Threshold: 10 GeV	1.82	1.42	1.48

Table 4.19: *Threshold muon trigger rates (Hz) for the second hardest p_T muon in the $bb \to \mu 6 \mu 4X$ event separated into barrel-barrel, barrel-endcap and endcap-endcap muon trigger regions.*

p_T (GeV)	1^{st} muon cross-section		2^{nd} muon cross-section	
	Differential (nb GeV^{-1})	Integrated (nb)	Differential (nb GeV^{-1})	Integrated (nb)
4	–	–	45.468	110.500
5	–	–	28.570	65.032
6	25.494	110.500	16.335	36.462
7	19.695	85.006	8.188	20.127
8	14.681	65.310	4.484	11.940
9	10.956	50.630	2.582	7.455
10	8.278	39.674	1.555	4.873
11	6.208	31.395	0.993	3.318
12	4.851	25.188	0.663	2.325
13	3.737	20.336	0.437	1.662
14	2.933	16.599	0.313	1.226
15	2.340	13.666	0.210	0.913
16	1.844	11.326	0.157	0.702
17	1.482	9.482	0.118	0.545
18	1.196	8.000	0.089	0.427
19	0.999	6.804	0.071	0.338
20	0.804	5.805	0.052	0.268
21	0.676	5.000	0.038	0.216
22	0.572	4.324	0.037	0.178
23	0.4817	3.7519	0.0280	0.1415
24	0.4177	3.2702	0.0222	0.1134
25	0.3685	2.8525	0.0114	0.0912
26	0.2965	2.4840	0.0101	0.0798
27	0.2594	2.1875	0.0119	0.0697
28	0.2258	1.9280	0.0082	0.0578
29	0.1956	1.7023	0.0082	0.0496

Table 4.20: *Values of p_T bins in accompanying Figure 4.14 for the hardest (1^{st}) muon and second hardest (2^{nd}) muon in the $bb \to \mu 6 \mu 4 X$ process.*

4.8.4 $bb \to J/\psi(\mu 6 \mu 4)X$

In contrast to the $bb \to \mu 6X$ and $bb \to \mu 6 \mu 4X$ processes, the b quark in the event in this case is left without constraints, whilst the $\bar{b}$ quark is constrained to be within $|\eta| \leqslant 4.5$ and with a $p_T \geqslant 10$ GeV and the final state is required to contain a muon with a $p_T \geqslant 6$ GeV within $|\eta| \leqslant 2.5$ (simulating a level 1 trigger cut) and a second muon with a $p_T \geqslant 4$ GeV also within the $|\eta| \leqslant 2.5$ fiducial volume. Rapidity cuts of $|y| \leqslant 3.5$ are also imposed on the event.

Due to the higher overall transverse momentum requirement of the final state, the `ckin(3)` cut on the maximum p_T of the hard process was increased to 9 GeV to improve efficiency of generation without adversely affecting the simulation. The cross-section of the process extracted from Pythia was found to be (11.06 ± 0.04) nb.

$bb \to J/\psi(\mu 6 \mu 4)X$	
Pythia process menu	`msel 1` – QCD jets
Hard scattering cut `ckin(3)`	$\widehat{p}_\perp \geqslant 9$ GeV
Cut on $\bar{b}$ quark	$p_T \geqslant 10$ GeV in $\lvert\eta\rvert \leqslant 4.5$
Generator level cuts	Require one muon within $\lvert\eta\rvert \leqslant 2.5$ and $p_T \geqslant 6$ GeV and one muon within $\lvert\eta\rvert \leqslant 2.5$ and $p_T \geqslant 4$ GeV
True rapidity cuts on hard process	`ckin(9)`=`ckin(11)`=-3.5, `ckin(10)`=`ckin(12)`= 3.5
PYTHIA forcings	see reference [122] for details
Cross-section	(11.06 ± 0.04) nb

Table 4.21: *Generation parameters and calculated cross-section for $bb \to J/\psi(\mu 6 \mu 4)X$.*

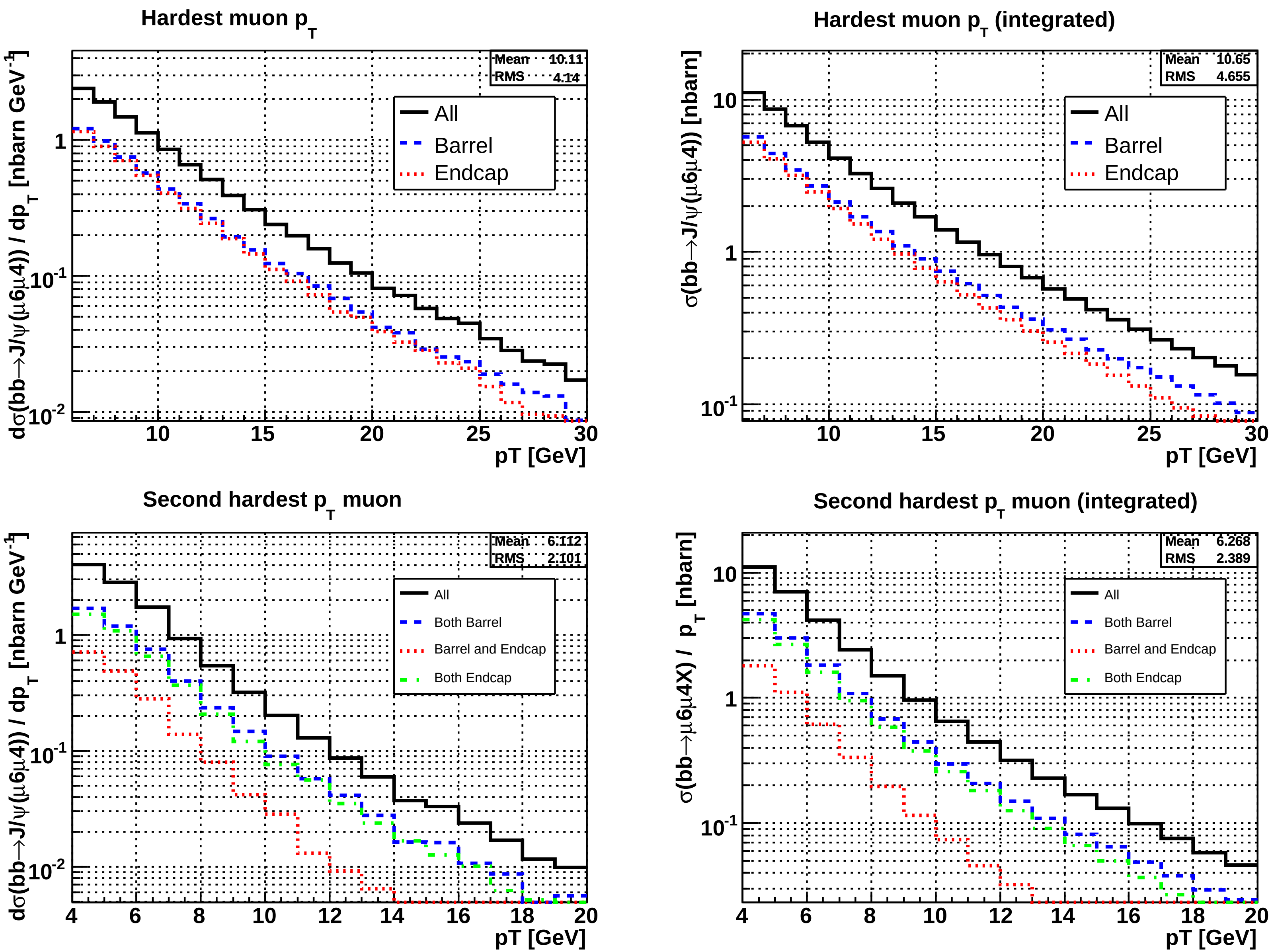

Figure 4.15: *Differential and integrated muon p_T spectra for the hardest and second hardest muon in the event for the $b\bar{b} \to J/\psi(\mu 6\mu 4)X$ process (no charge correlation). See Table 4.22 for corresponding numerical values.*

p_T (GeV)	1^{st} muon cross-section		2^{nd} muon cross-section	
	Differential (nb GeV^{-1})	Integrated (nb)	Differential (nb GeV^{-1})	Integrated (nb)
4	–	–	4.038	11.060
5	–	–	2.851	7.022
6	2.409	11.060	1.736	4.171
7	1.909	8.651	0.929	2.435
8	1.483	6.742	0.541	1.507
9	1.135	5.259	0.318	0.965
10	0.858	4.124	0.202	0.647
11	0.661	3.266	0.129	0.445
12	0.514	2.605	0.087	0.316
13	0.390	2.091	0.060	0.229
14	0.306	1.702	0.037	0.169
15	0.239	1.396	0.033	0.132
16	0.198	1.157	0.024	0.099
17	0.159	0.959	0.017	0.075
18	0.125	0.800	0.012	0.058
19	0.105	0.674	0.010	0.046
20	0.081	0.569	0.008	0.037
21	0.072	0.488	0.005	0.029
22	0.058	0.416	0.003	0.024
23	0.0487	0.3582	0.0045	0.0208
24	0.0449	0.3095	0.0022	0.0163
25	0.0345	0.2646	0.0022	0.0142
26	0.0283	0.2300	0.0020	0.0120
27	0.0236	0.2017	0.0016	0.0100
28	0.0225	0.1782	0.0012	0.0084
29	0.0172	0.1556	0.0010	0.0072

Table 4.22: *Values of p_T bins in accompanying Figure 4.15 for the hardest (1^{st}) muon and second hardest (2^{nd}) muon in the $bb \rightarrow J/\psi(\mu6\mu4)X$ process.*

4.8.5 $cc \to \mu 6X$

The process $cc \to \mu 6X$ is generated in PYTHIA without requiring any constraints on the c quarks into muons. As for $bb \to \mu 6X$, PYTHIA is permitted to freely generate events and waits until enough events have been produced satisfying the process requirements that the c quarks in the event are constrained to be within $|\eta| \leqslant 4.5$ and with a $p_T \geqslant 4$ GeV and the final state is required to contain a muon with a $p_T \geqslant 4$ GeV within $|\eta| \leqslant 2.5$, from which we subselect those events containing a muon with at least 6 GeV p_T for this analysis. The cross-section extracted from PYTHIA was (7.9 ± 0.02) μb.

In Table 4.24 threshold muon trigger rates for the hardest muon in the $cc \to \mu 6X$ event are presented separated into muon barrel and endcap trigger regions.

$cc \to \mu 6X$	
Pythia process menu	`msel 1` – QCD jets
Hard scattering cut `ckin(3)`	$\widehat{p}_\perp \geqslant 6$ GeV
Cut on $c\bar{c}$ quarks	$p_T \geqslant 4$ GeV within $|\eta| \leqslant 4.5$
Generator level cuts	Require one muon within: $|\eta| \leqslant 2.5$ and $p_T \geqslant 4$ GeV
Further offline cuts	Require muon $p_T \geqslant 6$ GeV
Cross-section	(7.9 ± 0.02) μb

Table 4.23: *Generation parameters and calculated cross-section for $cc \to \mu 6X$.*

Hardest p_T muon	Muon trigger rates (Hz), L=10^{33} cm^{-2}s^{-1}	
	Barrel	Endcap
Threshold: 6 GeV	3754.94	3918.99
Threshold: 8 GeV	1433.89	1435.39
Threshold: 10 GeV	654.40	640.58

Table 4.24: *Threshold muon trigger rates (Hz) for the hardest p_T muon in the $cc \to \mu 6X$ event separated into barrel and endcap muon trigger regions.*

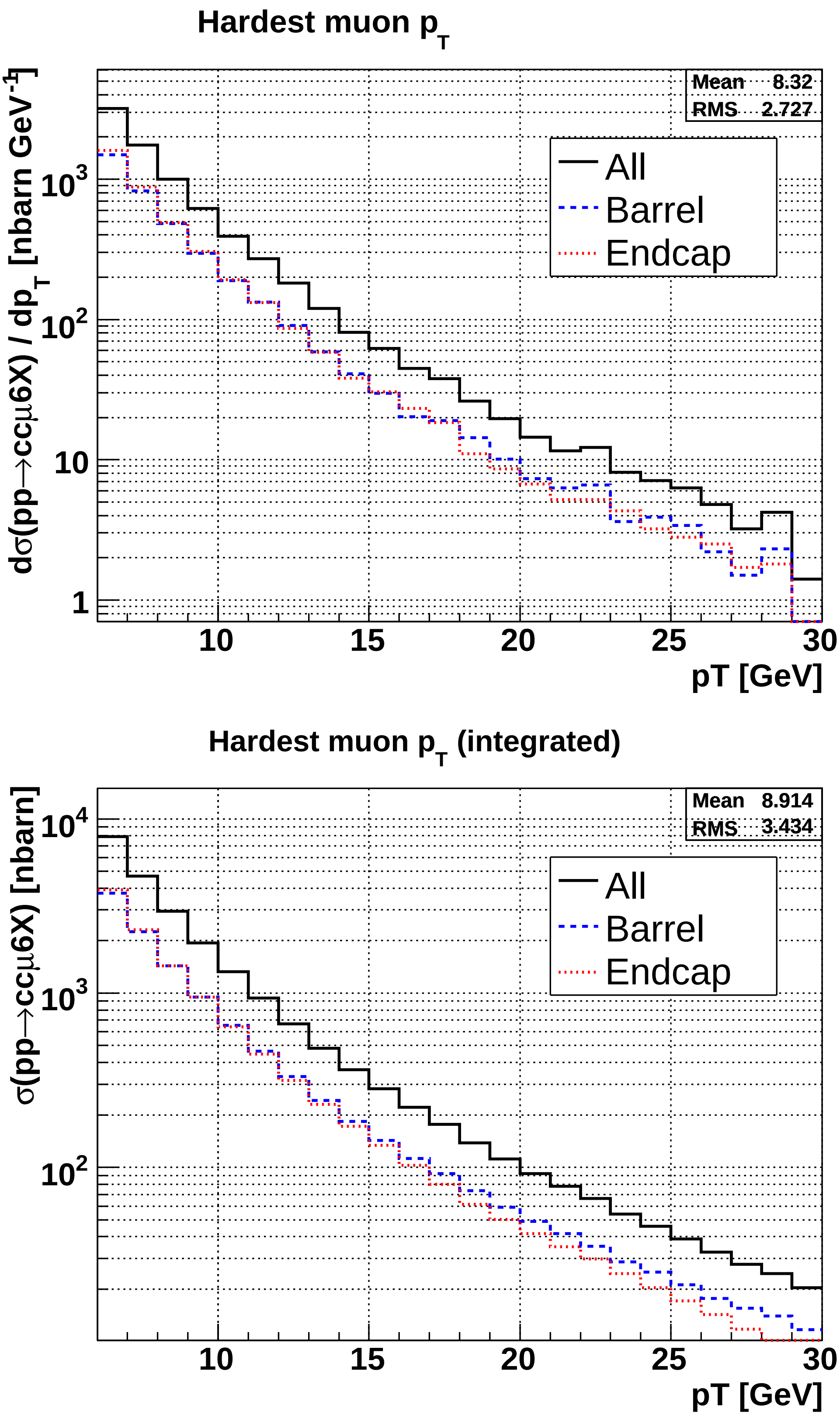

Figure 4.16: *Differential and integrated muon p_T spectra for the hardest muon in the event for the $cc \to \mu 6X$ process (no charge correlation). See Table 4.25 for corresponding numerical values.*

p_T (GeV)	1^{st} muon cross-section	
	Differential (nb GeV^{-1})	Integrated (nb)
6	3200.592	7902.379
7	1753.881	4701.787
8	1000.529	2947.906
9	619.347	1947.376
10	391.298	1328.030
11	271.415	936.732
12	181.578	665.317
13	119.783	483.739
14	81.124	363.956
15	62.195	282.832
16	44.568	220.637
17	37.958	176.069
18	26.240	138.111
19	19.630	111.871
20	14.4220	92.2410
21	11.5176	77.8189
22	12.2187	66.3013
23	8.1124	54.0827
24	7.1109	45.9703
25	6.3096	38.8594
26	4.8073	32.5498
27	3.2049	27.7424
28	4.2064	24.5375
29	1.4021	20.3311
30	2.2034	18.9289
31	2.4037	16.7256
32	1.2018	14.3219
33	1.3020	13.1201

Table 4.25: *Values of p_T bins in accompanying Figure 4.16 for the hardest (1^{st}) muon in the $cc \to \mu 6X$ process.*

4.8.6 Direct J/ψ production

The direct J/ψ dataset is composed of prompt charmonium events produced via singlet states but also through the production of intermediate colour-octet states that feed-down into their corresponding singlet states (with a 100% branching fraction) in the NRQCD framework. Feed-down from χ_J states is also taken into account but not the contribution from $\psi'(3686)$, which is expected to contribute an additional 1.3 nb to the $\mu6\mu4$ cross-section (see Section 4.7). The χ states are forced to $J/\psi\gamma$ and the J/ψ is forced into muons, with the appropriate normalisation for the branching fractions applied to the PYTHIA cross-section in the correct proportions after generation.

A hard scattering cut of `ckin(3)` ≥ 4.5 GeV was chosen to allow for efficiency of generation without sacrificing low p_T events near the trigger threshold. Di-muon trigger cuts on the transverse momentum of 6 and 4 GeV within $|\eta| \leqslant 2.5$ were applied on the generated events from PYTHIA with an acceptance of 1.3%. The cross-section of the process extracted from PYTHIA was found to be (21.7 ± 0.1) nb.

$pp \to J/\psi(\mu6\mu4)$	
PYTHIA process menu	`msel 61` – NRQCD charmonium production
Hard scattering cut `ckin(3)`	$\widehat{p}_\perp \geqslant 4.5$ GeV
NRQCD matrix elements	see Table 4.4 for details
BSignalFilter cuts	one muon within $|\eta| \leqslant 2.5$ and $p_T \geqslant 6$ GeV;one muon within $|\eta| \leqslant 2.5$ and $p_T \geqslant 4$ GeV
Cross-section	(21.7 ± 0.1) nb

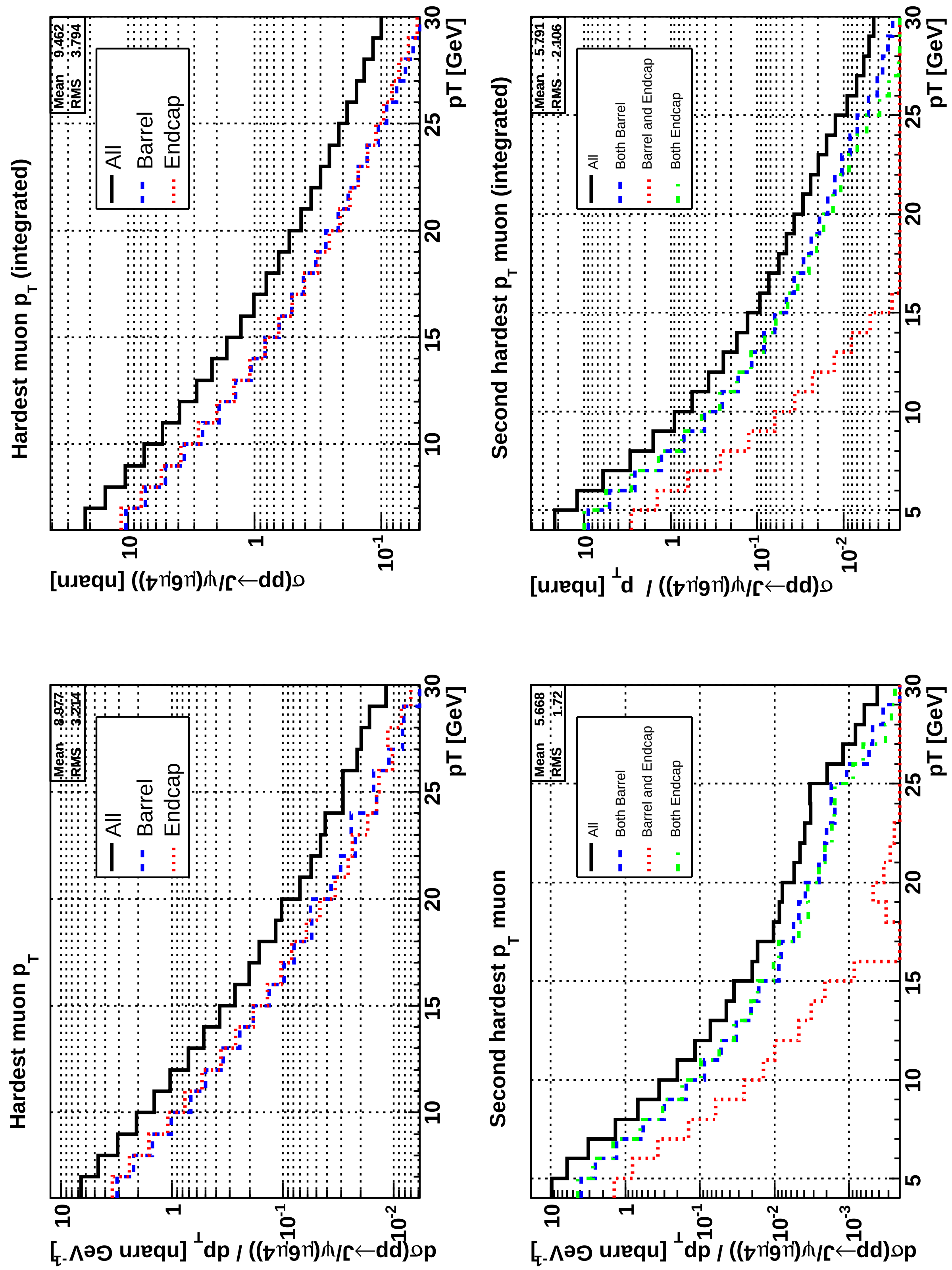

Figure 4.17: *Differential and integrated muon p_T spectra for the hardest and second hardest muon in the event for the $pp \to J/\psi(\mu6\mu4)$ process (no charge correlation). See Table 4.26 for corresponding numerical values.*

p_T (GeV)	1^{st} muon cross-section		2^{nd} muon cross-section	
	Differential (nb GeV^{-1})	Integrated (nb)	Differential (nb GeV^{-1})	Integrated (nb)
4	–	–	9.671	21.750
5	–	–	6.018	12.089
6	6.579	21.750	3.133	6.071
7	4.622	15.171	1.352	2.938
8	3.095	10.549	0.673	1.586
9	2.098	7.454	0.351	0.912
10	1.444	5.357	0.199	0.562
11	1.037	3.913	0.117	0.362
12	0.709	2.876	0.072	0.245
13	0.514	2.167	0.044	0.173
14	0.370	1.653	0.035	0.128
15	0.270	1.283	0.020	0.093
16	0.201	1.013	0.017	0.073
17	0.164	0.812	0.010	0.056
18	0.117	0.648	0.009	0.046
19	0.103	0.531	0.008	0.038
20	0.071	0.428	0.005	0.030
21	0.056	0.358	0.005	0.024
22	0.046	0.302	0.004	0.020
23	0.0415	0.2561	0.0033	0.0157
24	0.0286	0.2146	0.0033	0.0125
25	0.0289	0.1860	0.0020	0.0091
26	0.0214	0.1571	0.0012	0.0071
27	0.0197	0.1358	0.0008	0.0059
28	0.0167	0.1161	0.0006	0.0051
29	0.0118	0.0994	0.0004	0.0045

Table 4.26: *Values of p_T bins in accompanying Figure 4.17 for the hardest (1^{st}) muon and second hardest (2^{nd}) muon in the $pp \rightarrow J/\psi(\mu 6 \mu 4)$ process.*

4.8.7 Direct Υ production

As in the direct J/ψ case, the direct Υ dataset utilises the NRQCD colour-octet framework in PYTHIA to produce prompt bottomonium events not only through the production of singlet states but also through the production of intermediate colour-octet states. Feed-down from $\chi(1P)$ states is taken into account but not the contribution from higher Υ states, although these contributions are expected to be comparatively small. The χ states are forced to $\Upsilon\gamma$ and the Υ is forced into muons, with the appropriate normalisation for the branching fractions applied to the PYTHIA cross-section in the correct proportions after generation. Colour octet states decay into their corresponding singlet states and a very soft gluon, with the NRQCD matrix elements controlling the relative contributions of the various octet states.

A hard scattering cut of 1.0 GeV was chosen to allow for efficiency of generation without sacrificing low p_T events near the trigger threshold. Di-muon trigger cuts on the transverse momentum of 6 and 4 GeV within $|\eta| \leqslant 2.5$ were applied on the generated events from PYTHIA with an acceptance of 1.6%. The cross-section of the process extracted from PYTHIA was found to be (4.57 ± 0.02) nb.

This cross-section does not take into account feed-down from the higher Υ states $\Upsilon(2S)$ and $\Upsilon(3S)$ into $\Upsilon(1S)$, which are expected to contribute an additional 0.6 nb to the $\mu6\mu4$ cross-section (see Section 4.7).

$pp \rightarrow \Upsilon(\mu6\mu4)$	
PYTHIA process menu	`msel 62` – NRQCD bottomonium production
Hard scattering cut `ckin(3)`	$\widehat{p}_{\perp} \geqslant 1.0$ GeV
NRQCD matrix elements	see Table 4.4 for details
BSignalFilter cuts	one muon within $|\eta| \leqslant 2.5$ and $p_T \geqslant 6$ GeV; one muon within $|\eta| \leqslant 2.5$ and $p_T \geqslant 4$ GeV
Cross-section	(4.57 ± 0.02) nb

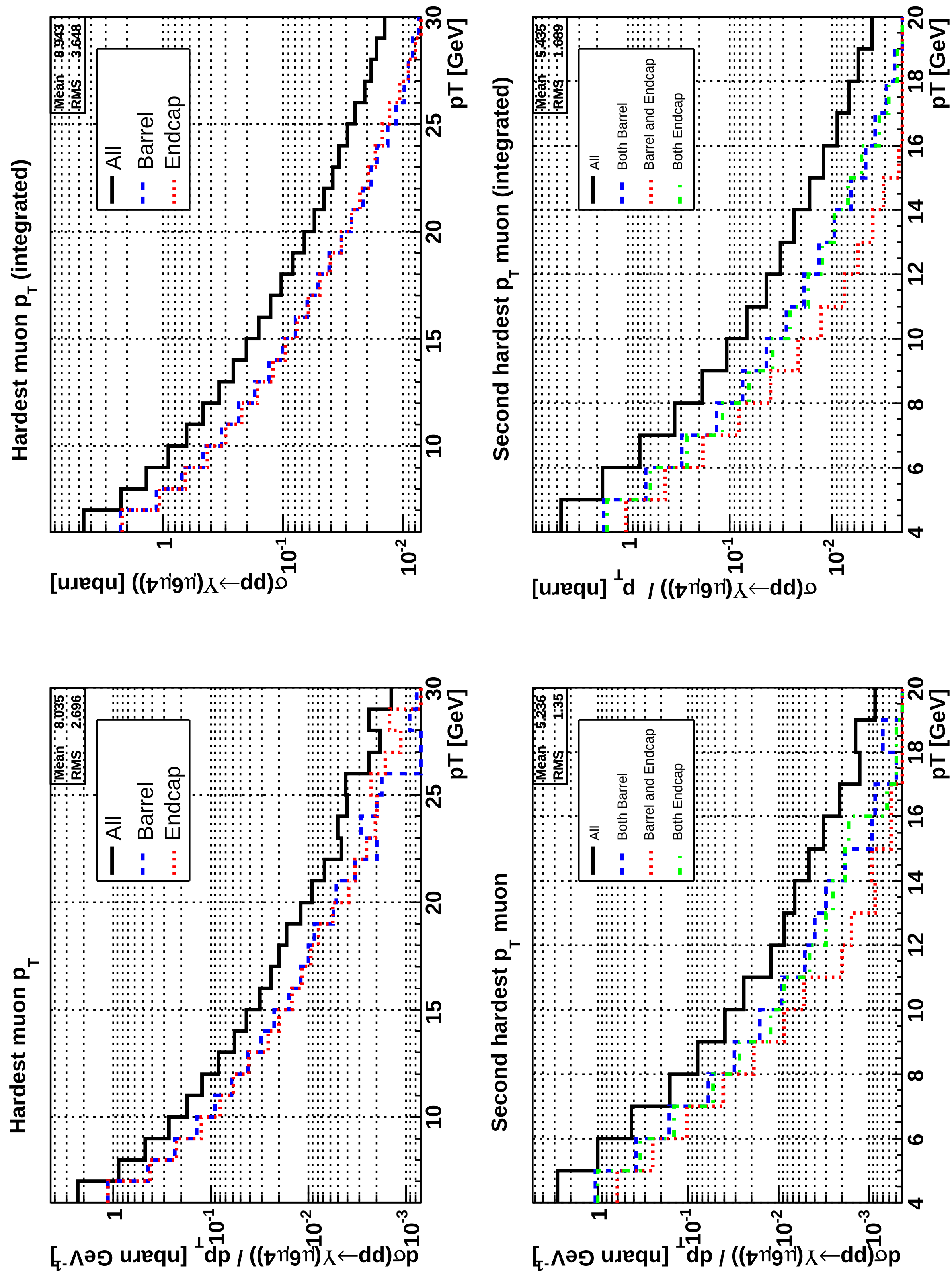

Figure 4.18: *Differential and integrated muon p_T spectra for the hardest and second hardest muon in the event for the $pp \to \Upsilon(\mu 6\mu 4)$ process (no charge correlation). See Table 4.27 for corresponding numerical values.*

p_T (GeV)	1^{st} muon cross-section		2^{nd} muon cross-section	
	Differential (nb GeV^{-1})	Integrated (nb)	Differential (nb GeV^{-1})	Integrated (nb)
4	–	–	2.795	4.570
5	–	–	1.003	1.775
6	2.314	4.570	0.425	0.772
7	0.875	2.256	0.160	0.347
8	0.471	1.380	0.079	0.187
9	0.270	0.909	0.039	0.108
10	0.174	0.639	0.024	0.069
11	0.123	0.465	0.012	0.044
12	0.084	0.343	0.009	0.032
13	0.057	0.259	0.007	0.023
14	0.043	0.202	0.005	0.017
15	0.031	0.159	0.003	0.012
16	0.024	0.127	0.002	0.009
17	0.0200	0.1034	0.0013	0.0067
18	0.0167	0.0834	0.0014	0.0054
19	0.0120	0.0667	0.0008	0.0040
20	0.0091	0.0547	0.0006	0.0032
21	0.0069	0.0456	0.0006	0.0025
22	0.0046	0.0387	0.0005	0.0020
23	0.0050	0.0341	0.0004	0.0015
24	0.0040	0.0292	0.0000	0.0011
25	0.0042	0.0251	0.0002	0.0011
26	0.0024	0.0209	0.0001	0.0009
27	0.0018	0.0185	0.0000	0.0008
28	0.0024	0.0167	0.0001	0.0008
29	0.0014	0.0143	0.0001	0.0006

Table 4.27: *Values of p_T bins in accompanying Figure 4.18 for the hardest (1^{st}) muon and second hardest (2^{nd}) muon in the $pp \to \Upsilon(\mu 6 \mu 4)$ process.*

4.9 Summary of single and di-muon rates at 14 TeV

This section contains muon rate summary plots combining into one plot the hardest muon p_T spectra (Figure 4.19) for all processes described in the previous section and also the second hardest muon p_T spectra (Figure 4.20) for processes with a di-muon trigger, with no charge correlation required for the second muon. Both the differential and integrated cross-section spectra are presented in each case and the relevant processes have been overlaid to allow for quick comparison. For the exact contents in each p_T bin refer to the tables given for each process earlier in this Chapter.

In addition to the di-muon $\mu6\mu4$ studies that have been detailed in the previous sections, an additional generation was performed lowering the higher muon threshold to 4 GeV to give additional di-muon $\mu4\mu4$ cross-sections for early running. A summary of the predicted rates for both thresholds is given in Table 4.28.

Process ($\mu6$ threshold)	Cross-section		Process ($\mu4$ threshold)	Cross-section	
$bb \to \mu6X$	6.14	μb	$bb \to \mu4X$	19.3	μb
$cc \to \mu6X$	7.9	μb	$cc \to \mu4X$	26.3	μb
$bb \to \mu6\mu4X$	110.5	nb	$bb \to \mu4\mu4X$	212.0	nb
$cc \to \mu6\mu4X$	248.0	nb	$cc \to \mu4\mu4X$	386.0	nb
$pp \to J/\psi(\mu6\mu4)X$	21.7	nb	$pp \to J/\psi(\mu4\mu4)X$	27.0	nb
$pp \to \Upsilon(\mu6\mu4)X$	4.57	nb	$pp \to \Upsilon(\mu4\mu4)X$	43.0	nb
$bb \to J/\psi(\mu6\mu4)X$	11.06	nb	$bb \to J/\psi(\mu4\mu4)X$	12.5	nb

Table 4.28: *Predicted cross-sections for various muon and di-muon sources.*

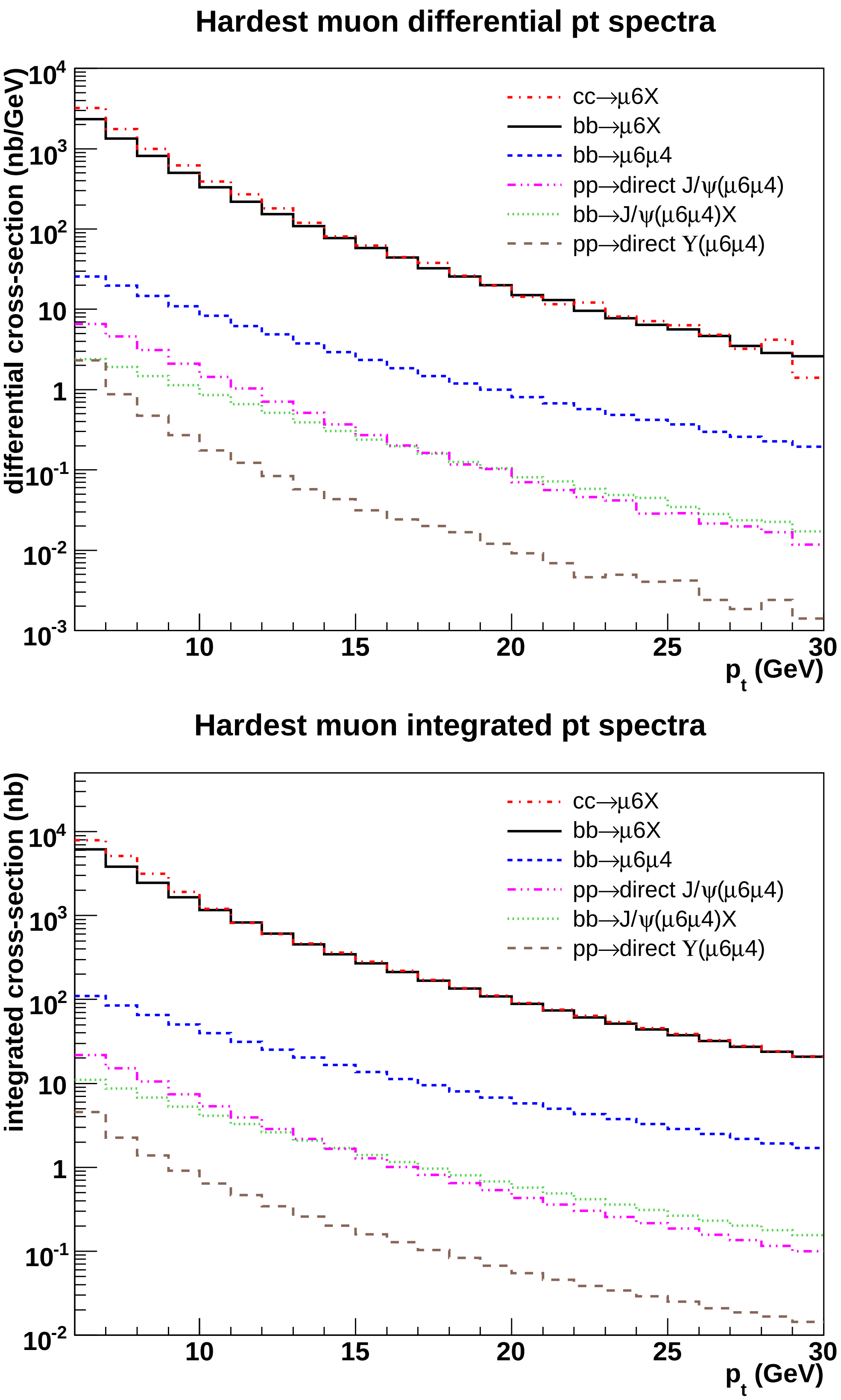

Figure 4.19: *Combined plots of differential and integrated muon p_T spectra showing hardest muon rates for $bb \to \mu 6X$, $bb \to \mu 6\mu 4X$, $bb \to J/\psi(\mu 6\mu 4)X$, $cc \to \mu 6X$, direct J/ψ and direct Υ processes (no charge correlation).*

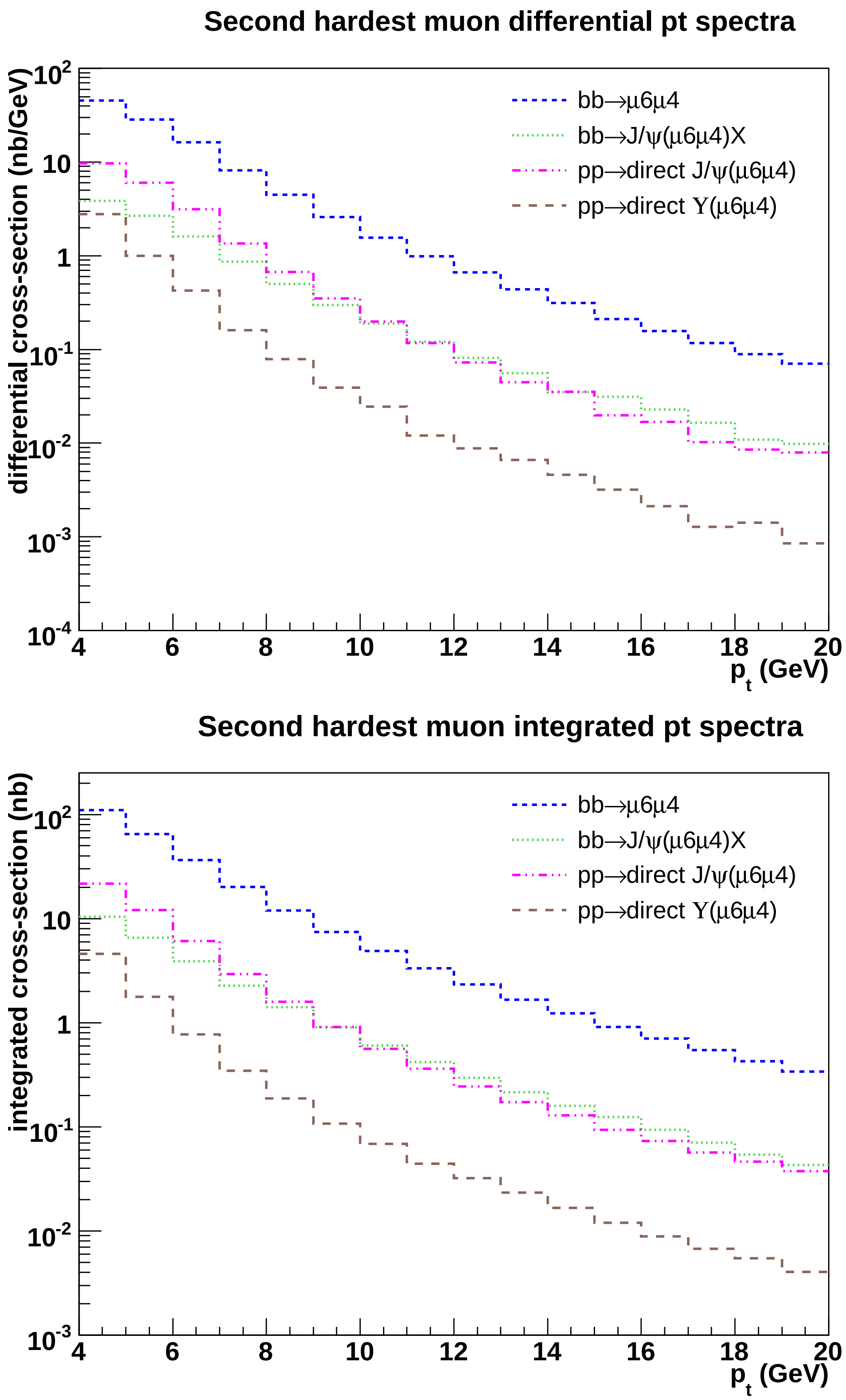

Figure 4.20: *Combined plots of differential and integrated muon p_T spectra showing rates of the second hardest muon in the event for $bb \rightarrow \mu 6 \mu 4$, $bb \rightarrow J/\psi(\mu 6 \mu 4) X$, direct J/ψ and direct Υ processes (no charge correlation).*

"Measure what is measurable, and make measurable what is not so."

Galileo Galilei

5

Event selection and analysis

The importance of $J/\psi \rightarrow \mu^+\mu^-$ and $\Upsilon \rightarrow \mu^+\mu^-$ decays for ATLAS is threefold: first, being narrow resonances, they can be used as tools for alignment and calibration of the trigger, tracking and muon systems and many activities are underway within ATLAS in these areas. Secondly, understanding the details of the prompt onia production is a challenging task and a good testbed for various QCD calculations, as discussed in Chapter 2. Last, but not least, heavy quarkonium states are among the decay products of heavier states, serving as good signatures for many processes of interest, some of which are quite rare and can utilise the clean signature of quarkonium in triggers. These processes also have prompt quarkonia as a background and, as such, a good description of the underlying quarkonium production process is crucial to the success of these studies.

Once generation of datasets was complete the processes described in the previous chapter were passed through the full chain ATLAS simulation. The event selection described in this chapter proceeds in effect as it would for analysis of real J/ψ or Υ candidate events once ATLAS begins taking data from collisions. These studies were performed on the so-called Computing System Commissioning (CSC) datasets at ATLAS. This chapter concentrates on the capabilities of the ATLAS detector to study various aspects of prompt quarkonium production at LHC and the methods of triggering, reconstructing and separating promptly produced J/ψ and Υ mesons from various backgrounds. The simulated and reconstructed data analysed for CSC analyses described in this chapter and Chapter 7 are based on an equivalent integrated luminosity of less than 10 pb^{-1}, which is the expected yield at standard low luminosity operation in approximately one week of data-taking.

5.1 Trigger considerations

Details of the triggers to be used in ATLAS *B*-physics programme can be found in [103] and in Section 3.5. Quarkonium production will be subject to trigger cuts on di-muons at level-1 and level-2[1)]. This section discusses the trigger signatures relevant for quarkonium production at ATLAS at the time of the CSC studies, the implications they have on the measured cross-section, and the expected effects they have on our ability to make various physics measurements. Two specific types of di-muon triggers dedicated to quarkonium are: the topological di-muon triggers, which require two level 1 regions of interest (RoIs) corresponding to two muon candidates with p_T thresholds of 4 and 6 GeV, and "TrigDiMuon" di-muon triggers that only require a single level-1 RoI above a threshold of 4 GeV and searches for the second muon of opposite charge in a wide RoI at level-2. Both of these trigger types will be used to select quarkonium in data-taking. They are discussed in Section 5.1.1. A further trigger scenario is based on a single muon trigger with a higher p_T threshold of 10 GeV, discussed in Section 5.1.3.

[1)]During the very first data-taking runs of ATLAS, it is expected that data-taking will be performed using level-1 trigger algorithms only, and all events written to tape at the HLT.

5.1.1 Di-muon triggers

Being able to determine the trigger efficiency of measured J/ψ and Υ is crucial to correctly infer the production cross-section of quarkonium at the LHC. Indeed, using J/ψ and Υ (as well as the Z boson) to construct a trigger efficiency map is a necessary step in order to perform cross section measurements in ATLAS.

Studies are being conducted in ATLAS into developing a calibration method to obtain the low p_T single muon trigger efficiency, and henceforth the di-muon trigger efficiency of events using real data by virtue of the so-called 'tag-and-probe' method (see reference [103] for details). I also outline a new method for single muon trigger efficiency determination using quarkonia in Section 6.3. While these studies are being finalised, we have performed our own studies of trigger efficiencies, based on available Monte Carlo simulations rather than data-driven methods for the CSC studies described in this chapter. Studies within ATLAS have shown that the tag-and-probe method provides for good agreement with the results of Monte Carlo simulation.

It is worth noting that the J/ψ and Υ are individually very good candidates for studying low p_T muon trigger efficiencies, as the different masses and complementary decay kinematics allow access to different momentum regions and different angular separation of the muons (see Section 5.2.1 for details).

Level 1 Trigger

If not stated otherwise, the quoted trigger efficiencies have been calculated with respect to the Monte Carlo samples, generated with the cuts $p_T(\mu_1) > 6$ GeV, $p_T(\mu_2) > 4$ GeV, where μ_1 (μ_2) is the muon with the largest (second largest) transverse momentum in the event.

The level-1 trigger is a hardware trigger that uses coarse calorimeter and muon spectrometer information to identify interesting signatures to pass to the High Level Trigger. The level-1 triggers that are relevant to production of quarkonium in the di-muon channel are the single muon p_T threshold triggers `L1_MUXX` (where `XX` indicates the p_T threshold in GeV) and the di-muon trigger L1_2MU06. Each p_T range of these individual trigger items is exclusive in CSC studies. Figure 5.1(a) shows the various individual level-1 trigger efficiencies for J/ψ as a function of the p_T of the di-muon system. The total trigger efficiency at level-1, running over direct J/ψ events, is 87%. The equivalent trigger efficiency for Υ is shown in Figure 5.1(b), with a total efficiency at level-1 of 84%. Note that at the time of these studies, specialised Υ resonance triggers were not available (trigger algorithms are currently being developed) so for the following studies we rely on the generic J/ψ and B-hadron triggers to identify Υ candidates, which leads to a lower trigger efficiency than might otherwise be expected (this is particularly true at level-2). Only the triggers with efficiencies greater than 2% in some region of p_T are displayed.

Level 2 Trigger

The level-2 trigger is software-based and is designed to reduce the output rate of the data, passed to it from level-1, by two orders of magnitude. Within the regions of interest defined by the level-1 trigger, full granularity of the detector is accessible. The level-2 trigger signatures of interest for quarkonium studies include single muon p_T threshold triggers L2_MUXX as for the level-1 case, di-muon p_T triggers L2_muXXL2muYY and topological triggers L2_BJpsimuXmuY which are specialised for searching for J/ψ [103].

The efficiency of the level-2 triggers for prompt J/ψ events is plotted in Figure 5.2(a) as a function of di-muon p_T. The total level-2 trigger efficiency in the reconstructed data (relative to level-1) is 97%. For Υ candidates (Figure 5.2(b)) the overall level-2 efficiency is 66% (again relative to level-1). The dramatic loss of trigger efficiency is, as stated for the level-1 trigger above, due to specialised Υ algorithms not being available at the time of these studies, meaning we must accept Υ events using J/ψ and B-hadron algorithms with different kinematics to the Υ, leading to inefficiencies particularly in the low p_T region. Again, only those triggers which have greater than 2% efficiency in this dataset in some region of p_T are displayed. The di-muon trigger scenario we call $\mu6\mu4$ uses all the above trigger signatures.

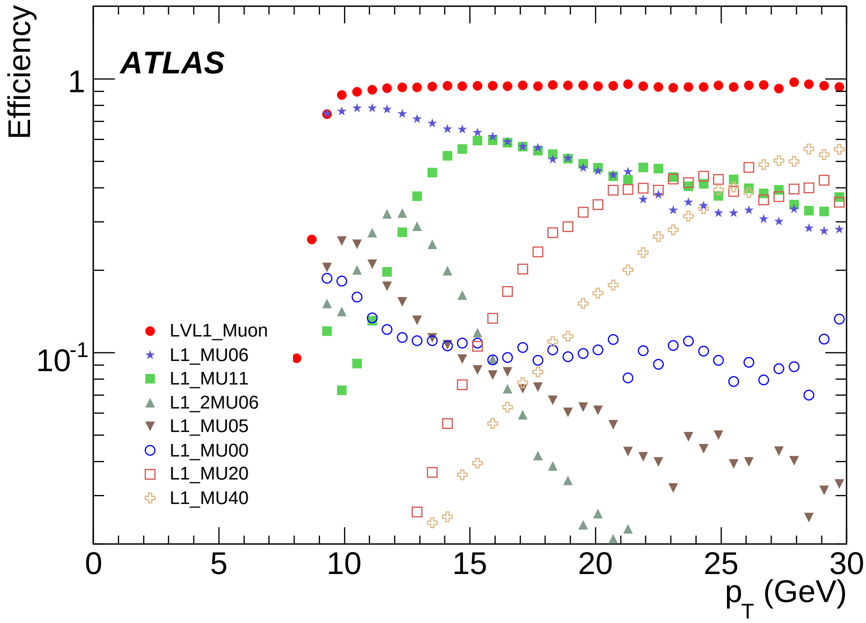

(a) Level-1 $J/\psi(\mu\mu)$ trigger efficiency

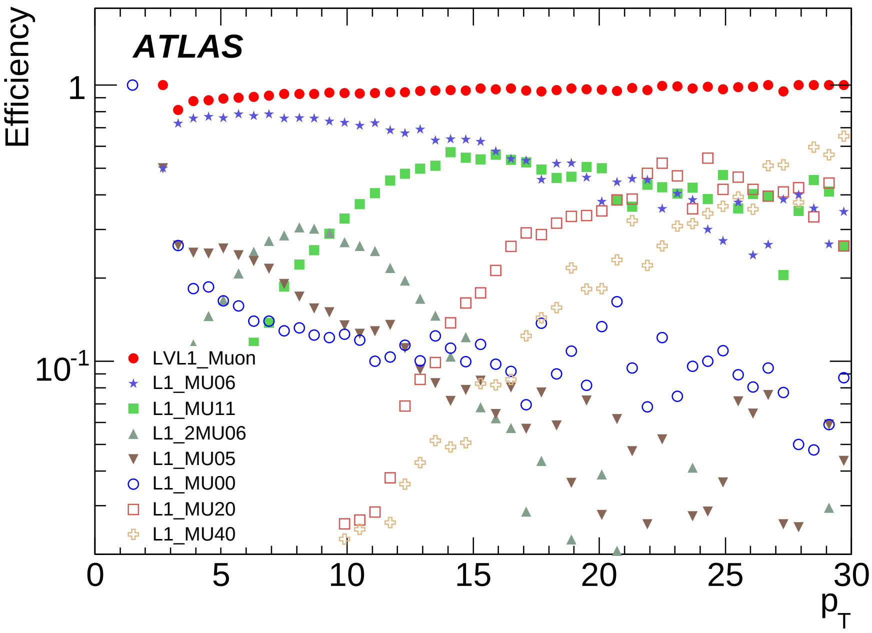

(b) Level-1 $\Upsilon(\mu\mu)$ trigger efficiency

Figure 5.1: *Efficiency of various Level-1 triggers on prompt J/ψ (top) and Υ (bottom) events as a function of p_T of the di-muon system. The efficiency curve labelled* `LVL1_Muon` *is the sum of all LVL1 single muon efficiencies* (excluding *the di-muon trigger* `L1_2MU06`) *The number following the trigger item name indicates the p_T threshold for that trigger.*

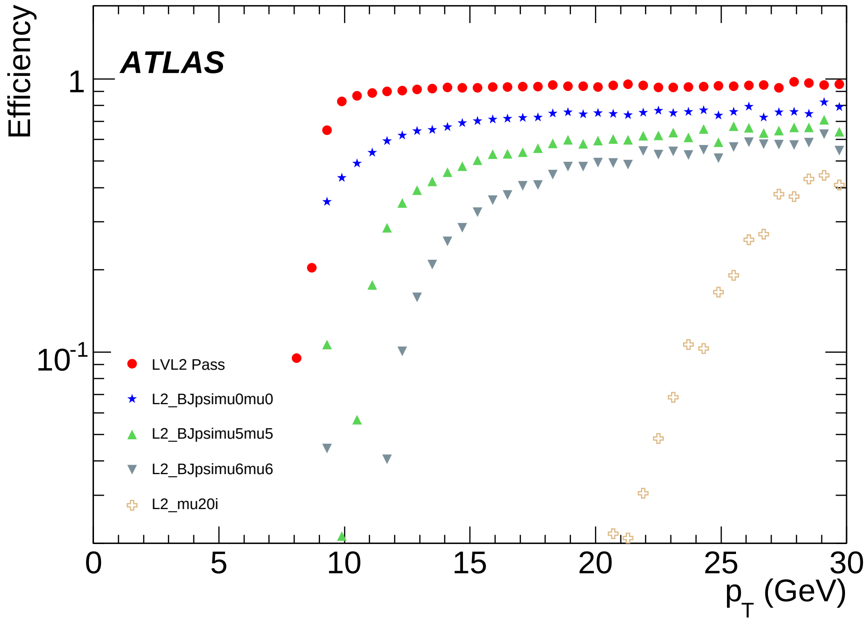

(a) Level-2 $J/\psi(\mu\mu)$ trigger efficiency

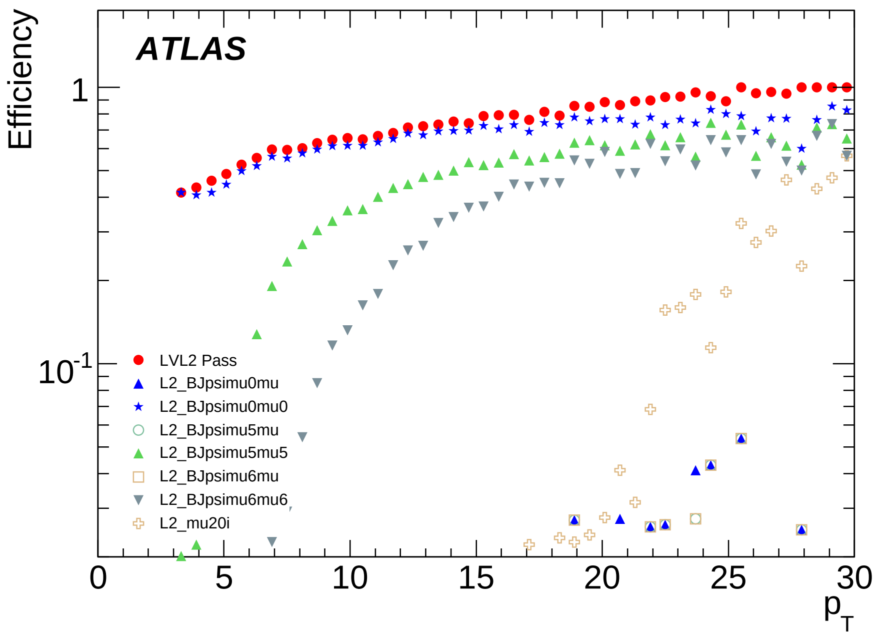

(b) Level-2 $\Upsilon(\mu\mu)$ trigger efficiency

Figure 5.2: *Efficiency of various Level-2 triggers on prompt J/ψ (top) and Υ (bottom) events as a function of p_T of the di-muon system. The efficiency curve labelled* `LVL2_Pass` *is the sum of all LVL2 trigger efficiencies.*

Effect of trigger cuts on analysis of octet states

As discussed in Chapter 2 the quarkonium cross-section in the NRQCD framework is composed of three classes of processes: direct colour singlet production, colour octet production and singlet/octet production of χ states. Figure 5.3 highlights the individual contributions of these three classes to the overall production rate for Υ, once the p_T trigger cuts of 6 and 4 GeV are applied to the muons. Lower p_T trigger cuts will strongly enhance the Υ rate and allow for

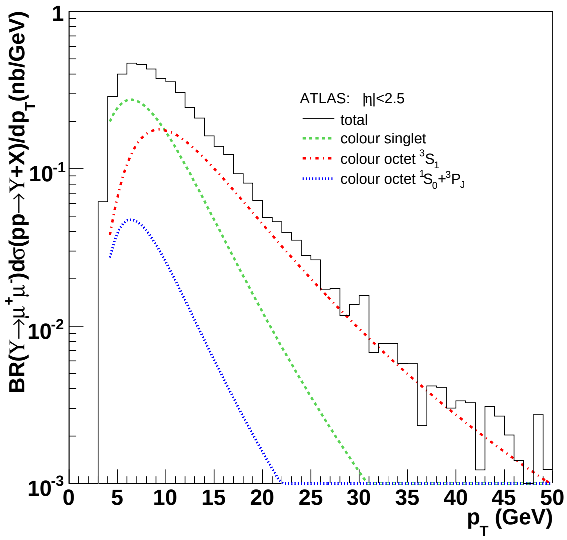

Figure 5.3: *Expected p_T-distribution for Υ production, with contributions from direct colour singlet, singlet χ production and octet production overlaid.*

analysis of colour singlet production, which is expected to dominate for Υ with $p_T < 10$ GeV. The relatively large mass of the Υ means that with a 6+4 GeV trigger Υ can be measured down to 3 or 4 GeV transverse momentum, but J/ψ with its lower mass can only be observed above around 8 GeV. Lower trigger cuts available during early running, such as the $\mu 4\mu 4$ trigger described previously, will allow the opportunity to extend the low p_T region down to $p_T \simeq 0$ in the case of Υ and provide additional data to compare the kinematic regions where either colour octet or colour singlet contributions should dominate.

5.1.2 Acceptance of $\cos\theta^*$ with di-muon triggers

An important consideration for calculating the di-muon trigger efficiencies of J/ψ and Υ is the angular distribution of the decay angle θ^*, the angle between the direction of the positive muon (by convention) from quarkonium decay in the quarkonium rest frame and the direction of quarkonium itself in the laboratory frame (Figure 5.4), see Section 7.1 for more details).

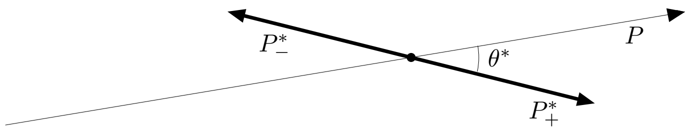

Figure 5.4: *Graphical representation of the θ^* angle used in the spin alignment analysis. The angle is defined by the direction of the positive muon in the quarkonium decay frame and the quarkonium momentum direction in the laboratory frame.*

The distribution in $\cos\theta^*$ is related to the relative contributions of the various production mechanisms (see Chapter 2) and is a necessary measurement to be able to determine the polarisation state of quarkonium, as of yet not understood. Crucially, Monte Carlo studies have shown that different production mechanisms (and thus different angular distributions) can have significantly different trigger acceptances, and without the measurement of the spin-alignment of quarkonium it will be difficult to be sure that the full trigger efficiency has been calculated correctly, and thus that the production cross-sections measured are correct.

In the absence of a comprehensive Monte Carlo generator capable of simulating all aspects of the theoretical quarkonium production models, we use the PYTHIA 6.403 [104]. Inevitably, this simulation is unable to reproduce adequately some features of the data, most notably the polarisation angle distributions and hadronic accompaniment of the quarkonium states. In the PYTHIA implementation the gluon emitted from the octet state has a phase space of 4 MeV (due to the corresponding invariant mass of the octet state being set at a dummy value of 3.1 GeV in PYTHIA), whereas theoretical predictions suggest that this value should be closer to $Mv_q \sim \mathscr{O}(1-3\ \text{GeV})$. In addition, due to the handling of production and decay of quarkonium in PYTHIA, there is no mechanism to allow information transfer of the spin-alignment of quarkonium between the production of a state and its eventual decay. Despite these limitations, we study polarisation effects by reweighting the output distributions from the generator before applying our trigger and reconstruction efficiencies and analysis techniques.

It can be shown that $\cos\theta^* \simeq 0$ corresponds to events with both muons having roughly equal transverse momenta, while in order to have $\cos\theta^*$ close to ± 1 one muon p_T needs to be very high while the other p_T is very low. In the case of a di-muon trigger, both muons from the J/ψ and Υ decays must have relatively large transverse momenta. Whilst this condition allows both muons to be identified, it also severely restricts acceptance in the polarisation angle $\cos\theta^*$, meaning that for a given p_T of J/ψ or Υ a significant fraction (up to 60% for particular quarkonium polarisation configurations) of the total cross-section is lost. With a di-muon trigger $\mu 6\mu 4$, events with large $|\cos\theta^*|$ are lost because of the p_T cut on the softer muon. Examples

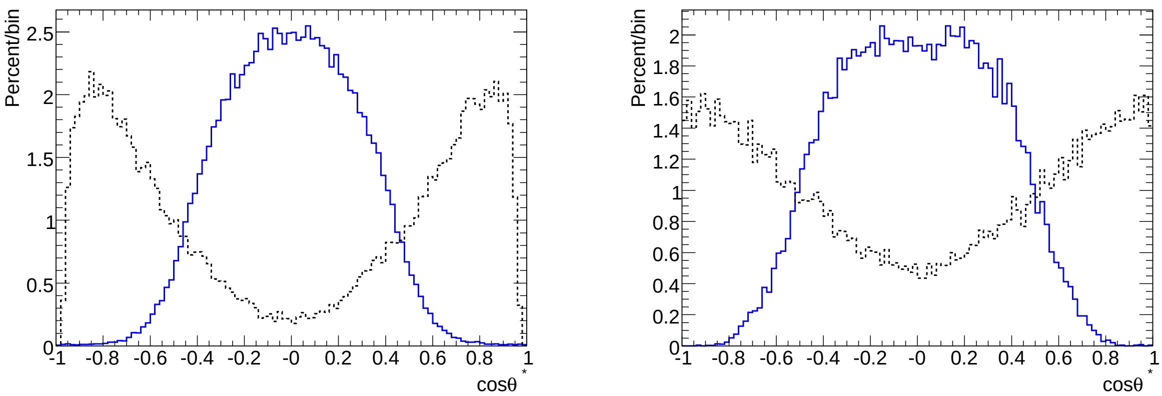

(a) J/ψ polarisation acceptance

(b) Υ polarisation acceptance

Figure 5.5: *Reconstructed polarisation angle distribution for $\mu 6\mu 4$ di-muon triggers (solid line) and a $\mu 10$ single muon trigger (dashed line), for (a) J/ψ and (b) Υ. The distributions are normalised to the unit area. The* true *distribution in both cases is flat.*

of the polarisation angle distributions for the MC simulated quarkonium events with a $\mu 6\mu 4$ trigger are shown by solid lines in Figure 5.5. The samples for both J/ψ and Υ were generated with zero polarisation, so with full acceptance the corresponding distribution in $\cos\theta^*$ should be flat, spanning -1 to $+1$. Clearly, narrow acceptance in $|\cos\theta^*|$ would make polarisation measurements difficult as one loses the ability to discriminate between the two extremes.

5.1.3 Single muon trigger

Another possibility for quarkonium reconstruction is to trigger on a single identified muon. The non-prescaled level-1 single muon trigger `L1_MU10` with a 10 GeV lower p_T threshold (referred to as the $\mu 10$ trigger in the following) is expected to produce manageable event rates at low luminosities [103]. Once this muon triggers the event, offline analysis can reconstruct the quarkonium by combining the identified muon with an oppositely-charged track in the event. The single muon trigger has an advantage over the di-muon trigger for polarisation studies, providing complementary acceptance in the polarisation angle compared to the di-muon triggered events, due to the event selection imposed by the high p_T single muon trigger effectively sub-selecting those events with one high p_T muon and one low p_T muon. The predicted cross sections for the single muon trigger are shown in Table 4.13.

By using a single muon trigger, one removes the trigger requirement of the other muon to have a large p_T. In this configuration, one has a ‘fast’ muon, which triggered the event, and one ‘slow’ (usually unidentified) muon, whose transverse momentum is only limited by the track reconstruction capabilities of ATLAS, with the threshold around 0.5 GeV [3], providing wider acceptance in the polarisation angle, thus the onium events with a single muon trigger typically have much higher values of $|\cos\theta^*|$, as illustrated by the dotted lines in Figure 5.5, complementing the di-muon trigger sample. So, the single- and di-muon samples may be used together to provide excellent coverage across almost the entire range of $\cos\theta^*$, and, crucially, in the same p_T range of onia.

An important consideration for onia reconstruction with a single muon trigger is the measured cross-section of both the quarkonium signal itself (which from Figures 4.5 and 4.9 can be seen to increase dramatically without a second muon requirement) and the backgrounds, which have much larger single muon cross-sections than the di-muon equivalents (see Section 4.9). The main background sources to quarkonium in this case are $K^\pm$ and $\pi^\pm$ decays in flight, $cc \to \mu X$ and $bb \to \mu X$. Out of these, the $bb \to \mu X$ process is expected to dominate in the area of interest $p_T(\mu) > 6$ GeV, with an estimated cross-section of 6.14 μb.

The single muon trigger cut of $p_T > 10$ GeV (the 'μ10' trigger) is advantageous as its rate is low enough for the trigger to not be prescaled, and reduces the combinatorial background under the J/ψ and Υ peaks. With this trigger, the cross section corresponding to the main background, $bb \to \mu X$, is about 1 μb, while the contribution of the 'signal' processes is about 23 nb for $pp \to J\psi X$ and 2.8 nb for $pp \to \Upsilon X$. Comparing with Section 4.9 it is already clear to see that the background rates are affected far more than the signal rates with this cut. It is worth noting that the di-muon and single muon samples have comparable cross sections and similar p_T dependence. They are not entirely independent however: at high transverse momenta the two samples have significant event overlap (see Table 4.13 for more details), which could be useful for independent calibration of muon trigger and reconstruction efficiencies.

5.2 Reconstruction and background suppression

In this section I discuss reconstruction performance for quarkonium based on both the $\mu 6 \mu 4$ di-muon trigger scenario (Section 5.2.1) and the μ10 single muon trigger scenario in Section 5.2.4. I present the expected reconstruction efficiencies, resolutions and acceptances for quarkonium at ATLAS and analysis of important backgrounds.

5.2.1 Quarkonium reconstruction with two muon candidates

In each event which passes the di-muon triggers described above, all reconstructed muon candidates are combined into oppositely charged pairs, of all candidates from combined, standalone and low p_T reconstruction algorithms and each of these pairs is analysed in turn. Truth-matching of reconstructed tracks is achieved using a η-ϕ match to the Monte Carlo truth, where the particle in the truth that has the correct PDG ID number and the closest match in $\Delta R = \sqrt{\Delta\eta^2 + \Delta\phi^2}$ is returned.

At ATLAS, muon candidates consist of tracks reconstructed in the Inner Detector, ID tracks tagged with muon spectrometer hits or simply standalone muons from the muon spectrometer.

The candidates are initially recorded by the trigger system described in Section 3.5. Once candidate muon pairs have been produced, their invariant mass is calculated and all muon pairs with a mass within 300 MeV of the J/ψ PDG mass are considered good candidates.

After this, the pairs are passed to the CTVMFT vertex fitter [123] where they are subject to an unconstrained vertex fit, which attempts to refit the tracks corresponding to the two muon candidates to a single vertex. For combined muons or tagged muons, the Inner Detector track corresponding to the muon track is used for vertexing as this generally has the more precise track parameters. Standalone muons simply use those muon spectrometer tracks for vertexing. For those pairs passing the trigger for which the vertex fit is successful (more than 99% forJ/ψ and 93% for Υ), the invariant mass is recalculated. If a good vertex fit is achieved, the pair is accepted for further analysis.

For those pairs failing the vertex fit one can look at the reconstructed Monte Carlo samples of direct quarkonium without any backgrounds to see why this was the case. It was found that real quarkonium that failed vertexing failed due to one or more badly measured track parameters of at least one of the muon tracks.

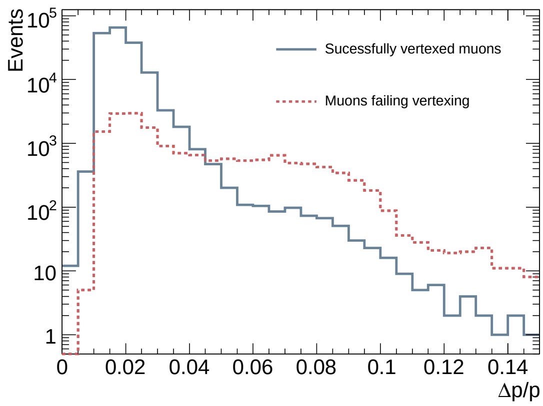

Figure 5.6: *Relative momentum error of muon pairs coming from quarkonium that pass (solid line) and fail (dashed line) vertex fits. All real quarkonium failing vertexing fits can be identified as having one or more large track parameter errors.*

Figures 5.6 and 5.7 show the error distributions of the five track parameters (p, θ, ϕ, d_0 and z_0). Errors on the two track parameters θ, ϕ are the most sensitive and cause the most

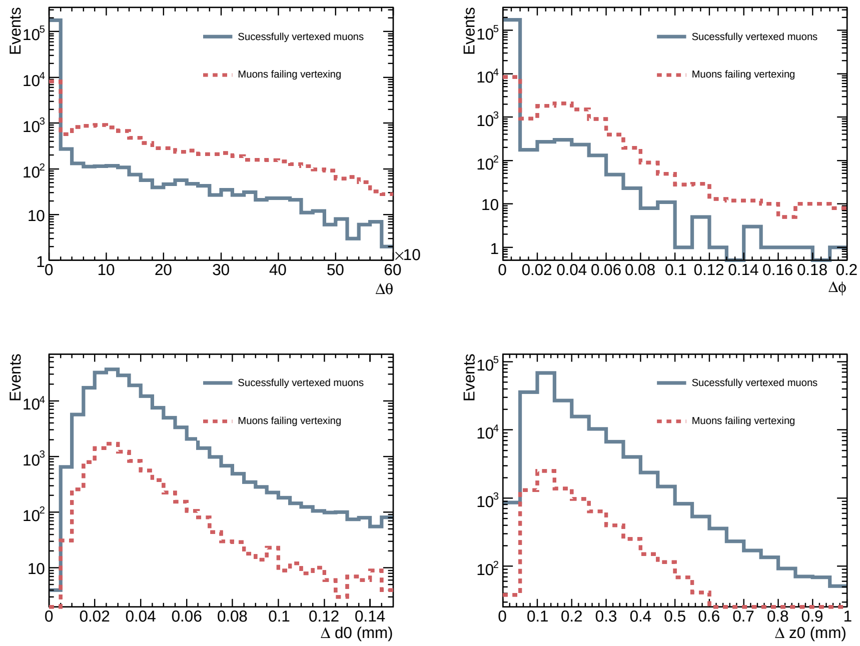

Figure 5.7: *Track parameter errors of muon pairs coming from quarkonium that pass (solid line) and fail (dashed line) vertex fits. All real quarkonium failing vertexing fits can be identified as having one or more large track parameter errors.*

significant effect on vertexing, although quarkonia can fail to be vertexed due to errors on the other parameters too.

If the invariant mass of the refitted tracks is within 300 MeV of the PDG mass in the case of J/ψ, or 1 GeV in the case of Υ, the pair is considered as a quarkonium candidate. The mass windows are chosen to be about six times the expected average mass resolution. These invariant mass distributions are plotted in Figure 5.8.

The invariant mass resolution depends on the pseudorapidities of the two muon tracks, due to differences in resolution of the detectors and extra material in different parts of the detector. To illustrate this effect, all accepted onia candidates are divided into three classes depending on η of the muons, and gaussian fits are performed to determine the resolutions and mass shifts. Here ‘Barrel’ refers to the region $|\eta| < 1.05$ and ‘Endcap’ refers to the region $1.05 < |\eta| < 2.7$. The results are presented in Table 5.1.

It is found that the mass resolution is the highest when both tracks are reconstructed in the

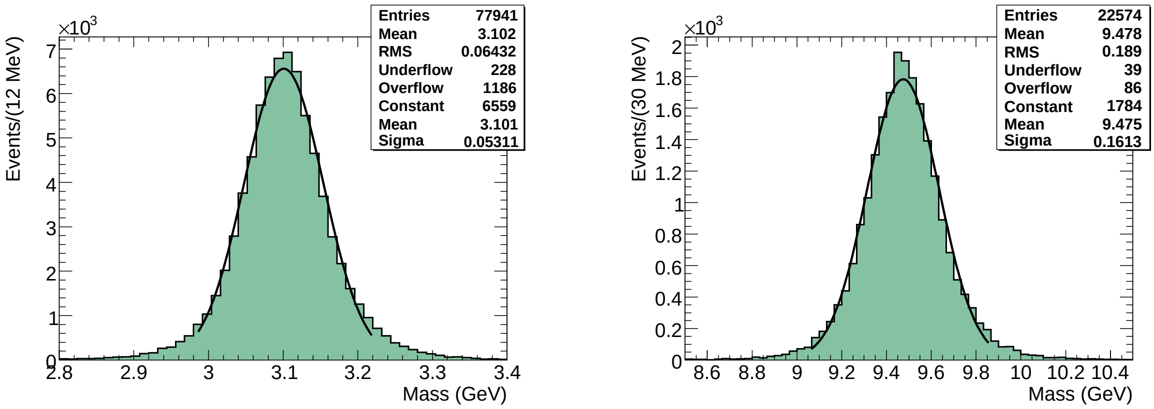

(a) $J/\psi(\mu\mu)$ (b) $\Upsilon(\mu\mu)$

Figure 5.8: *Reconstructed invariant mass for quarkonium candidates after the vertex fit.*

Quarkonium	$M_{\text{rec}} - M_{\text{PDG}}$, MeV	Resolution σ, MeV			
		Average	Barrel	Mixed	Endcap
J/ψ	$+5 \pm 1$	53	42	54	75
Υ	$+15 \pm 1$	161	129	170	225

Table 5.1: *Mass shifts and resolutions for di-muon invariant mass distributions after the vertex fit, for J/ψ and Υ candidates.*

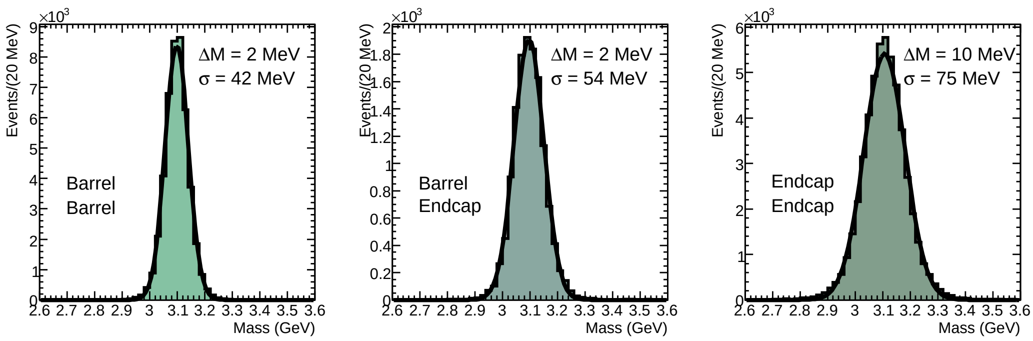

Figure 5.9: *Invariant mass plots highlighting mass shift and resolution of J/ψ invariant mass peak from direct J/ψ events split by η region of the two muons. 'Barrel' refers to the region $|\eta| < 1.05$ and 'Endcap' refers to the region $1.05 < |\eta| < 2.7$.*

barrel area, degrades somewhat if both tracks are reconstructed in the endcap region, and is close to its average value for the mixed η events. It should be noted that no significant non-gaussian tails are observed in either of these distributions, and the fit quality is good. Also shown in the table are the shifts of the mean reconstructed invariant mass from the respective PDG values (3097 MeV for J/ψ and 9460 MeV for Υ). The equivalent invariant mass distributions in the three η regions can be seen in Figure 5.9 for J/ψ and Figure 5.10 for Υ. The observed mass shifts are largely due to a problem with simulation of material effects in the endcap that were present in the datasets under study, a software problem that has since been understood and corrected.

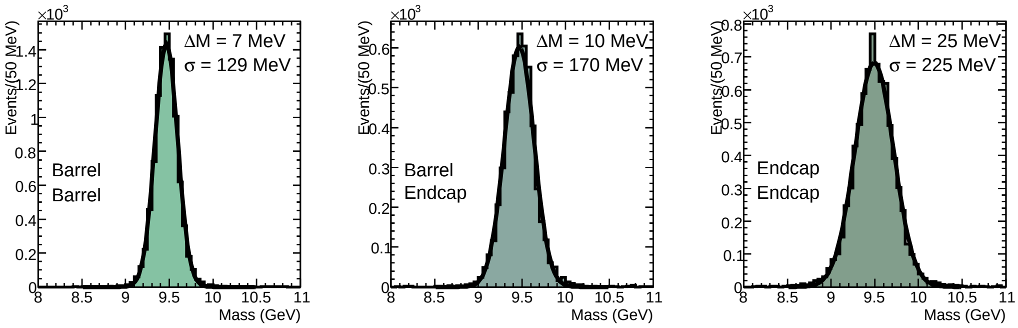

Figure 5.10: *Invariant mass plots highlighting mass shift and resolution of Υ invariant mass peak from direct Υ events split by η region of the two muons. 'Barrel' refers to the region* $|\eta| < 1.05$ *and 'Endcap' refers to the region* $1.05 < |\eta| < 2.7$.

Figure 5.11 shows the total energy loss experienced by muons coming from identified J/ψ candidates as a function of η. One can clearly identify here a reflection of the material description of the detector in Figure 3.6. We can also see why muons need to be of significant transverse momentum to be reconstructed in ATLAS: the average muon from a quarkonium decay, registered in the muon spectrometer, loses ~ 3.6 GeV of energy on its path through the detector. Those reconstructed muon pairs that remain after trigger selection, reconstruction and vertexing cuts are considered to be good quarkonium candidates and further analysis is done using these pairs only. The transverse momentum distributions of these candidates are shown in Figure 5.12.

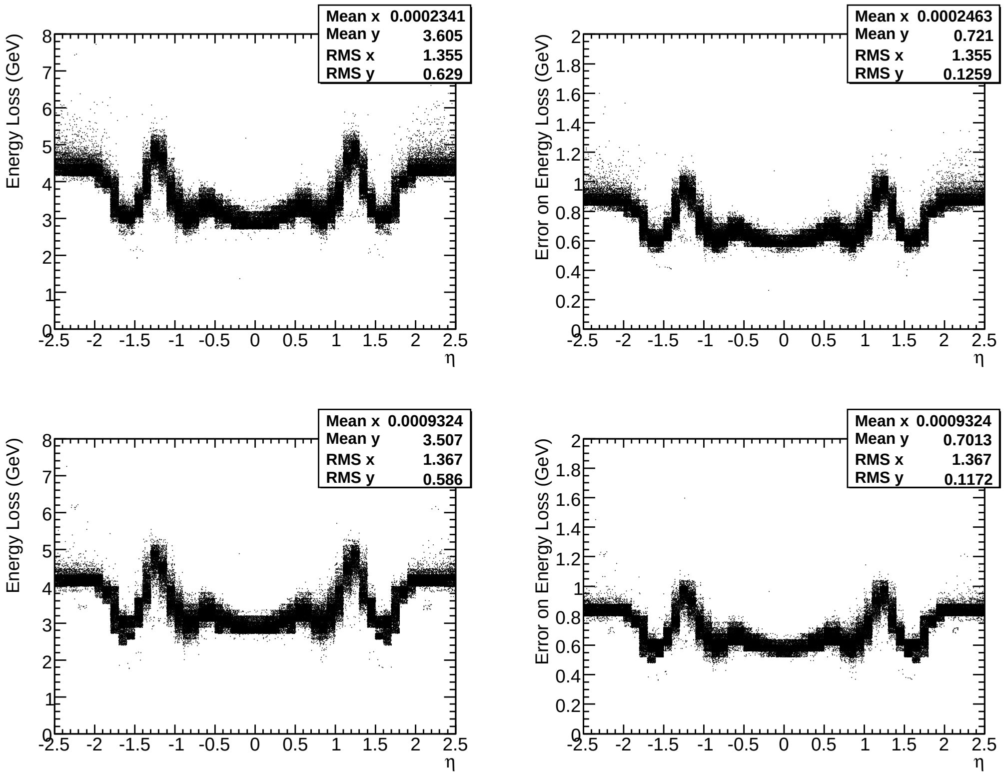

Figure 5.11: *Energy loss (and errors) of muons from J/ψ decays in ATLAS as a function of η (muons from Υ are not significantly different). The high p_T muon in the pair corresponds to the top row, the low p_T muon to the bottom row.*

As can be seen from the Figure 5.12(a), prompt J/ψ are mainly produced with p_T above around 10 GeV, simply as a consequence of the di-muon trigger cuts applied to the events. Some J/ψ are accepted past the trigger at lower p_T values but these are accepted due to the event being triggered by one or more muons not from the J/ψ itself, allowing the muons from the J/ψ to be accepted with lower p_T. We can remove any adverse consequences these additional J/ψ (and Υ) may have on our trigger and reconstruction efficiencies by placing an offline cut on the two muons in the pair, requiring that they both have an offline measured p_T larger than the thresholds in the trigger (in the di-muon case, one with 6 GeV and one with 4 GeV p_T).

The mean J/ψ p_T from events with a $\mu6\mu4$ trigger cut is 14.6 GeV. The statistical errors on this sample correspond to the number of events that will be produced within two weeks of early data-taking at low luminosity (assuming 10^{31} cm^{-2} s^{-1}).

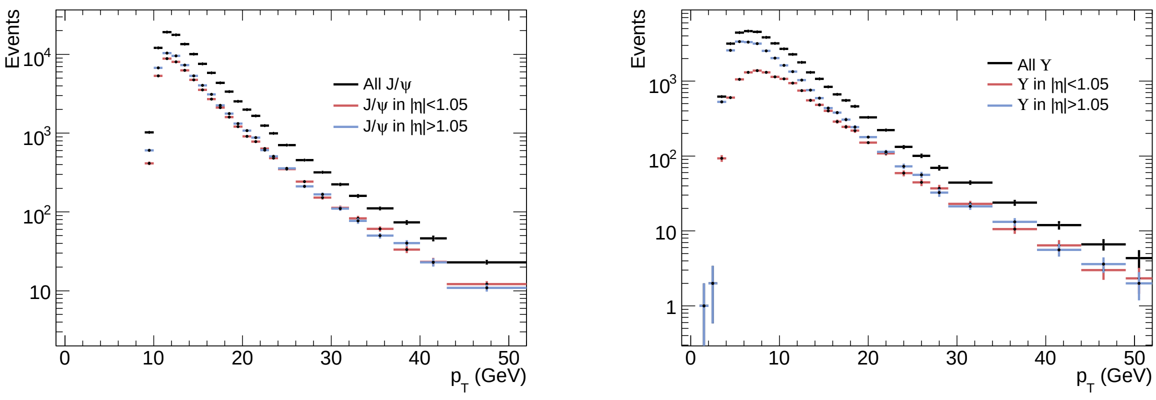

(a) J/ψ (b) Υ

Figure 5.12: *Transverse momentum distribution of triggered reconstructed quarkonium candidates, also separated into distributions for quarkonia found in the barrel and end-cap regions of the detector. Statistics shown in the figures correspond to integrated luminosities of about 6 pb^{-1} and 10 pb^{-1} for J/ψ and Υ, respectively.*

Systematic differences in the J/ψ invariant mass distribution were studied by sub-selecting those J/ψ in particular pseudorapidity and transverse momentum ranges. It was found that in the J/ψ p_T range available for study (around 9–25 GeV with sufficient statistics) the mass shift from the true mass and the overall mass resolution did not change in any significant way.

The decay kinematics of Υ is somewhat different due to its larger mass, thus allowing Υ to be produced with as low as 4 GeV p_T. The mean p_T of Υ produced in this sample is 9.6 GeV. Even at these relatively low statistics one expects to see significant numbers of both types of quarkonia at large p_T, which will allow statistically significant high-p_T analyses beyond the reach of the Tevatron.

Reconstruction acceptance varies significantly with p_T and η. Figure 5.13(a) presents the J/ψ acceptance as a function of the J/ψ transverse momentum, relative to the Monte Carlo generated dataset, which requires the two muons be in $|\eta| < 2.5$ and have transverse momenta greater than 6 and 4 GeV, respectively. These plots take into account geometric acceptance of the detector and reconstruction efficiency losses due to vertexing, as well as trigger efficiencies.

When J/ψ are produced with a transverse momentum above 10 GeV we see a sharp rise in the acceptance as J/ψ above this threshold are able to satisfy the muon trigger requirements

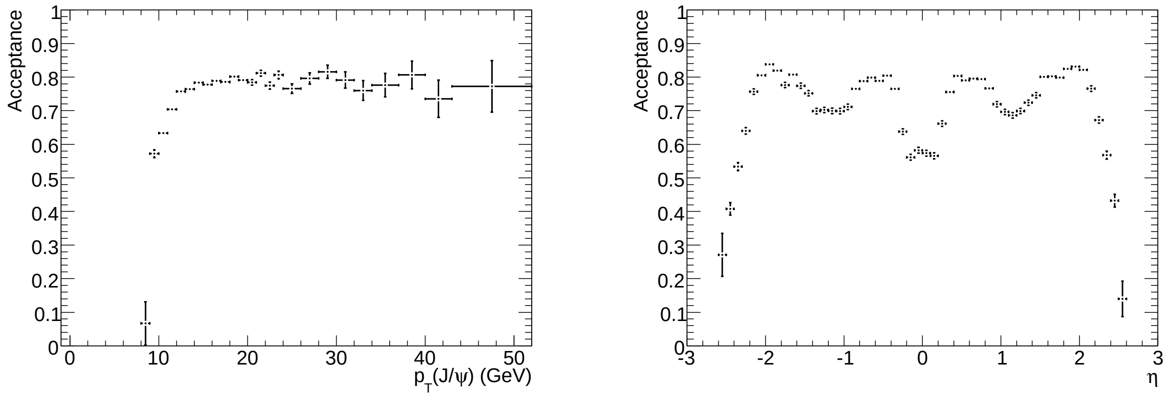

(a) J/ψ acceptance with p_T

(b) J/ψ acceptance with η

Figure 5.13: *Acceptance of reconstructed prompt J/ψ with J/ψ transverse momentum and pseudorapidity (relative to the MC generated dataset with $\mu 6 \mu 4$ cuts).*

within a certain kinematic configuration.

The structure in the plot of the η-dependence of J/ψ reconstruction efficiency, shown in Figure 5.13(b), highlights the configuration necessary in order for muons from the J/ψ to be able to pass the di-muon trigger. The distribution of reconstructed quarkonium candidates with the angular separation of the two muons, described by the variable $\Delta R = \sqrt{\Delta\phi^2 + \Delta\eta^2}$, is shown in Figure 5.14. On average, muons from reconstructed J/ψ ($\mu 6 \mu 4$) candidates are separated by $\Delta R \simeq 0.47$, and are restricted from being produced at separations larger than around 0.7.

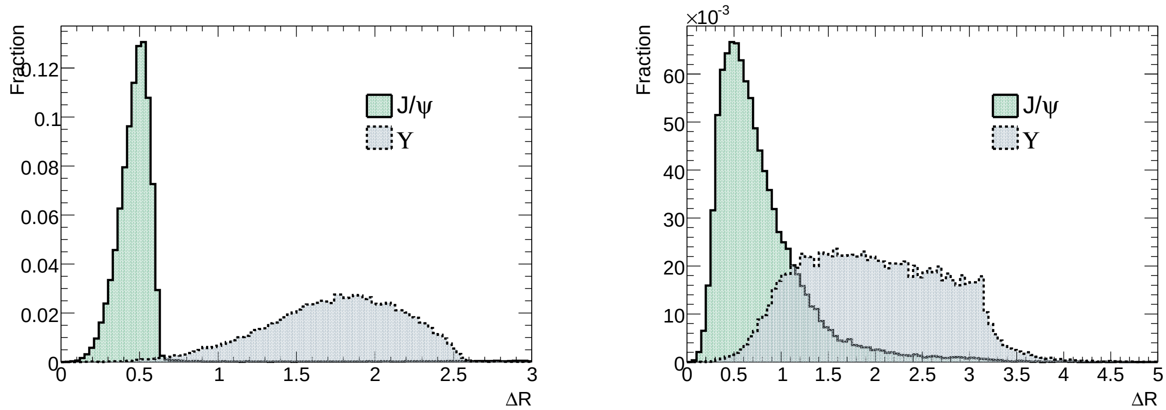

(a) ΔR with $\mu 6 \mu 4$ cuts

(b) ΔR with $\mu 10$ cuts

Figure 5.14: *Distribution of ΔR separation of the two muons from J/ψ and Υ candidates with di-muon $\mu 6 \mu 4$ generator-level cuts (left) and single muon $\mu 10$ cuts (right) applied.*

In comparison, the higher mass of Υ requires the muons in the $\mu 6\mu 4$ case to have much larger opening angle, with a broad distribution in ΔR peaking at around 1.8 and spanning up to 2.6. One can see that for the single $\mu 10$ case in Figure 5.14(b) the distributions are much broader, and generally with smaller separation in ΔR, reflecting the lower p_T constraint on the second muon.

The small separation of muons in ΔR for the J/ψ ($\mu 6\mu 4$) case has consequences for the J/ψ reconstruction efficiency as a function of pseudorapidity, shown in Figure 5.13(b). Significant dips in efficiency are seen near $\eta \pm 1.2$ and $\eta = 0$, due to the muon spectrometer layout (see Section 3.4 and reference [3]). As the muons from J/ψ are on average separated by only $\Delta R = 0.47$, they are subject to similar material and detector effects, and so these effects are carried over into the J/ψ reconstruction with very little smearing. Hence, this distribution has a similar shape to the individual muon reconstruction efficiency distribution in ATLAS.

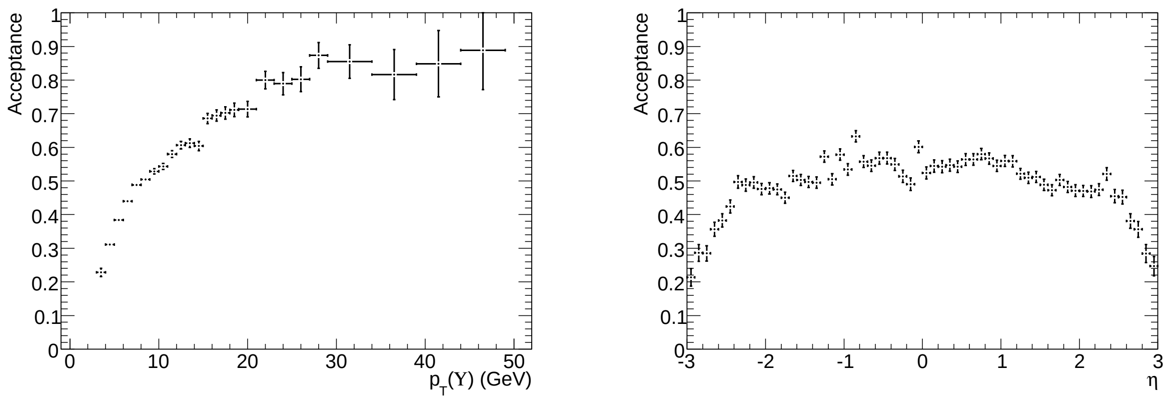

(a) Υ acceptance with p_T

(b) Υ acceptance with η

Figure 5.15: *Acceptance of reconstructed prompt Υ with transverse momentum and pseudorapidity of the quarkonium state (relative to the MC generated dataset with $\mu 6\mu 4$ cuts).*

This contrasts with the Υ reconstruction efficiency dependence on pseudorapidity, shown in Figure 5.15(b), which is much smoother than in J/ψ case: the two muons have large angular separation and the detector layout effects are smeared over a broader range of η values. Figure 5.15(a) shows the variation of acceptance with the Υ transverse momentum, and reflects the fact that with the $\mu 6\mu 4$ trigger Υ can be reconstructed with a lower p_T threshold. In the absence of a dedicated topological trigger for Υ, trigger efficiency at low p_T suffers due to the differing decay kinematics between J/ψ and Υ as only specialised J/ψ triggers exist in reconstruction software used in this analysis. At larger p_T both acceptances reach a similar plateau at around 80–85%.

Figure 5.16 shows an event display of an example of a prompt $J/\psi \rightarrow \mu^+\mu^-$ event triggered and reconstructed successfully from CSC simulated data samples. This is what a typical prompt J/ψ event is expected to look like in the ATLAS detector during early running, with no pileup.

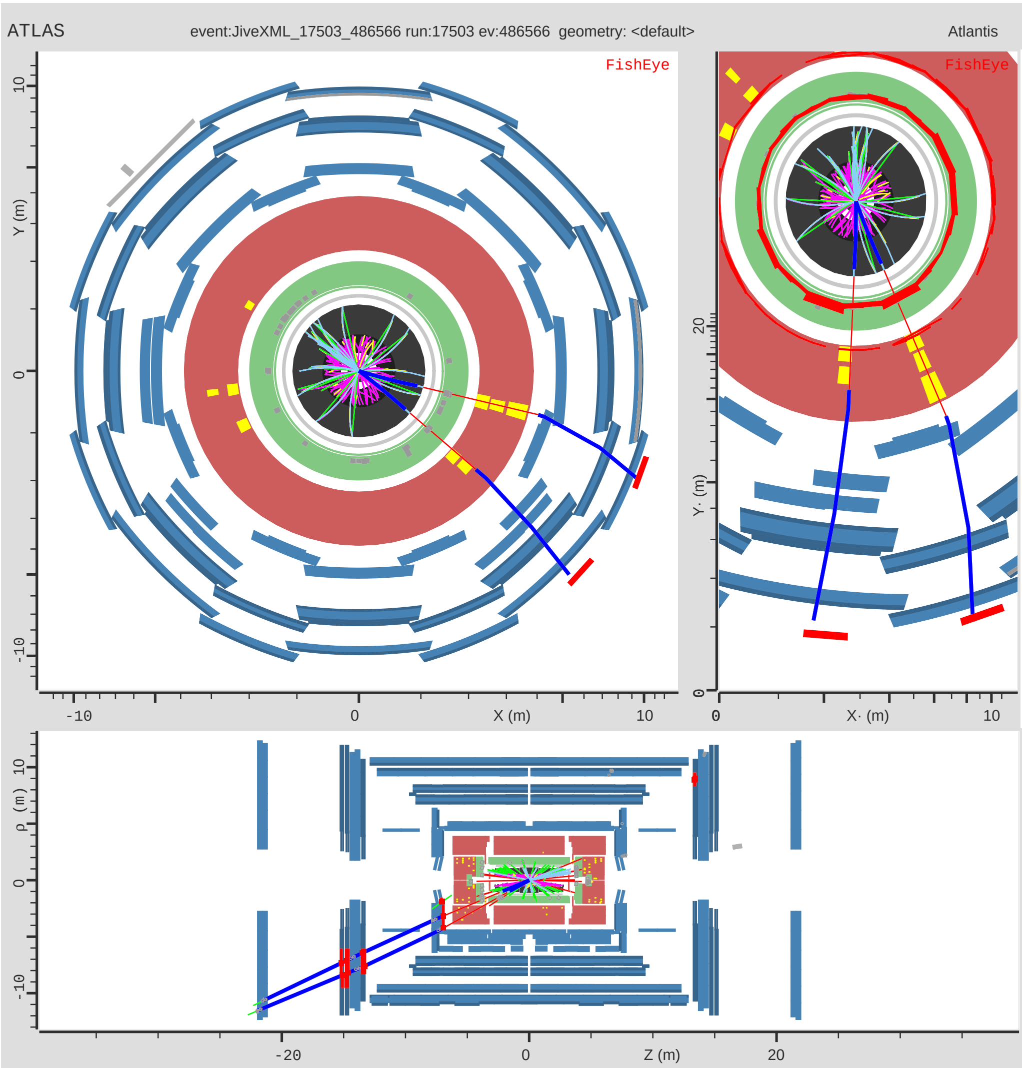

Figure 5.16: *An example of a $pp \rightarrow J/\psi(\mu\mu)$ event shown in the Atlantis [124] event display in an $X-Y$ (beampipe) and $X-Z$ (side) projection, along with an $X-Y$ projection focusing closely on the two muon tracks.*

Along with many other charged tracks, two muons can clearly be seen in the Inner Detector (white [Pixel], black [SCT] and grey [TRT] regions at the centre of the $X-Y$ projections, extending beyond the solenoid (white, grey line) traversing the electromagnetic calorimeter (green) before depositing some energy (yellow) in the hadronic calorimeter (red) before penetrating the muon spectrometer (blue). The highest p_T muon has 71 hits in the Inner Detector and has a measured track p_T of 7.70 GeV; it deposits 2.77 GeV of energy in the calorimeter and has an energy-corrected measurement in the spectrometer of 7.70 GeV also. The lower transverse momentum muon has 45 hits in the Inner Detector and measured p_T of 6.42 GeV. It deposits 1.24 GeV of energy in the calorimeter and is measured in the spectrometer with a transverse momentum of 6.42 GeV.

At the furthest reaches of the muon spectrometer in the $X-Y$ projection (and throughout in the $Y-Z$) can be seen red segments which represent the Level-1 muon trigger regions of interest. Note how they correspond to the offline identified muon tracks. The muon RoIs include a coarse measurement of the muon p_T, measuring the two muons to have transverse momenta of 10 GeV and 6 GeV.

5.2.2 Background suppression in the di-muon case

Following the successful reconstruction of quarkonium candidates, one would wish to understand the backgrounds and try to reduce them as much as possible for the purposes of physics analysis (see Chapter 7). The expected sources of background for prompt quarkonium with a di-muon $\mu6\mu4$ trigger are:

- Indirect J/ψ production from beauty decays;
- Continuum of muon pairs from beauty decays;
- Continuum of muon pairs from charm decays;
- Di-muon production via the Drell-Yan process;
- Decays in flight of $\pi^{\pm}$ and $K^{\pm}$ mesons.

The most important background contributions are expected to come from the decays $b \rightarrow J/\psi + X$, and the continuum of di-muons from $b\bar{b}$ events. Both of these have been simulated and analysed. The estimated total contribution from charm decays is higher than that from beauty decays. However, this background has not been simulated, as it is not expected to cause too many problems for prompt quarkonium reconstruction because the transverse momentum spectrum of the muons falls very steeply and the probability of producing a di-muon with an invariant mass within the range of interest is well below the level expected from beauty decays. Only a small fraction of the Drell-Yan pairs survive the di-muon trigger cuts of $\mu 6 \mu 4$ in the $J/\psi - \Upsilon$ mass range, which makes this background essentially negligible, as estimated from generator-level simulation. Muons from decays in flight also have a steeply falling muon momentum spectrum, and in addition require random coincidences with muons from other sources in the quarkonium invariant mass range. This is estimated to be at the level of a few percent of the signal rate, spread over a continuum of invariant masses.

All background di-muon sources mentioned above, apart from Drell-Yan pairs, contain muons which originate from secondary vertices, which makes it possible to suppress these backgrounds by removing such di-muons whenever the secondary vertex has been resolved.

5.2.3 Separation of prompt and indirect J/ψ

Once the two muons forming a candidate J/ψ are reconstructed, the radial displacement of the two-track vertex from the beamline is used to distinguish between prompt J/ψ, which have a pseudo-proper time of zero, and B-hadron decays into $J/\psi + X$ having an exponentially decaying pseudo-proper time distribution due to the non-zero lifetime of the parent B-hadrons. The pseudo-proper time is defined as

$$\text{Pseudo-proper time} = \frac{L_{xy} \cdot M_{J/\psi}}{p_T(J/\psi) \cdot c}, \tag{5.1}$$

where M_J/ψ and $p_T(J/\psi)$ represent the J/ψ invariant mass and transverse momentum, c is the speed of light in vacuum, and L_{xy} is the measured transverse decay length (the distance in the transverse $x-y$ plane traversed by the J/ψ from the primary vertex). The pseudo-proper time (rather than the proper time) is used because of its better resolution. The proper-time calculation requires use of the 3D decay length L_{xyz}, which has a worse resolution than L_{xy}.

The dependence of the resolution in radial decay length L_{xy} on di-muon pseudorapidity η is shown in Figure 5.17. The resolution is stable at around 125 μm in the barrel region, but gradually degrades, peaking at around 160 μm in the high η region (see Section 6.1 for more details of secondary vertex resolution studies of the ATLAS Inner Detector). The variation of the resolution in the pseudo-proper time with di-muon p_T is shown in Table 5.2. Here a perfect detector alignment is assumed, with the resulting average resolution estimated at around 0.1 ps.

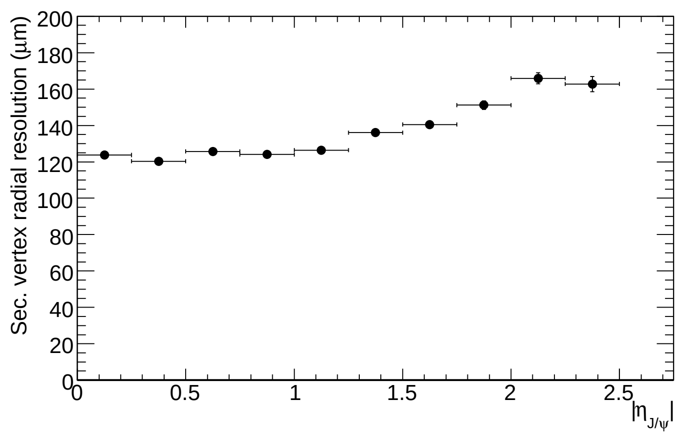

Figure 5.17: *Radial position resolution of secondary vertex for J/ψ decays as a function of the J/ψ pseudorapidity.*

Figure 5.18 illustrates the pseudo-proper time distribution for both the prompt and indirect J/ψ samples. Note the distinctive long positive pseudo-proper time tail of J/ψ candidates from b-decays.

By making a cut on the pseudo-proper time, one can efficiently separate most of the indirect J/ψ from a prompt J/ψ sample (or vice-versa). The efficiency and purity of the pseudo-proper time cuts for prompt J/ψ and indirect J/ψ are presented in Figures 5.19(a) and 5.19(b) respectively. Here, we define purity for direct J/ψ as the ratio of the total number of direct J/ψ

J/ψ transverse momentum (GeV)	$9-12$	$12-13$	$13-15$	$15-17$	$17-21$	>21
Pseudo-proper time resolution (ps)	0.107	0.103	0.100	0.093	0.087	0.068

Table 5.2: *Pseudo-proper time resolution of direct J/ψ events as a function of J/ψ p_T.*

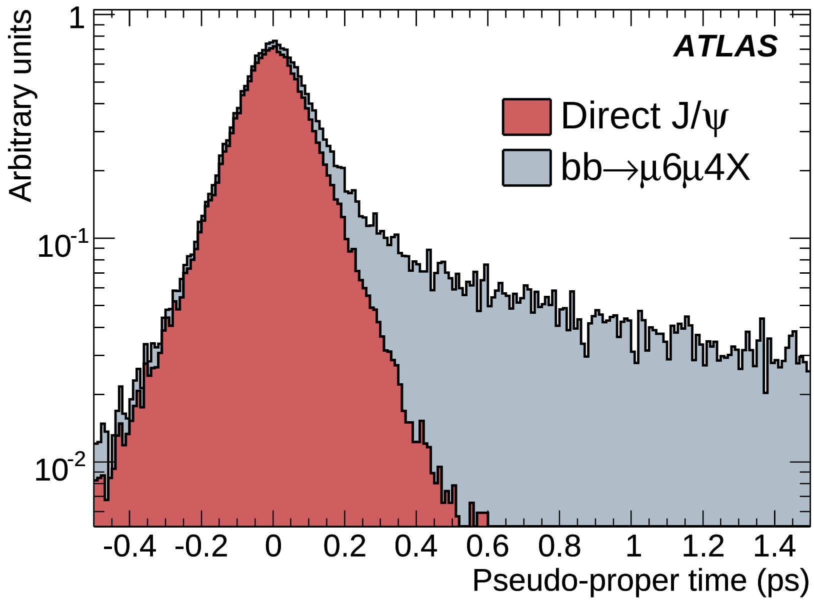

Figure 5.18: *Pseudo-proper time distribution for reconstructed prompt J/ψ (dark red shading) and the indirect B-decay J/ψ candidates (light grey shading).*

candidates retained below a particular pseudo-proper time cut, t, and the total number of events.

$$\text{Purity}(<t) = \frac{N_{J/\psi}(<t)}{N_{\text{Events}}(<t)} \tag{5.2}$$

For purity of the indirect J/ψ candidates, we use the same definition but with a reversal in the direction of the cut, retaining only those *above* a certain cut t.

We define efficiency as the number of direct J/ψ candidates retained below a certain cut value and the total number of direct J/ψ candidates in the sample.

$$\text{Efficiency}(<t) = \frac{N_{J/\psi}(<t)}{N_{J/\psi}} \tag{5.3}$$

Again, the direction of the cut is reversed for the indirect J/ψ case. A pseudo-proper time cut

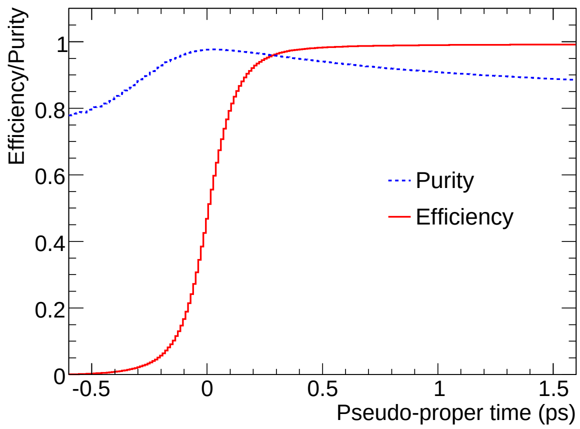

(a) Prompt J/ψ candidates

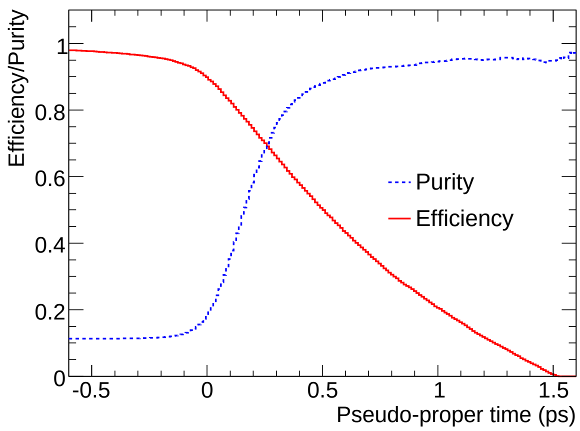

(b) Indirect J/ψ candidates

Figure 5.19: *Efficiency (solid line) and purity (dotted line) for (a) prompt J/ψ candidates and (b) indirect J/ψ candidates as a function of the pseudo-proper time cut.*

of less than 0.2 ps allows one to retain prompt J/ψ with the efficiency of 93% and the purity of 97%, or conversely (Figure 5.19(b)) indirect J/ψ with efficiency of 75% with 61% purity (cuts can be optimised for whatever sample is required; here we choose them for high direct J/ψ efficiency and purity, different cuts may be used for study of B-decays). Note that the distribution shown in Figure 5.18 is, in a sense, self-calibrating; the left slope can be used to determine the resolution σ, and an appropriate cut of 2σ can be applied to remove the “tail” of secondary J/ψ candidates on the right hand side.

The background levels of beauty and Drell-Yan production under the Υ peak are similar to those for the J/ψ, except that here one does not have to contend with sources of non-prompt quarkonia from B-decays. However, the $bb \to \mu6\mu4$ background continuum under the Υ is more problematic: higher invariant masses around the Υ mean that the two triggered muons will necessarily come from two separate decays, meaning that the pseudo-proper time cut is far less effective.

Fortunately, flags associated to individual reconstructed muon tracks provide further vertexing information, which could be used for suppressing of the $bb \to \mu6\mu4$ continuum background. Reconstructed tracks are assigned to either come from the primary vertex, a secondary vertex, or are left undetermined. By requiring that both of the muons, combined to make a J/ψ or a Υ candidate, are determined to have come from the primary vertex, background from the $bb \to \mu6\mu4$ continuum can be reduced by a factor of three or more, whilst reducing the number of signal events by around 5% in both cases.

As for the J/ψ, prompt Υ have a proper time distribution centred about zero. However, unlike the J/ψ case where both muons are likely to come from the same B-decay, higher invariant masses around the Υ mean that the two triggered muons will necessarily come from two separate decays. This means that the transverse decay length of the vertexed muons (and hence the proper time) is centred about zero as for the signal and has the same positive and negative range.

Again, as for the J/ψ, individual muon vertexing flags can be used, requiring that both muons in the candidate pair are flagged as having come from the primary vertex. We find that along with the proper time cut this again reduces the continuum under the Υ by a factor of three without significant reduction of the Υ signal itself, to the situation displayed in Figure 5.20, which illustrates the quarkonium signal and main background invariant mass distributions in the mass range $2-12$ GeV, for those events which satisfy the $\mu6\mu4$ trigger requirements, with reconstruction efficiencies and background suppression cuts taken into account.

Peaks from the J/ψ and $\Upsilon(1S)$ clearly dominate the background. As no higher ψ and Υ states were simulated for this analysis, their peaks are not shown. The dotted line indicates the

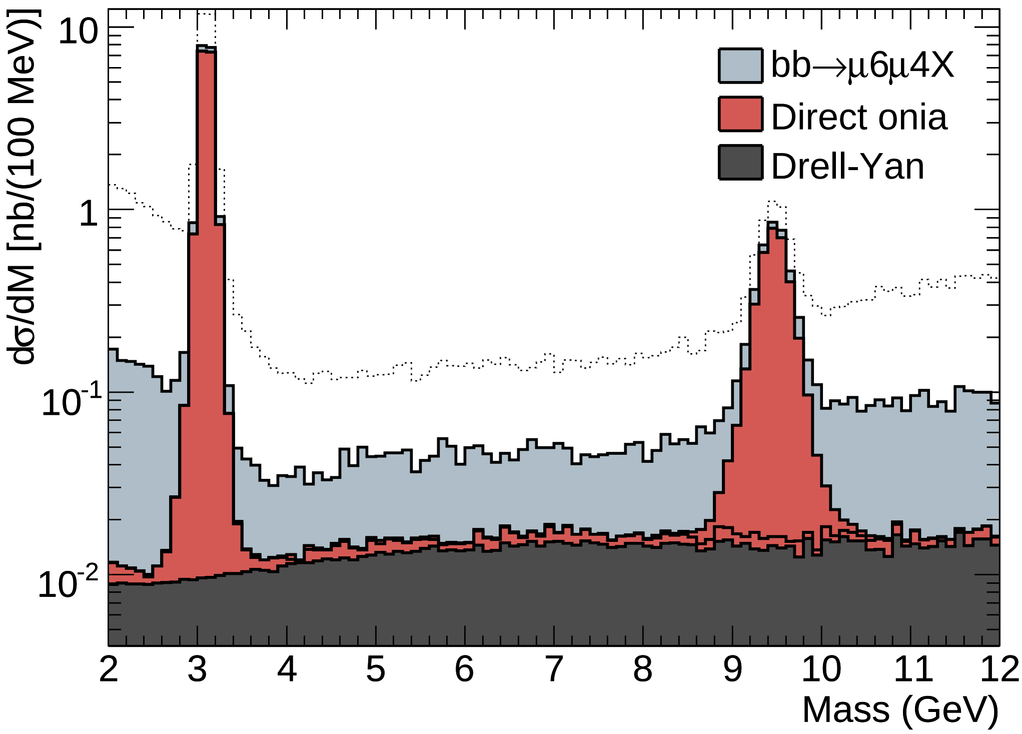

Figure 5.20: *Sources of low invariant mass di-muons, reconstructed with a $\mu6\mu4$ trigger, with the requirement that both muons are identified as coming from the primary vertex and with a proper time cut of 0.2 ps. The light dotted line highlights the background level before vertexing cuts. The tail of the J/ψ peak extending under the Υ peak represents the combinatorial background from prompt J/ψ events that fall inside the Υ mass window.*

level of the background continuum before the vertexing cuts. In conclusion, we find that the level of the backgrounds considered for both J/ψ and Υ do not represent any serious problem for reconstruction and analysis of direct quarkonia with the di-muon $\mu6\mu4$ trigger.

5.2.4 Reconstruction and backgrounds with a single muon candidate

By using the $\mu10$ trigger, one selects events with at least one identified muon candidate with a p_T above 10 GeV. In this part of the analysis, each reconstructed single muon candidate is combined with oppositely-charged *tracks* reconstructed in the same event. The identified muon candidate must have a $p_T > 10$ GeV. For both J/ψ and Υ reconstruction, we insist that any other reconstructed track to be combined with the identified trigger muon has an opposite electric charge and is within a cone of $R = 3.0$ around the muon direction, so as to retain over 99% (91%) of the signal events in the J/ψ (Υ) case. We require that the invariant mass of the muon+track pair is above 2.5 GeV for J/ψ candidates and above 7 GeV for Υ candidates to limit the combinatorics to be considered. No upper invariant mass cut is imposed.

As in the di-muon analysis, we require that both the identified muon and the track are flagged as having come from the primary vertex. In addition, we impose a cut on the transverse impact parameter d_0. We require that $|d_0| < 0.04$ mm for the identified muon and $|d_0| < 0.10$ mm for the track, in order to further suppress the number of background pairs from B-decays, which have a somewhat broader impact parameter distribution than prompt decays.

The invariant mass distribution for the remaining pairings of a muon and a track is shown in Figure 5.21(a) for J/ψ p_T larger than 9 GeV and in Figure 5.21(b) for J/ψ p_T larger than 17 GeV. The distributions are fitted using a single gaussian for the signal and a straight line for the background. Clear J/ψ peaks can be seen, with mass shifts of $\Delta M = 1 \pm 1$ MeV and resolution of $\sigma = 50$ MeV above 9 GeV, and a mass shift of $\Delta M = 2 \pm 1$ MeV and resolution of $\sigma = 54$ MeV above 17 GeV, similar to that in the di-muon sample. We choose these two points, at the extremes of the p_T range accessible with the given statistics, to illustrate the effect of increasing the transverse momentum cuts.

The large tails from the MC J/ψ sample in Figure 5.21(a) (not so significant in Figure 5.21(b)) is due to the additional combinatorial background present in the true direct J/ψ events (red) themselves. Note that as we impose higher p_T requirements, the contribution of combinatorial background in events with true J/ψ decays significantly decreases. It is worth noting that the overall signal-to-background ratio around the J/ψ peak improves slightly with increasing transverse momentum of J/ψ, and at higher p_T the $\cos\theta^*$ acceptance also becomes broader, which should help independent polarisation measurements.

For Υ the situation is less favourable, due to the combination of a lower signal cross section and a higher background. Figure 5.21(c) shows the expected invariant mass distribution in the Υ mass region after applying the cuts described above, for the Υ transverse momenta above 17 GeV. In this area the $\cos\theta^*$ distribution for Υ becomes flat with broad acceptance, but the

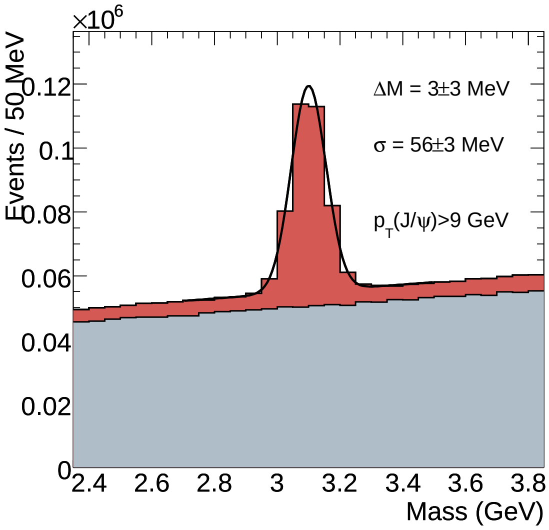

(a) J/ψ @ 9 GeV p_T

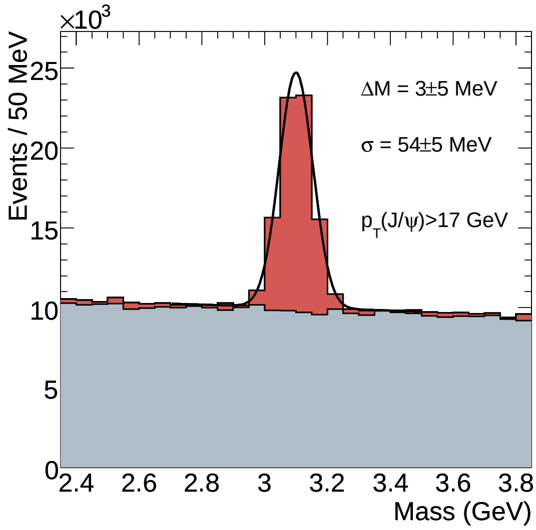

(b) J/ψ @ 17 GeV p_T

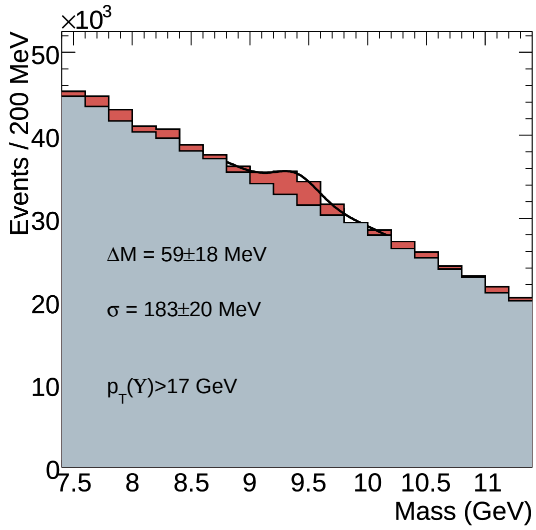

(c) Υ @ 17 GeV p_T

Figure 5.21: *Prompt quarkonium signal and $bb \to \mu X$ background events selected with the $\mu 10$ trigger, in the mass range around (a) J/ψ with p_T above 9 GeV, (b) J/ψ with p_T above 17 GeV, and (c) Υ with p_T above 17 GeV, corresponding to 10 pb^{-1} of data. We do not consider study of the Υ resonance with lower p_T cuts due to the increased background from B-decays at lower momenta. The background from B decays is shown in grey. Cuts described in the text have been applied.*

background from beauty decays clearly dominates. Although the Υ peak can be seen above the smooth background, its statistical significance is rather low. Hence, with an analysed dataset corresponding to the integrated luminosity simulated in this study, the use of the single muon sample for Υ cannot be justified, and in the following we will only rely on the di-muon sample.

In conclusion, we expect that the single muon trigger with a 10 GeV threshold can be successfully used to select prompt J/ψ events. The expected background here, although much larger than in di-muon case, is well under control. For Υ however, the single muon sample is only likely to be useful at significantly higher statistics and higher transverse momenta.

5.3 Summary of cuts and efficiencies

Table 5.3 summarises the efficiencies of all the selection and background suppression cuts described above, for both the single and di-muon trigger samples.

	Quarkonium Trigger type	J/ψ $\mu 6 \mu 4$	J/ψ $\mu 10$	Υ $\mu 6 \mu 4$	Υ $\mu 10$
	MC cross section	23 nb	23 nb	5.2 nb	2.8 nb
ε_{L1}	Level 1 trigger	86.6%	*96%*	83.7%	*96%*
ε_{L2}	Level 2 trigger	96.6%	*>99%*	66.1%	*>99%*
ε_{Rec}	Reconstruction	89.2%	*96%*	92.5%	*96%*
ε_{Vtx}	Vertex fit	99.9%	*99%*	99.9%	*99%*
ε_1	$\varepsilon_{L1} \cdot \varepsilon_{L2} \cdot \varepsilon_{Rec} \cdot \varepsilon_{Vtx}$	74.5%	*90%*	51.1%	*90%*
ε_{t0}	Pseudo-proper time cut	93.2%	*93%*	n/a	n/a
ε_{Flg}	Only primary vertex tracks	96.4%	92%	94.9%	*92%*
$\varepsilon_{\Delta R}$	Second track inside cone	n/a	99%	n/a	91%
ε_{d0}	Impact parameter cut	n/a	90%	n/a	90%
ε_2	$\varepsilon_{t0} \cdot \varepsilon_{Flg} \cdot \varepsilon_{\Delta R} \cdot \varepsilon_{d0}$	89.8%	76%	94.9%	75.3%
ε	Overall efficiency $\varepsilon_1 \cdot \varepsilon_2$	67%	69%	49%	68%
	Observed signal cross section	15 nb	16 nb	2.5 nb	2.0 nb
	N_S for 10 pb^{-1}	150,000	160,000	25,000	20,000
	N_B in mass window for 10 pb^{-1}	7000	700,000	16,000	2,000,000
	Signal/Background at peak	60	1.2	10	0.05

Table 5.3: *Predicted and observed cross-sections for prompt vector quarkonia, and efficiencies of various selection and background suppression cuts for both the single and di-muon scenarios described in this chapter.*

Not all cuts are applicable to all samples; those which are not are labelled “n/a” accordingly. The efficiencies for $\mu6\mu4$ samples are calculated relative to MC samples generator level cuts requiring two muons of p_T 6 and 4 GeV. For the $\mu10$ samples, a cut of 10 GeV was applied to the p_T of the fastest muon.

Expected yields N_S of quarkonia for 10 pb^{-1} are given at the bottom of the table, along with background yields N_B within the invariant mass window of ±300 MeV for J/ψ and ±1 GeV for Υ, and the signal-to-background ratios at respective J/ψ and Υ peaks for each sample. For excited quarkonium states with vector quantum numbers the efficiencies are expected to be similar, but not necessarily identical. The biggest differences are expected for ψ', where the production mechanisms as well as decay kinematics are significantly different. One should recall that the yields expected in the single muon and di-muon datasets are partially overlapping, so the total number of independent events triggered in ATLAS will be less than simply the sum of the single and di-muon yields. See Table 4.13 for further details.

"Any sufficiently advanced technology is indistinguishable from magic."

Arthur C. Clarke

6

Quarkonium as a performance and monitoring tool

Due to the high predicted rate and clean signature (to di-muons) of quarkonium at ATLAS, the J/ψ and Υ form useful tools for a wide range of studies of detector performance and data quality monitoring activities, once reconstructed and passed through the event selection process described in Chapter 5. In this chapter I outline a selection of studies conducted with ATLAS early data-taking in mind.

6.1 Secondary vertex resolution from prompt charmonium

Secondary vertex identification and resolution is a central component of Inner Detector tracking in ATLAS, crucial for particle reconstruction and identification. Calculating the secondary vertex resolution from B-decays requires determining the resolution of the $L_{xy}(reco) - L_{xy}(true)$ residual distribution, which, although possible in Monte Carlo simulations, requires detailed knowledge of the B-hadron admixture in LHC collisions in order to deconvolve the various lifetimes from the intrinsic detector resolution.

A more straightforward and largely self-calibrating way of determining the secondary vertex resolution is to consider the decays of prompt J/ψ . Prompt J/ψ have a true transverse (or radial) decay length of identically zero and as such (as shown in Figure 5.18), the residual radial decay length distribution of reconstructed J/ψ can be determined directly from the prompt L_{xy} distribution resolution. This in itself can be extracted from the negative L_{xy} sample (as the purity of prompt J/ψ is particularly high there), or better still, by extracting the gaussian prompt component from the inclusive decay lifetime.

From the reconstructed datasets considered in Chapter 5, we subselect prompt J/ψ candidates and consider these for determination of the secondary vertex resolution. We use the Inner Detector tracks associated with the reconstructed muons for determination of the ID vertex performance. This excludes the presence of standalone muon tracks. We fit a single gaussian to the core of the reconstructed transverse decay length distribution in slices of $\Delta\eta = 0.4$ (and one slice of $\Delta\eta = 0.5$) from $|\eta| = 0 - 2.5$. The residual distributions can be seen in Figure 6.1.

$\lvert\eta\rvert$ slice	$0.0-0.4$	$0.4-0.8$	$0.8-1.2$	$1.2-1.6$	$1.6-2.0$	$2.0-2.5$
$\sigma_{68.3\%}$ (μm)	106	106	105	119	136	160
$\sigma_{95.0\%}$ (μm)	133	133	130	143	157	178

Table 6.1: *Secondary vertex resolutions as a function of absolute pseudorapidity of the J/ψ corresponding to data in Figure 6.1, comparing fits made with 68.3% and 95% coverage as a measure of gaussianity of the distributions.*

To these residual distributions we first fit a gaussian encompassing 68.3% of the data, and another with 95% coverage (corresponding to one and two sigma fit coverage) to ascertain the

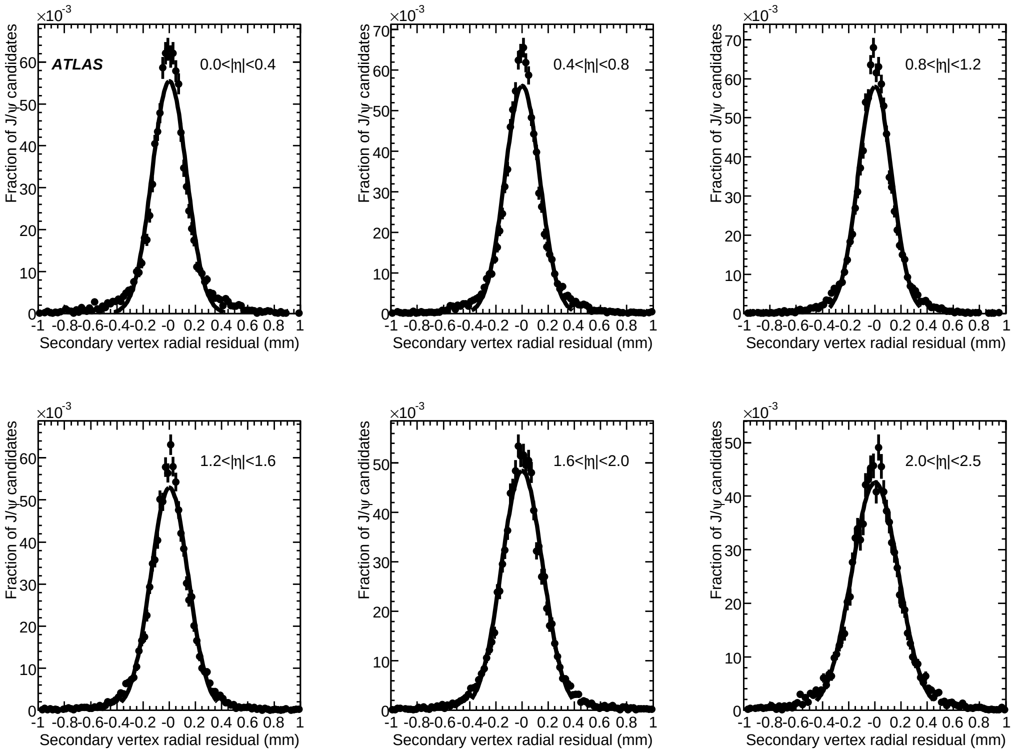

Figure 6.1: *Secondary vertex radial residuals in $J/\psi \rightarrow \mu^+\mu^-$ decays in slices of $|\eta|$.*

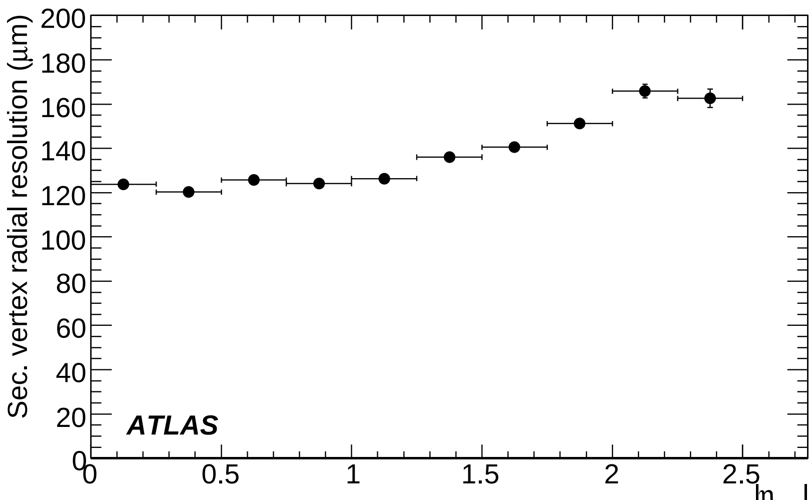

Figure 6.2: *Expected resolution on radial position of secondary vertex from prompt $J/\psi \rightarrow \mu^+\mu^-$ decays, as a function of absolute pseudorapidity of the J/ψ.*

resolution and gaussianity of these distributions. Table 6.1 shows the resolutions obtained from these fits and Figure 6.2 shows the dependence of the secondary vertex resolution on the $|\eta|$ of the J/ψ using the two-sigma coverage fits. By doing this we can determine how gaussian these residual distributions are, and in doing some obtain some measure (in various variables) of these distributions 'gaussianity' by the discrepancy between the one and two sigma fits.

We see some variation of the resolution with $|\eta|$, increasing as we move into the endcap region, but also see the gaussianity of the distribution improves as we increase in η (reflected in the convergence of resolutions obtained with the 68.3% and 95% coverage fits). Long tails that spoil gaussianity come from low quality reconstructed tracks, so one can see that although vertexing performance decreases in the endcap, the overall track residual distribution becomes more gaussian.

The secondary vertex resolution was also found to vary as a function of the transverse momentum of the J/ψ. Figure 6.3 shows the residual distributions in p_T slices chosen to contain approximately similar statistics of J/ψ events. The corresponding resolutions for 68.3% and 95% coverage are shown in Table 6.2.

$p_T(J/\psi)$ (GeV) slice	$9-12$	$12-13$	$13-15$	$15-17$	$17-21$	>21
$\sigma_{68.3\%}$ (μm)	104	116	122	128	131	144
$\sigma_{95.0\%}$ (μm)	129	139	145	152	163	183

Table 6.2: *Secondary vertex resolutions as a function of J/ψ p_T corresponding to data in Figure 6.3, comparing fits made with 68.3% and 95% coverage as a measure of gaussianity of the distributions.*

The resolution variation with transverse momentum is only significant at low p_T, but this effect is caused not by an intrinsic increase in resolution of low p_T tracks but from the diluted effect of η constraints on the muons from the decay in low p_T J/ψ. As the kinematics of the decay clearly plays an important role in the secondary vertex resolution, studies were conducted to isolate a sample of J/ψ decays where the effect on vertex resolution could be seen most strongly.

Rather than considering the quarkonium transverse momentum, we investigate the muon transverse momentum, a variable more closely related to ID performance. Specifically I inves-

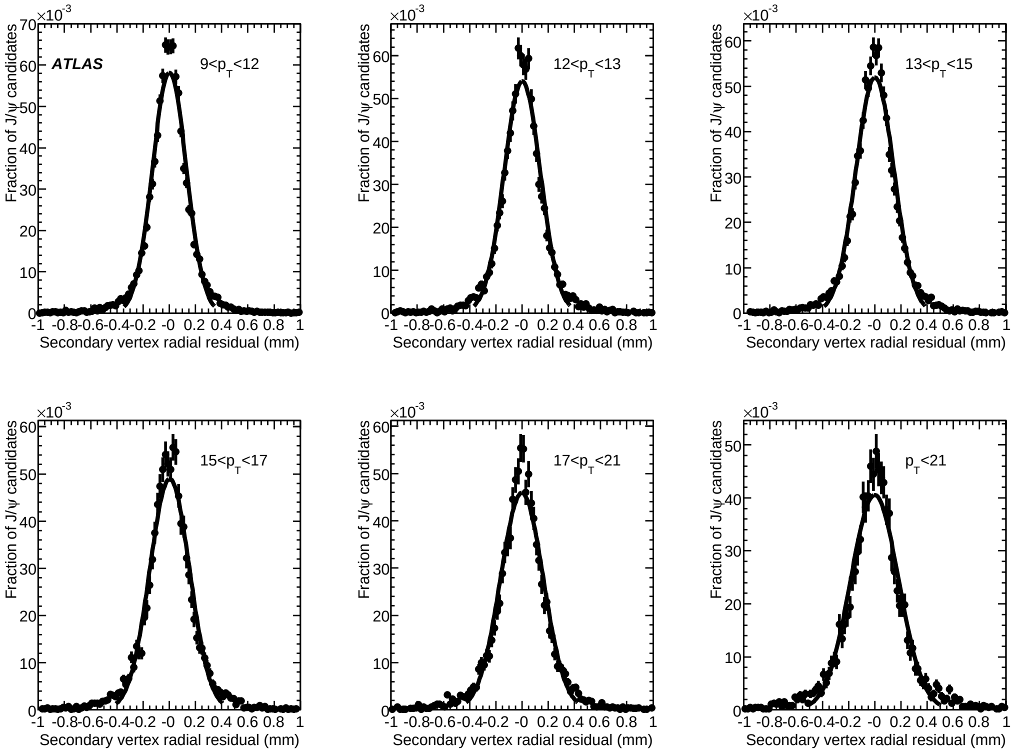

Figure 6.3: *Secondary vertex radial residuals in $J/\psi \to \mu^+\mu^-$ decays in slices of J/ψ transverse momentum in units of GeV.*

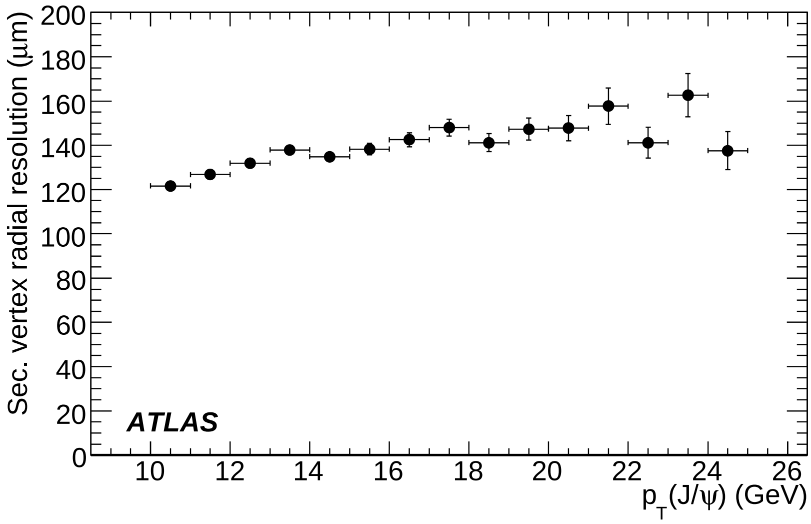

Figure 6.4: *Expected resolution on radial position of secondary vertex from prompt $J/\psi \to \mu^+\mu^-$ decays, as a function of transverse momentum of the J/ψ.*

tigated whether the p_T difference between the two muons in the decay had any significant effect on the resolution.

Table 6.3 shows the resolutions obtained with the one and two sigma fit coverages for events with Δp_T greater and less than 2 GeV (an average p_T difference in the sample). An increase was seen, but as the dependence was not strong as the variation between the two samples was less than seen in other variables, indicating the real effect was being diluted across the samples.

$\Delta p_T(\mu_1, \mu 2)$ slice	< 2 GeV	> 2 GeV
$\sigma_{68.3\%}$ (μm)	106	126
$\sigma_{95.0\%}$ (μm)	108	136

Table 6.3: *Secondary vertex resolution of $J/\psi \rightarrow \mu^+\mu^-$ decays with p_T difference between the two muons in the decay, comparing fits made with 68.3% and 95% coverage as a measure of gaussianity of the distributions.*

The η difference between the two muons did show significant effects on the vertex resolution. Table 6.4 and Figure 6.5 and show the resolutions in three $\Delta\eta_\mu$ slices (the η difference distribution is narrow in J/ψ decays due to kinematic restrictions imposed by the trigger – see Section 5.2.1 for more details).

Muon $\|\eta\|$ slice	$0.0 - 0.2$	$0.2 - 0.4$	$0.4 - 0.6$
$\sigma_{68.3\%}$ (μm)	96	123	163
$\sigma_{95.0\%}$ (μm)	114	150	188

Table 6.4: *Secondary vertex resolutions as a function of η difference between the two muons in the $J/\psi \rightarrow \mu^+\mu^-$ decay corresponding to data in Figure 6.5, comparing fits made with 68.3% and 95% coverage as a measure of gaussianity of the distributions.*

We see the most significant variation in the resolution when we bin the available events in this variable. We also see very little change in gaussianity implying the tracks selected in each are not biased by improved track parameter resolution. As the muons from J/ψ decays (with $\mu 6\mu 4$ trigger cuts) are forced into a quite narrow ΔR window ($\overline{\Delta R} = 0.47$, see Figure 5.14(a)), the η separation must be generally quite small. The ΔR value can come from η, ϕ or a combination of the two, and the two muons are essentially forced to be produced with a roughly fixed opening angle in $\eta - \phi$ space; if we vary the $\Delta\eta$ we are thus also varying $\Delta\phi$.

At small $\Delta\eta$ the ϕ measurement error dominates and as the ϕ measurement is generally better than η measurement this significantly improves resolution in this region, being the dominant effect on what is essentially a fixed opening angle probe of the Inner Detector.

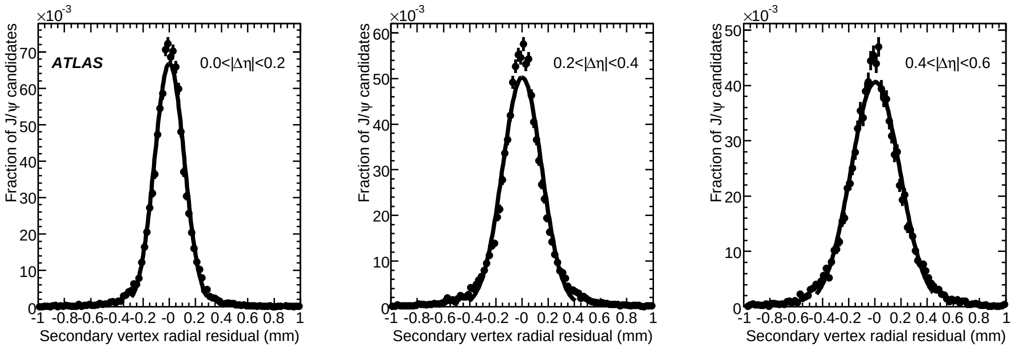

Figure 6.5: *Secondary vertex radial residuals in prompt $J/\psi \rightarrow \mu^+\mu^-$ decays in slices of difference in pseudorapidities ($\Delta\eta_\mu$) between the two muons from the decay.*

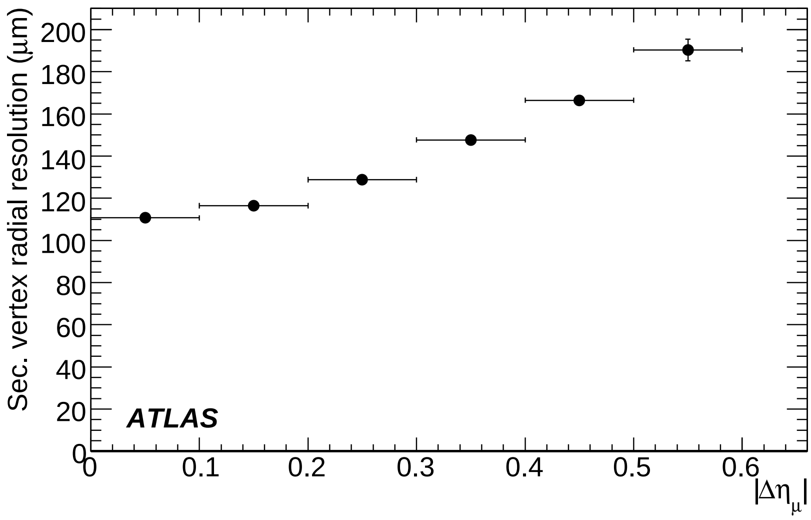

Figure 6.6: *Expected resolution on radial position of secondary vertex from prompt $J/\psi \rightarrow \mu^+\mu^-$ decays plotted as a function of the difference in pseudorapidities ($\Delta\eta_\mu$) between the two muons from the decay.*

6.2 Studies with Muon Stream data

In the ATLAS data-taking phase, inclusive data streams will separate the massive flow of data from ATLAS into *overlapping* collections of events sharing common characteristics. For the low luminosity 10^{31} cm^{-2}s^{-1} run, four 'physics' streams have been defined that contain all events passing any of a large list of predefined triggers. The four streams are `egamma` (which generally contain events with photon or electron activity), `jetTauEtMiss` (containing events with jet, tau or missing transverse energy signatures), `minBias` (containing events for minimum bias studies) and `muon` (containing events passing triggers involving at least one muon).

In early 2008, a full-scale preparation for data-taking known as the "Full Dress Rehearsal" (FDR) took place, in which all event samples expected to be present in ATLAS collisions were mixed in the correct proportions corresponding to their predicted cross-sections, fully simulated in the ATLAS framework, triggered according to the low luminosity trigger tables and reconstructed with no access to Monte Carlo truth data. To simulate real data-taking the events were reconstructed in ten one-hour long runs (split into thirty two-minute luminosity blocks) with an average instantaneous luminosity of 10^{31} cm^{-2}s^{-1}, corresponding to a total integrated luminosity of 0.8 pb^{-1}, known as FDR-1. This represents a data sample equivalent to one day of data-taking at low luminosity running. The data analysed in this section and in Section 6.3 are based on studies using these FDR-1 datasets.

6.2.1 Event selection

We analyse the full 0.8 pb^{-1} of Muon Stream data available, which corresponds to runs 3048 – 3057 inclusive. We do not require that any specific trigger is passed, but instead rely on the Muon Stream selection to determine those events of interest. All events in the Muon Stream are triggered by high-level trigger items containing at least one muon (although there may be requirements of additional items such as jets or electrons), to reduce the number of events that must be processed for analysis of quarkonium signatures and the di-muon backgrounds. Any further selection is performed 'offline' in private analysis code: we require in addition that at least two muons are reconstructed in the event, and that they both have a p_T larger than 4 GeV. All oppositely-charged muon pairs reconstructed in the event are analysed and constrained to a common vertex, and those pairs with an invariant mass within 300 MeV of the J/ψ PDG mass are considered J/ψ candidates, while those pairs with an invariant mass within 2.5 GeV of the Υ PDG mass are considered Υ candidates. No cut is placed on the pseudo-proper time. Table 6.5 contains details of the breakdown of analysed events and J/ψ and Υ candidates and Figure 6.7 illustrates the di-muon invariant mass spectrum of these events.

FDR-1 Muon Stream (0.8 pb^{-1})	Number
Events triggered	102,762
Di-muon pairs ($p_{T:1,2} > 4$ GeV)	52,384
Candidates in J/ψ mass window	10,222
Candidates in J/ψ peak	8,360
Candidates in Υ mass window	5,808
Candidates in Υ peak	1,928

Table 6.5: *Breakdown of events and candidates reconstructed in FDR-1 Muon Stream.*

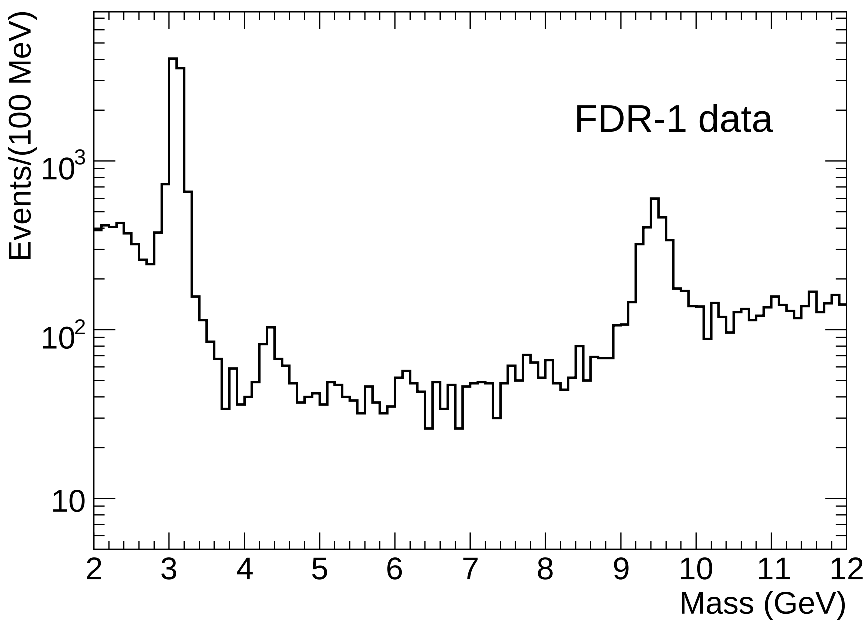

Figure 6.7: *Di-muon invariant mass distribution in the region of J/ψ and Υ from analysed FDR-1 Muon Stream data (compare with Figure 5.20, with truth information).*

6.2.2 Kinematic distributions of reconstructed quarkonia

Figure 6.7 shows the J/ψ and Υ peaks clearly visible above the background coming mainly from charm, beauty and Drell-Yan decays (see Chapter 5). Unlike the CSC studies discussed in that chapter, FDR data uses lower thresholds that are expected to run during early data analysis, using a 4 GeV p_T cut on both muons, rather than the $\mu6\mu4$ di-muon trigger previously discussed.

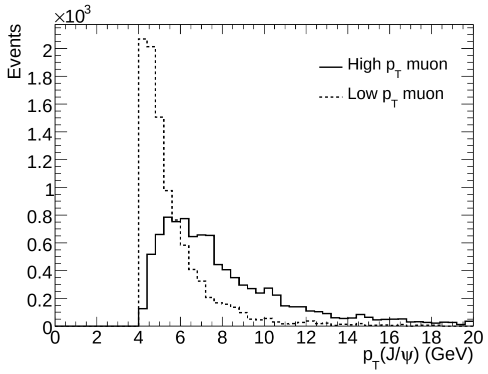

(a) Muons from J/ψ

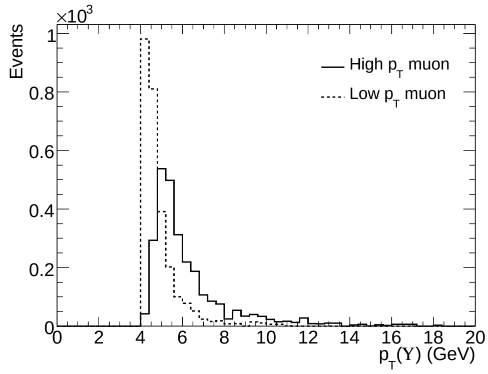

(b) Muons from Υ

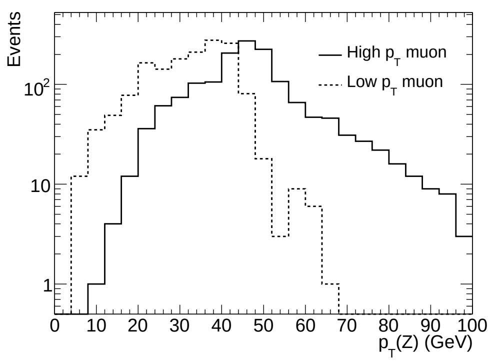

(c) Muons from Z

Figure 6.8: *Distribution of the transverse momenta of the harder and softer muon from the decays of (a) J/ψ, (b) Υ and (c) Z from an analysis of the FDR-1 Muon Stream.*

The p_T distribution of the harder and softer muon from the J/ψ and Υ candidates are shown in Figure 6.8 along with the corresponding plot for Z candidates in the sample. It is clear from these plots why the J/ψ and Υ are necessary for low p_T performance studies, and to provide complementary data quality monitoring reference points in addition to resonances like the Z.

The p_T distributions of muons from quarkonium decays cover a near disjoint range of momenta to the Z, and the resultant decay kinematics coupled with the imposed trigger constraints mean that the decays can have quite different properties. For example, whilst muons from Z decays are generally produced back-to-back, muons from J/ψ decays are again produced with small opening angles, with Υ providing a bridge between the two extremes (see Figure 6.9).

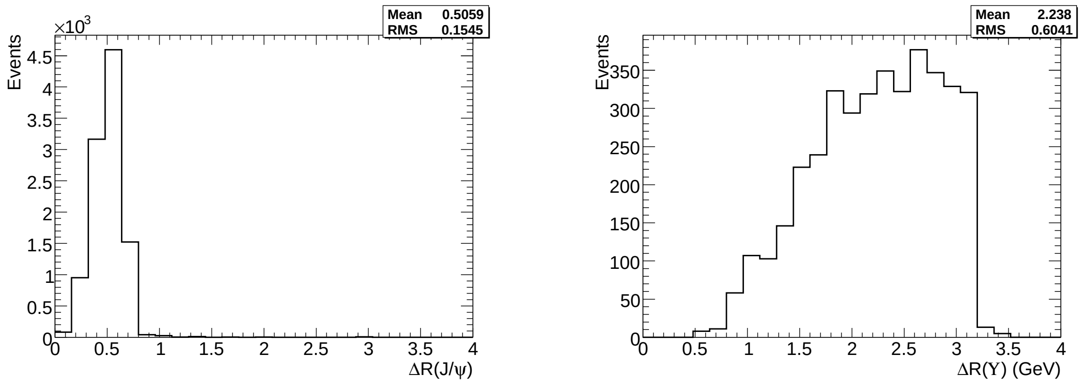

(a) J/ψ candidate ΔR (b) Υ candidate ΔR

Figure 6.9: *ΔR distributions of the two muons coming from J/ψ and Υ candidates in the FDR-1 Muon Stream.*

Note that the muon spectra near the 4 GeV cutoff are very steep for quarkonia, particularly for Υ. As the observed Υ cross-section peaks near the $\mu 4\mu 4$ trigger cuts (Figure 4.9) this cross-section is very sensitive to the single muon trigger and reconstruction efficiency dependence near this threshold, which must be carefully determined from data.

Figure 6.10 shows the reconstructed invariant mass spectra in the mass windows of the J/ψ and Υ. We use a gaussian plus linear background to fit to the mass spectra to determine the background-subtracted quarkonium yield and the mass resolution. In this plot we also require each of the muons to have an associated Inner Detector track and we use the ID track parameters to build the invariant mass distribution. We find the mass resolution of the J/ψ to be 60 MeV and of the Υ to be 169 MeV.

Figure 6.11 shows the transverse decay length distributions of the J/ψ and Υ candidates. The faint dotted line on the positive axis is a mirror image of the negative part of the distribution, representing the distribution that should be present in the absence of indirect quarkonia decays

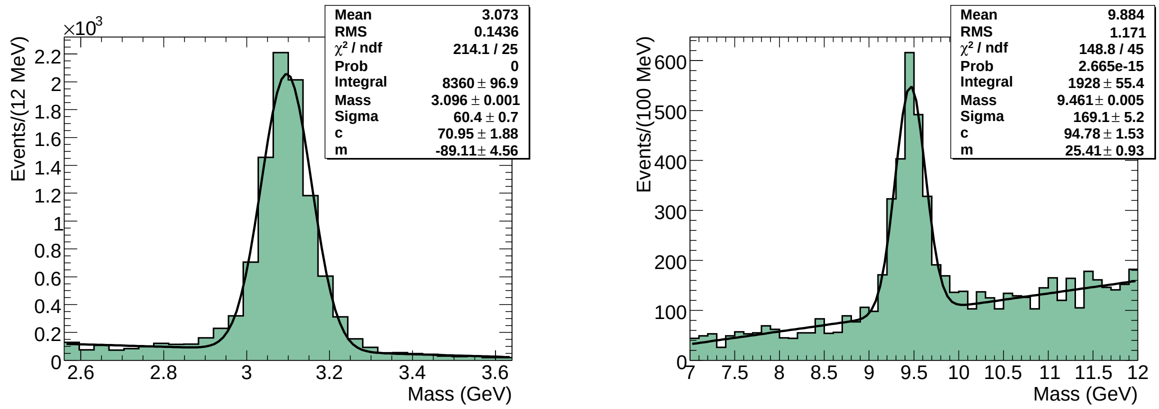

(a) J/ψ after refit (b) Υ after refit

Figure 6.10: *Di-muon invariant mass of the (a) J/ψ and (b) Υ resonances from FDR-1 Muon Stream data after muons have been refitted to a common vertex. Track parameters of identified muons are taken from the Inner Detector tracks only.*

and background contributions. As we have not placed any proper-time cuts, the inclusive J/ψ spectrum is visible. For Υ it can be seen that the distribution is far more symmetric, as the Υ does not have any significant sources of indirect production. Despite the presence of the

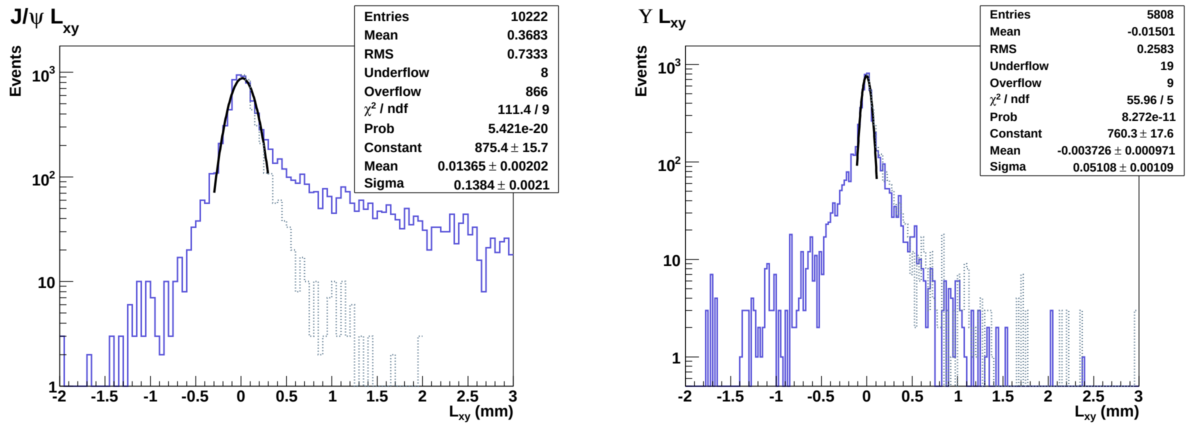

(a) J/ψ candidate L_{xy} (b) Υ candidate L_{xy}

Figure 6.11: *Transverse decay length distributions of J/ψ and Υ candidates in the FDR-1 Muon Stream.*

backgrounds, we can estimate the average vertex resolution by fitting a gaussian to the core of this distribution. As the rate of prompt J/ψ production is predicted to be around twice that of indirect J/ψ, the symmetric core centred at zero should always be visible above the long tail of indirect decays. From the J/ψ decays we can determine the resolution to be 138.4 ± 2.0 μm in this sample. As Υ decays have a larger opening angle, the vertex in the Υ kinematic regime has a much better resolution 51.7 ± 1.0 μm, largely due to muon tracks with an opening angle of around $\pi/2$, which provide far better vertexing constraints than those of the J/ψ which are near-collinear.

Figures 6.12(a) and 6.13(a) show the reconstructed, background-subtracted J/ψ and Υ transverse momentum differential distributions. A gaussian plus linear background function is fitted to the distributions in 2 GeV intervals of the J/ψ p_T, from $7-35$ GeV, and 4 GeV intervals of the Υ p_T, from $0-32$ GeV, the binning reflecting both the available statistics and range over which the respective quarkonia are produced. In each of these intervals the quarkonium yield is calculated from the integral of events under the gaussian peak, and plotted along with the associated error calculated from the fit.

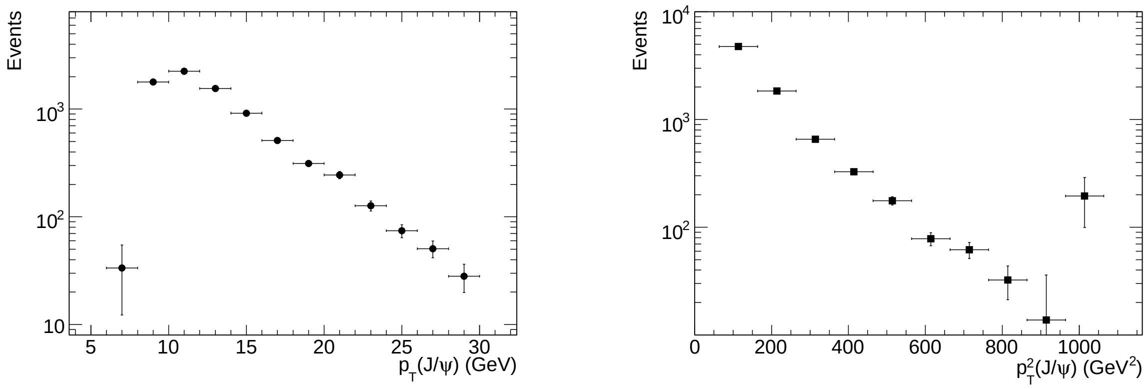

(a) p_T

(b) p_T^2

Figure 6.12: *Reconstructed J/ψ p_T and p_T^2 differential spectra, after background subtraction, from the FDR-1 Muon Stream.*

Figures 6.12(b) and 6.13(b) show similar distributions for the J/ψ and Υ, extracted from the data in the same way as the previous figures, but this time plotted as a function of p_T^2. The $d\sigma/d^2p_T$ distribution has advantages over the standard $d\sigma/dp_T$ distribution in that it does not have a zero as $p_T \to 0$, but instead provides a more meaningful quantity, directly related to the production matrix element.

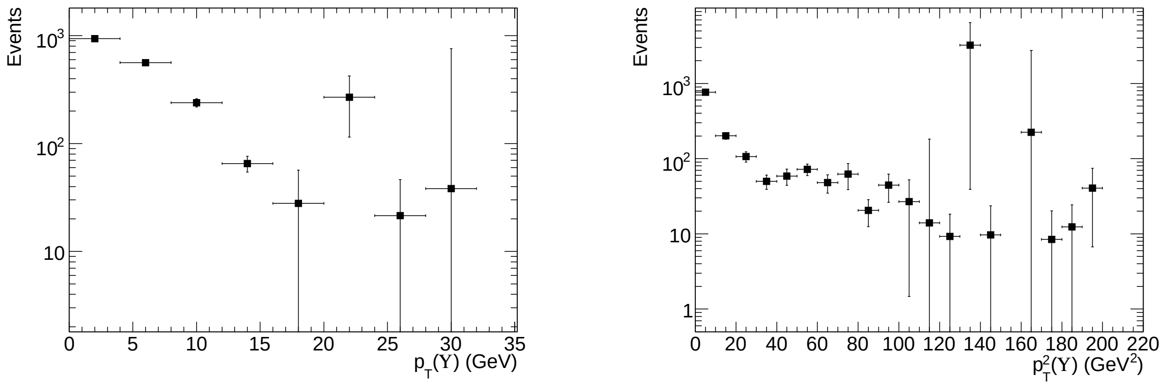

(a) p_T (b) p_T^2

Figure 6.13: *Reconstructed Υ p_T and p_T^2 differential spectra, after background subtraction, from the FDR-1 Muon Stream.*

I have provided these $d\sigma/d^2p_T$ plots here to both highlight the qualitative difference between these and the standard differential p_T distributions, and show their usefulness in understanding the underlying production models. Figure 6.13(a) does not provide any obvious information that we have entered the colour singlet dominated regime as we approach low transverse momenta (which we know, in this instance, is the case as this was how the events were generated in Monte Carlo). However, the sharp change in p_T^2 dependence at $p_T^2 \sim 35$ GeV in Figure 6.13(b) clearly illustrates something about the dominant production mechanism changes in this region. We know that the different production mechanisms have a different predicted p_T dependence (see Chapter 2) and as such these distributions can help detect the contributions of various production mechanisms.

Unfortunately, we do not see such an effect in the J/ψ sample (Figure 6.12(b)). This is because in these reconstructed samples we do not have any acceptance for J/ψ below around 7 GeV p_T, and so are not sensitive to the region where colour singlet contributions are important, so we only see the octet spectrum. Nevertheless, these figures give an indication of what should be possible to achieve with just one day's worth of physics-quality data in ATLAS.

6.3 Data-driven muon reconstruction efficiency determination

The determination of reconstruction efficiency of any particle in the ATLAS detector is crucial to any conclusion, and indeed any measurement, one would wish to draw from the analysed data. The reconstruction efficiency is not a simple single number but a non-trivially varying function in all the degrees of freedom allowed by the system under study. It is possible to make some estimate of the expected efficiency for reconstruction as a function of these variables by relying on true Monte Carlo data and a comparison of the data after being passed through the detector simulation. However, such an enterprise is reliant on an unwarranted belief in the fidelity of the Monte Carlo model and detector simulation in question.

This naturally leaves us with so-called 'data-driven' methods of efficiency determination, where efficiencies (dependent on what we do not see) are inferred wholly from reconstructed data (what we do see) in such a way as to provide an unbiased judgment of reconstruction performance. A leading method in ATLAS is the "tag-and-probe" method, developed with studies of $Z \to \mu^+\mu^-$ in mind, but similarly applicable to quarkonia. In the tag-and-probe method, a 'probe' object (in this case, a muon) is used to make the performance measurement, with a 'tag' muon having tagged a suitable sample of events for study. The di-muon decay of a Z, for example, leaves two tracks in the Inner Detector. One muon, the tag muon, is required to also leave a track in the Muon Spectrometer. The other muon, the probe muon, is (after track quality cuts) presumed to be from a Z, and relative to the ID reconstruction efficiency it is possible to determine the Muon Spectrometer reconstruction efficiency by investigating if this probe muon was reconstructed by the Muon System. This method assumes (and requires) that the two measurements are uncorrelated. The ID reconstruction efficiency has the benefit of being independent of the trigger detectors.

From studies of FDR-1 Muon Stream data on J/ψ and Υ it appears that there may be a further way of determining the reconstruction efficiency of muons from data without relying on the lack of correlation between tag and probe muons, such that it adds no bias from the selection of tag muons and which would also provide an independent cross-check for the tag-and-probe method.

The FDR-1 Muon Stream data are analysed, corresponding to an integrated luminosity of 0.8 pb^{-1}, which at low-luminosity (10^{31} $cm^{-2}s^{-1}$) is expected to be achieved in one day of running. Events passing *any* Muon Stream trigger were used so as to be able to consider the maximum statistics available for this study. In real data, this method could be applied to all data in a run to provide a global trigger efficiency, or split into efficiencies for particular triggers (which would, of course, require a larger dataset than studied here).

6.3.1 Reconstruction of J/ψ and Υ candidates

To reconstruct quarkonia candidates in FDR-1 Muon Stream data, we first combine identified muon candidates in each event and make all combinations of oppositely-charged di-muon pairs with muon transverse momentum greater than 4 GeV As we have a lower p_T threshold than in CSC data and no Monte Carlo truth to compare to, we open the mass window to allow better handling of the background. For J/ψ candidates in this study, the mass window considered was $[2.54, 3.64]$ GeV, for Υ candidates, the mass window considered was $[7.0, 12.0]$ GeV.

Out of 102,762 events processed in the Muon Stream, 52,384 di-muon candidates were reconstructed (passing at least one of the Event Filter triggers defined in the Muon Stream). Before restricting analysis to the J/ψ and Υ mass windows, the invariant mass distribution of all muon pairs (passing the basic selection criteria in Table 6.6) is plotted in Figure 6.14. The track parameters used for plotting were those of the Inner Detector track associated with the combined muon. In this figure, the peaks from the J/ψ and Υ resonances are clearly visible above the backgrounds.

An inspection of the muon-identified mass spectrum in Figure 6.14, shows however that the cross-section of the Υ peak is significantly suppressed relative to the J/ψ peak. This suggested that the suppression was either caused by differences in trigger acceptance for J/ψ and Υ,

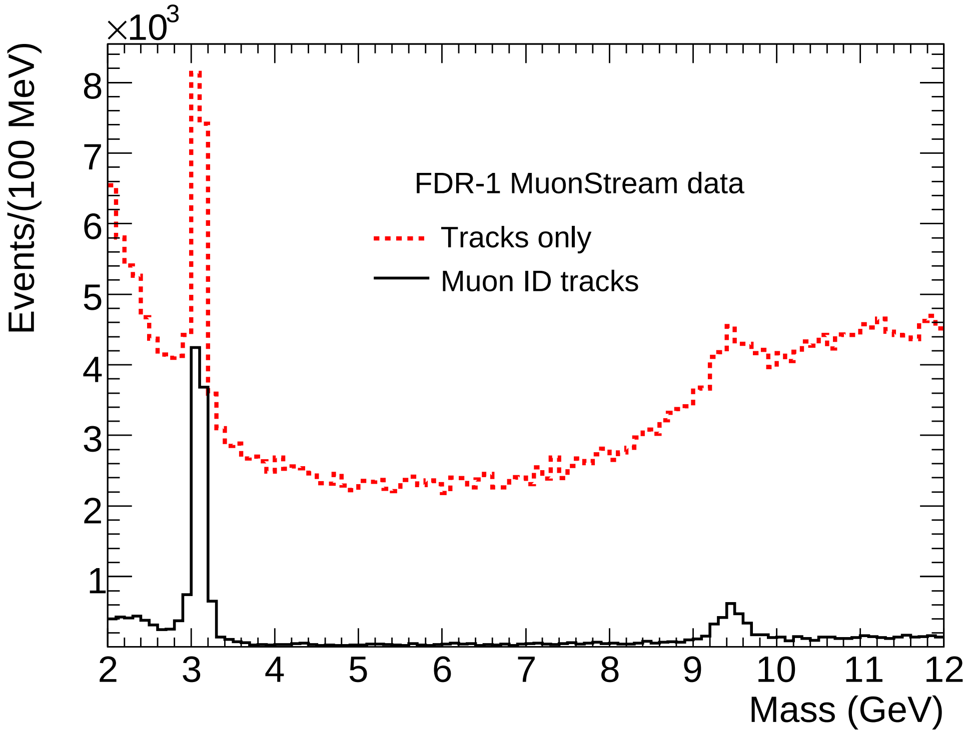

Figure 6.14: *Invariant mass distribution of Inner Detector reconstructed tracks in the J/ψ and Υ mass region in FDR-1 Muon Stream data, comparing the case where the both ID tracks have been identified as muons by the muon system, and the case where all oppositely-signed di-track combinations are plotted. A cut on $p_T > 4$ GeV is imposed on all tracks.*

FDR-1 muon criteria	Value
Number of muons triggered in event	At least one muon
Both muons identified by muon system	Yes
Muon tracks with Inner Detector TrackParticle	Two
Transverse momentum of measured ID track	Both > 4 GeV

Table 6.6: *Basic di-muon selection criteria before beginning further analysis in FDR-1.*

or due to differences in muon reconstruction efficiency between the two peaks. Re-analysing the Muon Stream events and looking at oppositely-charged tracks (`InDetTrackParticles`) reconstructed by the Inner Detector, instead of the ID tracks from Muon Spectrometer tagged tracks allowed for an independent study of the events. The ID tracks combined were again required to have a $p_T > 4$ GeV but were not required to have been identified in the muon system, so have no explicit muon identification. As muon tracks in the previous muon-identified case were required to have an ID track (and the measurements were taken from the parameters of this track), the muon identified pairs are necessarily a subset of the ID track pairs.

Clearly, without muon identification there is a greatly increased combinatorial background, but the trigger decision from the FDR Muon Stream is still used to ensure that there is at least one muon in the event. The muon trigger chambers are separate from the muon measurement chambers, providing a degree of independence improved by the use of only ID tracks for measurement and tagging. Figure 6.14 also shows the invariant mass spectrum in this `InDetTrackParticle`-only case (without Muon ID) Again, the J/ψ and Υ peaks are clearly visible, in spite of the increased background.

Figure 6.15 shows a comparison of the J/ψ and Υ mass windows with and without muon identification, after the selections described above. Due to the high background in the non-identified muon case for Υ, track vertexing flags (as used for di-muon CSC studies) were applied to the two tracks from Υ candidates in both muon ID and non-muon ID cases. This significantly reduced the background underneath the Υ peak by requiring the two tracks to have come from the primary vertex.

By constraining the two ID tracks in both cases to point to a common vertex by performing an unconstrained (no mass constraint, no vertex pointing) vertex fit with the CTVMFT fitter [123], it was possible to further reduce the combinatorial background in all cases without significant (within statistics) reduction of the events contained within the peak. The results of the fit can be seen in Figure 6.16. A single gaussian was used to approximate the signal peak and a linear (or quadratic, where appropriate) fit was used to model the background.

The parameters of the gaussian were modified so that the fit mean was defined centered

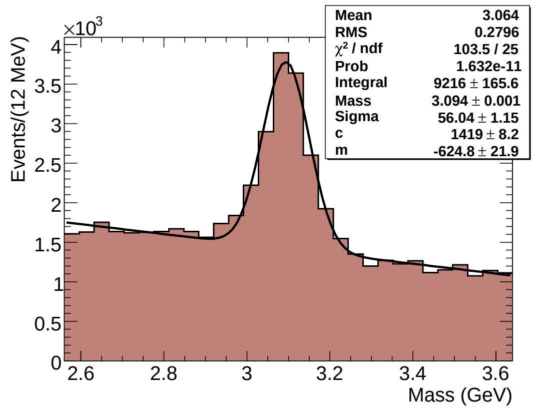

(a) J/ψ without Muon ID

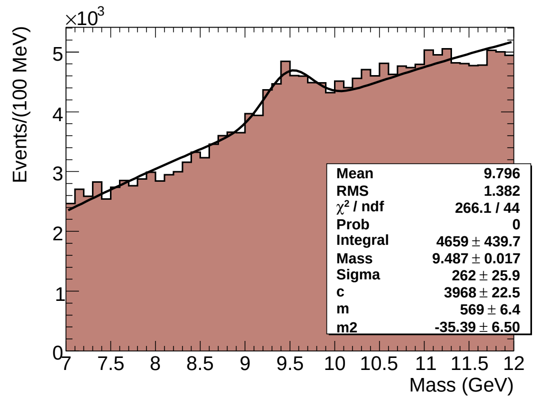

(b) Υ without Muon ID

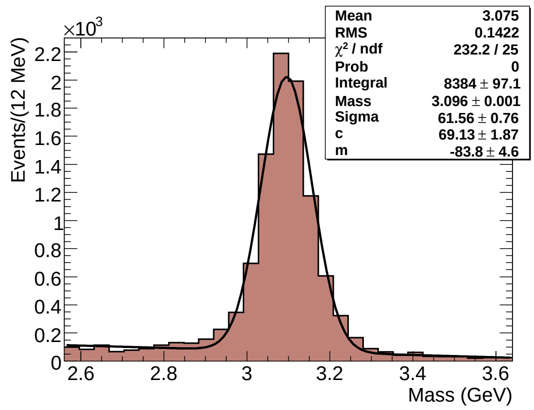

(c) J/ψ with Muon ID

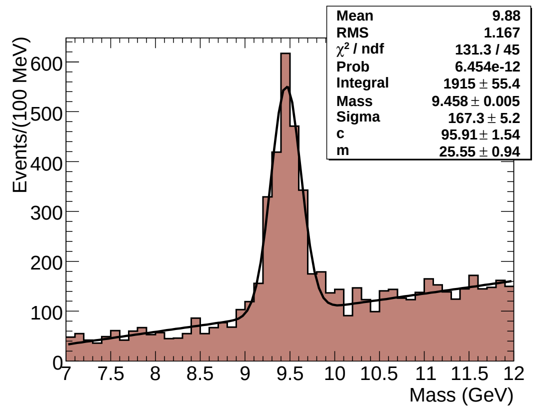

(d) Υ with Muon ID

Figure 6.15: *Di-track invariant mass in the J/ψ and Υ mass windows, before refit of the Inner Detector tracks to a common vertex. The top row illustrates the invariant mass peaks when tracks were required to come from identified muons with $p_T > 4$ GeV, the bottom row when muon identification constraints were imposed. All data was analysed from the FDR-1 Muon Stream and as such contains events which fired at least one of the FDR-1 muon triggers.*

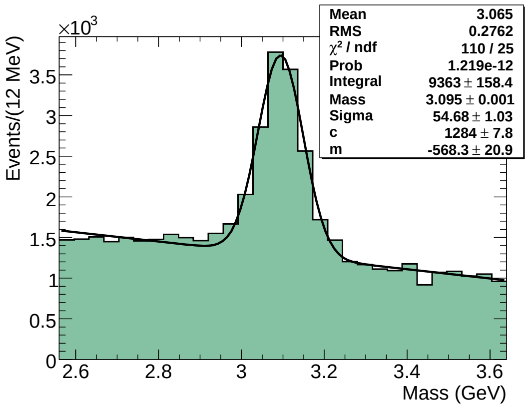

(a) J/ψ without Muon ID

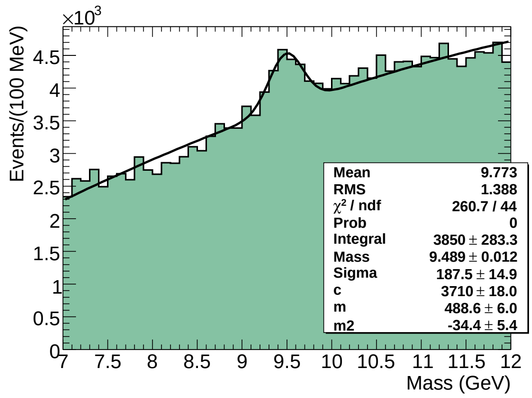

(b) Υ without Muon ID

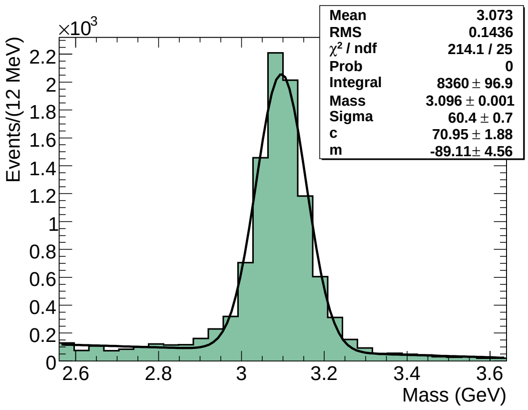

(c) J/ψ with Muon ID

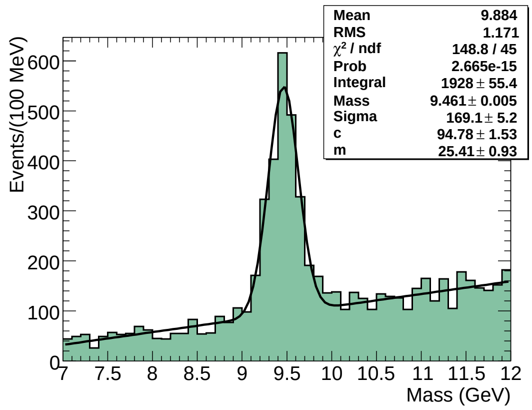

(d) Υ with Muon ID

Figure 6.16: *Di-track invariant mass in the J/ψ and Υ mass windows, after refit of the Inner Detector tracks to a common vertex. Cuts and requirements on the tracks in each case are as for Figure 6.15.*

about the PDG value of the J/ψ (or Υ) to improve fit stability and the constant of the gaussian was redefined so as to return the integral of the number of entries in the fitted gaussian peak rather than the height (H) with the following parameterisation:

$$f(x) = H\frac{w}{|\sigma|\sqrt{2\pi}}\exp(-\frac{x-\bar{x}}{\sigma^2}) \tag{6.1}$$

where w is the bin width (the range of the histogram divided by the number of bins), σ is the standard deviation of the gaussian calculated from the fit and $\bar{x}$ is the PDG mass of the quarkonium state in question. That reasonable fits to these distributions can be achieved in all cases highlights that for the J/ψ and Υ resonances the backgrounds are controllable at a 4 GeV threshold even without explicit muon identification of the tracks.

6.3.2 Analysis of the reconstructed samples

The fits to the muon-identified and ID track-only vertexed spectra immediately highlight the reconstruction deficit in the muon-identified case. Table 6.7 summarises the true J/ψ and Υ yield inferred from the integral of the gaussian peak in both cases.

Quarkonium	Yield (ID track-only)	Yield (muon ID)
J/ψ	9363 ± 158	8360 ± 97
Υ	3850 ± 283	1928 ± 55

Table 6.7: *Quarkonium yield in FDR-1 Muon Stream data after selection in the muon identified and ID track-only cases.*

There is some loss evidenced in the J/ψ case, but in the Υ case around half of all possible Υ fail to be reconstructed in the muon spectrometer. Figures 6.17 and 6.18 show the p_T and η distributions of the reconstructed high and low p_T muons in the pair, for both the muon identified and track-only cases. One can see from these distributions that there are some deficits in acceptance (particularly visible in η) when we require muon identification of the tracks. In Figures 6.17(b) and 6.17(d) we again see how strongly peaked the Υ muon spectra are towards low p_T values, compared to the J/ψ . No significant differences were seen in the $\Delta\eta$ or ΔR

distributions of accepted muon pairs in either case.

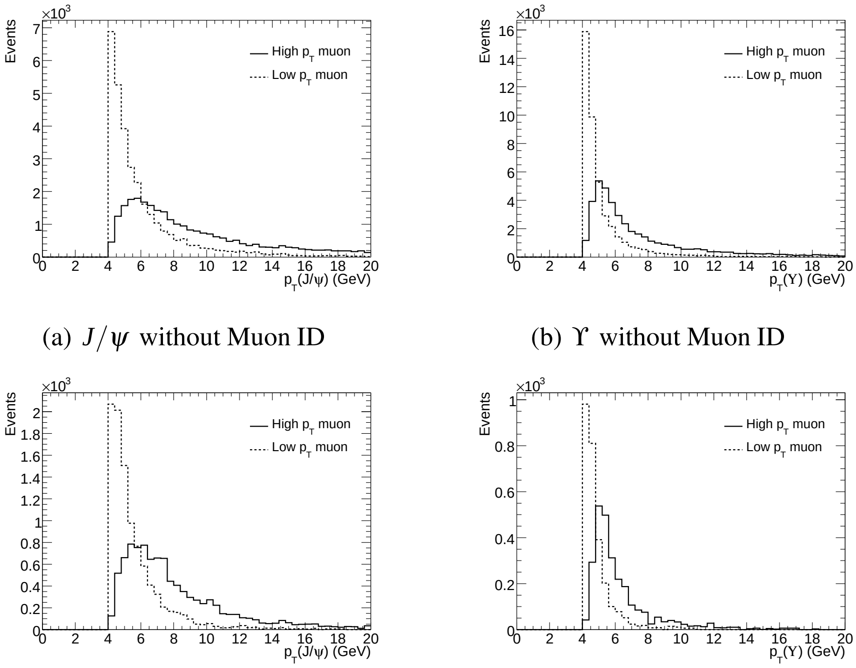

(a) J/ψ without Muon ID (b) Υ without Muon ID

(c) J/ψ with Muon ID (d) Υ with Muon ID

Figure 6.17: *Individual muon p_T spectra for J/ψ and Υ candidates in the FDR-1 Muon Stream, with and without muon identification on tracks.*

6.3.3 Determination of di-muon reconstruction efficiency

All muon identified pairs are contained within the ID track-only set. As there are legitimate quarkonia reconstructed by the Inner Detector that are not reconstructed by the Muon System (using Inner Detector tracks), the ratio of the integral $N(Q\overline{Q})$ of the gaussian fit in the muon identified to the tracks-only case gives a good measure of the di-muon reconstruction efficiency:

$$\varepsilon_{\text{dimuon}} = \frac{N(Q\overline{Q})_{\text{Muon}}}{N(Q\overline{Q})_{\text{ID}}} \tag{6.2}$$

We study this effect separately in broad muon η bins. The J/ψ and Υ invariant masses are plotted in three regions corresponding to whether both muons from the decay are to be found in the Inner Detector barrel region ($|\eta| < 1.05$), if they are both found in the endcap region

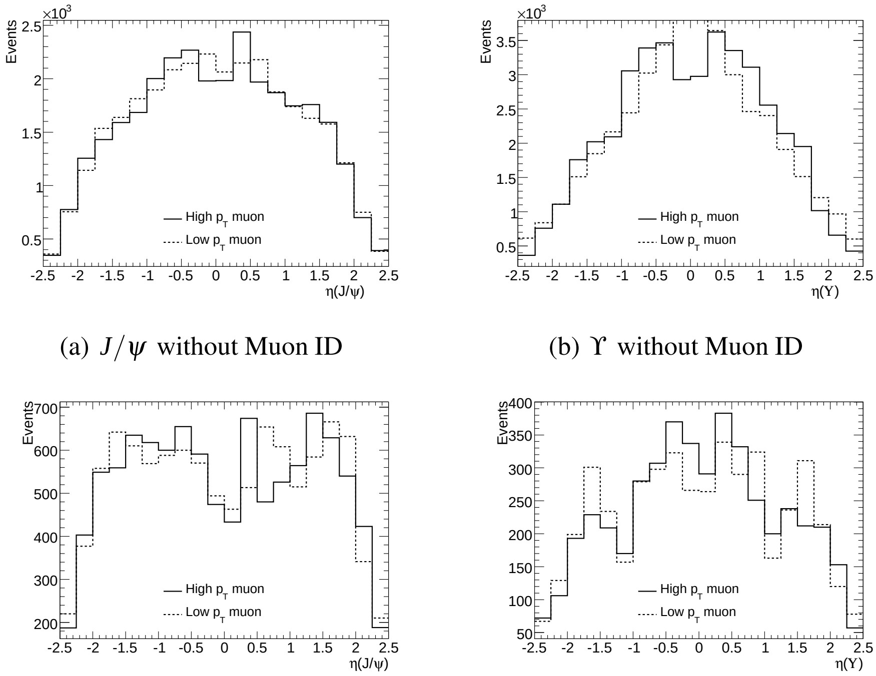

(a) J/ψ without Muon ID

(b) Υ without Muon ID

(c) J/ψ with Muon ID

(d) Υ with Muon ID

Figure 6.18: *Individual muon η distributions for J/ψ and Υ candidates in the FDR-1 Muon Stream, with and without muon identification on tracks.*

$(1.05 < |\eta| < 2.7)$, or if one muon is found in each region. We perform a fit to these invariant mass distributions for both the tracks-only and muon-identified datasets. The results are shown in Figures 6.19 and 6.20 along with the fit parameters and candidate yields in both cases.

Due to the additional background under the Υ peak, we from here on place an additional cut on both the track-only and muon-identified samples for Υ analysis, requiring that both tracks in each candidate pair have been identified as having come from the primary vertex. This lowers the background enough without reduction of the signal to be able to perform a stable fit to the low statistics peak in the Υ case. The efficiencies calculated with this fit can be found in Table 6.8. Note that Υ has no observed signal peak in the "Barrel-Endcap" track-track case due to kinematics. The trigger cuts mean that true Υ are rarely produced with muons in this configuration, whilst the track-track combinatorial background has no such constraints and so dominates over the small signal peak which is lost in fluctuations at these low statistics. In any case, it is clear from the comparative yields in the above figures that the efficiency in the

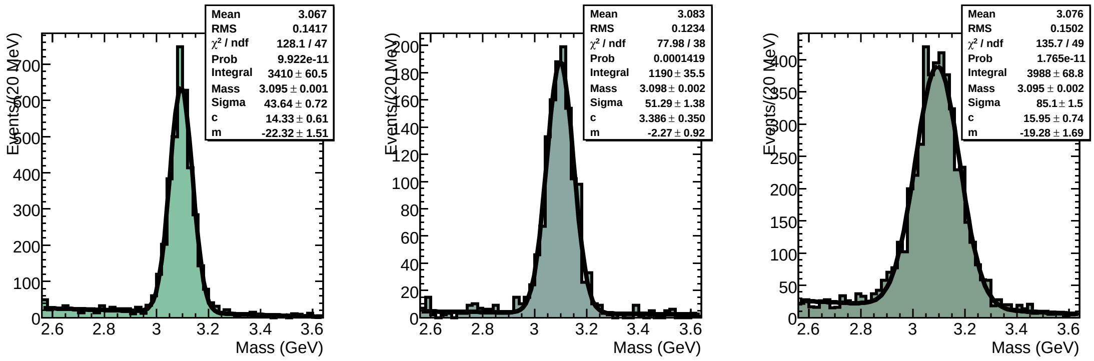

(a) J/ψ with Muon ID

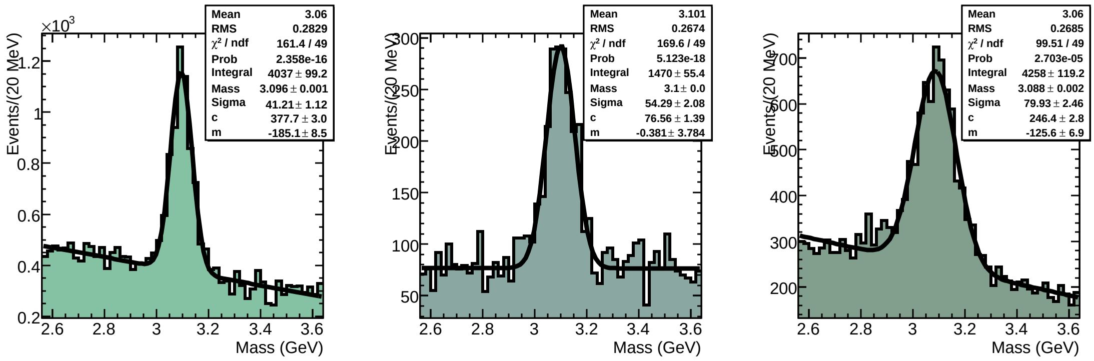

(b) J/ψ without Muon ID

Figure 6.19: *J/ψ candidate invariant mass from FDR-1 Muon Stream data split by η region of the two muons. The left-hand plot is the "Barrel-Barrel" case, the centre plot is the "Barrel-Endcap" case and the right-hand plot is the "Endcap-Endcap" case. 'Barrel' refers to the region $|\eta| < 1.05$ and 'Endcap' refers to the region $1.05 < |\eta| < 2.7$.*

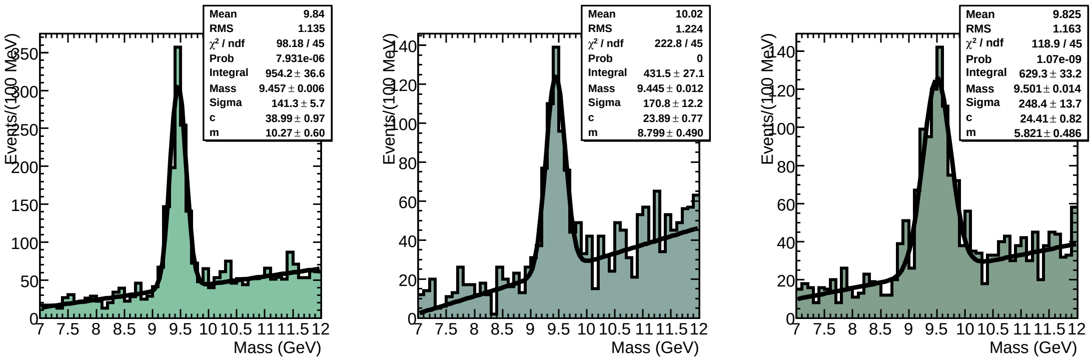

(a) Υ with Muon ID

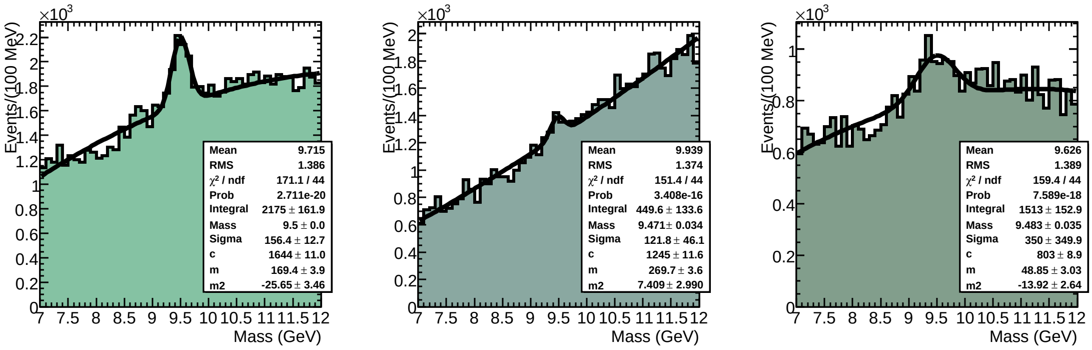

(b) Υ without Muon ID

Figure 6.20: Υ *candidate invariant mass from FDR-1 Muon Stream data split by* η *region of the two muons. The left-hand plot is the "Barrel-Barrel" case, the centre plot is the "Barrel-Endcap" case and the right-hand plot is the "Endcap-Endcap" case. 'Barrel' refers to the region* $|\eta| < 1.05$ *and 'Endcap' refers to the region* $1.05 < |\eta| < 2.7$.

Υ case is significantly lower than that of J/ψ, and lower than seen in CSC datasets studied in Chapter 5.

Table 6.8 shows the calculated di-muon reconstruction efficiencies for J/ψ and Υ in these Inner Detector regions. We see very reasonable efficiencies for J/ψ reconstruction similar to those seen in CSC studies (taking into account different trigger thresholds are used), and improving in the endcap where measurement is better. For Υ the efficiency is closer to 50% (albeit with large errors), a significant reduction.

J/ψ mass window		Υ mass window	
Muon η region	Efficiency %	Muon η region	Efficiency %
Barrel-Barrel	86.3 ± 3.0	Barrel-Barrel	46.2 ± 6.4
Barrel-Endcap	85.1 ± 4.8	Barrel-Endcap	N/A
Endcap-Endcap	100.0 ± 3.3	Endcap-Endcap	50.0 ± 16.0

Table 6.8: *Di-muon reconstruction efficiency in J/ψ (left) and Υ (right) mass windows split by η region of the two muons, calculated from analysis of the FDR-1 Muon Stream data. 'Barrel' refers to the region $|\eta| < 1.05$ and 'Endcap' refers to the region $1.05 < |\eta| < 2.7$.*

Table 6.9 shows the di-muon reconstruction efficiency for J/ψ candidates split further as a function of the J/ψ p_T (no such analysis was possible for Υ due to low statistics).

$p_T(J/\psi)$ GeV	$8-13$	$13-16$	$16-19$	$19-22$	$22-24$
Efficiency %	84.5 ± 2.5	92.7 ± 4.2	81.8 ± 7.5	99.5 ± 11.0	89.0 ± 16.0

Table 6.9: *Di-muon reconstruction efficiency as a function of J/ψ p_T calculated from analysis of the FDR-1 Muon Stream data.*

Error calculation

The errors used in this calculation are not standard binomial errors due to the presence of background in the fits. Particularly important in the case of the samples considered here (representing one day's worth of data), background fluctuations can introduce correlations between signal samples in the muon-identified and track-only cases. Instead, we calculate the errors (as has been done for those quoted above) using the following formalism. We define dN as the error on the track-only fit and dn as the error on the muon-identified fit. $N \pm dN$ then represents the fit result in the track-only case, $n \pm dn$ in the muon-identified case. Then $N \pm dN$ can be split into $n \pm dn$ and an additional $m \pm dm$, where we let $N = n + m$ and $dN^2 = dn^2 + dm^2$.

As we define the efficiency in this framework as:

$$\varepsilon_{\text{dimuon}} = \frac{n}{N} = \frac{n}{n+m}, \tag{6.3}$$

then

$$d\varepsilon^2 = \left(\frac{ndm}{(n+m)^2}\right)^2 + \left(\frac{mdn}{(n+m)^2}\right)^2 \tag{6.4}$$

and so

$$d\varepsilon^2 = \left(\varepsilon\frac{dN}{N}\right)^2 + (1-2\varepsilon)\left(\frac{dn}{N}\right)^2 \tag{6.5}$$

which reduces to a standard binomial error in the no-background limit $dN \to \sqrt{N}$, $dn \to \sqrt{n}$. In this way we extract correct errors for the efficiencies calculated in this study.

Di-muon efficiencies as a function of muon p_T

Due to the difficulty in splitting the Υ signal into intervals in p_T or η whilst retaining a clear signal peak, as a result of limited statistics and high backgrounds, we now limit the rest of this discussion to consideration of the J/ψ samples. Having determined a method of calculating the di-muon reconstruction efficiency that is independent of the muon system but for the trigger decision (as we select events from the Muon Stream), we can continue this enterprise to split the efficiency as a function of the individual muon transverse momenta, in increments of 0.5 GeV.

Low p_T muon					
$5.5-6.0$	–	–	–	91.7 ± 12.8	77.8 ± 8.6
$5.0-5.5$	–	–	66.3 ± 6.2	65.1 ± 6.9	63.9 ± 4.8
$4.5-5.0$	–	76.4 ± 12.6	61.9 ± 4.3	56.3 ± 5.2	62.6 ± 7.0
$4.0-4.5$	33.7 ± 4.6	52.9 ± 4.3	69.6 ± 4.5	46.6 ± 4.2	57.5 ± 7.1
Muon p_T (GeV)	$4.0-4.5$	$4.5-5.0$	$5.0-5.5$	$5.5-6.0$	$6.0-6.5$
	High p_T muon				

Table 6.10: *Di-muon reconstruction efficiency (as a percentage) in bins of muon p_T from J/ψ calculated from analysis of the FDR-1 Muon Stream data.*

Using fits to the signal core in the track-only and muon-identified J/ψ invariant mass spectra, we obtain the results shown in Table 6.10 with errors calculated as above, using only techniques that will be available with real ATLAS data without any reliance on Monte Carlo predictions. We obtain reasonable results, showing the fast increase in efficiency as a function of both the low p_T and high p_T muon as we move away from the trigger threshold.

6.3.4 Single muon efficiency determination

As we have developed a method of calculating the di-muon reconstruction efficiency as a function of the individual muon p_T, the next step is to extract a single muon efficiency parametrisation from this data. If we assume the efficiencies of the two muons in a pair to be uncorrelated, the di-muon reconstruction efficiencies in Table 6.10 are effectively combinations of just five independent parameters representing five average single muon efficiencies in p_T intervals over the range studied.

Taking this into account, there are two ways of extracting these parameters to determine a fit for the single muon efficiency. The first is to perform a two-dimensional fit to the di-muon efficiencies in Table 6.10 by fitting for each of the parameters separately, which leads to the efficiencies shown in Table 6.11. The other method is to perform a simultaneous fit to the di-muon efficiency, which produces a parameterisation for the single muon efficiency curve shown in Equation 6.6:

$$f(p_T) = \frac{A}{1+\exp[-a(p_T-b)]} \tag{6.6}$$

where $A = 0.83, a = 3.0$ GeV^{-1} and $b = 3.8$ GeV. The output of both methods are overlaid in Figure 6.21, which represents the final result of this muon efficiency calculation with this small amount of FDR-1 data.

From this result it can be seen that it is possible to determine the single muon reconstruction efficiency by an independent data-driven method using Inner Detector tracks to a relatively high degree of accuracy with 0.8 pb^{-1} of data. The errors and reach of this study are limited, but show the effectiveness of the method, which can be extended in p_T and to multi-dimensional

$p_T(\mu)$	Efficiency
$4.0-4.5$	0.65 ± 0.02
$4.5-5.0$	0.77 ± 0.03
$5.0-5.5$	0.84 ± 0.03
$5.5-6.0$	0.80 ± 0.04
$6.0-6.5$	0.82 ± 0.04

Table 6.11: *Single muon efficiency as a function of muon p_T (GeV), calculated from fits to two-dimensional di-muon efficiency data determined from FDR-1 Muon Stream data corresponding to $\int \mathscr{L} = 0.8\ pb^{-1}$ in direct J/ψ events.*

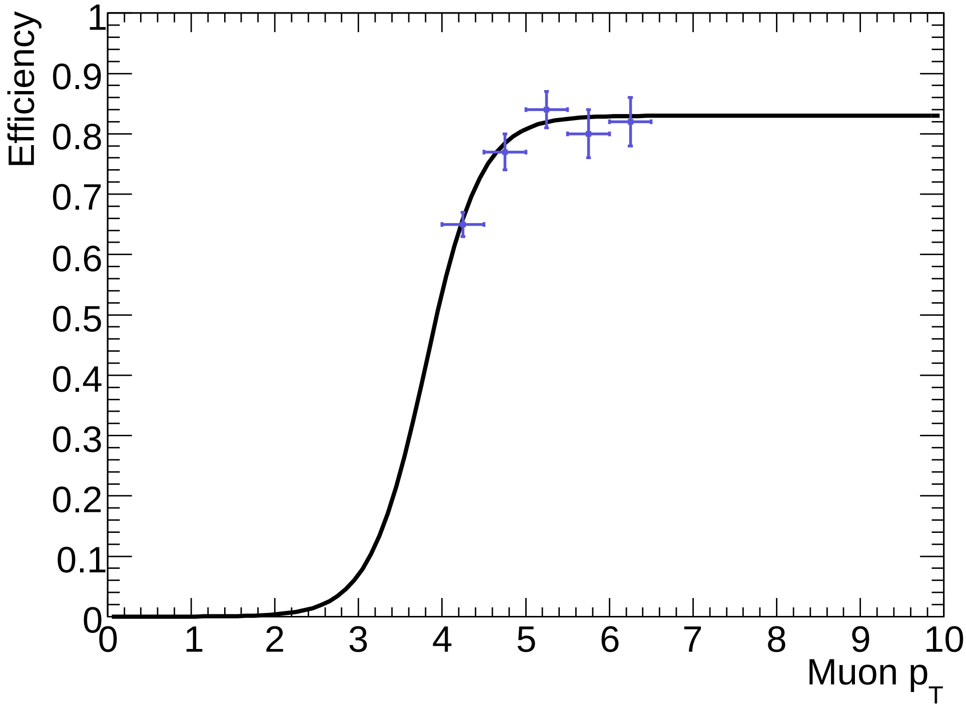

Figure 6.21: *Single muon efficiency curve as a function of p_T (GeV), determined from FDR-1 Muon Stream data ($\int \mathscr{L} = 0.8\ pb^{-1}$) in direct J/ψ events. The points represent one alternate method of calculating the efficiency, the curve another. The curve is not a fit to the points displayed.*

$\eta - p_T$ maps with higher statistics, split into finer binning or performed for individual trigger decisions. Note that this can also be done with Υ (with correspondingly higher statistics), but has additional complications due to the need to isolate the $\Upsilon(1S)$ from the Υ higher states. It was not possible to do any comparison to the correct true efficiency by studying the Monte Carlo truth for these samples, as the FDR datasets purposefully do not contain any MC data.

This efficiency calculation also highlights why the measured Υ efficiency was so low. The turn-on curve for the muon efficiency at 4 GeV is steep, and as such the observed cross-section of Υ is far more sensitive than that of J/ψ to changes in efficiency due to the steep rise in cross-section near the lower edge of muon momenta accessible.

The methodology used in this section to analyse the track-only quarkonia samples also have application to other performance studies. Building J/ψ and Υ just using Inner Detector tracks (in events triggered by muon trigger) allows for independent checks of the Inner Detector and Muon Spectrometer with manageable backgrounds. For early data-analysis these studies have also shown it will be possible, if necessary, to make studies of quarkonia without reference to the muon spectrometer measurements. In addition, the increased yield of J/ψ candidates could outweigh the cost of the additional combinatorial background.

6.4 Data quality monitoring with quarkonium

Quarkonium in the di-muon channel are now being used in ATLAS for a variety of data quality monitoring (DQM) purposes. In this section I give an overview of some of the DQM activities I have been involved in and motivation for the analysis of these quantities in ATLAS. Section 6.4.1 discusses studies of mean mass shifts from PDG values of fits to the quarkonia resonances in a variety of variables as a means of determining problems with alignment, material distortions and reconstruction software issues.

These studies are ongoing in ATLAS and take their inspiration from very successful applications of these mass shifts at CDF [125, 126]. In addition, prompt J/ψ are being used for magnetic field mapping and monitoring of the Inner Detector, making use of the small opening angle of the muons from the J/ψ decay along with observed mass shifts as a magnetic field probe. These studies require relatively high statistics but due to the high rate of quarkonium production expected to be observed in ATLAS, we are able to extend the applicability of the CDF studies and apply these material and alignment monitoring techniques at Tier 0 in order to provide quick-response feedback to the ATLAS control centre for calibration of the detector. In addition, quarkonium is being used as a monitoring tool for the High Level Trigger algorithms. Again due to the high rate and clean signature J/ψ and Υ can provide fast indication of a variety of problems in the detector. This is discussed further in Section 6.4.4.

6.4.1 Quarkonium mass shifts as a monitoring tool

The di-muon decays of J/ψ and Υ will be used in both online and offline monitoring at ATLAS. A typical 10 hour block of data is expected to include around tens of thousands of quarkonia (with di-muon $\mu4\mu4$ trigger cuts), which will be used for quasi-real-time calibration and alignment of the detector. Mass shifts for the reconstructed quarkonium states, plotted versus a number of different variables, have been proposed to monitor detector alignment, material effects, magnetic field scale and its stability, as well as to provide checks of muon reconstruction algorithm performance. The CDF collaboration extensively and successfully used this method but it took many years at the Tevatron to collect sufficient statistics across a range of variables to allow for proper correction for material and alignment and the disentanglement of various detector effects [126].

The expected rate of quarkonium production at ATLAS is such that we can expect to be able to perform meaningful monitoring and corrections online at Tier 0. There are many examples of where monitoring of quarkonium mass shifts can be useful in data-taking. Mass shifts in quarkonia as a function of transverse momentum can reveal problems with energy loss corrections and the muon momentum scale. As a function of pseudorapidity this can be a good probe of over- or under-correction of material effects in the simulated detector geometry and of magnetic field uniformity. J/ψ mass shifts in Monte Carlo simulations have already helped improve muon reconstruction algorithms in ATLAS.

An example of a reconstructed J/ψ mass shift measurement at ATLAS with the statistics corresponding to 6 pb^{-1}, i.e. about a weeks worth of data at the luminosity of 10^{31} cm^{-2}s^{-1} is presented in Figure 6.22. This is the dependence of ΔM on the difference in curvatures of

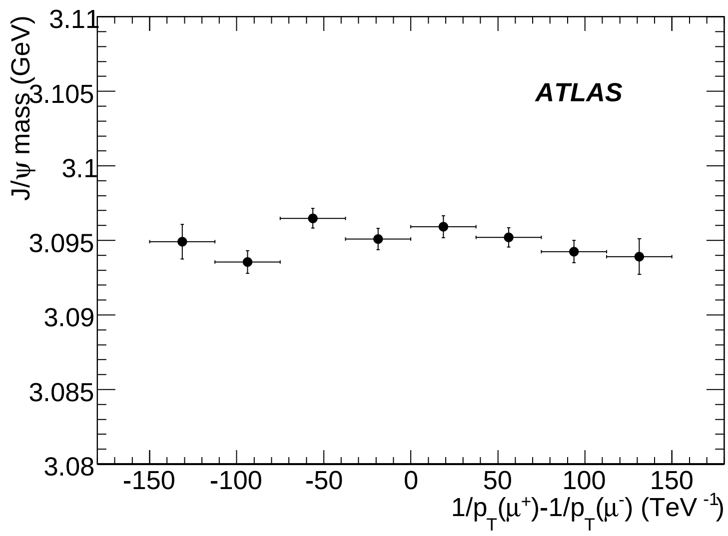

Figure 6.22: *J/ψ mass shift plotted versus the difference of curvature between the positive and negative muons. Statistics corresponds to the integrated luminosity of about 6 pb^{-1}.*

positive and negative muons, which allows for checks of a potentially important effect seen at CDF: horizontal misalignments in some detector elements may result in a constant curvature offset that can lead to significant charge-dependent tracking effects.

A misalignment may be such that a negative track has a higher assigned curvature (and hence lower momentum) than is truly the case, whilst a positive track would be affected in the opposite way, affecting the reconstructed mass of the original quarkonium state. The sample shown in the figure is simulated with ideal geometry and does not show any significant effects of this kind, but will be a key variable to consider with real data.

Similar plots for 0.8 pb^{-1} of integrated luminosity as a function of a number of variables for J/ψ and Υ are shown in Figure 6.23 using FDR data. Here a significant bias as a function of curvature are seen, due to a distorted geometry present in these samples. Dependencies can also be seen in other variables, but a particularly interesting here is the ϕ dependency

(Figures 6.23(d) and 6.23(h)) which show a significant shift in masses for positive ϕ.

This effect is due to the presence of additional material in these datasets, which was purposefully placed in the positive ϕ region of the Inner Detector. Full details of this additional material can be found in reference [127], but Figure 6.24 illustrates the presence of the additional material at a particular pseudorapidity value. From this we can see that the mass shifts of quarkonia can also be sensitive to the presence of additional material (or rather, an incorrect material description of ATLAS in the reconstruction software) with a relatively small amount of collected data.

6.4.2 Effect of misaligned geometry on quarkonia

From the start-up of ATLAS efforts to align the various detector components that would otherwise introduce biases in physics variables will be an ongoing process. Alignment of the Inner Detector components is particularly important in order to achieve the desired tracking performance. Whilst many studies focus on track parameter residual distributions to improve the determination of the spatial positions of the individual silicon modules and TRT straws, quarkonia can also play a complementary role in such studies.

In di-muon decays of J/ψ and Υ, the requirement of having two ID tracks fitted to a common decay vertex places extra constraints on the two tracks and thus can provide additional sensitivity to systematic correlations between detector components that the single track distributions cannot. The following studies are conducted comparing two different alignment scenarios in reconstructed $B_d \to J/\psi K_0^*$ (indirect B-decay J/ψ) events. The first alignment is what might be a typical alignment at some given time in early data (known as the `CSC-01-02-00` geometry), the second alignment (`OFLCOND-CSC-00-01-05` alignment) then represents what is known as a 'first-pass' alignment that can be expected after the first major correction of alignment problems in a given geometry description.

The `OFLCOND-CSC-00-01-05` alignment attempts to correct for three alignment issues in the `CSC-01-02-00` geometry:

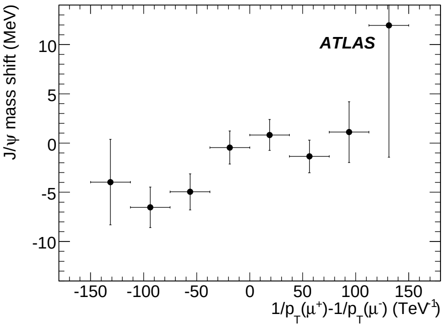

(a) J/ψ muon curvature difference

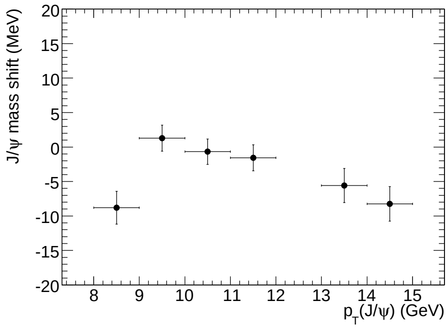

(b) J/ψ transverse momentum

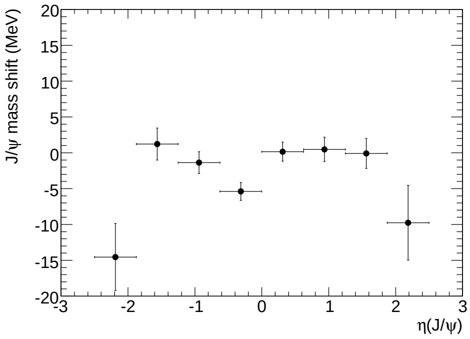

(c) J/ψ pseudorapidity

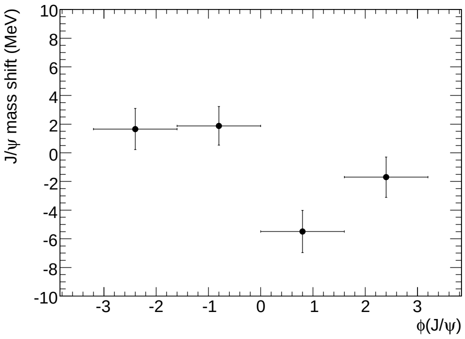

(d) J/ψ azimuthal angle

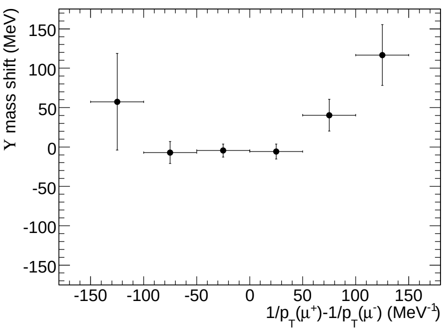

(e) Υ muon curvature difference

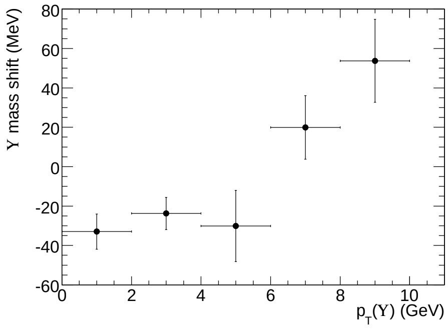

(f) Υ transverse momentum

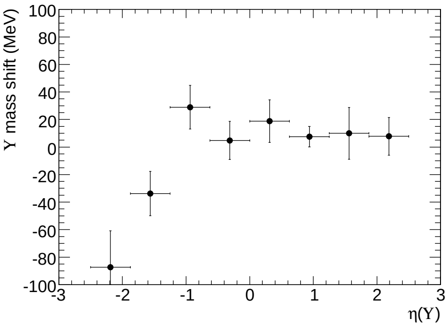

(g) Υ pseudorapidity

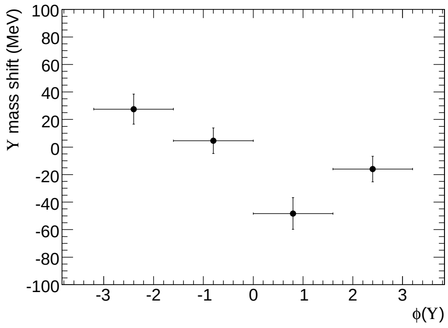

(h) Υ azimuthal angle

Figure 6.23: *Mass shifts in J/ψ and Υ candidates from FDR-1 Muon Stream data as a function of (a),(e) muon curvature difference, and (b),(f) transverse momentum, (c),(g) pseudorapidity and (d),(h) azimuthal angle ϕ of the Υ.*

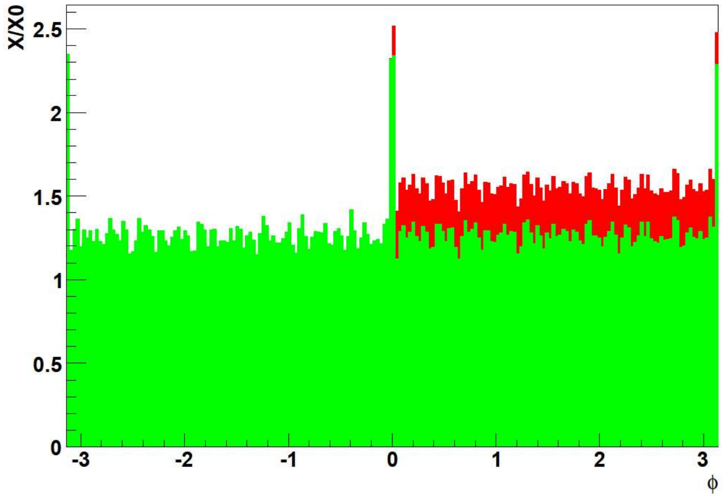

Figure 6.24: *Total radiation length in the Inner Detector for $\eta = +1.5$, as an illustration of the asymmetric additional material present in the positive ϕ region in CSC and FDR simulations (taken from [127]). Spikes at $\phi = 0$ and π are due to the Inner Detector support rails.*

- Random translations of silicon modules by 30–150 microns and up to 1 mrad rotations
- Shifts of entire silicon layers by 10–200 microns and up to 1 mrad rotations
- Barrel and endcap shifts of 1–3 mm and up to 1 mrad rotations

by analysing single track-based distributions including impact parameter resolution, track momentum systematics and tracking efficiency.

For this study we have access to the truth information and precisely the same events are reconstructed using the same software release but using different alignment constants. As such, *any* differences seen between the two samples are solely the effect of alignment and are not a statistical effect.

We reconstruct these events and search for J/ψ candidates in each case, requiring a common vertex fit for the two tracks. Two key distributions, the J/ψ invariant mass and transverse decay length, are shown in Figure 6.25. Notice that although there are some small differences between the two alignments, the change in alignment does not affect fit parameters for either of these distributions (within the fit errors) and thus we might feel that the alignment has not positively

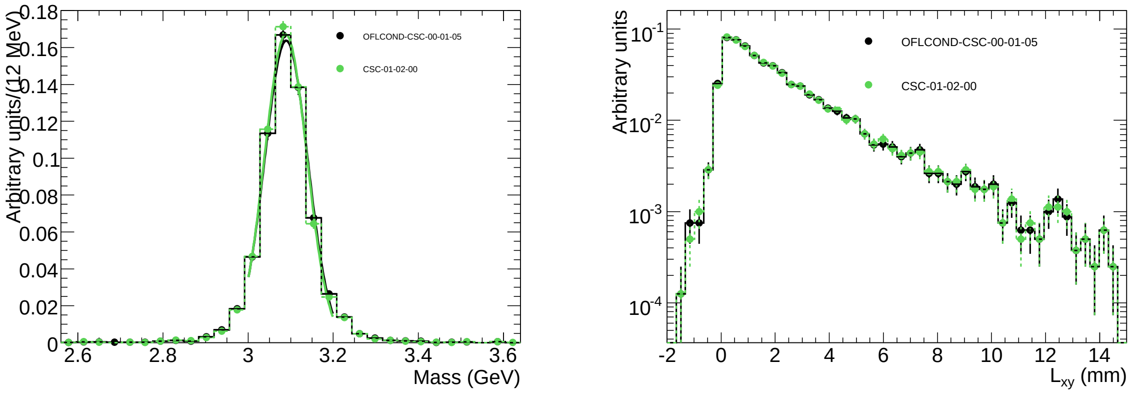

(a) J/ψ invariant mass (b) J/ψ transverse decay length

Figure 6.25: *Comparison of invariant mass and transverse decay length distributions of reconstructed J/ψ candidates from $B_d \to J/\psi K_0^*$ events with nominal CSC alignment and with the `OFLCOND-CSC-00-01-05` 'first-pass' alignment.*

nor adversely affected reconstruction of quarkonium states.

However, if we look at the mass shift monitoring plots for a selection of variables, (see Figure 6.26 for examples), we see the effects of this alignment much more clearly. Whilst mass shifts as a function of transverse momentum of the J/ψ and transverse decay length are not sensitive to these particular alignment changes, we do see a slight improvement in ΔR and ϕ, where definite biases are present in the `CSC-01-02-00` dataset (green points) that are slightly improved by this first-pass alignment (black points). The most striking difference in this instance however comes from the mass shift with curvature difference between the two muons. While a bias is seen in the `CSC-01-02-00` dataset, an even stronger bias has been introduced in the `OFLCOND-CSC-00-01-05` alignment.

This is indicative of the presence of horizontal shifts in the Inner Detector tracking planes being introduced, presumably to correct single track distributions. However, as this example shows, without considering the effect a re-alignment has on physics objects like the J/ψ in addition to single tracks, tracking performance can seem to be improved whilst introducing systematic effects in physics variables.

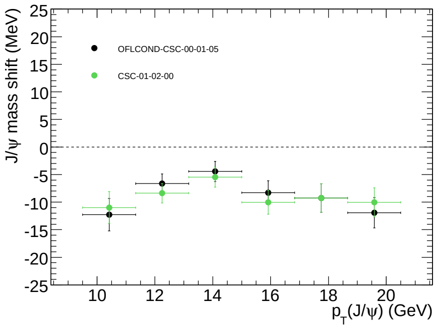

(a) J/ψ mass shift with p_T

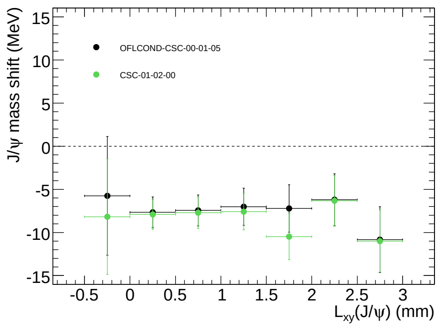

(b) J/ψ mass shift with L_{xy}

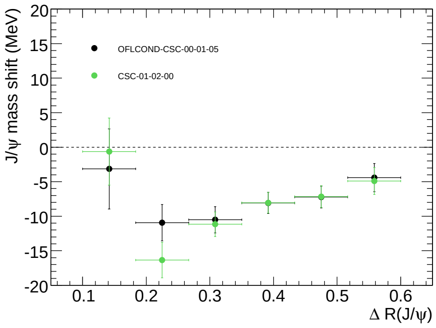

(c) Mass shift with ΔR

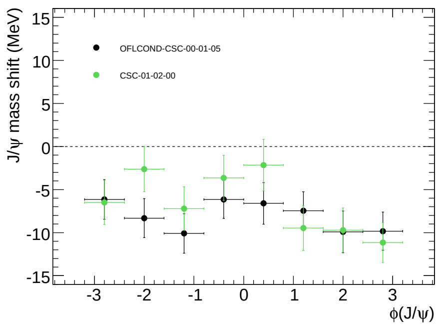

(d) Mass shift with ϕ

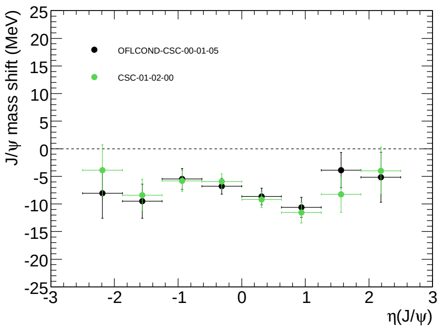

(e) Mass shift with η

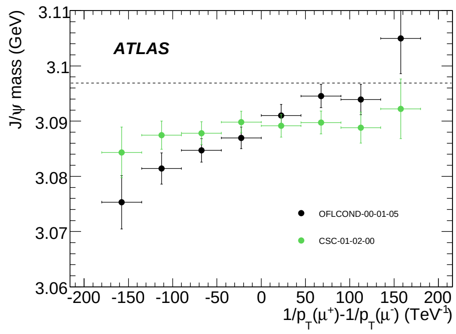

(f) Mass shift with muon curvature difference

Figure 6.26: *Comparison of the variation of mass peak position of reconstructed J/ψ candidates (in $B_d \to J/\psi K_0^*$ events) from PDG value, with nominal CSC alignment and the* `OFLCOND-CSC-00-01-05` *'first-pass' alignment, as a function of muon J/ψ p_T, L_{xy}, ΔR, position of J/ψ in η and ϕ, and curvature difference between the positive and negative muons.*

6.4.3 Quarkonium for software performance monitoring

In addition to being crucial for understanding of the detector, analysis of mass shifts on reconstructed Monte Carlo data can also be useful as a cross-check of algorithm performance. Mass shifts in the J/ψ have already been used to find previously unobserved large shifts in the quarkonium mass in the forward detector regions (see Figure 6.27). In this case, the problem was found to be due to an overcorrection of the Geant 4 muon energy loss at high η in the muon reconstruction algorithms, which is now fixed since Athena release 13.0.30. The effect of the fix is overlaid in the same figure. Note that we still see some variation of mass with η after the

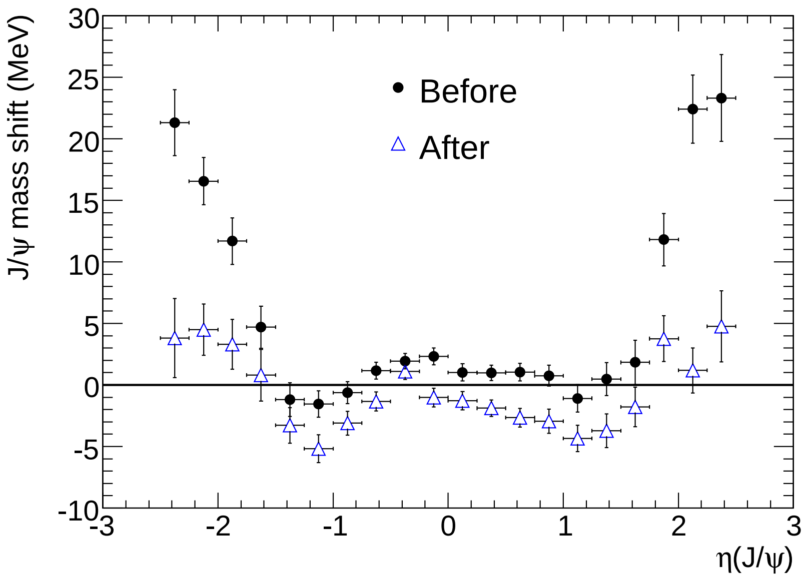

Figure 6.27: *J/ψ mass shift in η before (black dots; 12.0.6) and after (blue triangles; 13.0.30) correction of muon reconstruction algorithms for Geant 4 energy loss.*

correction. This simply highlights that the mass shifts in a particular variable are invariably a convolution of many different effects. The key is to be able to identify these effects in a particular variable, correct the problem, reprocess the data and continue this calibration cycle until systematic effects have been eliminated.

Another example of the use of quarkonium for DQM has already been tested on FDR data in a dedicated data quality monitoring framework set up to analyse data as it came from Tier 0 in the simulated data-taking runs. Figure 6.28 shows an example of a DQM histogram recording the J/ψ and Υ transverse decay length on a run-by-run basis. The grey histogram shows a previous run considered to be a suitable reference histogram for a 'good' run, the blue line shows the same distribution in the current run. That the distribution is completely different automat-

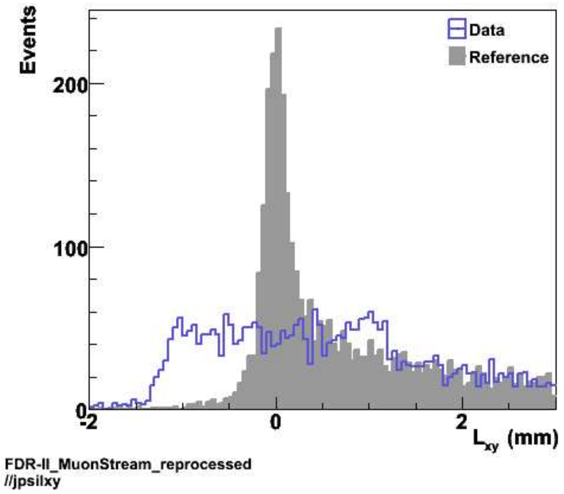

(a) J/ψ monitoring plot

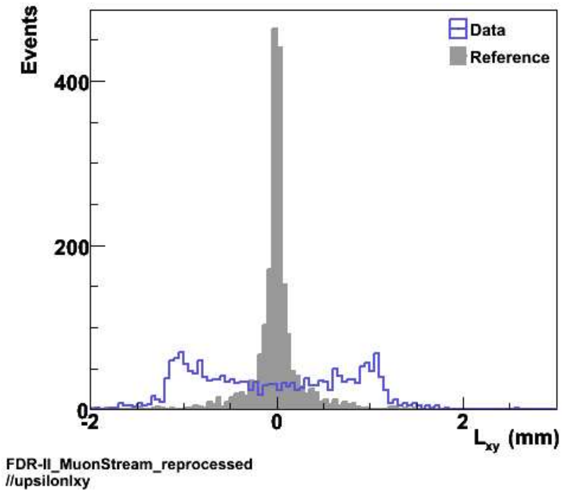

(b) Υ monitoring plot

Figure 6.28: *J/ψ and Υ transverse decay length distributions in an FDR data quality monitoring run (blue line) compared to a reference distribution (grey filled) where due to a software problem the primary vertex was undefined.*

ically raises a flag that something is problematic with the run, despite other distributions such as the invariant mass looking largely unchanged. A problem with the quarkonium transverse decay length histograms immediately suggested a vertexing problem. The problem was tracked down to a change of track perigee definition in a new software release between the two runs that caused problems with primary vertex finding.

In these simulations, the primary vertex is, as standard, shifted by 1 mm from the detector origin point $(0,0,0)$. In the absence of a primary vertex, vertexing software reverted to using $(0,0,0)$ as a reference point. As such, all vertices were shifted by ± 1 mm from the correct position (as can be seen in Figure 6.28) and smeared between these two points by variation in ϕ. This example serves to highlight the versatility of quarkonium data quality monitoring to a wide range of problems.

6.4.4 High Level Trigger data quality monitoring

In addition to study of alignment and material effects, quarkonia are good candidates for monitoring of the effectiveness of the various trigger algorithms on a run-by-run basis. By studying histograms of the correlations between track parameters and invariant masses calculated at the level-1 and high level triggers with those calculated offline, systematic biases in acceptance can be flagged and corrected.

Monitoring of the high level trigger algorithms has been introduced and was used in runs for the second phase of the Full Dress Rehearsal, known as FDR-2. As for FDR-1, the second phase again provides data simulating the output from real ATLAS collisions, providing representative runs, this time for an average instantaneous luminosity of 10^{32} cm^{-2}s^{-1}. One example of the application of trigger monitoring to FDR-2 data is given in this section.

Two pairs of runs are considered, produced over two days using different alignment scenarios. Run numbers 52280 and 52283 were played first using a misaligned geometry, followed[1)] by runs 52290 and 52293, which use an 'ideal' alignment. The ideal geometry runs are also known as FDR-2 runs 1 and 2, the misaligned geometry runs as FDR-2 runs 3 and 4. Figure 6.29 shows the invariant mass distribution in the $J/\psi-\Upsilon$ range for both sets of FDR-2 runs (normalised to the same number of input events from Tier 0) for those events passing any event filter trigger in the Muon Stream.

Note that despite the ideal geometry used in runs 1 and 2, we observe a reduction in J/ψ candidate acceptance, see a loss of efficiency of around a factor of two across the range under consideration, and most distinctively an almost complete suppression of the Υ peak. In real data this could reflect a problem with B-trigger algorithms. To investigate the problem, the J/ψ and Υ candidate events were broken down by trigger selection, and the most significant trigger items for di-muon quarkonia decays were studied at each trigger level. Tables 6.12, 6.13 and 6.14 detail the number of (normalised) events seen in both sets of runs at the L1, L2 and EF trigger levels for trigger items of interest in the FDR J/ψ and Υ candidate mass windows.

[1)]The run numbers 52280, 52283, 52290 and 52293 considered here are, despite the numbering, four sequential runs. Each unique run was duplicated twice with each given a run number following the original in sequence.

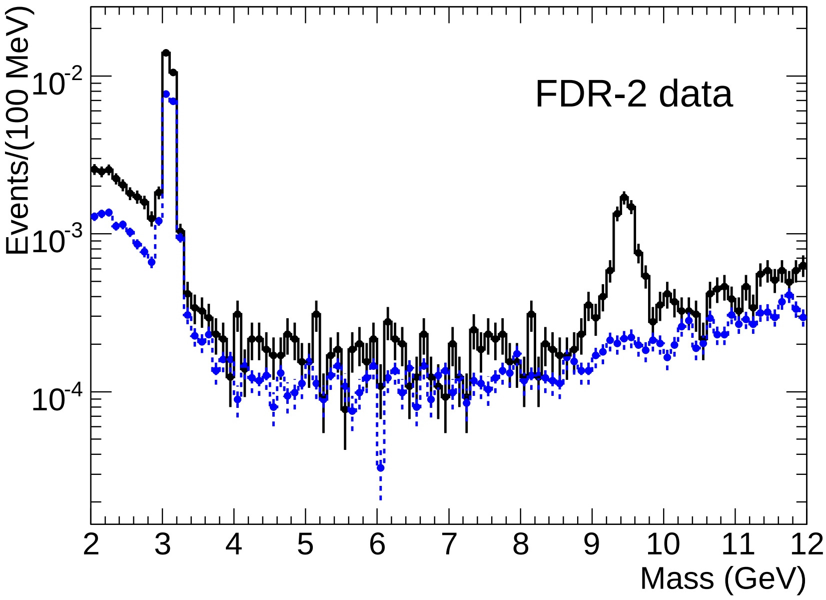

Figure 6.29: *Di-muon invariant mass distribution in the region of J/ψ and Υ from analysed FDR-2 Muon Stream data (compare with Figure 6.7 from the FDR-1 Muon Stream analysis). Black lines are for run numbers 52280 and 52283 (runs $3-4$) where the Υ is visible, blue dashes are the equivalently normalised data analysed from run numbers 52290 and 52293 (runs $1-2$). In both cases the Event Filter trigger items are the same.*

L1 trigger item	J/ψ mass window		Υ mass window	
	Runs 3–4	Runs 1–2	Runs 3–4	Runs 1–2
`L1_2MU10`	4,194	2,261	1,511	569
`L1_2MU4`	5,856	3,554	3,462	1,576
`L1_2MU6`	5,574	3,332	2,953	1,254
`L1_MU10`	6,057	3,529	2,953	1,252
`L1_MU20`	2,789	1,916	775	472
`L1_MU40`	1,724	1,132	476	262
`L1_MU6`	6,178	3,736	3,498	1,611

Table 6.12: *Events selected in runs 3–4 and runs 1–2 for the most significant level-1 trigger items in FDR-2 data for quarkonium triggering.*

L2 trigger item	J/ψ mass window		Υ mass window	
	Runs 3–4	Runs 1–2	Runs 3–4	Runs 1–2
L2_2MU4_Jpsimumu	5,544	3,179	33	19
L2_2MU4_Upsimumu	7	10	1,974	579
L2_2mu10	930	689	200	127
L2_2mu4	5,824	3,529	3,449	1,560
L2_2mu6	4,799	2,942	1,770	824
L2_Bmu4mu4	5,656	3,272	309	193
L2_mu10	3,734	2,583	1,021	657
L2_mu20	1,202	960	313	247
L2_mu40	184	124	33	31
L2_mu6_Bmumu	4,796	3,140	214	231
L2_mu6_Jpsimumu	4,789	3,135	141	152
L2_mu6_Upsimumu	3	3	138	66

Table 6.13: *Events selected in runs 3–4 and runs 1–2 for the most significant level-2 trigger items in FDR-2 data for quarkonium triggering.*

EF trigger item	J/ψ mass window		Υ mass window	
	Runs 3–4	Runs 1–2	Runs 3–4	Runs 1–2
EF_2MU4_Jpsimumu	5,544	3,179	33	19
EF_2MU4_Upsimumu	7	10	1,974	579
EF_2mu4	5,659	3,416	3,330	1,531
EF_2mu6	4,631	2,842	1,669	783
EF_Bmu4mu4	5,656	3,272	309	193
EF_mu10	3,622	2,467	976	607
EF_mu20	1,094	871	299	224
EF_mu40	109	80	16	19
EF_mu6_Bmumu	4,796	3,140	214	231
EF_mu6_Jpsimumu	4,789	3,135	141	152
EF_mu6_Upsimumu	3	3	138	66

Table 6.14: *Events selected in runs 3–4 and runs 1–2 for the most significant event filter trigger items in FDR-2 data for quarkonium triggering.*

The breakdown of trigger decisions for each set of runs can be very informative, but it is clear that the suppression of quarkonia in runs $1-2$ is already present at the level-1 trigger, and can be seen across all triggers of interest, although the effect is more pronounced at low p_T thresholds. The high level triggers include both the topological and TrigDiMuon triggers, at which point we can see a loss of over around 71% of Υ candidates in the `L2_2MU4_Upsimumu` and `EF_2MU4_Upsimumu` items, and 57% losses for J/ψ candidates in the `L2_2MU4_Jpsimumu` and `EF_2MU4_Jpsimumu` items. Other trigger items are also affected, but it is clear at this stage that the rate loss is dependent on the p_T threshold of the identified muons (note that even similar algorithms like `EF_mu6_Jpsimumu` with slightly higher thresholds have less suppression).

Figure 6.30(a) shows monitoring histograms of the invariant mass distribution for each EF trigger under consideration, in the range $2-12$ GeV, particularly informative for the behaviour of each EF algorithm. Figure 6.30(b) shows the corresponding plot of the high p_T muon distribution from Υ candidates for the same EF trigger items in both sets of runs. Immediately it is clear that it is the acceptance of low p_T muons that is being affected in runs $1-2$. This also explains why the suppression of Υ was seen to be so drastic in these runs: as the accessible cross-section of Υ rises steeply near the 4 GeV trigger cut threshold, any loss of low p_T acceptance is particularly visible as a drop in observed Υ rate. Whilst this effect is also visible in J/ψ and the background processes, the effect on Υ is enough to reduce the rate sufficiently as to make its mass peak almost inseparable from the background at these statistics.

Whilst in this case the loss of acceptance was later found to be due to a simulation problem that indirectly removed low p_T muons in these samples, that a problem could be immediately spotted in the HLT monitoring histograms highlights the uses that quarkonia can have for detecting issues with real data. Indeed, as this was a low p_T issue, and the effect is reduced at higher momenta, if monitoring was performed with solely other 'standard candles' such as the Z, this effect would have been harder to see.

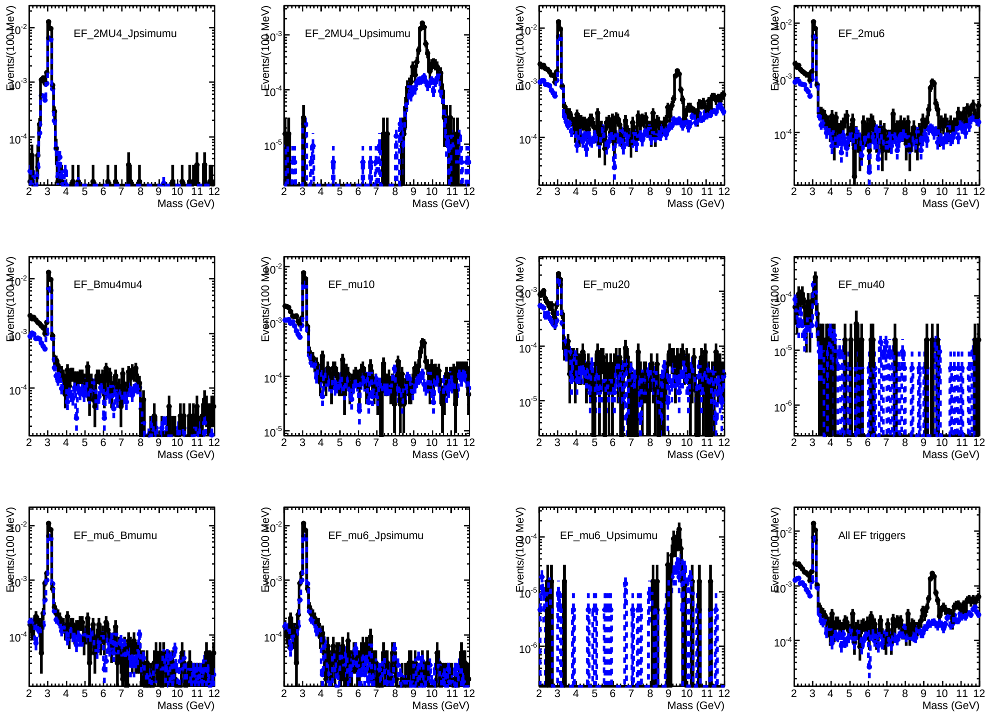

(a) $J/\psi - \Upsilon$ invariant mass by EF trigger decision

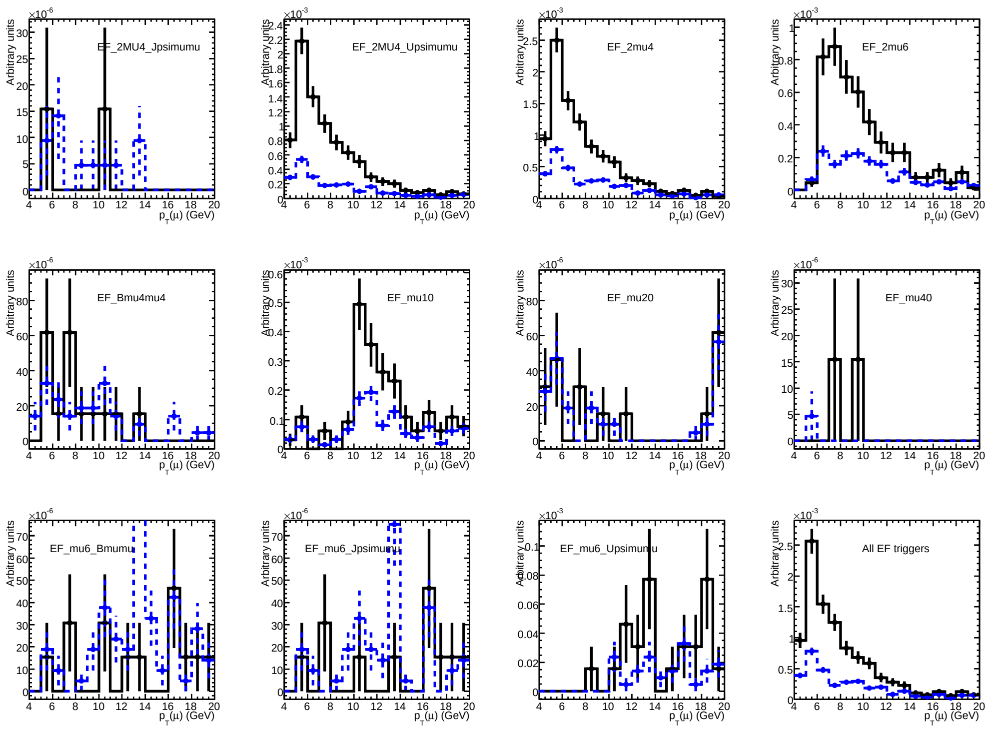

(b) Υ high p_T muon distributions by EF trigger decision

Figure 6.30: *Di-muon invariant mass distributions in the region of J/ψ and Υ, and high p_T muon distributions, both split by EF trigger decision in FDR-2 Muon Stream data. Black lines are runs 3–4, blue dashes are normalised data analysed from runs 1–2.*

"Science may set limits to knowledge, but should not set limits to imagination"

Bertrand Russell

7

Polarisation and cross-section measurements of quarkonium states

Once detector performance and calibration in ATLAS has reached a reasonable level in ATLAS and efficiencies and acceptances can be accurately determined, it will then be possible to use reprocessed data to make physics measurements. Using the datasets and event selection described in Chapter 5 this chapter describes early data techniques for cross-section and polarisation measurements of various quarkonium states and the predicted sensitivities possible with up to 10 pb^{-1} of recorded 'physics-ready' data.

7.1 Polarisation & cross-section measurement of J/ψ and Υ

The Colour Octet Model predicts that prompt quarkonia produced in pp collisions are transversely polarised, with the degree of polarisation increasing as a function of the transverse momentum (see Chapter 2 for more details). Other production models predict different p_T dependencies of the polarisation and so this quantity serves as an important measurement for discrimination of these models.

Quarkonium polarisation can be assessed by measuring the angular distribution of the muons produced in the decay. In the case of direct production, the appropriate axis for defining a decay angle is the direction of the J/ψ movement in the pp centre-of-mass frame (which is also the ATLAS lab frame). The decay angle we call θ^* is defined to lie between the μ^+ direction in the rest frame and the J/ψ direction in the lab frame. This reference frame is known as the helicity frame, and the relevant decay angle θ^* is defined in Figure 7.1.

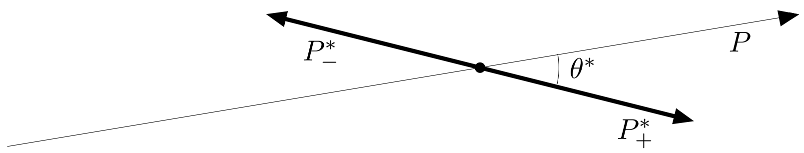

Figure 7.1: *Graphical representation of the θ^* angle used in the spin alignment analysis. The angle is defined by the direction of the positive muon in the quarkonium decay frame and the quarkonium momentum direction in the laboratory frame.*

The spin alignment of the parent vector quarkonium state can be determined by measuring the polarisation parameter α in the distribution

$$\frac{dN}{d\cos\theta^*} = C\,\frac{3}{2\alpha+6}\left(1+\alpha\cos^2\theta^*\right). \tag{7.1}$$

The quantity $\cos\theta^*$ varies between -1 and $+1$; where a factor $3/2(\alpha+3)$ is used to normalise the distribution to a unit. The choice of parameters in Equation 7.1 is such that the distribution is normalised to C. The parameter α is defined by

$$\alpha = \frac{\sigma_T - 2\sigma_L}{\sigma_T + 2\sigma_L} \tag{7.2}$$

where the σ_T and σ_L are the fractions of transversely and longitudinally polarised quarkonia respectively. α is equal to $+1$ for transversely polarised production (helicity $= \pm 1$), whilst for a longitudinal polarisation (helicity $= 0$), α is equal to -1. Between these two extremes lies a mixture of transverse and longitudinal production. Unpolarised production consists of equal fractions of helicity states $+1$, 0 and -1, and corresponds to $\alpha = 0$.

The difficulty of quarkonium polarisation measurement is evidenced by the discrepancies between DØ and CDF results shown in Figures 2.12 and 2.13. Results have so far proved inconclusive, largely down to available statistics in the high p_T region where theoretical predictions are more robust, and due to limited acceptance at high $|\cos\theta^*|$. This is the key distribution for discriminating different polarisation states and thus for separating acceptance corrections from spin alignment effects.

An example of the acceptance range at CDF [128] is illustrated by Figure 7.2, which shows the measured $\cos\theta^*$ distribution for J/ψ decays in the transverse momentum slice $7 \leq p_T(\text{ GeV}) < 9$, compared to the Monte Carlo templates for the two extreme polarisations.

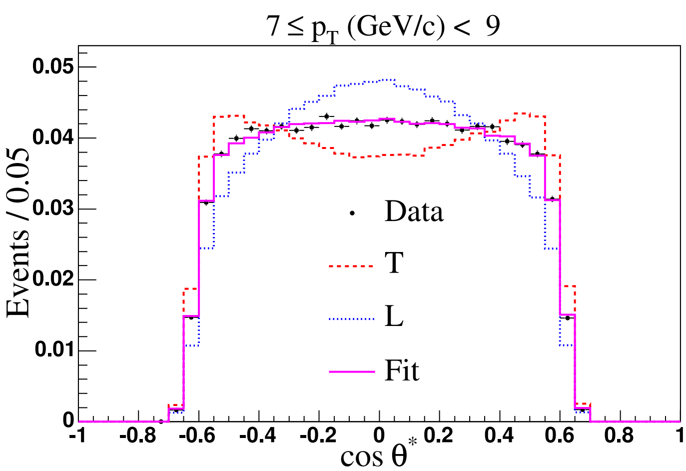

Figure 7.2: *Angular distribution for $J/\psi \to \mu\mu$ decays in the $7 \leq p_T(\text{ GeV}) < 9$ region at CDF [128], along with MC templates for longitudinal and transverse polarisations.*

The high predicted rates at ATLAS coupled with high reconstruction efficiency mean that large statistics datasets for quarkonium transverse momenta above 10 GeV will be available within weeks, rather than years, of data-taking once the detector response is well-understood. In addition, using the methods outlined in this section along with the event selection of the di-muon and single muon samples from Chapter 5, it is possible to significantly increase the range of acceptance of the $\cos\theta^*$ distribution in ATLAS. We aim to measure the polarisation of prompt vector quarkonium states, at transverse momenta far beyond that accessible at the Tevatron, with extended coverage in $\cos\theta^*$ which will allow for improved fidelity of efficiency measurements and thus reduced systematics.

Note that the feed-down from χ_J state and b-hadron decays dilute the prompt quarkonia samples we reconstruct, and these states may exhibit different spin alignment properties, hence leading to a possible effective depolarisation which is hard to estimate. The promptly produced J/ψ mesons and those that originated from B-hadron decays can be separated using the displaced decay vertices, as explained in Chapter 5. With a high production rate of quarkonia at LHC, it will be possible to place cuts to achieve a higher degree of purity of prompt J/ψ in the analysed sample, reducing the depolarising effect from B-decays, and to measure and account for the fraction of χ_J states contributing to the prompt J/ψ cross-section.

7.1.1 Methodology and acceptance corrections

Several effects need to be dealt with and incorporated into the measurement. The first is the dependence of the detector acceptance with respect to $\cos\theta^*$. For example, in a decay with a large value of $\cos\theta^*$, one muon emerges nearly in the same direction as the quarkonia, but the other is emitted almost backwards and so has a low momentum in the lab frame. With a di-muon trigger signature such as $\mu6(4)\mu4$, the second muon with a low transverse momentum is likely to fail the trigger or the selection requirements. Therefore, events with large values of $|\cos\theta^*|$ have significantly lower probability of entering the data sample.

The general idea of measuring the quarkonium polarisation is to use a template fit. This method fits a weighted superposition of two Monte Carlo generated 'templates' to the angular distribution of the data; one Monte Carlo sample contains transversely polarised events, while the other contains longitudinally polarised ones. The fitted weights between longitudinal and transverse templates will provide the measurement of the polarisation parameter α. The absence of properly weighted polarised Monte Carlo samples and the shortage of statistics in the unpolarised sample prevented us from following the analysis outlined above. We have, however, considered several effects that need to be dealt with and incorporated into the measurement.

In Chapter 5 we have shown the feasibility of measuring quarkonium production with a high rate and manageable backgrounds in both the di-muon $\mu6(4)\mu4$ and single muon $\mu10$ scenarios. As explained in Section 5.1.2, with the di-muon trigger signature such as $\mu6\mu4$, the acceptance at large values of $|\cos\theta^*|$ (where the difference between various polarisation states is the biggest) is strongly reduced, especially at low transverse momenta of quarkonium.

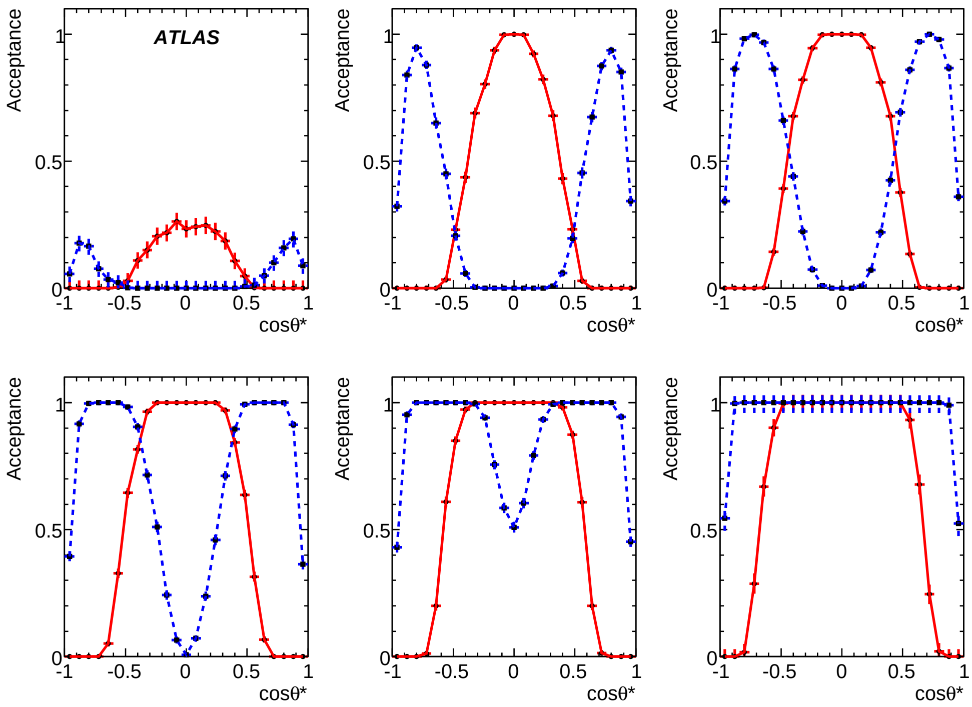

Figure 7.3: *Kinematic acceptances for J/ψ with $\mu6\mu4$ (solid red lines) and $\mu10\mu0.5$ (dashed blue lines) generator level cuts, calculated with respect to a sample with no generator level cuts on muon momenta, in slices of J/ψ p_T: left to right, top to bottom* $9-12$ *GeV*, $12-13$ *GeV*, $13-15$ *GeV*, $15-17$ *GeV*, $17-21$ *GeV, above 21 GeV.*

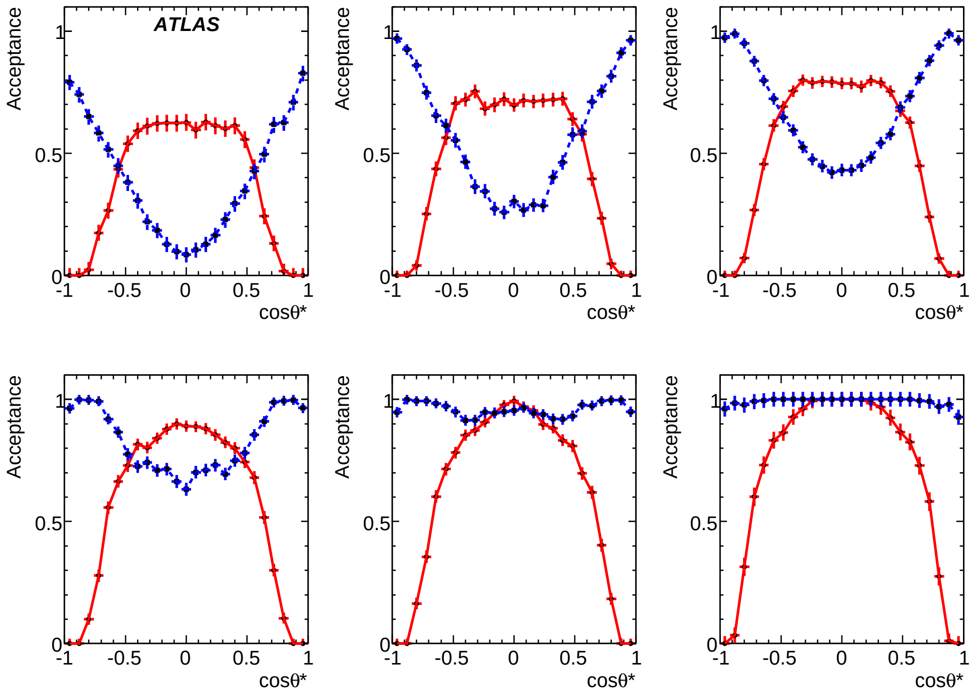

Figure 7.4: *Kinematic acceptances for* Υ *with* $\mu6\mu4$ *(solid red lines) and* $\mu10\mu0.5$ *(dashed blue lines) generator level cuts, calculated with respect to a sample with no generator level cuts on muon momenta, in slices of* Υ p_T*: left to right, top to bottom* $9-12$ *GeV,* $12-13$ *GeV,* $13-15$ *GeV,* $15-17$ *GeV,* $17-21$ *GeV, above 21 GeV.*

The kinematic acceptance $\mathscr{A}(p_T, \cos\theta^*)$ of the $\mu6\mu4$ cuts applied at generator level, with respect to the full generator-level sample with no cuts on muon transverse momenta, is shown with solid red lines for the J/ψ and Υ candidates in Figures 7.3 and 7.4 respectively, for various p_T slices of the quarkonium state. The acceptance is seen to be quite low at J/ψ and Υ p_T, below 12 GeV, but in higher p_T slices there is an area in the middle of $\cos\theta^*$ range with essentially 100% acceptance, which becomes broader with increasing p_T of quarkonium, but never goes beyond $|\cos\theta^*| \simeq 0.5$. The mass of the Υ means that its range of acceptance is somewhat broader than that of the J/ψ, but still acceptance is lacking at high values.

The acceptance for the single muon trigger sample, shown by the dashed blue lines in Figures 7.3 and 7.4, is crucially different: here the areas of 100% acceptance are at *high* $|\cos\theta^*|$, and the dip in the middle gradually fills up with increasing p_T. This sample essentially has a full acceptance at $p_T > 20$ GeV, apart from the drop at $|\cos\theta^*| > 0.95$ due to the cut of 0.5 GeV on the p_T of the track of the second muon (limited by the threshold for track reconstruction in ATLAS). The plots in Figures 7.3 and 7.4 were obtained using dedicated generator-level Monte Carlo samples, and the error bars shown in the figure reflect both statistical errors and the uncertainties due to possible dependence on η coverage effects. Note that for this study we look specifically at high p_T quarkonia, so the available statistics at 10 pb^{-1} for Υ measurements are particularly low.

The simulated "raw" measured distributions $dN^{\text{raw}}/d\cos\theta^*$, for the same slices of J/ψ and Υ transverse momenta, are shown in Figures 7.5 and 7.6. These figures show how the J/ψ and Υ polarisation distributions look when we first analyse the two distributions without efficiency and acceptance corrections. The input samples to this study were generated with zero quarkonium polarisation. As before, solid red and dashed blue lines represent the events selected by the di-muon $\mu6\mu4$ and the single muon $\mu10$ triggers respectively.

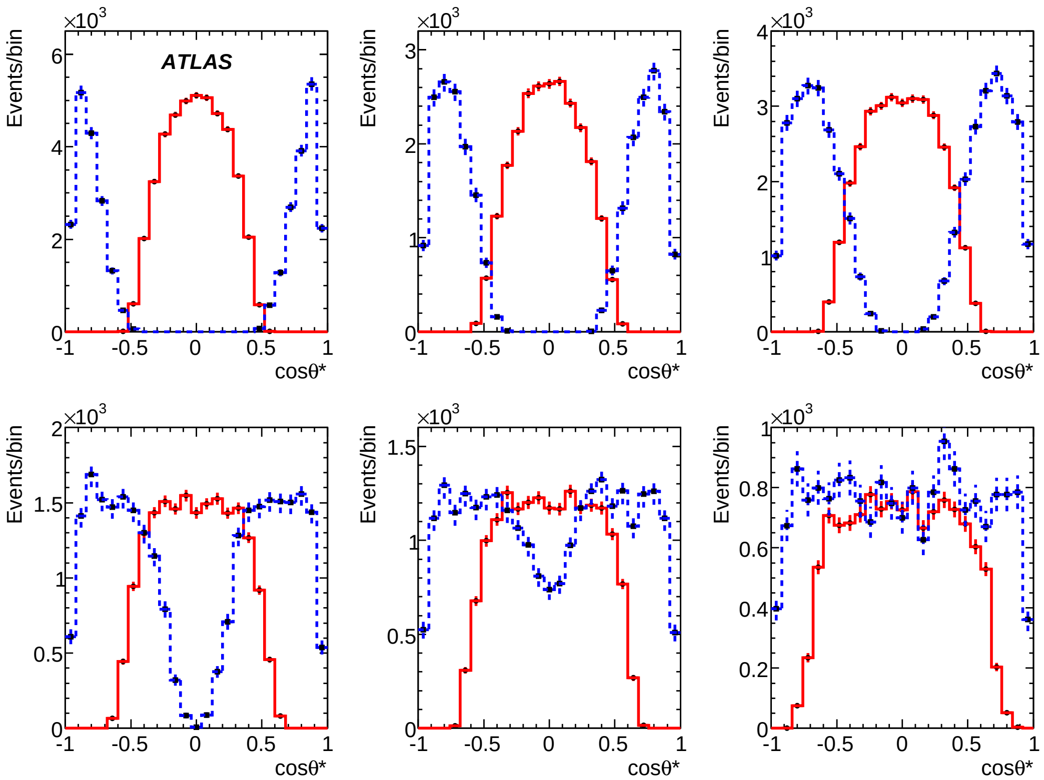

Figure 7.5: *Measured* $\cos\theta^*$ *distributions for* $\mu6\mu4$ *(solid red lines) and* $\mu10$ *(dashed blue lines) triggered events for* J/ψ *candidates, in the same* p_T *slices of the* J/ψ *as in Figure 7.3. The simulated data sample is unpolarised. Statistics correspond to 10 pb*$^{-1}$.

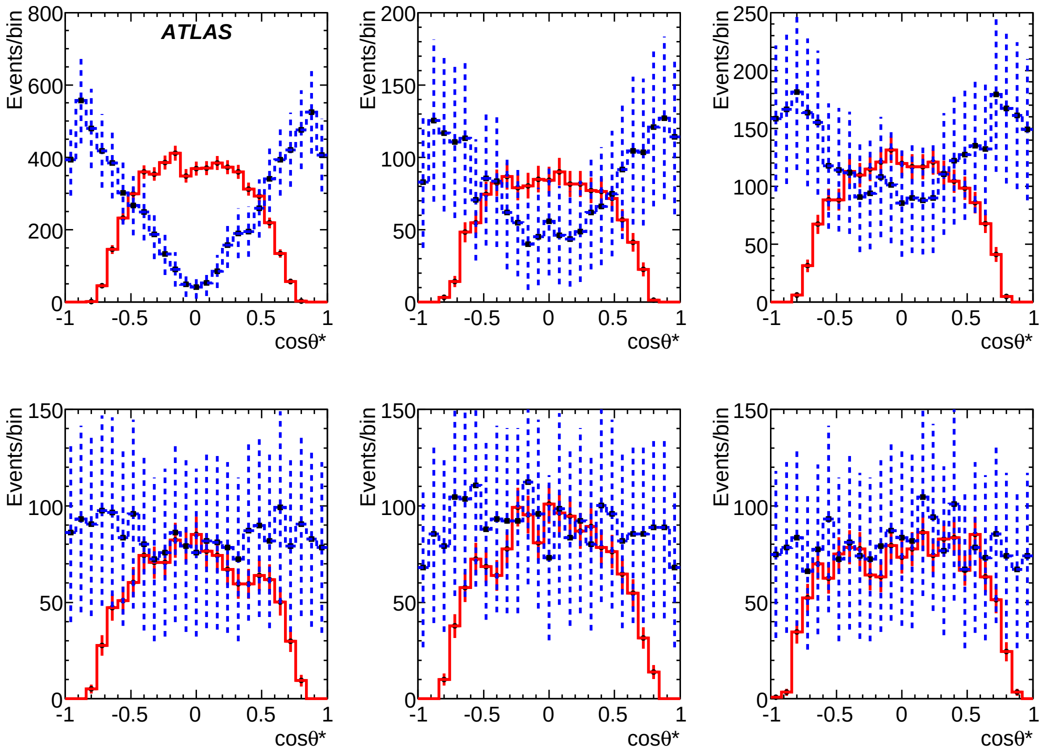

Figure 7.6: *Measured* $\cos\theta^*$ *distributions for* $\mu6\mu4$ *(solid red lines) and* $\mu10$ *(dashed blue lines) triggered events for* Υ *candidates, in the same* p_T *slices of the* Υ *as in Figure 7.4. The simulated data sample is unpolarised. Statistics correspond to 10 pb*$^{-1}$.

What is immediately clear from the Υ datasets in Figure 7.6 is that the Υ analysis is statistically limited at these integrated luminosities. The di-muon sample has visually larger statistical errors than the corresponding plots for J/ψ, and the single muon sample is dominated by errors from the systematics caused by decreased rates (at these high p_T) and the increased background (see Figure 5.21(c)).

Note that whilst the large errors on the single muon sample reflect the expected fluctuations at such integrated luminosities, the datapoints themselves follow a very reasonable distribution. This is because in this study the generated statistics available corresponding to the background processes were far below that which would accompany such an Υ yield, and so were scaled up in order to correctly estimate the errors.

This has had the effect however, of meaning that whilst the errors themselves are correct, the datapoints themselves do not show significant fluctuations within these errors, as would be the case with real data and a high statistics background. As such, this effectively renders the single muon sample unusable for polarisation studies of Υ at these integrated luminosities in real data, and we are forced to use just the di-muon analysis sample in the polarisation fit.

The raw numbers of measured events in the $\mu 10$ sample were obtained by fitting the invariant mass distributions with a gaussian peak and a linear background, for each bin of $\cos\theta^*$ in each p_T slice. With the estimated signal-to-background ratios shown in Figure 5.21(a), this causes an increase in the statistical errors, typically by a factor of 2.

7.1.2 Measurement results

The measured distributions are corrected for acceptance and trigger efficiencies to produce the corrected distributions $dN^{\rm cor}/d\cos\theta^*$ according to the following formula:

$$\frac{dN^{\rm cor}}{d\cos\theta^*} = \frac{1}{\mathscr{A}(p_T, \cos\theta^*)\cdot\varepsilon_1\cdot\varepsilon_2}\cdot\frac{dN^{\rm raw}}{d\cos\theta^*} \tag{7.3}$$

Here ε_1 is the trigger and reconstruction efficiency, while ε_2 denotes the efficiency of background suppression cuts for each sample, as defined in Table 5.3. Their values have been averaged over the accessible phase space within the relevant p_T slice. Studies have shown that while ε_1 depend on p_T (cf. Figure 5.13(a)), ε_2 remain essentially constant over the phase space of interest. The efficiencies ε_1 and ε_2 for both samples are listed in Table 7.1, while the acceptances $\mathscr{A}(p_T, \cos\theta^*)$ are as shown in Figure 7.3 and 7.4.

p_T, GeV	$9-12$	$12-13$	$13-15$	$15-17$	$17-21$	>21
$\varepsilon_1(\mu6\mu4)$, %	67 ± 1	75 ± 1	77 ± 1	78 ± 1	79 ± 1	80 ± 1
$\varepsilon_2(\mu6\mu4)$, %	90 ± 1	90 ± 1	90 ± 1	90 ± 1	90 ± 1	90 ± 1
$\varepsilon_1(\mu10)$, %	86 ± 1	89 ± 1	90 ± 1	90 ± 1	90 ± 1	90 ± 1
$\varepsilon_2(\mu10)$, %	76 ± 1	76 ± 1	76 ± 1	76 ± 1	76 ± 1	76 ± 1

Table 7.1: *Efficiencies for the $\mu6\mu4$ and $\mu10$ samples, averaged over each of the six p_T slices under consideration.*

At high p_T the two samples increasingly overlap, thus allowing for a cross-check of acceptance and efficiency corrections. Particularly for cross-normalisation of the two samples the areas of 100% acceptance play an important role. However, for measurement purposes the $\mu6\mu4$ samples are used whenever possible due to their smaller backgrounds, complemented by $\mu10$ samples at high $\cos\theta^*$. In order to achieve this, the distributions shown in Figure 7.5 were appropriately masked in $\cos\theta^*$ where the two samples overlapped and then the results of both datasets combined. Where possible, we use the $\mu10$ sample to provide all data at large $|\cos\theta^*|$, with $\mu6\mu4$ solely being used at small $|\cos\theta^*|$. This is particularly noticeable in the first plot in Figure 7.7. The combined distributions $dN^{\mathrm{cor}}/d\cos\theta^*$, corrected according to Equation 7.3,

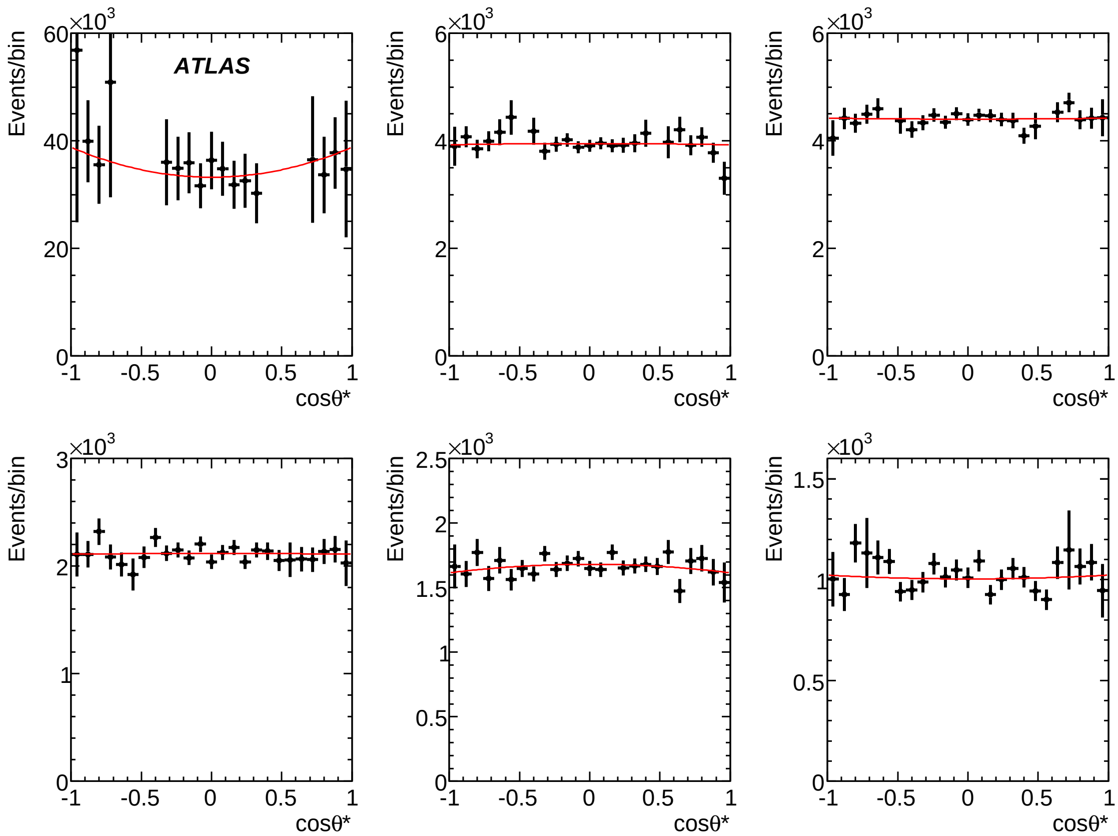

Figure 7.7: *Combined and corrected distributions in J/ψ polarisation angle $\cos\theta^*$, for the same p_T slices as in Figure 7.3. The data sample is unpolarised. Statistics correspond to 10 pb^{-1} of data.*

are shown in Figure 7.7.

The errors shown in the plots include the statistical errors on the raw data, as well as the uncertainties on the acceptance and efficiencies. These $\cos\theta^*$ distributions are fitted using

Equation 7.1, with α and C as free parameters for each p_T slice. The corresponding fit results are presented in Table 7.2, with constant C rescaled to output the measured cross section σ, corresponding to an integrated luminosity of 10 pb^{-1}.

A similar analysis can be (and was) performed for the polarisation and cross section of Υ, but at the integrated luminosity of 10 pb^{-1} these measurements are expected to be far less precise than in J/ψ case. The main reasons are lower Υ cross sections at high transverse momenta, and higher backgrounds for the $\mu 10$ sample. The limited acceptance of the $\mu 6 \mu 4$ sample at high $|\cos\theta^*|$ makes a precise measurement difficult. Nevertheless, the corrected Υ distributions from consideration of the $\mu 6 \mu 4$ sample are shown in Figure 7.8.

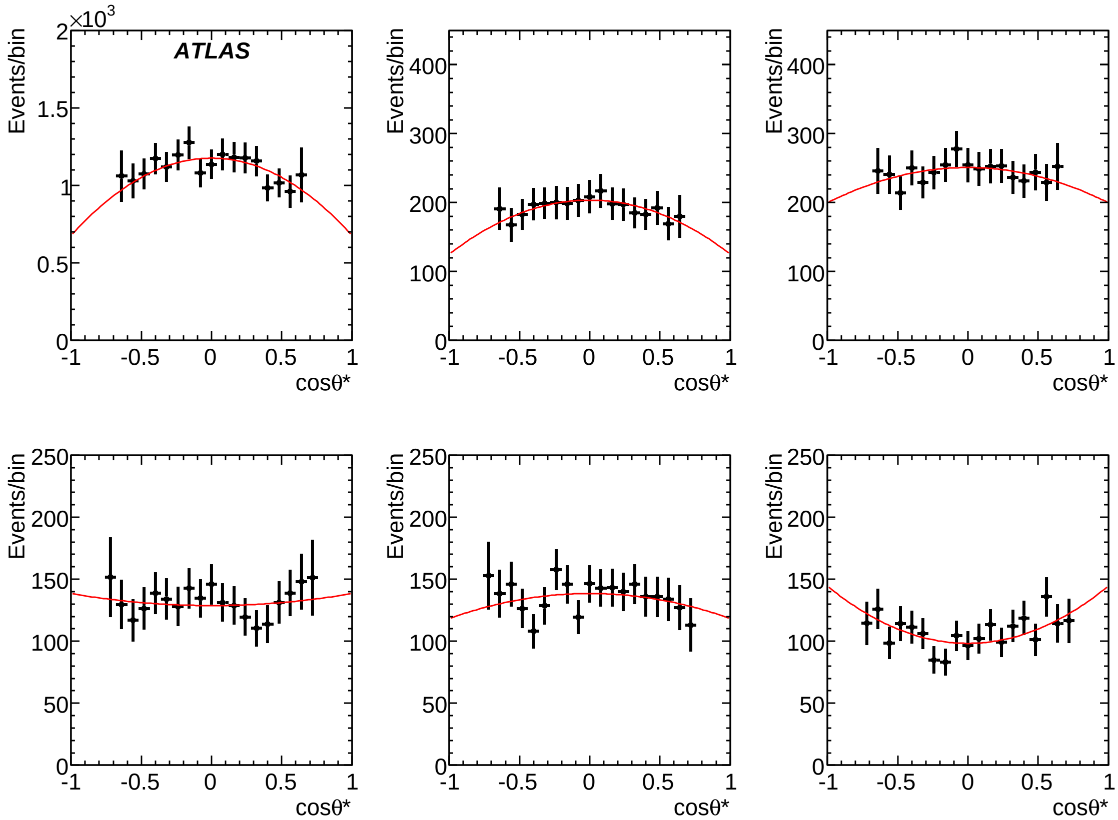

Figure 7.8: *Corrected distributions in polarisation angle $\cos\theta^*$, for unpolarised Υ mesons, in the same slices of Υ transverse momentum as in Figure 7.4. Only the $\mu 6 \mu 4$ sample has been used. Statistics correspond to 10 pb^{-1} of data.*

Again the normalisation is matched to the integrated luminosity of 10 pb^{-1} to output the corrected cross-section and these are also tabulated, in addition to the polarisation measure-

Sample	p_T, GeV	$9-12$	$12-13$	$13-15$	$15-17$	$17-21$	>21
J/ψ, $\alpha_{\text{gen}}=0$	α	0.156 ±0.166	-0.006 ±0.032	0.004 ±0.029	-0.003 ±0.037	-0.039 ±0.038	0.019 ±0.057
	σ, nb	87.45 ±4.35	9.85 ±0.09	11.02 ±0.09	5.29 ±0.05	4.15 ±0.04	2.52 ±0.04
J/ψ, $\alpha_{\text{gen}}=+1$	α	1.268 ±0.290	0.998 ±0.049	1.008 ±0.044	0.9964 ±0.054	0.9320 ±0.056	1.0217 ±0.088
	σ, nb	117.96 ±6.51	13.14 ±0.12	14.71 ±0.12	7.06 ±0.07	5.52 ±0.05	3.36 ±0.05
J/ψ, $\alpha_{\text{gen}}=-1$	α	-0.978 ±0.027	-1.003 ±0.010	-1.000 ±0.010	-1.001 ±0.013	-1.007 ±0.014	-0.996 ±0.018
	σ, nb	56.74 ±2.58	6.58 ±0.06	7.34 ±0.06	3.53 ±0.04	2.78 ±0.03	1.68 ±0.02
Υ, $\alpha_{\text{gen}}=0$	α	-0.42 ±0.17	-0.38 ±0.22	-0.20 ±0.20	0.08 ±0.22	-0.15 ±0.18	0.47 ±0.22
	σ, nb	2.523 ±0.127	0.444 ±0.027	0.584 ±0.029	0.330 ±0.016	0.329 ±0.015	0.284 ±0.012

Table 7.2: *J/ψ and Υ acceptance and efficiency-corrected measured polarisation and cross sections in slices of p_T, for a range of polarisation scenarios, with an integrated luminosity of 10 pb^{-1}.*

ment, in the last section of Table 7.2. With the integrated luminosity increased by an order of magnitude the $\mu10$ sample should become useful, and the estimated errors on Υ polarisation measurement could be reduced by a factor of 5.

To further check our ability to measure the spin alignment of J/ψ, the raw distributions shown in Figure 7.3 were reweighted to emulate transversely polarised ($\alpha_{\text{gen}}=+1$) and longitudinally polarised ($\alpha_{\text{gen}}=-1$) J/ψ samples, representing the extremes of possible polarisations that could be measured, and the analysis described above was repeated. The results are shown in Figure 7.9 and in the middle two sections of Table 7.2. Due to limited statistics, this extension is not performed for Υ.

The errors shown in Figures 7.7, 7.8 and 7.9, and in Table 7.2, include the statistical uncertainties on the measured numbers of events as well as statistical errors stemming from the uncertainties on acceptances and efficiencies described above.

The overall uncertainty on the integrated luminosity needs to be added to all measured cross

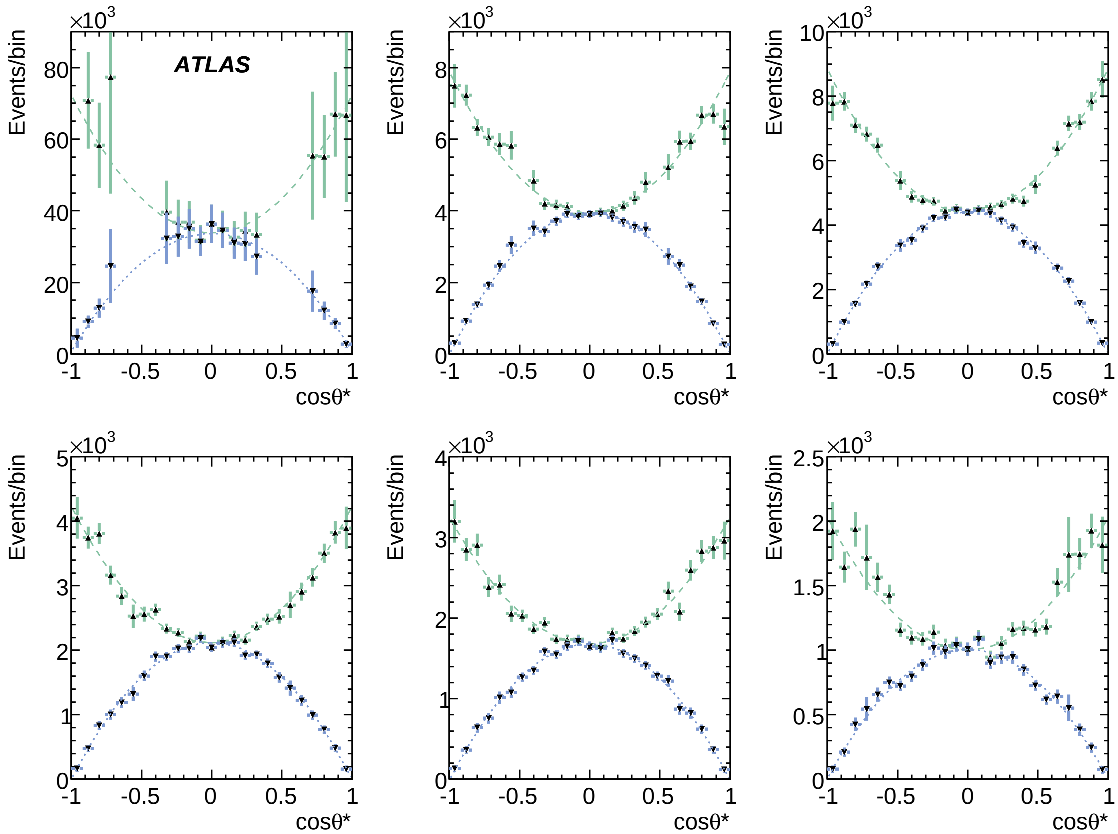

Figure 7.9: *Combined and corrected distributions in polarisation angle* $\cos\theta^*$*, for longitudinally (dotted lines) and transversely (dashed lines) polarised* J/ψ *mesons, in the same* p_T *slices as in Figure 7.3. Statistics correspond to 10* pb^{-1} *of data.*

sections, and is expected to be rather large during the initial LHC runs. This uncertainly will not, however, affect the relative sizes of the cross sections measured in separate p_T slices, or the measured values of the polarisation coefficient α.

Systematic effects have also been studied, such as the influence of finite resolution in p_T and $\cos\theta^*$, changes in binning, details of the functions used for fitting the invariant mass distributions, and variations of cuts used for background suppression. Their respective uncertainties on the measured values of α and σ have been found not to exceed a small fraction of the quoted errors, and have thus been deemed negligible.

In conclusion, with the integrated luminosity of 10 pb^{-1} it should be possible to measure the polarisation of J/ψ with the precision of order $0.02-0.06$, depending on the level of polarisation itself, in a wide range of transverse momenta, $p_T \simeq 10-20$ GeV and beyond, in the region important for the determination of the underlying quarkonium production mechanism. This level of polarisation precision is equal to that of currently published Tevatron results (but at higher p_T in ATLAS) and is more that sufficient to distinguish between the leading theoretical production models. By using a totally data-driven method of measuring the true polarisation, these measurements should also be more reliable than methods requiring Monte Carlo based template fits.

In addition, the production cross-section of J/ψ can be measured in bins of p_T to an accuracy of approximately 1%. In case of Υ, the expected precision is somewhat lower at this integrated luminosity. We expect a polarisation measurement precision of order 0.20, and an error on the cross-section of $\sim 4-6\%$, requiring 100 pb^{-1} of data to match the precision possible for the J/ψ in ATLAS and previous Tevatron measurements for Υ. In both cases, the p_T dependence of the cross-section should be measured reasonably well with just 10 pb^{-1}.

7.2 Analysis of χ_c and χ_b production

Once the reconstruction of J/ψ and Υ candidates has been achieved it is possible to do further analysis on these quarkonium states to determine whether they came from the decay of a χ_J state. Reconstructing $\chi_{c,b}$ candidates requires associating a reconstructed J/ψ (or Υ) with the photon emitted from the $\chi_{c,b}$ decay.

Quarkonium states with even C parity, such as $\eta_{c,b}$ and $\chi_{c,b}$, have a strong coupling to the colour-singlet two-gluon state, and hence a significantly higher production cross section than vector quarkonia. Their dominant production mechanism in the phase space area accessible in ATLAS is via the subprocess shown in Figure 4.1(c) in Chapter 2. Their detection, however, is rather more difficult than for J/ψ and Υ due to the absence of fully leptonic decays.

About 30 to 40 % of J/ψ and Υ are expected to come from decays $\chi_c \to J/\psi\gamma$ and $\chi_b \to \Upsilon\gamma$. Unfortunately, the energies of these photons tend to be quite small. The ability of ATLAS to detect these photons and resolve various χ states is analysed in this section.

7.2.1 Radiative decays of χ_c and χ_b states

Taking the prompt J/ψ and Υ candidates selected in any given event as in Chapter 5, we loop over all objects reconstructed in the `egamma` container, which contains candidate electrons and photons in an event. To reduce the number of fake photons we consider, we request that only those egamma objects identified as a photon candidate are stored. The reconstruction and identification of photons is based on analysis of electromagnetic calorimeter and track based information, and is detailed in reference [129].

For χ_c reconstruction, each selected J/ψ candidate is combined with every reconstructed and identified photon candidate in the event, and the invariant mass of the $\mu\mu\gamma$ system is calculated using the information from the electromagnetic calorimeter. No explicit cut is applied to the p_T of the photon. The transverse momentum distribution for all identified photon candidates in events with a prompt J/ψ, as measured by the ATLAS electromagnetic calorimeter, is shown by the light grey histogram in Figure 7.10(a).

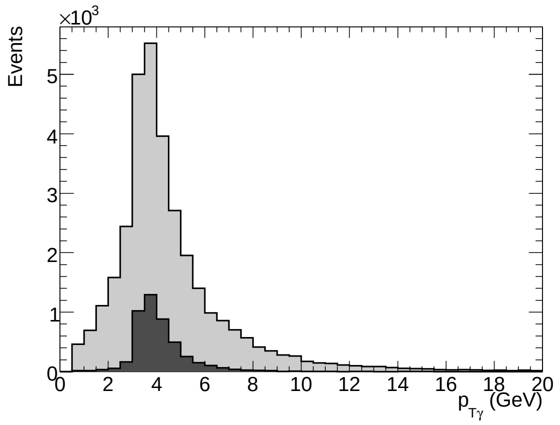

(a) (b)

Figure 7.10: *(a) Transverse momentum distribution of photons reconstructed in prompt J/ψ events before (light histogram) and after (dark histogram) the cut on the opening angle α between the photon and the J/ψ momentum direction. (b) Distribution of* $\cos\alpha$ *for each reconstructed γ in an event. All true photons from $\chi \to J/\psi\gamma$ decays have* $\cos\alpha >$ 0.97. *The sample corresponds to an integrated luminosity 10 pb^{-1}.*

The $\mu\mu\gamma$ system is considered to be a χ candidate, if the difference ΔM between the invariant masses of the $\mu\mu\gamma$ and $\mu\mu$ systems lies between 200 and 700 MeV (chosen because of the known monochromatic energy of the photon emitted in true $\chi \to J/\psi\gamma$ decays), and the cosine of the opening angle α between the J/ψ and γ is larger than 0.97.

The last requirement comes from the observation that for the correct $\mu\mu\gamma$ combinations, the angle α is usually very small (see reconstructed distribution in Figure 7.10(b)). By analysing Monte Carlo information, it was found that all of the true χ decays were found in the peak near $\cos\alpha = +1$, with the long tail in the reconstructed distribution representing the combinatorial background (note that the *x*-axis of Figure 7.10(b) has been cropped so that only the range $0.8 - 1.0$ is viewable), the background contributions extending smoothly down to $\cos\alpha = -1$.

The transverse momentum distribution for those photon candidates satisfying the above requirements is presented in Figure 7.10(a) by the dark grey histogram. With these cuts, the combinatorial background is strongly reduced but it becomes clear that the efficiency to reconstruct χ in this decay mode using calorimetry is relatively low (as is expected from Tevatron results). ATLAS is not designed with efficiency in measuring very low transverse momentum photons in mind, and as such the efficiency in reconstructing them drops sharply below ~ 3 GeV, as illustrated by Figure 7.10(a). The kinematics of the decay mean the radiated photon enters the calorimetry between the two muons in the J/ψ decay. The small muon opening angle means that photons below this p_T threshold are largely indistinguishable from the muon energy deposits (see Figure 5.11). Despite this, we calculate the invariant mass of all $J/\psi(\mu\mu)\gamma$ pairs in the dataset, and plot the mass difference $\Delta M = M(\mu^+\mu^-\gamma) - M(\mu^+\mu^-)$ in order to identify $\chi_c(nJ)$ signals. Figure 7.11 shows the ΔM distribution of the $\mu\mu\gamma$ and $\mu\mu$ systems for the selected χ_c decay candidates.

Shown as arrows extending upwards are the expected mean positions of the peaks corresponding to χ_0, χ_1 and χ_2 signals (at 318, 412 and 460 MeV, respectively). The dark grey histogram shows the background contribution from indirect J/ψ production from *B*-hadron decays (some of which survive the pseudo-proper time cut), when combined with photon candidates in an event.

The solid line in Figure 7.11 is the result of a simultaneous fit to the measured distribution, with the three peak positions fixed at their expected values, but with freely varying

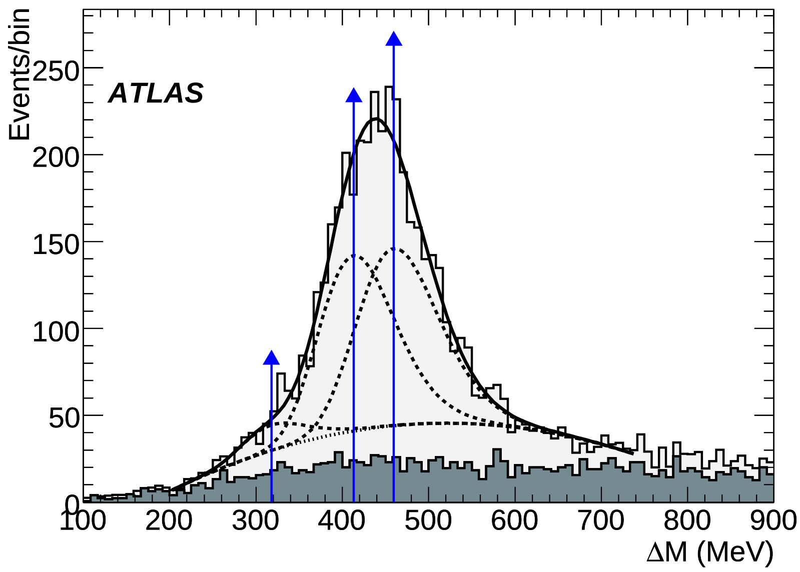

Figure 7.11: *Difference in invariant masses of $\mu\mu\gamma$ and $\mu\mu$ systems in prompt J/ψ events with $bb \to \mu 6\mu 4X$ background surviving cuts (dark grey). The arrows represent the true signal peak positions, and the lines show the results of the fit described in the text. Event yields correspond to an integrated luminosity of 10 pb^{-1}.*

relative normalisations and with a common resolution function $\sigma(\Delta M)$. The resolution in $\sigma(\Delta M)$ is expected to increase with increasing ΔM, and was empirically parameterised as $\sigma(\Delta M) = a \cdot \Delta M + b$. The dashed lines show the shapes of individual peaks and of the background continuum from the sum of the indirect J/ψ decay background described above, and combinatorial background from fake or unrelated photons in an event.

The fit parameters are the heights of the three gaussian peaks h_0, h_1, h_2, the constants a and b, and the three parameters describing the smooth polynomial background. The true amplitudes of the peaks (15, 123 and 87, respectively) are reproduced reasonably well:

$$\begin{aligned} h_0 &= 15 \pm 3(\text{stat.}) \pm 10(\text{syst.}), \\ h_1 &= 101 \pm 4(\text{stat.}) \pm 12(\text{syst.}), \\ h_2 &= 103 \pm 4(\text{stat.}) \pm 9(\text{syst.}), \end{aligned} \tag{7.4}$$

with a strong negative correlation between the last two. The resolution is found to increase from about 35 MeV at χ_0 to about 48 MeV at χ_2, The overall reconstruction efficiency of χ_c states at ATLAS is estimated from this study to be about 4%. It may be possible to significantly improve the resolution by using photon conversions (software still in development), but this is unlikely to yield a big increase in efficiency. With 10 pb^{-1} of data in ATLAS it will thus be possible to observe χ_c states, but the low efficiency means more data will need to be accumulated to perform any detailed studies.

The procedure of reconstructing χ_b decays into $\Upsilon + \gamma$ is the same as in the charmonium case, except the di-muon pair is required to be an Υ candidate. However, the higher di-muon mass and hence smaller expected boost makes the photon much softer and hence more difficult to detect. With the available simulated statistics (50,000 events corresponding to 10 pb^{-1}), only 20 χ_b candidates have been found in the appropriate mass window, which gives an efficiency estimate of 0.03%. As such, no further analysis of these states is able to be performed. In order to reliably observe $\chi_b \rightarrow \Upsilon + \gamma$ decays, integrated luminosity of at least 1 fb^{-1} will be needed.

8

Conclusions and outlook

During the initial run of the LHC with the luminosity of 10^{31} cm^{-2} s^{-1}, one day of running roughly corresponds to the integrated luminosity of 1 pb^{-1}. With the $\mu6\mu4$ trigger and this integrated luminosity, one would then expect about 15,000 $J/\psi \rightarrow \mu\mu$ and 2,500 $\Upsilon \rightarrow \mu\mu$ recorded events. If the $\mu4\mu4$ trigger is used, these numbers would increase to about 17,000 and 20,000 respectively, with these additional events mainly concentrated at the lower end of the quarkonium transverse momenta, with the exact yield being strongly dependent on the behaviour of the low p_T threshold of the muon triggers. Additional, largely independent statistics will be provided by the $\mu10$ trigger: 16,000 J/ψ and 2,000 Υ with transverse momenta above about 10 GeV, with distributions similar to those from the $\mu6\mu4$ samples. Quite separate from these, another 7,000 of $J/\psi \rightarrow \mu\mu$ events are expected from b-decay events.

Initial data studies with quarkonium will focus (as in other areas) on detector commissioning and performance. I have presented in this thesis a wide variety of areas where analysis of quarkonium signatures are already being used for data quality monitoring and performance studies. The J/ψ and Υ will be key for low p_T trigger efficiency determination in the tag-and-probe method as well as the 'probe-and-probe' method introduced in Section 6.3. Similarly, quarkonia are also being used in ATLAS for monitoring of the high level trigger algorithms.

Before any precision physics studies can begin, the various sub-detectors of ATLAS must be well-aligned, and the presence of distortions or any additional material must be identified and understood. The study of systematic biases in the invariant mass distributions of the J/ψ and Υ, across a range of variables, can quickly and precisely identify material or alignment problems, reconstruction software bugs, and can be used to calibrate the detector response.

Most importantly, as I have discussed in this thesis, these calibrations can be performed to a relatively high level of precision at very small integrated luminosities. Single muon efficiencies as a function of transverse momentum can, for example, be measured to an accuracy of a few percent with just a few hours of good quality data.

With a relatively well-understood detector and an integrated luminosity of about 10 pb^{-1}, recorded numbers of $J/\psi \to \mu\mu$ and $\Upsilon \to \mu\mu$ will be roughly equal to the statistics considered in Chapters 5 and 7. Based on studies in the previous chapter, this should be enough data to allow for first measurements of the cross sections, p_T and η distributions and measurement of the polarisation of J/ψ and Υ as functions of their transverse momenta. With these statistics, the p_T dependence of the cross section for both J/ψ and Υ should be measured reasonably well, in a wide range of transverse momenta, $p_T \simeq 10-50$ GeV, far beyond the ranges previously measured.

The precision of J/ψ polarisation measurement can be expected to reach $0.02-0.06$ (depending on the level of polarisation itself), which is competitive with the best measurements published from the Tevatron, despite the ATLAS measurement precision being based on less than $1/100^{\text{th}}$ the integrated luminosity. This level of precision, combined with the reduced possibility of systematic errors due to the increased acceptance in $\cos\theta^*$, will mean ATLAS will be able to easily distinguish between different theoretical production models, both in the area covered by the Tevatron and at higher transverse momenta than ever before probed for this measurement. This means ATLAS will be able to make world-leading contributions to the physics of quarkonium production with 10 pb^{-1} of data. The expected error on Υ polarisation with a 10 pb^{-1} is unlikely to be better than about 0.20, requiring an order of magnitude increase in recorded data to make accurate measurement. Also at the 10 pb^{-1} stage, first attempts may be made to understand the performance of the electromagnetic calorimetry at very low photon energies (< 3 GeV), and to try and reconstruct χ_c states from their radiative decays.

With an integrated luminosity of of 100 pb^{-1}, the range of J/ψ and Υ transverse momentum spectra accessible at ATLAS are expected to reach about 100 GeV and possibly beyond. With several million $J/\psi \to \mu\mu$ and more than 500,000 of $\Upsilon \to \mu\mu$ decays, and (hopefully) good understanding of the detector, high precision polarisation measurements, at the level of few percent, should become possible for both J/ψ and Υ.

This means that with 100 pb^{-1} J/ψ and Υ polarisation will be measured more accurately than ever before, with reduced systematics, at transverse momenta where theoretical predictions are at their most predictive. As such, it should be possible with this measurement to make a very strong statement regarding the underlying production mechanism behind the formation of quark-antiquark bound states, and by association improve our understanding of QCD. At these integrated luminosities $\chi_b \to \Upsilon\gamma$ decays should also become observable.

Further increases in the integrated luminosity should make it possible to observe the resonant production of J/ψ meson pairs in the mass range of the Υ system. During the future high luminosity running, the need to keep event rates manageable will cause the increase of thresholds of relevant single- and di-muon triggers, and the prescaling of lower threshold triggers. This will further expand the range of reachable transverse momenta and allow further tests of the production mechanisms, as well as make χ_b reconstruction easier. This era will also be dominated by the precision measurement of inclusive and exclusive B hadron production cross-sections, following on from an improved understanding of the J/ψ, Υ and inclusive c and b production rates.

"The electron is not as simple as it looks."

William Lawrence Bragg, 1890 – 1971.

A

Bremsstrahlung recovery

The reconstruction of tracks in the Inner Detector is conducted by the use of statistical algorithms which combine a series of discrete hits on active surfaces in the Pixel, SCT and TRT layers into continuous paths based on a consideration of charged particle dynamics in a stationary magnetic field and the effects of multiple scattering and energy loss. These algorithms try to efficiently recreate as many particle tracks as possible whilst trying to minimise the possibility of producing fake tracks, where hits from one track are associated with another. Clearly the amount of information about the paths taken by the particles and any physical processes they undergo during propagation is limited, and so track reconstruction is typically an exercise in maximising the information we have using statistical techniques.

The effects of multiple scattering are well-understood and the small changes caused to the direction of flight of the particle are approximately modelled by a gaussian distribution. Bremsstrahlung[1)] energy losses are caused by the emission of electromagnetic radiation from the deceleration of a charged particle when deflected by another charged particle. The energy of the emitted photon is inversely proportional to the mass of the particle squared, so is of particular importance for electrons. An electron passing through the Inner Detector will emit bremsstrahlung as it crosses material which can cause very large distortions in the track which would not be predicted by track reconstruction algorithms.

Radiation length X_0 is defined as the mean path for an electron to travel before it loses all but $1/e$ of its energy to bremsstrahlung. Figure 3.6 summarises the amount of material present in the Inner Detector in units of radiation length. The amount of material implies the existence of a significant amount of bremsstrahlung which will affect the reconstruction of electron tracks, leading to reduced signal resolution for a wide variety of processes.

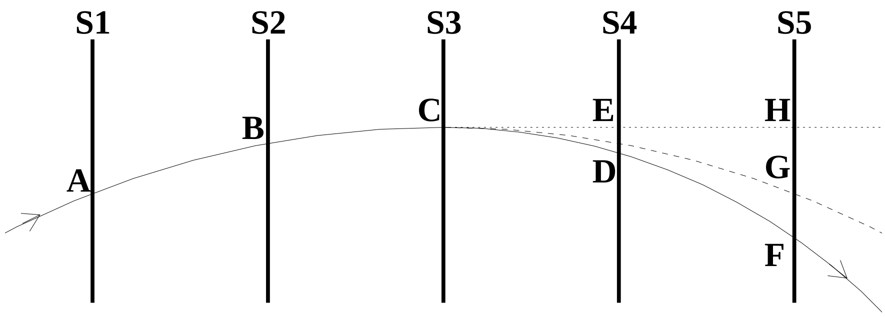

Figure A.1: *Illustration of the path of a charged particle through detector layers, in a magnetic field. Point C represents the position where bremsstrahlung occurred, with point F the position of the particle at S5. Point G represents where the particle would have intersected S5 in the absence of bremsstrahlung, point H its position in the absence of a magnetic field.*

Figure A.1 shows an illustration of a charged track traversing a magnetic field. If the particle undergoes bremsstrahlung at point C, the track of the particle will have a smaller radius of curvature after that point, ending at point F rather than point G. A tracking algorithm not taking

[1)] From the German for 'braking radiation'.

into account the possibility of bremsstrahlung will then obtain a track fit which underestimates the particle momentum.

Kalman filtering

A particle track can be considered a dynamic system where the state of the system at any given time is defined by the track parameters and the dynamics (the motion of a charged particle in a stationary magnetic field) are well-understood. The Kalman filtering algorithm [130] is a recursive filter which takes the estimated hit position at the current time from propagation of the particle using known dynamics and combines it with information of the actual measured hit, weighted in combination with information about measurement error and process noise (for example, bremsstrahlung) to provide an updated estimate for the real hit position.

The filtering method proceeds via three main steps:

1. Track parameters y and covariance matrix C are extrapolated from current layer $k-1$ to layer k.

$$y_{k-1} \rightarrow y_k, \qquad C_{k-1} + Q_{k-1} \rightarrow C_k^- \tag{A.1}$$

   Here Q_k is the covariance matrix of the Kalman system noise, which may incorporate such effects as bremsstrahlung.

2. Calculation of Kalman gain K_k at layer k.

$$K_k = \frac{C_k^-}{C_k^- + V_k} \tag{A.2}$$

3. Perform measurement update, using measurement m_k at layer k.

$$y_k = y_k^- + K_k(m_k - y_k^-), \qquad C_k = (1 - K_k)C_k^- \tag{A.3}$$

The Kalman filtering technique is efficient, but relies on process noise and measurement noise being gaussian in distribution and independent of each hit to be optimal. Whilst measurement noise can be considered gaussian and independent at each detector layer, the distribution of energy of electrons that have undergone bremsstrahlung is far from gaussian and the effects of bremsstrahlung are 100% correlated — once an electron has emitted a photon, this information must be considered at each detector layer thereafter.

An accurate model of fractional energy remaining after bremsstrahlung is given by the Bethe-Heitler [131] distribution:

$$f(z) = \frac{(-\ln(z))^{c-1}}{\Gamma(c)} \qquad c = \frac{t}{\ln 2} \tag{A.4}$$

where t is the amount of material traversed in radiation lengths, z is the fraction of energy remaining after bremsstrahlung and $\Gamma(c)$ is the standard Gamma function. Figure A.2 shows the behaviour of the Bethe-Heitler function with z for a range of material thicknesses.

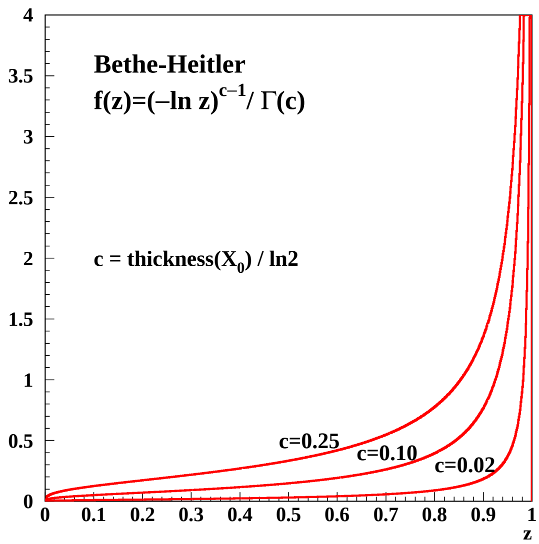

Figure A.2: *Variation of the Bethe-Heitler distribution with material thickness c (taken from reference [132]).*

A simple treatment of radiating track reconstruction could use Kalman filtering with bremsstrahlung modelled by a gaussian distribution with width and rms equal to that of the true bremsstrahlung distribution. However, this is insufficient, as the proper probability distribution needs to be taken into account for proper track reconstruction. For example, on rare occasions a single bremsstrahlung photon can take away almost all the energy of an electron.

A.1 Studies with a standalone model

Effectively, bremsstrahlung just changes one track parameter — energy. All other track parameters may be consequently modified by this change, but are done so according to the standard dynamics. With this in mind, a one-dimensional model was implemented with bremsstrahlung modelled by a Bethe-Heitler distribution and a gaussian measurement error of 3% at ten detector surfaces. All particles begin with 100 units of energy and pass through the detectors, at each layer k having an energy $x_k = z.x_{k-1}$ where z is taken randomly from the bremsstrahlung distribution. Due to computational difficulties resulting from calculation of Equation A.4, an approximation

$$f(z) = c(1-z)^{c-1} \tag{A.5}$$

with similar behaviour is used in the model. Each measurement we take has a covariance $V_k = \sigma_m^2$ so that $m_k = x_k + \sigma_m$. Bremsstrahlung noise can be treated by setting $z = z_0 + v\sigma(z)$, where z_0 is the median of the bremsstrahlung distribution and v is a gaussian variable with unit sigma mapped onto the distribution $f(z)$:

$$G(v) = F(z) \equiv \int_{-\infty}^{z} dz' f(z') \implies v = G^{-1}(F(z)) \tag{A.6}$$

and so:

$$\sigma(z) = \frac{z - z_0}{G^{-1}(F(z))} \tag{A.7}$$

In this way we may use the formalism of the Kalman filter but map onto it a non-gaussian bremsstrahlung distribution (see Figure A.3 for illustration of this mapping). At each measurement layer a single parameter fit is performed to flag hits that may be associated with a bremsstrahlung event. If no candidate is detected, standard Kalman filtering is used, but in the case of bremsstrahlung activity the energy fraction z is used to calculate the effective system noise following the procedure in Figure A.3.

Figure A.4 shows the result of applying this technique to energy measurements in the 1D

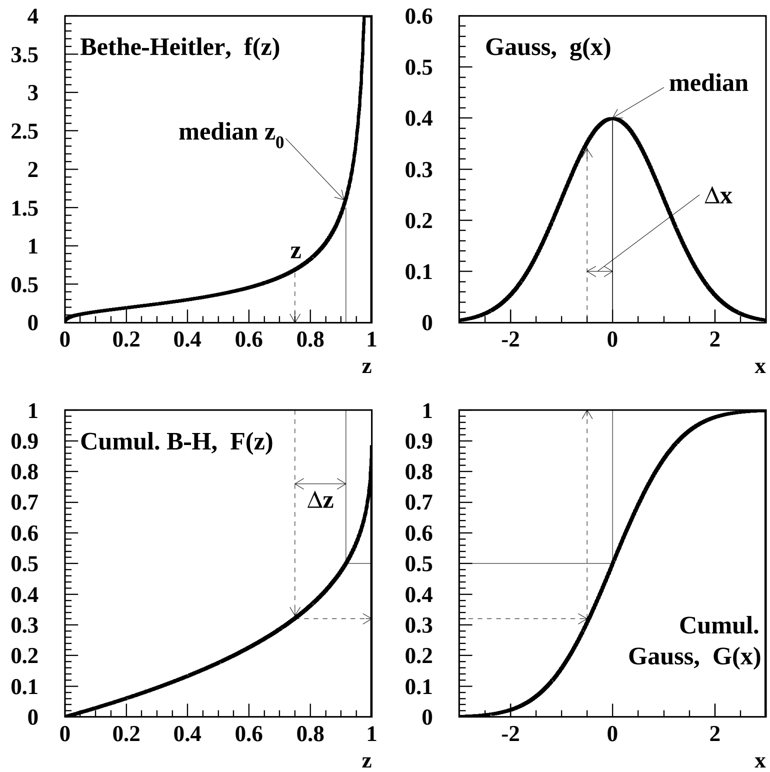

Figure A.3: *Mapping of the Bethe-Heitler distribution onto a gaussian distribution to calculate the effective system-noise variance in the Kalman approach (from [132]).*

model track reconstruction. The top plot shows the electron energy distribution at the second measurement layer where a gaussian fit to the peak illustrates the 3% measurement error combined with some bremsstrahlung noise. In this model, bremsstrahlung is artificially not allowed to occur until after the first measurement layer for the purposes of having a record of the true distribution; the second measurement layer actually represents the first measurement in a real detector by which time some bremsstrahlung may have already occurred which would be impossible to recover without prior knowledge of it having happened. After ten measurement layers, the electron energies measured are smeared across a large range with a small peak left around the initial energy of 100 units. The bottom plot shows the result of the Kalman filtering reconstruction of the true energies, the fit having a sigma of 1.656, much lower than the sigma from just the first measurement (3.045), and close to the theoretical best of 1.0, showing that the Kalman filter was able to extract useful information from further measurements after bremsstrahlung had occurred.

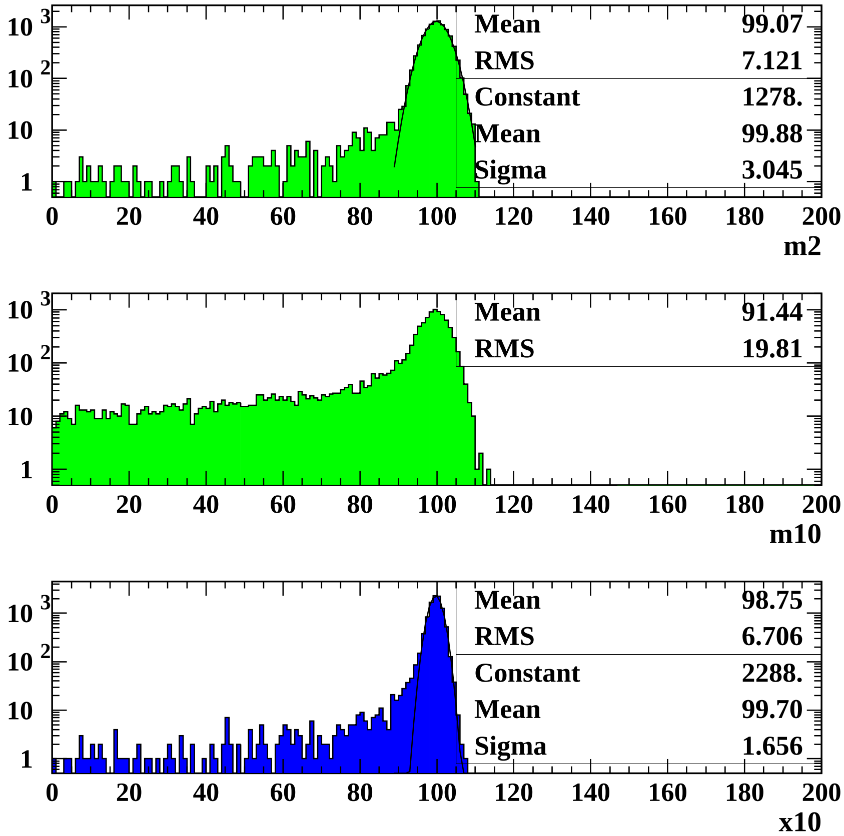

Figure A.4: *Example plots from 1D models of bremsstrahlung recovery with a Bethe-Heitler distribution. Top and middle plots show energy distribution after second and tenth measurement layers, bottom plot shows reconstructed distribution after Kalman filter has been applied.*

A.2 Implementation of DNA in ATLAS

On the basis of the success of this model, a full implementation of the Bethe-Heitler based method was introduced to the Athena Inner Detector tracking package, called the Dynamic Noise Adjustment (DNA) method. As in the standalone algorithm, we flag events which may be associated with a strong bremsstrahlung and an estimate of the fraction of energy z retained by the electron after bremsstrahlung is calculated for such flagged events. The effective $\sigma(z)$ matching the probability of such a z in a Bethe-Heitler cumulative distribution is used to adjust the Kalman noise term as outlined above, to better reconstruct electron events in the Inner Detector. The value of $\sigma(z)$ in the DNA method is not only dependent on the energy fraction, but varies with thickness of the corresponding measurement layer, as shown in Figure A.5.

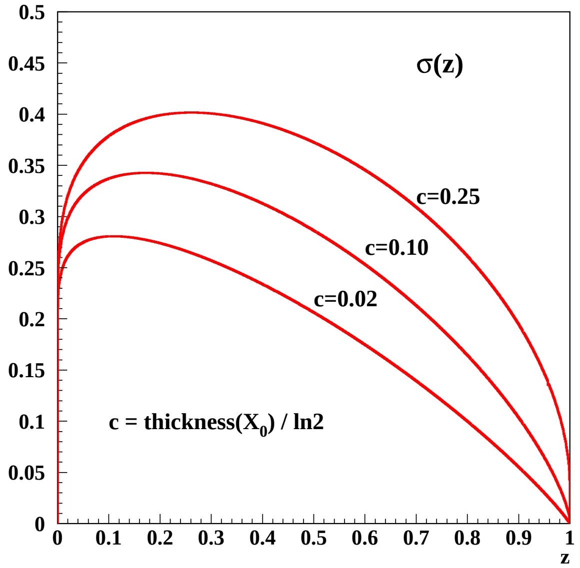

Figure A.5: *Variation of the effective DNA variance term with material thickness c (taken from [132]).*

Figures A.6 and A.7 show a comparison of the results of the DNA method to the standard Kalman algorithm for track reconstruction of a sample of 3000 electrons with a 2 GeV and 20 GeV initial energy respectively. In each case, the top row shows the results for standard track reconstruction and the bottom row shows the preliminary results from the DNA fit without any tuning or optimisation. The first plot shows the reconstructed momentum and in both cases the DNA method outperforms the standard tracking both in terms of number of events reconstructed and the accuracy of reconstruction (although the difference is more pronounced for the 2 GeV case). The second and third plots illustrate the errors assigned to the reconstructed momentum values and the accuracy of this error assignment. Again the DNA method better estimates the errors for each events, producing a pull distribution closer to the ideal standard normal distribution and error assignment exhibiting multiple peaks, each peak corresponding to those events which experience a certain number of bremsstrahlung emissions.

As the DNA algorithm is tuned for electron reconstruction, when applied to other particles such as pions or muons a slight deterioration in fit quality is observed. Efforts are ongoing to investigate the differences in behaviour in fitted momentum between electron and other particle tracks to reduce this effect. Table A.1 gives an indication of the false activation activity of the

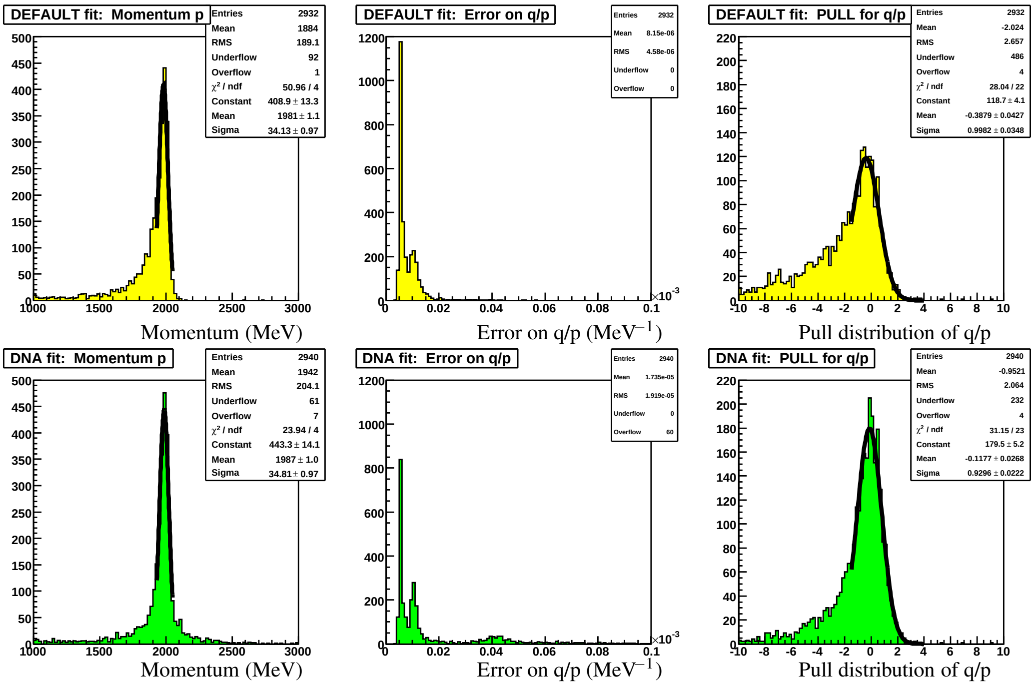

Figure A.6: *Plots of reconstructed momentum (MeV) (left), error distribution (centre) and pull distribution (right) for a sample of 3000 reconstructed 2 GeV electrons. Y-axis in each plot shows number of events reconstructed.*

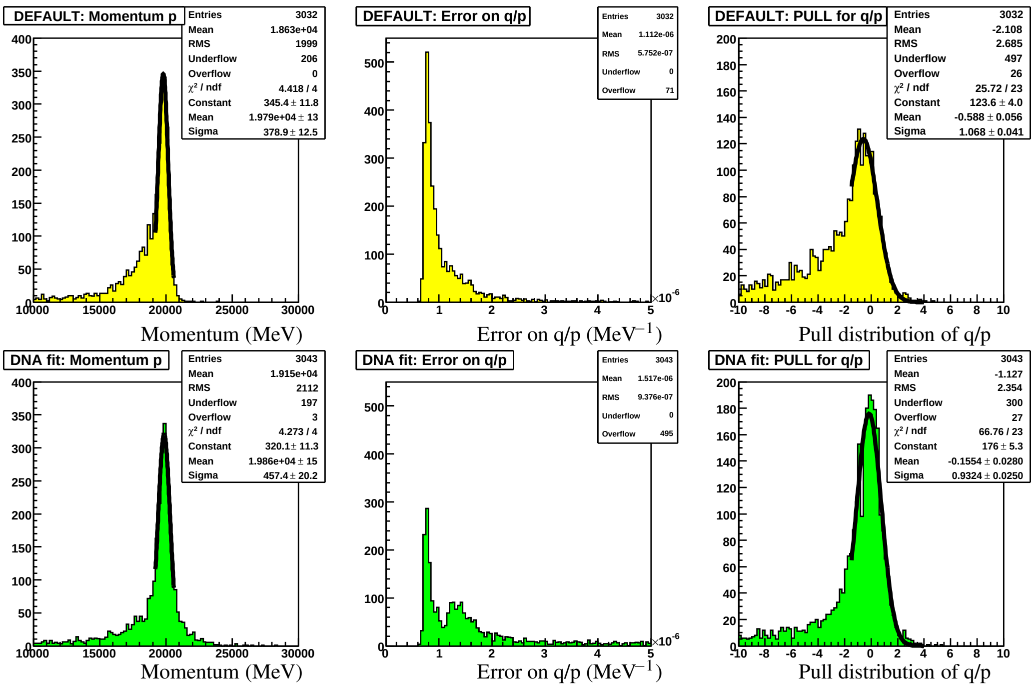

Figure A.7: *Plots of reconstructed momentum (MeV) (left), error distribution (centre) and pull distribution (right) for a sample of 3000 reconstructed 20 GeV electrons. Y-axis in each plot shows number of events reconstructed.*

DNA fit when applied to pions and muons. In the electron case 27% of electron tracks have flagged bremsstrahlung activity. Pions and muons should be unaffected by DNA, but around 1% have their tracks modified by the algorithm.

Particle	# DNA activity	# Standard tracking	Total
Pion	135	7573	7708
Muon	92	8317	8409
Electron	1978	5472	7350

Table A.1: *The effect of DNA intervention on reconstructed 2 GeV single pion, electron and muon 10k event test samples.*

Overall, the DNA tracking method produces reconstruction results that outperform the standard tracking 'out-of-the-box' without any fine-tuning, providing both improved resolution and reconstruction efficiency. The algorithm employs a method based more closely on the underlying physical process and is fast enough to be used for online correction of tracks during the initial track reconstruction, adding approximately a 10% overhead to the default fit when the DNA algorithm is employed.

A.2.1 Other bremsstrahlung tracking algorithms in ATLAS

Kalman fitter (KF)

The Kalman fitter (KF) is the default track fitter in ATLAS, based on the Kalman filtering technique for track fitting described in reference [130]. The algorithm employs progressive calculation of the track parameters at each measurement point to improve overall track determination, using both forward filtering and backward 'smoothing' of the track to improve fit quality.

Due to the requirements of the Kalman method this algorithm uses a gaussian distribution for modeling of bremsstrahlung energy loss. The Dynamic Noise Adjustment method uses this algorithm as a base, and extends it with improved bremsstrahlung modeling and electron identification handling.

Gaussian Sum Filter (GSF)

The Gaussian Sum Filter (GSF) [133] algorithm has a different approach to connecting a good description of the bremsstrahlung energy loss to the requirement of the Kalman fitter that such a process needs to be described by gaussian-distributed noise.

GSF approximates the Bethe-Heitler distribution by a sum of several gaussian distributions that take into account the asymmetry of the true distribution and the long low energy tail. In the GSF method several Kalman filters run in parallel. Despite algorithmic techniques to reduce complexity of the calculations, GSF has the major disadvantage that it takes one to two orders of magnitude longer to perform the track fit calculation than the Kalman Fitter.

GSF does however perform successfully at dealing with bremsstrahlung effects, improving the effective track resolution for 10 GeV electrons from around 10% to 8%, showing similar levels of improvements to the DNA fitter.

Global χ^2 fitter (GXF)

The Global χ^2 fitter (GXF) uses a different philosophy to the previous algorithms for fitting tracks. In this method the track is fitted through the minimisation of a global χ^2 value (hence the name) following a technique as described in reference [134]. The GXF method uses a gaussian noise term and minimises the χ^2 of hit residuals at every measurement surface to calculate the best track trajectory.

Unlike the previous algorithms therefore, the GXF fitter does not perform measurement updates progressively at each detector surface, but performs a global fit through the solution of a set of linear equations. GXF performs well in efficiency of reconstructing electrons that have undergone bremsstrahlung, but as described in the next section, many of those electrons the algorithm does reconstruct do not have their track parameters corrected properly for bremsstrahlung.

A.3 Application to quarkonium reconstruction

Moving beyond single track reconstruction, the ultimate aim is to be able to improve the identification and reconstruction efficiency of the parent particles of electrons and hence the measured resolutions of these particles. In this section I present a study of the application of various algorithms to the reconstruction of $J/\psi(e^+e^-)$ in $B_d \to J/\psi(e^+e^-)K_s^0$ events.

Studying this places more stringent requirements on the performance of the algorithms as a di-electron invariant mass spectrum is much more sensitive to bremsstrahlung. The $J/\psi(e^+e^-)$ peak requires that both electrons in a particular decay are well-reconstructed, rather than just one, if a good candidate is to be observed near the true mass, and the constraint that the two electrons meet at a common vertex also force the track parameters to be well-measured. In addition, the inclusion of the electrons in 'real' physics events with variations of quantities such as electron pair opening angle and J/ψ momentum provide a more realistic setting in which to study performance.

In the following datasets we require that the reconstructed tracks are within $|\eta| < 2.5$, and that Monte Carlo matched tracks are not created by Geant-4 simulation. We impose the following track quality cuts:

1. Reconstructed track transverse momentum $p_T > 0.5$ GeV
2. Vertexing requirements: $|z_0^{\text{rec}}| < 1$ mm, $|d_0^{\text{rec}}| < 2$ mm, $|d_0^{\text{rec}}/\sigma(d_0^{\text{rec}})| < 500$
3. At least one silicon pixel hit (to give a high quality measurement point)

In addition, each oppositely-charged reconstructed and Monte Carlo matched electron pair is constrained to a common vertex using the CTVMFT vertex fitter. Only those pairs for which convergence of the fit is achieved are considered.

We consider a sample of the same 2,500 $B_d \to J/\psi(e^+e^-)K_s^0$ events, reconstructed with the standard Kalman Fitter, Global χ^2 Fitter and Dynamic Noise Adjustment algorithms. In each case, electron tracks are reconstructed, and matched to the Monte Carlo $J/\psi(e^+e^-)$ tracks to ensure the correct electrons are considered in each case. The results are tabulated in Table A.2.

	KF	GXF	DNA		
			Activity	None	Total
MC Matched	4752 (95.0%)	4827 (96.5%)	–	–	4785 (95.7%)
1-track	281	224	79	176	255
2-track	4348 (87.0%)	4454 (89.1%)	1239	3175	4414 (88.3%)
3(+)-track	123	149	24	92	116

Table A.2: *Analysis of GXF, KF and DNA algorithm performance on 2,500 reconstructed $J/\psi(e^+e^-)$ events (5,000 electron tracks). The '2-track' row corresponds to successfully reconstructed and Monte Carlo matched e^+e^- pairs. The DNA column is split by those events where bremsstrahlung activity is seen and those where it is not.*

The '1-track' row contains those events where only one electron was successfully reconstructed or matched, so no J/ψ can be reconstructed: the event is effectively lost. The '3(+)-track' row contains events where more electron candidates have been matched to the two true electrons, representing ambiguity in the reconstructed candidates. This leads to additional combinatorial background, and should be considered an instance of failure for the J/ψ reconstruction. The '2-track' row contain events where both electrons from the J/ψ have been successfully reconstructed.

From Table A.2 one can see that the GXF algorithm has slightly better efficiency at reconstructing MC-matched electron tracks (96.5%) versus DNA (with 95.7%) and associating these with a J/ψ (89.1% versus 88.3%). The standard Kalman Filter performs the worst, as would be expected. Note the bremsstrahlung activity seen in the DNA algorithm: 1239 out of 4414 electron tracks associated with a J/ψ are found to have a significant bremsstrahlung corrected for by the DNA algorithm.

Fitter	Total	Above 2.5 GeV	Above 2.8 GeV
GXF	4454	2336	1426
KF	4348	2488	1632
DNA	4414	2668	1854

Table A.3: *Comparison of the DNA, GXF and Kalman algorithms for the reconstruction of $J/\psi(e^+e^-)$ (shown in Figure A.8) with progressively tighter invariant mass cuts.*

However, this is not the final word, as Table A.2 contains electrons from J/ψ successfully reconstructed with no further quantification. Of central importance to J/ψ reconstruction is the

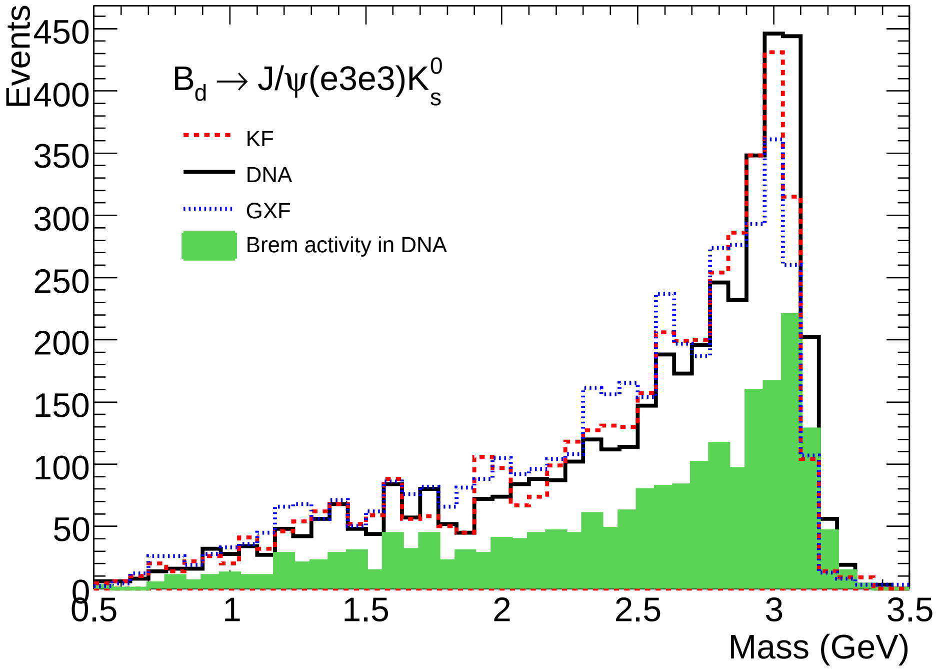

Figure A.8: *Comparison of the DNA, GXF and Kalman algorithms for the reconstruction of $J/\psi(e^+e^-)$ in $B_d \rightarrow J/\psi(e^+e^-)K^0_S$ events. The shaded region shows the specific J/ψ where bremsstrahlung was seen in DNA and, where possible, corrected.*

invariant mass of the electron pair. Figure A.8 shows a comparison of the success of the KF, GXF and DNA algorithms in reconstructing the J/ψ mass. Table A.3 gives the total number of candidates along with the number above two lower mass cuts on the J/ψ peak. An algorithm performing better will have a higher proportion of events nearer the true J/ψ mass position.

Here we see that despite performing best at efficiency of identification of electrons, the Global χ^2 Fitter actually performs worst at reconstruction of the J/ψ invariant mass, surpassed in the high mass ($M > 2.5$) region by even the Kalman Fitter, with DNA performing by far the best, successfully reconstructing over 17% more J/ψ than GXF and nearly 9% more than KF for masses greater than 2.8 GeV. This suggests that the additional electron efficiency for GXF comes from extremely badly measured electrons, which turn out to be of little use for J/ψ reconstruction[2)].

In contrast, DNA reconstruction is very successful: the green shaded area in Figure A.8

[2)] This exemplifies the importance of performing studies on physics events in addition to single particle samples.

shows those J/ψ reconstructed where at least one of the electrons suffered a significant bremsstrahlung. These are events that would otherwise be badly measured or lost, but with the DNA correction the distribution of this subset of events is in fact measured than their standard reconstruction counterparts, having distributions similar (or better) to the well-reconstructed J/ψ with standard algorithms.

A breakdown of the performance of the DNA algorithm on J/ψ reconstruction is illustrated in Figure A.9. This figure compares the KF and DNA algorithms and extracts the additional contribution of the DNA extension to KF from the standard KF reconstruction. The shaded area shows those J/ψ where no bremsstrahlung activity was recorded, so these events are common to KF and DNA. The dashed and solid lines show the KF and DNA attempts on the rest of the events: from Table A.3 we know DNA has an additional 222 J/ψ in the $M > 2.8$ GeV mass region, but in this plot we also see that the DNA activity events have a better mass resolution and have a mean closer to the true mass.

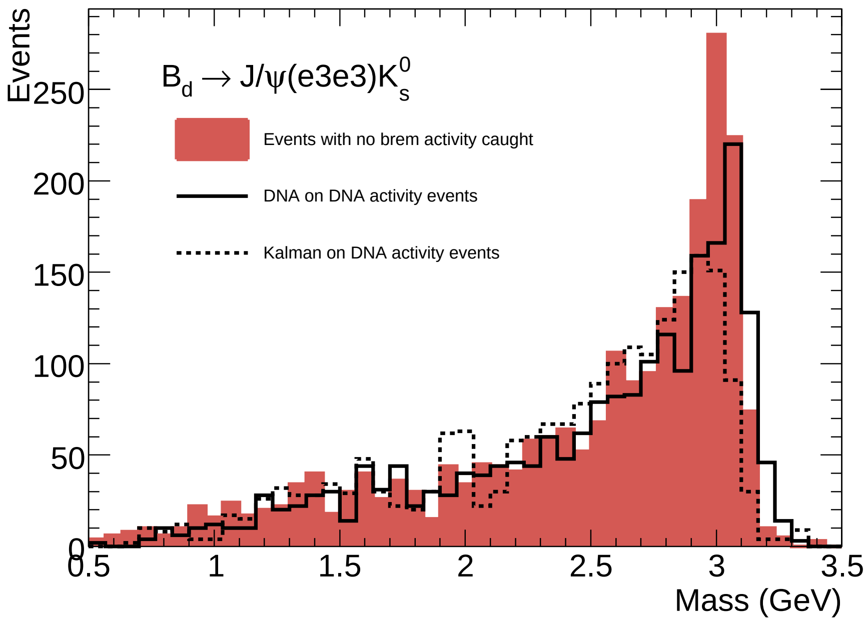

Figure A.9: *Effect of DNA intervention in reconstructed $J/\psi(e^+e^-)$ events. The shaded region shows events without any identified bremsstrahlung activity. The solid and dotted lines show a comparison between the DNA and Kalman algorithms on reconstructing events flagged as having bremsstrahlung activity.*

References

[1] E. Etzion, J. Ginzburg, V. G. Kartvelishvili, D. Price, *"Heavy Quarkonium Production Simulations at ATLAS,"* [ATL-PHYS-INT-2007-001] (2007).

[2] D. Price, A. Dewhurst, J. Ginzburg, M. Smizanska, T. Stahl, W. Walkowiak, *"Low p_T muon and di-muon rates in ATLAS,"* [ATL-PHYS-INT-2008-040, ATL-COM-PHYS-2007-089] (2007).

[3] ATLAS Collaboration, G. Aad et al., *"The ATLAS Experiment at the CERN Large Hadron Collider,"* JINST **3** (2008) S08003

[4] ATLAS Collaboration, *"The Expected Performance of the ATLAS Inner Detector,"* [ATL-COM-PHYS-2008-105] and in *"Expected Performance of the ATLAS Experiment – Detector, Trigger and Physics,"* CERN-OPEN-2008-020, Geneva (2008).

[5] ATLAS Collaboration, *"Heavy quarkonium physics with early ATLAS data,"* [ATL-PHYS-INT-2008-017] and in *"Expected Performance of the ATLAS Experiment – Detector, Trigger and Physics,"* CERN-OPEN-2008-020, Geneva (2008).

[6] D. D. Price, *"Quarkonium production and polarisation with early data at ATLAS,"* Conference proceedings of the 23rd Lake Louise Winter Institute, World Scientific, 2008, ATL-PHYS-PROC-2008-001, arXiv:0808.3367 [hep-ex].

[7] S. L. Glashow, Nucl. Phys. **22**, 579 (1961); A. Salam and J. C. Ward, Phys. Lett. **13** (1964) 168; S. Weinberg, Phys. Rev. Lett. **19**, 1264 (1967).

[8] F. J. Hasert *et al.* [Gargamelle Neutrino Collaboration], Phys. Lett. B **46** (1973) 138.

[9] G. Arnison *et al.* [UA1 Collaboration], Phys. Lett. B **122** (1983) 103; M. Banner *et al.* [UA2 Collaboration], Phys. Lett. B **122** (1983) 476.

[10] C. Amsler *et al.* [Particle Data Group], Phys. Lett. B **667** (2008) 1.

[11] N. Cabibbo, Phys. Rev. Lett. **10** (1963) 531.

[12] J. H. Christenson, J. W. Cronin, V. L. Fitch and R. Turlay, Phys. Rev. Lett. **13** (1964) 138; A. Angelopoulos *et al.* [CPLEAR Collaboration], Phys. Lett. B **444** (1998) 43; B. Aubert *et al.* [BABAR Collaboration], Phys. Rev. Lett. **87** (2001) 091801 [arXiv:hep-ex/0107013]; K. Abe *et al.* [Belle Collaboration], Phys. Rev. D **66** (2002) 071102 [arXiv:hep-ex/0208025].

[13] D. J. Gross and F. Wilczek, Phys. Rev. Lett. **30** (1973) 1343.

[14] R. K. Ellis, W. J. Stirling and B. R. Webber, Camb. Monogr. Part. Phys. Nucl. Phys. Cosmol. **8** (1996) 1.

[15] R. Tarrach, Nucl. Phys. B **183** (1981) 384.

[16] A. S. Kronfeld, Phys. Rev. D **58** (1998) 051501 [arXiv:hep-ph/9805215].

[17] S. Narison, Phys. Rept. **84** (1982) 263; S. Narison, Phys. Lett. B **197** (1987) 405.

[18] I. I. Y. Bigi, M. A. Shifman, N. G. Uraltsev and A. I. Vainshtein, Phys. Rev. D **52** (1995) 196 [arXiv:hep-ph/9405410]; I. I. Y. Bigi, M. A. Shifman, N. Uraltsev and A. I. Vainshtein, Phys. Rev. D **56** (1997) 4017 [arXiv:hep-ph/9704245].

[19] A. H. Hoang *et al.*, Eur. Phys. J. direct C **2** (2000) 1 [arXiv:hep-ph/0001286].

[20] S. L. Glashow, J. Iliopoulos and L. Maiani, Phys. Rev. D **2** (1970) 1285.

[21] J. J. Aubert *et al.* [E598 Collaboration], Phys. Rev. Lett. **33** (1974) 1404.

[22] J. E. Augustin *et al.* [SLAC-SP-017 Collaboration], Phys. Rev. Lett. **33** (1974) 1406.

[23] S. Okubo, Phys. Lett. **5**, 165 (1963); G. Zweig, CERN Reports TH 401 and TH412 (1964); J. Iizuka, Progr. Ther. Phys. Suppl. **37**, 21 (1966).

[24] G. Goldhaber *et al.*, Phys. Rev. Lett. **37** (1976) 255.

[25] W. M. Yao *et al.* [Particle Data Group], J. Phys. G **33** (2006) 1.

[26] S. W. Herb *et al.*, Phys. Rev. Lett. **39** (1977) 252.

[27] F. Abe *et al.* [CDF Collaboration], Phys. Rev. D **50** (1994) 2966; F. Abe *et al.* [CDF Collaboration], Phys. Rev. Lett. **73** (1994) 225 [arXiv:hep-ex/9405005].

[28] I. I. Y. Bigi and H. Krasemann, Z. Phys. C **7** (1981) 127.

[29] B. Aubert *et al.* [BABAR Collaboration], To be published in Phys. Rev. Lett. [arXiv:0807.1086] [hep-ex].

[30] V. M. Aulchenko *et al.* [KEDR Collaboration], Phys. Lett. B **573** (2003) 63 [arXiv:hep-ex/0306050].

[31] W. W. MacKay *et al.* [CUSB Collaboration], Phys. Rev. D **29** (1984) 2483.

[32] A. S. Artamonov *et al.* [OLYA Collaboration], Phys. Lett. B **474** (2000) 427 [arXiv:hep-ex/0001040].

[33] D. P. Barber *et al.* [ARGUS Collaboration], Phys. Lett. B **135** (1984) 498.

[34] T. Appelquist, A. De Rujula, H. D. Politzer and S. L. Glashow, Phys. Rev. Lett. **34** (1975) 365.

[35] N. Brambilla *et al.* [Quarkonium Working Group], *"Heavy quarkonium physics,"* arXiv:hep-ph/0412158.

[36] M. Beneke, *"Nonrelativistic effective theory for quarkonium production in hadron collisions,"* arXiv:hep-ph/9703429.

[37] M. Kramer, Prog. Part. Nucl. Phys. **47** (2001) 141 [arXiv:hep-ph/0106120].

[38] T. Appelquist and H. D. Politzer, Phys. Rev. Lett. **34** (1975) 43.

[39] E. Eichten, K. Gottfried, T. Kinoshita, J. B. Kogut, K. D. Lane and T. M. Yan, Phys. Rev. Lett. **34** (1975) 369 [Erratum-ibid. **36** (1976) 1276].

[40] M. Peter, Phys. Rev. Lett. **78** (1997) 602 [arXiv:hep-ph/9610209]; Y. Schroder, Phys. Lett. B **447** (1999) 321 [arXiv:hep-ph/9812205].

[41] E. Eichten, K. Gottfried, T. Kinoshita, K. D. Lane and T. M. Yan, Phys. Rev. D **17** (1978) 3090 [Erratum-ibid. D **21** (1980) 313]; E. Eichten, K. Gottfried, T. Kinoshita, K. D. Lane and T. M. Yan, Phys. Rev. D **21** (1980) 203.

[42] E. J. Eichten, K. Lane and C. Quigg, Phys. Rev. D **73** (2006) 014014 [Erratum-ibid. D **73** (2006) 079903] [arXiv:hep-ph/0511179].

[43] A. Martin, Phys. Lett. B **100** (1981) 511.

[44] C. Quigg and J. L. Rosner, Phys. Lett. B **71** (1977) 153.

[45] J. L. Richardson, Phys. Lett. B **82** (1979) 272.

[46] B. Z. Kopeliovich and J. Raufeisen, Lect. Notes Phys. **647** (2004) 305 [arXiv:hep-ph/0305094].

[47] W. Buchmuller and S. H. H. Tye, Phys. Rev. D **24** (1981) 132.

[48] M. B. Voloshin, *"Charmonium,"* arXiv:0711.4556 [hep-ph].

[49] G. Altarelli and G. Parisi, Nucl. Phys. B **126** (1977) 298; V. N. Gribov and L. N. Lipatov, Sov. J. Nucl. Phys. **15** (1972) 438 [Yad. Fiz. **15** (1972) 781]; Y. L. Dokshitzer, Sov. Phys. JETP **46** (1977) 641 [Zh. Eksp. Teor. Fiz. **73** (1977) 1216].

[50] J. Pumplin, D. R. Stump, J. Huston, H. L. Lai, P. Nadolsky and W. K. Tung, JHEP **0207** (2002) 012 [arXiv:hep-ph/0201195].

[51] A. D. Martin, R. G. Roberts, W. J. Stirling and R. S. Thorne, Eur. Phys. J. C **23** (2002) 73 [arXiv:hep-ph/0110215].

[52] Durham HEP Database, http://durpdg.dur.ac.uk/

[53] J. C. Collins, D. E. Soper and G. Sterman, Nucl. Phys. B **261** (1985) 104; G. T. Bodwin, Phys. Rev. D **31** (1985) 2616 [Erratum-ibid. D **34** (1986) 3932]; J. C. Collins, D. E. Soper and G. Sterman, Nucl. Phys. B **308** (1988) 833.

[54] V. G. Kartvelishvili, A. K. Likhoded, S. R. Slabospitsky, Sov. J. Nucl. Phys. **28** (1978) 678; M. Gluck, J. F. Owens and E. Reya, Phys. Rev. D **17** (1978) 2324; V. G. Kartvelishvili, A. K. Likhoded, Sov. J. Nucl. Phys. **39** (1984) 298; E. L. Berger and D. L. Jones, Phys. Rev. D **23** (1981) 1521; R. Baier and R. Rückl, Z. Phys. C **19** (1983) 251; B. Humpert, Phys. Lett. B **184** (1987) 105.

[55] C. Albajar *et al.* [UA1 Collaboration], Phys. Lett. B **256** (1991) 112.

[56] E. W. N. Glover, A. D. Martin and W. J. Stirling, Z. Phys. C **38** (1988) 473 [Erratum-ibid. C **49** (1991) 526].

[57] F. Abe *et al.* [CDF Collaboration], Phys. Rev. Lett. **69** (1992) 3704.

[58] F. Abe *et al.* [CDF Collaboration], Phys. Rev. Lett. **79** (1997) 578.

[59] F. Abe *et al.* [CDF Collaboration], Phys. Rev. Lett. **75** (1995) 4358.

[60] E. Braaten and S. Fleming, Phys. Rev. Lett. **74** (1995) 3327 [arXiv:hep-ph/9411365].

[61] E. Braaten and T. C. Yuan, Phys. Rev. Lett. **71** (1993) 1673 [arXiv:hep-ph/9303205].

[62] H. Fritzsch, Phys. Lett. B **67** (1977) 217.

[63] J. F. Amundson, O. J. P. Eboli, E. M. Gregores and F. Halzen, Phys. Lett. B **390** (1997) 323 [arXiv:hep-ph/9605295].

[64] R. Gavai, D. Kharzeev, H. Satz, G. A. Schuler, K. Sridhar and R. Vogt, Int. J. Mod. Phys. A **10** (1995) 3043 [arXiv:hep-ph/9502270].

[65] R. Balest *et al.* [CLEO Collaboration], Phys. Rev. D **52** (1995) 2661.

[66] S. Chen *et al.* [CLEO Collaboration], Phys. Rev. D **63** (2001) 031102 [arXiv:hep-ex/0009044].

[67] A. Abulencia *et al.* [CDF Run II Collaboration], Phys. Rev. Lett. **98** (2007) 232001 [arXiv:hep-ex/0703028].

[68] C. Morel *et al.* [UA6 Collaboration], Phys. Lett. B **252** (1990) 505 [Helv. Phys. Acta **63** (1990) 541].

[69] A. Edin, G. Ingelman and J. Rathsman, Phys. Lett. B **366** (1996) 371 [arXiv:hep-ph/9508386]; A. Edin, G. Ingelman and J. Rathsman, Z. Phys. C **75** (1997) 57 [arXiv:hep-ph/9605281].

[70] A. Edin, G. Ingelman and J. Rathsman, Phys. Rev. D **56** (1997) 7317 [arXiv:hep-ph/9705311].

[71] J. Damet, G. Ingelman and C. Brenner Mariotto, JHEP **0209** (2002) 014 [arXiv:hep-ph/0111463].

[72] G. T. Bodwin, E. Braaten and G. P. Lepage, Phys. Rev. D **51** (1995) 1125 [Erratum-ibid. D **55** (1997) 5853] [arXiv:hep-ph/9407339].

[73] M. Cacciari and M. Kramer, Phys. Rev. Lett. **76** (1996) 4128 [arXiv:hep-ph/9601276].

[74] C. Adloff *et al.* [H1 Collaboration], Eur. Phys. J. C **10** (1999) 373 [arXiv:hep-ex/9903008].

[75] G. P. Lepage, L. Magnea, C. Nakhleh, U. Magnea and K. Hornbostel, Phys. Rev. D **46** (1992) 4052 [arXiv:hep-lat/9205007].

[76] G. T. Bodwin, E. Braaten, T. C. Yuan and G. P. Lepage, Phys. Rev. D **46** (1992) 3703 [arXiv:hep-ph/9208254]; G. T. Bodwin, E. Braaten and G. P. Lepage, Phys. Rev. D **46** (1992) 1914 [arXiv:hep-lat/9205006].

[77] M. L. Mangano, AIP Conf. Proc. **357** (1996) 120 [arXiv:hep-ph/9507353].

[78] G. C. Nayak, J. W. Qiu and G. Sterman, Phys. Rev. D **74**, 074007 (2006) [arXiv:hep-ph/0608066].

[79] M. Cacciari and M. Kramer, Phys. Rev. Lett. **76** (1996) 4128 [arXiv:hep-ph/9601276]; P. Ko, J. Lee and H. S. Song, Phys. Rev. D **54** (1996) 4312 [Erratum-ibid. D **60** (1999) 119902] [arXiv:hep-ph/9602223].

[80] A. A. Affolder *et al.* [CDF Collaboration], Phys. Rev. Lett. **85** (2000) 2886 [arXiv:hep-ex/0004027].

[81] M. Beneke and M. Kramer, Phys. Rev. D **55** (1997) 5269 [arXiv:hep-ph/9611218].

[82] E. Braaten, B. A. Kniehl and J. Lee, Phys. Rev. D **62** (2000) 094005 [arXiv:hep-ph/9911436].

[83] [DØ Collaboration], *"Measurement of the polarization of the $\Upsilon(1S)$ and $\Upsilon(2S)$ states in $p\bar{p}$ collisions at $\sqrt{s}$ =1.96 TeV,"* arXiv:0804.2799 [hep-ex].

[84] S. P. Baranov, Phys. Rev. D **66** (2002) 114003; S. P. Baranov, Phys. Rev. D **74**, 074002 (2006); S. P. Baranov and N. P. Zotov, JETP Lett. **86**, 435 (2007) [arXiv:0707.0253 [hep-ph]].

[85] J. Collins and J. W. Qiu, Phys. Rev. D **75** (2007) 114014 [arXiv:0705.2141 [hep-ph]].

[86] J. Campbell, F. Maltoni and F. Tramontano, Phys. Rev. Lett. **98**, 252002 (2007) [arXiv:hep-ph/0703113].

[87] P. Artoisenet, J. Campbell, J. P. Lansberg, F. Maltoni and F. Tramontano, *"Upsilon production at the Tevatron and the LHC,"* arXiv:0806.3282 [hep-ph].

[88] B. Gong and J. X. Wang, *"QCD corrections to polarization of J/psi and Upsilon at Tevatron and LHC,"* arXiv:0805.2469 [hep-ph].

[89] J. P. Lansberg, J. R. Cudell and Yu. L. Kalinovsky, Phys. Lett. B **633** (2006) 301 [arXiv:hep-ph/0507060]; P. Artoisenet, J. P. Lansberg and F. Maltoni, Phys. Lett. **B653**, 60 (2007); P. Artoisenet, *"J/psi production in association with a charm-quark pair at the Tevatron,"* [arXiv:0804.2975 [hep-ph]].

[90] T. V. Uglov, Eur. Phys. J. C **33** (2004) S235.

[91] L. Evans and P. Bryant, *"LHC Machine,"* JINST **3** (2008) S08001

[92] ATLAS Collaboration, *"ATLAS: Detector and physics performance technical design report, Vol. I,"* CERN-LHCC-99-014, ATLAS-TDR-14, (1999).

[93] ATLAS Collaboration, *"ATLAS inner detector: Technical design report, Vol. I,"* CERN-LHCC-97-016, ATLAS-TDR-004, (1997).

[94] ATLAS Collaboration, *"In-Situ Determination of the Performance of the ATLAS Muon Spectrometer"* in *"Expected Performance of the ATLAS Experiment – Detector, Trigger and Physics,"* CERN-OPEN-2008-020, Geneva, (2008).

[95] S. Hassani, L. Chevalier, E. Lancon, J. F. Laporte, R. Nicolaidou and A. Ouraou, Nucl. Instrum. Meth. A **572** (2007) 77.

[96] D. Adams *et al.*, *"Track reconstruction in the ATLAS Muon Spectrometer with* MOORE*,"* [ATL-SOFT-2003-007].

[97] T. Lagouri *et al.*, IEEE Trans. Nucl. Sci. **51** (2004) 3030.

[98] S. Tarem, Z. Tarem, N. Panikashvili, O. Belkind, Nuclear Science Symposium Conference Record, 2006, IEEE **1** (2006) 617.

[99] ATLAS Collaboration, *"Muon Reconstruction and Identification Performance in ATLAS: Studies with Simulated Monte Carlo Samples"* in *"Expected Performance of the ATLAS Experiment – Detector, Trigger and Physics,"* CERN-OPEN-2008-020, Geneva, (2008).

[100] ATLAS Collaboration, *"The ATLAS high-level trigger, data acquisition and controls: Technical design report,"* LHCC 2003-022, CERN, 2003.

[101] ATLAS Collaboration, *"The ATLAS Level-1 Trigger: Technical Design Report,"* LHCC 1998-14, ATLAS-TDR-12, CERN, 1998.

[102] ATLAS Collaboration, *"The ATLAS Trigger for Early Running,"* in *"Expected Performance of the ATLAS Experiment – Detector, Trigger and Physics,"* CERN-OPEN-2008-020, Geneva, (2008).

[103] ATLAS Collaboration, *"Triggering on low p_T muons and di-muons for B-physics,"* in *"Expected Performance of the ATLAS Experiment – Detector, Trigger and Physics,"* CERN-OPEN-2008-020, Geneva, (2008).

[104] T. Sjostrand, S. Mrenna and P. Skands, "PYTHIA *6.4: Physics and manual,"* JHEP **0605** (2006) 026 [arXiv:hep-ph/0603175].

[105] M. Bahr *et al.*, *"Herwig++ Physics and Manual,"* arXiv:0803.0883 [hep-ph].

[106] M. Smizanska, *"PythiaB: An interface to Pythia6 dedicated to simulation of beauty events,"* [ATL-COM-PHYS-2003-038] (2003).

[107] M. Dobbs and J. B. Hansen, Comput. Phys. Commun. **134** (2001) 41.

[108] S. Agostinelli *et al.* [GEANT4 Collaboration], Nucl. Instrum. Meth. A **506** (2003) 250.

[109] E. Richter-Was, D. Froidevaux and L. Poggioli, *"ATLFAST 2.0: a fast simulation package for ATLAS,"* [ATL-PHYS-98-131] (1998).

[110] G. Duckeck *et al.* [ATLAS Collaboration], *"ATLAS computing: Technical design report,"* [CERN-LHCC-2005-022] (2005).

[111] F. Akesson *et al.*, *"ATLAS Inner Detector Event Data Model,"* [ATL-SOFT-PUB-2007-006] (2007).

[112] Worldwide LHC Computing Grid, http://cern.ch/lcg/, retrieved September 2008.

[113] Gaudi/Athena and Grid Alliance (Ganga), http://cern.ch/ganga/, retrieved September 2008.

[114] P. Artoisenet, F. Maltoni and T. Stelzer, JHEP **0802** (2008) 102 [arXiv:0712.2770 [hep-ph]].

[115] M. A. Sanchis-Lozano, Nucl. Phys. Proc. Suppl. **86** (2000) 543 [arXiv:hep-ph/9907497].

[116] P. Nason *et al.*, "Bottom production," arXiv:hep-ph/0003142.

[117] ATLAS Collaboration, *"Cross-sections, Monte Carlo simulations and systematic uncertainties,"* in *"Expected Performance of the ATLAS Experiment – Detector, Trigger and Physics,"* CERN-OPEN-2008-020, Geneva, (2008).

[118] B. Cano-Coloma and M. A. Sanchis-Lozano, Nucl. Phys. B **508** (1997) 753 [arXiv:hep-ph/9706270].

[119] G. A. Schuler, Int. J. Mod. Phys. A **12** (1997) 3951 [arXiv:hep-ph/9702230].

[120] V. M. Abazov *et al.* [DØ Collaboration], Phys. Rev. Lett. **94** (2005) 232001 [Erratum-ibid. **100** (2008) 049902] [arXiv:hep-ex/0502030].

[121] F. Abe *et al.* [CDF Collaboration], Phys. Rev. Lett. **79** (1997) 572; D. E. Acosta *et al.* [CDF Collaboration], Phys. Rev. Lett. **88** (2002) 161802.

[122] E. V. Bouhova-Thacker, *"Model for* $bb \to J/\psi X$ *generation"*, October 2004, unpublished, http://cern.ch/msmizans/production/dc2/generators/Btojpsix_note.pdf .

[123] J. Marriner, CDF Internal Note 1996 (1993).

[124] N. Konstantinidis *et al.*, *"The Atlantis event visualisation program for the ATLAS experiment,"* In *"Interlaken 2004, Computing in high energy physics and nuclear physics,"* 361-364.

[125] A. Korn, *"Measurement of B-hadron masses at CDF Run II,"* Ph.D. Thesis, Massachusetts Institute of Technology (2004).

[126] D. E. Acosta *et al.* [CDF Collaboration], Phys. Rev. Lett. **96** (2006) 202001 [arXiv:hep-ex/0508022].

[127] A. Ahmad, D. Froidevaux, S. Gonzalez-Sevilla, G. Gorfine and H. Sandaker, *"Inner Detector as-built detector description validation for CSC,"* [ATL-INDET-INT-2007-002] (2007).

[128] A. Abulencia *et al.* [CDF Collaboration], Phys. Rev. Lett. **99** (2007) 132001 [arXiv:0704.0638 [hep-ex]].

[129] ATLAS Collaboration, *"Reconstruction and Identification of Photons"* in *"Expected Performance of the ATLAS Experiment – Detector, Trigger and Physics,"* CERN-OPEN-2008-020, Geneva, (2008).

[130] R. Fruhwirth, Comput. Phys. Commun. **100** (1997) 1.

[131] H. Bethe and W. Heitler, Proc. Roy. Soc. Lond. A **146** (1934) 83.

[132] V. Kartvelishvili [ATLAS Collaboration], Nucl. Phys. Proc. Suppl. **172**, 208 (2007).

[133] R. Fruhwirth, Comput. Phys. Commun. **154** (2003) 131.

[134] L. Bugge and J. Myrheim, Nucl. Instrum. Meth. **179** (1981) 365.